SHEAR LAYER DYNAMICS OF A REACTING JET IN A VITIATED CROSSFLOW

A Dissertation
Presented to
The Academic Faculty

by

Vedanth Nair

In Partial Fulfillment
of the Requirements for the Degree
Doctor of Philosophy in the
School of Aerospace Engineering

Georgia Institute of Technology
December 2020

SHEAR LAYER DYNAMICS OF A REACTING JET IN A VITIATED CROSSFLOW

Approved by:

Dr. Timothy C. Lieuwen, Advisor
School of Aerospace Engineering
Georgia Institute of Technology

Dr. Adam Steinberg
School of Aerospace Engineering
Georgia Institute of Technology

Dr. Suresh Menon
School of Aerospace Engineering
Georgia Institute of Technology

Dr. Ann R. Karagozian
Mechanical & Aerospace Engineering
University of California, Los Angeles

Dr. Devesh Ranjan
School of Mechanical Engineering
Georgia Institute of Technology

Date Approved: 11/25/2020

ACKNOWLEDGEMENTS

First and foremost, I would like to acknowledge my advisor, Professor Timothy Lieuwen and thank him for giving me the opportunity to be a part of his high-achieving research group. His steadfast support and encouragement not only guided the work presented here, but also gave me the confidence to continue my path in research. I would like to thank Professor Adam Steinberg for providing valuable feedback regarding my diagnostic setup as well as the opportunity to further explore my passion of laser diagnostics. I would also like to thank the rest of my dissertation committee, Professors Devesh Ranjan, Ann Karagozian as well as Suresh Menon for their support, invaluable expertise and feedback that has improved the quality of this work. In addition to my committee members, I would like to thank Professor Jerry Seitzman for his expansive discussions that have helped me develop an inquisitive spirit and strengthened my fundamentals in combustion.

The collaborative and highly supportive atmosphere at the Ben T. Zinn combustion lab, inculcated through Prof. Lieuwen's tireless efforts, have made the time spent working towards my PhD enjoyable and highly stimulating. A large part of this credit also goes to the research and technical staff, who were always accessible and went out of their way to help me navigate technical, administrative as well as personal crises. In this regard, I would like to thank Dr. Ben Emerson, Dr. Vishal Acharya, Dr. Oleksandr Bibik, Subodh Adhikari and, David Wu for their infinite patience while answering my every question, as well as their continued support and collaboration, which has made this research possible. I would also like to thank my collaborators at Spectral Energies – Dr. Chris Fugger, Dr. Naibo

Jiang, Dr Tongxun Yi and Dr. Joseph Felver for providing me with the opportunity of working with them on challenging experimental setups and inculcating in me a passion for laser diagnostics.

I would like to thank my friends and colleagues at the combustion lab for providing a sense of community and support. Specifically, I would like to thank Matthew Sirignano for being a mentor, colleague as well as a friend to me. His calm and intelligent approach to problem solving has helped me become a more patient and methodical researcher. I would like to thank Hanna Ek and Debolina Dasgupta, for being a constant source of encouragement, friendship and inspiration. In addition, I would like to thank Sam Grauer, Chris Douglas, Sampath Adusumilli and Dan Fries for providing me with stimulating conversation and valuable support with respect to my research. I have had the good fortune of working with some incredibly skilled graduate and undergraduate researchers. With this regard I would like to thank Lane Dillon and Sydney Hallas for the exhaustive amount of work that they have into our collaborations and being capable, dependent colleagues.

Finally, I would like to acknowledge and thank my family. My significant other, Sanjana Vijayakumar has supported and encouraged me through every step of my PhD and I thank her for her patience, understanding and being a constant source of comfort. I would like to acknowledge the role my parents, Archana and Sanjiv, my grandmother, Gowri and, my brother Advaith, have played in enabling and encouraging me to pursue my passion and providing me with the resources to make it possible. I would also like to thank my cousins, Vinod and Chitra for their support and making my transition to living in the US smooth and enjoyable.

This work was largely supported by the National Science Foundation through the contract #1705649.

TABLE OF CONTENTS

LIST OF TABLES

LIST OF FIGURES

NOMENCLATURE

A_i	Vortex area
A	JICF empirical scaling constant
Λ	Counter-current mixing layer ratio
λ_{ci}	Swirling Strength
b	JICF empirical scaling constant
d_j	Jet diameter
f	Mixture fraction
f_{st}	Stoichiometric mixture fraction
J	Jet to crossflow momentum Flux ratio
l_0	Flow length scale
n	Jet centerline based transverse coordinate
θ	Momentum thickness
p	Pressure
ρ_j	Jet Density
ρ_∞	Crossflow density
R	Jet to crossflow velocity ratio
Re_j	Jet Reynolds number
Re_∞	Crossflow Reynolds number
R_0	Characteristic vortex radius
S	Jet to crossflow density ratio

s	Jet centerline based streamwise coordinate
S'	CCSL density stratification parameter
St	Strouhal number
St_k	Stokes number
St_{δ_ω}	Strouhal number based on vorticity thickness
St'_{δ_ω}	Strouhal number based on vorticity thickness and vortex convection speed
δ_ω	Vorticity thickness
δ_∞	Boundary layer thickness
τ	Shear stress
Γ	Vortex circulation
Γ_2	Vortex identification criterion
t_0	Particle time scale
T_{ad}	Adiabatic flame temperature
T_j	Jet temperature
T_∞	Crossflow temperature
u	Velocity (vector)
u_0	Flow velocity scale
U_C	Vortex convection speed
U_e	Core velocity
u_j	Jet velocity
u_∞	Crossflow velocity
u, v, w	Velocity components
U_u, U_v, U_w	Uncertainty of each velocity component
μ_∞	Crossflow fluid dynamic viscosity

μ_j	Jet fluid dynamic viscosity
$\nabla\vec{v}$	Velocity gradient tensor
ω	Vorticity (vector)
χ	Mole fraction
Y	Mass fraction
y^+	Wall coordinate

SUMMARY

The effects of combustion on the hydrodynamic stability of shear flows is a topic that has warranted attention from researchers over the last fifty years. This is because of the wide range of practical devices that employ combusting flow configurations. The hydrodynamic instabilities in these shear configurations can respond dynamically to the presence of combustion, providing a pathway towards combustion instability, a highly undesirable if not dangerous operational state. Assessing the complex coupling between the flow stability and combustion in these highly turbulent flow configurations is a challenging task and often researchers are limited either by computational costs or the difficulty in experimentally extracting high fidelity flowfield information from reacting flows. In addition, these multi-dimensional systems are highly sensitive to its initial and boundary conditions, parameters that are not always easy to isolate.

This thesis seeks to expand the understanding of the effect of combustion on the hydrodynamic behavior specific to the jet in crossflow (JICF). The JICF is a canonical shear flow that is present in a number of practical configurations including industrial gas turbines. Its complex flow topology, heavily influenced by underlying hydrodynamic instabilities, makes it an attractive configuration to implement when the mixing performance is critical. But, even in its most simple manifestation – a single reacting jet in crossflow, there are a number of governing parameters including the momentum flux ratio (J) and the density ratio (S) as well as jet size (d_j) that significantly change the flowfield dynamics. Consider the presence of a flame and there are now a myriad of new parameters that can have an effect on the flow physics. This consequently increases the dimensionality

of any design problem trying to incorporate this configuration in a practical system. Given the computational cost of simulating such a complex system, the global behavior of a JICF configuration is usually approximated through empirical models. Given that reacting flowfield are relatively poorly studied, these models utilize scalings based on non-reacting flow physics. Given that combustion can fundamentally change the underlying hydrodynamics there is a need to quantify these effects to help incorporate these effects into the design process.

This study seeks to address this gap in literature on how exactly combustion manipulates JICF physics. Previous work has shown that combustion has a suppressive effect on the growth of shear layer instabilities in a JICF. But combustion itself cannot usually assumed to have a global effect on a flow configuration as subtle differences in the local heat release or density stratification can cause significantly different stability behavior. Thus, this work expands the parameters of interest for an RJICF configuration to consider the effect of moving the flame position with respect to the shear layer, in addition to the effects of changing J and S. A series of experiments were designed around systematically varying these parameters with the objective of capturing high-fidelity flow field data using high-speed time resolved Stereo particle image velocimetry (SPIV) to describe the velocity and OH- planar laser induced fluorescence (OH-PLIF) to infer the flame and reaction zone structure.

The velocity data was used to extract metrics correlated with the shear layer strength allowing for the spatial growth rate to be assessed across the different experimental parameters. To this effect the range of momentum flux ratios, $6 < J < 30$ and density ratios, $0.35 < S < 1.75$ were chosen based on quantifying the shear layer growth across

conditions that lay on either side of the convective to global instability transition ($J_{crit} < 10, S_{crit} < 0.45$). For the reacting cases, two flame configurations – one with the flame outside the shear layer (R1) and one with the flame inside (R2), were used to observe the effect of changing the location of local heat release with respect to the shear center. The results indicated that structural characteristics of the JICF including the growth of shear layer instabilities and the turbulent breakdown of the jet structure were highly dependent on the presence of combustion as well as S but were weakly dependent on J. Moving the flame inside the shear layer was also noted to have a dramatic effect on the flow topology leading to the almost complete suppression of vortex rollup in the nearfield.

Time-resolved SPIV data was further used to extract the characteristic frequencies and enable the classification of instability behavior (convective vs globally unstable) based on the spectral characteristics. Attempts to collapse the dependencies of these characteristic frequencies with a Strouhal number (St) led to the understanding that density stratification influences both the characteristic length scales as well as the characteristic velocity scales of the shear layer instabilities. This observation was used to collapse the effect of combustion for the R1 type configurations by representing them through an analogous stratification parameter but was unsuccessful in collapsing the behavior for cases where the flame lay inside the shear layer (R2). Thus, the effect of combustion was noted to be highly configuration specific. In some cases it could be explained purely by accounting for the impact of the flame through quantifying the imposed stratification, while in other cases, the presence of local heat release had a significant impact on the vorticity dynamics and shear layer stability unrelated to any imposed density stratification.

Based on the extracted stability characteristics including the growth rate and the transitional behavior, the traditional JICF parameters J and S were unable to uniquely describe the stability behavior of both non-reacting and reacting conditions in this study. Thus, the counter-current shear layer (CCSL) model was evaluated to try to address this by mapping the parameters J and S into a new set of parameters Λ, the counter current velocity ratio and S', a density ratio which is equivalent to S for NR cases but attempts to capture the flame imposed density stratification in the reacting cases. The stability behavior of the NR and R1 cases collapse well in the $S' - \Lambda$ parametric space and show good agreement with theoretically predict transitional values for these parameters. The R2 cases, on the other hand, further demonstrate that the topology of this configuration is fundamentally different and therefore its impact on the flowfield cannot be simply quantified through the parameters S' or Λ.

The $S' - \Lambda$ mapping demonstrated that transition through global instability occurred through two pathways – 1) through increasing the magnitude of counterflow and thereby reaching Λ_{crit} similar to a CCSL and 2) through the reduction in density and transition via S'_{crit}. This has broader implications on the design of JICF experiments since the dependence between J and Λ is not unique. To understand which pathway to global instability will be dominant requires characterizing the boundary conditions of the system in order to obtain this mapping from J to Λ.

CHAPTER 1. INTRODUCTION

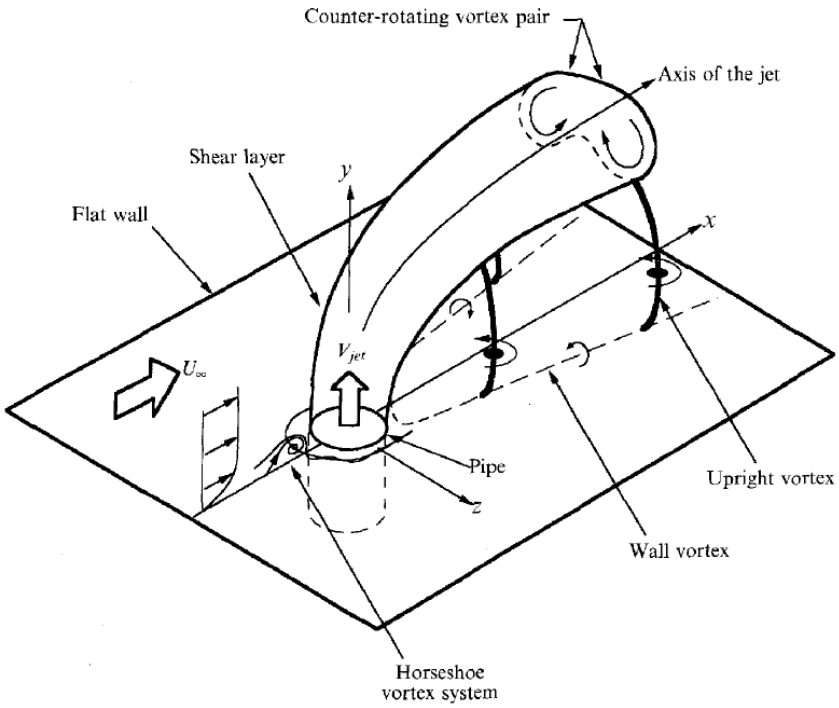

Figure 1.1: JICF schematic detailing major flow features [1].

The jet in crossflow (JICF) is a flow configuration that, in many forms, is ubiquitous in many practical aerospace/thermal power systems. In essence, the flow configuration consists of a single jet injected transversely to a crossflow that can form a small part of a much larger flowfield, for example, cooling jets along a combustor liner [2] or, even the focal point of the system, as in the case of an axially staged fuel jet in a gas turbine [3]. The term JICF has come to encompass a diverse set of flow types, including multiphase flows such as, liquid jets injected into a gaseous crossflow, granular flows on an atmospheric scale, i.e. volcanic plumes, or compressible flows like jets injected into a supersonic crossflow. This thesis will focus on the subtype of single-phase gaseous jets injected transversely into a gaseous crossflow (Figure 1.1).

While there are a plethora of implementations of single phase gaseous JICF, the practical applications most relevant to the conditions studied in this thesis are gas turbine combustor flowfields, where the JICF is a popular choice of mixing two fluids due to its excellent mixing behavior and ease of implementation. As a result, its implementation is highly intertwined with combustor design goals, such as reducing emissions, controlling the pattern factor through mixing, avoiding thermo-acoustic instabilities and improving the efficiency [4]. Despite its simplicity, analyzing the behavior of transverse jets in a combustor environment increases the number of design variables and expands the parametric space. This has motivated over half a century of research on the behavior of this canonical flowfield [5, 6].

This chapter will provide some background on the wealth of literature that has laid the foundation for JICF research and explore the gaps which motivate the current study. Section 1.1 will cover the implementation of JICF in practical applications limited to gas turbine combustors to provide motivation for the study of JICF behavior from the perspective of combustor design. Section 1.2 will cover the fundamental global parameters for non-reacting and reacting JICF. The complex coherent structures that form the JICF flowfield and associated hydrodynamic instability behavior will be covered in Sections 1.3 and 1.4. While there are few studies specifically analyzing the effect of combustion on the flow topology and instabilities in a JICF, there have been a lot of studies on other free-shear type flowfields, which provide an important basis for similar analysis in a JICF and will be covered in Section 1.5. Finally, Section 1.6 will outline the specific research goals and layout of this thesis.

1.1 Gas-turbine specific applications

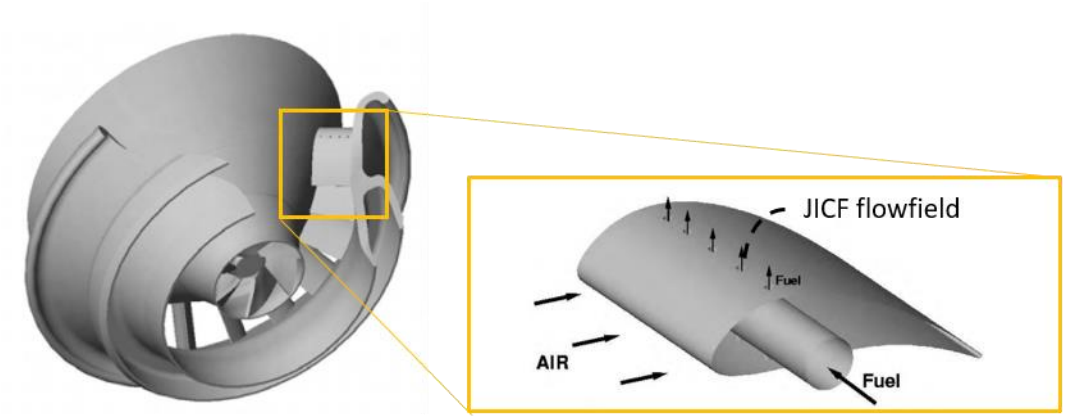

Figure 1.2: JICF type fuel injection on a single vane in the premixing section of a swirl type Lean Premixed combustor; adapted from Schlüter et al. [7].

In ground power and aviation gas turbines, the quest for lowering emissions while improving efficiency has pushed manufacturers into evaluating novel design strategies. One such strategy involves premixing the air and the fuel before introduction in the combustor, and it is coined as Lean Premixed (LP) technology. The challenge is often to premix the fuel with the main flow containing air to a high degree prior to combustion, while keeping in mind geometric constraints governing the length of the combustor. As a result, injecting the fuel transversely is an attractive option due to the excellent mixing characteristics of the JICF. Here, design parameters including the size and shape of the hole and, the velocity ratio between the fuel and the cross-stream, are chosen to optimize mixing while also minimizing the possibility of flashback into the jet [7]. Typically, the mixing problem in this configuration occurs in a non-reacting environment in the premixing section before the combustion chamber as seen in Figure 1.2.

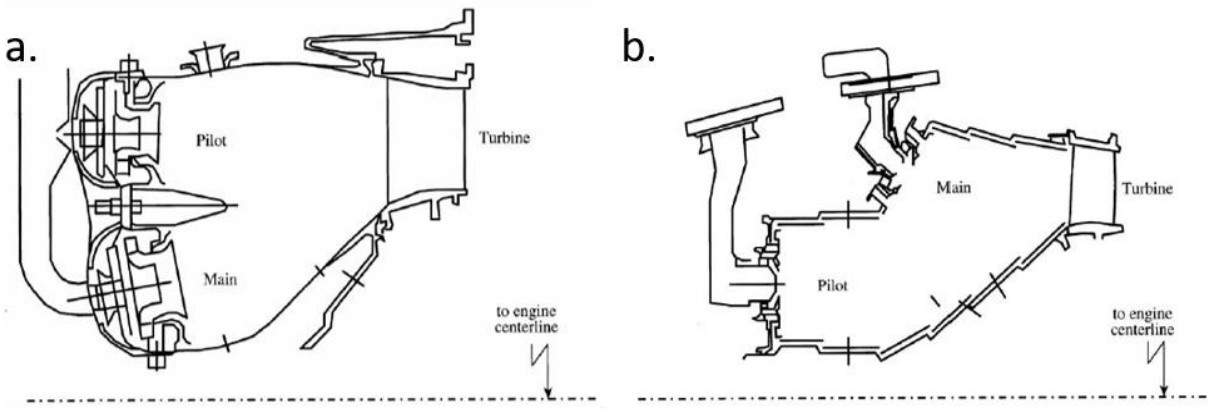

Figure 1.3: Schematics of a) radial and b) axial fuel staging concepts in a LP-type combustor; adapted from Correa [3].

While the LP concept is simple, in practice there are difficulties associated with ensuring lean-premixed and stable combustion at all locations while allowing for turndown or part load conditions. To achieve this while ensuring lean combustion, axial or radial staging is often used to provide greater control at part load. While the JICF can manifest itself in either implementation, radial staging typically involves staggered use of multiple injector assemblies where the JICF is present in a non-reacting environment as covered in the earlier paragraph. Successfully implementing axial staging on the other hand requires an in-depth knowledge of flow physics of the JICF in reacting environment.

Most axially staged combustion concepts involve secondary reaction zone through introducing a fuel and/or a premixed fuel-air mixture in the combustion chamber or transition section of a gas turbine. In the case of staged lean combustion, as in Figure 1.4, the secondary fuel mixture is injected into a vitiated flow where the high temperature and presence of excess oxygen, from the lean combustion in the primary zone, allow for flame-stabilization. Another variant of the staged combustion concept is manifested in aero engine, Rich-Quench-Lean (RQL) type combustors where large JICF type injectors are

used to add dilution air to a crossflow consisting of the products of rich combustion in the primary burner (Figure 1.5). The primary burner is run at a fuel-rich condition, which has the added benefit of being more stable, followed by the addition of dilution air to significantly bring down the flow temperature and burn out the excess fuel while mitigating NOx emissions.

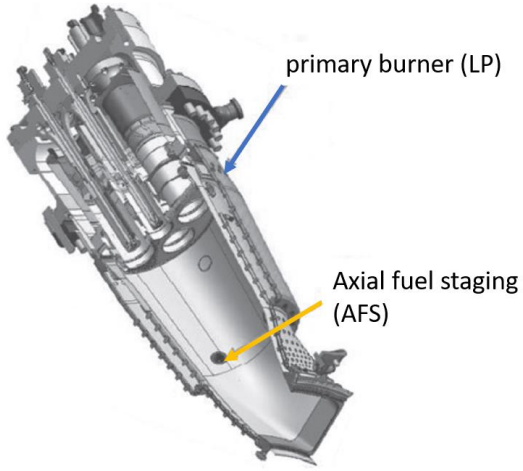

Figure 1.4: Schematic of a GE DLN 2.6+ combustion chamber with axial fuel staging (AFS) in the transition section [8].

From a design point of view of either of the staged combustion strategies listed above, the introduction of a secondary fuel/air source considerably increases the complexity of the combustor. This is because engine design metrics like efficiency, emissions generation (particularly NOx) and turbine pattern factor depend primarily on the local combusting environment in the combustor, which is considerably more complex due to the secondary reaction zone and reacting jet in crossflow (RJICF). In addition to this, geometric constraints and thermal loss considerations provide practical limits on the length of the combustor permissible which makes controlling mixing and the flame stabilization location a key challenge. Thus, RJICF research has been motivated by the following goals:

1) understanding the sensitivity of global metrics like NOx production and mixedness to JICF design parameters such as the geometry of the injector, mass flow splits and choice of fuel [9]. 2) The in-depth analysis of the flow physics associated with a reacting jet in crossflow and the impact of reactions on the known non-reacting flowfield [10]. 3) Understanding JICF/RJICF behavior in noisy combusting environments and interactions with unsteady flow phenomena and acoustic instabilities.

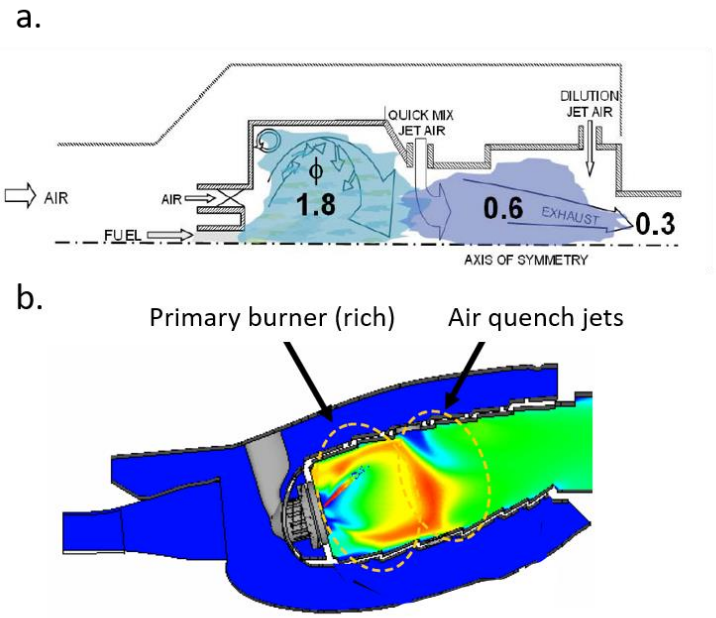

Figure 1.5: a) Schematic of an RQL type combustor architecture [2] and b) sketch of a Pratt & Whitney TALON X combustor [11].

1.2 Global JICF dynamics

Before delving into a more detailed review of relevant JICF literature, this section will introduce the primary governing parameters of the problem as well as global jet metrics for both non-reacting and reacting jets. These parameters often appear as design parameters while designing the JICF flowfield in practical combustion systems and thus,

most of the results presented in this thesis will demonstrate sensitivities of both local and global jet behavior to these parameters.

1.2.1 Jet trajectory

Starting with the canonical description of the flowfield, a jet of velocity u_j and density ρ_j is injected transversely into a crossflow of bulk velocity u_∞ and density ρ_∞. As the jet fluid pushes into the crossflow it bends and deflects until the bulk of its momentum is aligned with the crossflow. Although the mechanisms involved in this deflection are complex on an instantaneous basis and involve the redistribution of vorticity (Section 1.3), there is an interest from a design standpoint in simply quantifying the global form or path of the jet flow, called the jet trajectory. While this may seem simple conceptually, the choice of flow metric is ambiguous and studies in the past have used varied metrics including the locus of maximum velocity [12], the maximum scalar concentration [13], temperature distribution [14] or the center-streamline [15]. Pratte and Baines [16] investigated the JICF trajectory and provided an empirical scaling based on the jet-to-crossflow momentum flux ratio J which is related to the flow quantities by:

$$J = \frac{\rho_j u_j^2}{\rho_\infty u_\infty^2} \tag{1.1}$$

The scaling takes the form:

$$\frac{y}{Rd_j} = A\left(\frac{x}{Rd_j}\right)^b \tag{1.2}$$

where x and y are the horizontal and vertical Cartesian coordinates, d_j is the jet diameter, R is the density weighted velocity ratio (referred to as just the velocity ratio, r in iso-density conditions) and is related to J as $R = \sqrt{J}$. The constants are empirically determined constants and were found to have the values A = 2.05 and b = 0.28 [16]. Another important parameter is the density ratio, generally denoted as $S = \rho_j/\rho_\infty$, particularly in practical applications where there is often a large density difference between the jet and the crossflow due to the difference of gases or flows with combustion/vitiation. Broadwell and Briedenthal [17] modeled the JICF flowfield using two counter-rotating vortex lines and derived an expression, similar to Eq. **1.2**, based on the lift induced by the vortices, finding that b = 0.33. Empirically, there is a wide variation in the computed constants and values from multiple studies which span $1.2 \leq A \leq 2.6$ and $0.25 \leq b \leq 0.34$ [6]. This variance suggests that there may be other flow parameters which contribute to the trajectory behavior which may not be captured in Eq. **1.2**, leading to Kamotani and Greber [13] suggesting that the constant $A \sim R^C$.

Some studies, including Hasselbrink and Mungal [18], investigated the possibility of breaking up the scaling into two separate models for the near-field and the far-field region. This is supported by the hypothesis that the near field has a 'jet' like behavior, where the transverse momentum dominates the scaling and that the far field has a 'wake' like behavior governed by the axial momentum deficit. Typically, most analytical scalings of this type require an entrainment model and as a result are considerably more complex than the scaling presented in Eq. **1.2**.

Muppidi and Mahesh [19] demonstrated that, in addition to the bulk flow parameters, the shape of the jet and the crossflow velocity profile can have a significant impact on the trajectory. Assuming that jet deflection is dominated by crossflow entrainment [20] rather than viscous effects or pressure differentials [18], the Reynolds numbers of the jet (Re_j) should have a negligible effect. Differences in the momentum distributions of laminar and turbulent jets have led to observations that laminar jets penetrate deeper into the crossflow compared with turbulent jets at a fixed J. In addition to this, the crossflow boundary layer thickness, a function of the crossflow Reynolds number Re_∞, has a significant impact on the jet deflection since flows with a large boundary layer will have lower crossflow momentum entrainment in the nearfield and consequently higher penetration. Considering the crossflow variational effects are especially important in developing scalings when the nozzle protrudes into the flow causing the local flow velocity faced by the jet to be much higher than in the flush nozzle case [21]. The resulting scaling law proposed by Muppidi and Mahesh [19] incorporates the boundary layer thickness as:

$$\frac{y}{Rd_j} = A\left(\frac{x}{Rd_j}\right)^b\left(\frac{h}{d_j}\right)^C \tag{1.3}$$

Where they found C = 0.15 and the length scale based on the boundary layer thickness, h, can be approximated as:

$$\frac{h}{d_j} = \begin{cases} \left(\frac{3}{4}\pi C_m R^2 \frac{\delta_\infty^2 D^2}{d_j^4}\right)^{0.33} & : h \le \delta_\infty \\ \frac{2}{3}\frac{\delta_\infty}{d_j} + \frac{\pi}{4} C_m R^2 \frac{D^2}{d_j^2} & : h \ge \delta_\infty \end{cases} \tag{1.4}$$

with $C_m \approx 0.05$ and the effective diameter defined by the expression:

$$\rho_j \int_{A_j} \langle V_{y=0}^2 \rangle^2 dA_j = \frac{\pi D^2}{4} \rho_j U_j^2 \qquad 1.5$$

These trajectory scalings make no explicit distinction between capturing the jet in crossflow behavior under reacting and non-reacting conditions, despite the fact that exothermicity/sharp density gradients can have significant impact on global shear flow behavior. Most non-reacting scaling models are based on mass entrainment of the crossflow into the jet by the counter-rotating vortex pair, a flow feature which will be covered in greater detail in Section 1.3. The models suggested by Broadwell [17] and the vortex-pair model suggested by Karagozian [22] to capture the flame length both assume that the global RJICF structure is fundamentally similar to non-reacting cases. While some experimental studies of reacting jets and flames have supported this assumption by demonstrating qualitatively similar large scale features in the flowfield [17, 23] and similar trajectories [24], others have demonstrated that the scalings are unable to capture both reacting and non-reacting behavior accurately [25-28]. For the most part, reacting jets have similar behavior in the near field, while in the far field, the jets tend to penetrate further, along with a longer potential core. This could be because of a decrease in crossflow entrainment due to the flame/exothermicity as well as the presence of gas expansion in the leeward, typically low pressure, wake region of the flow [26]. In addition, the discrepancies between non-reacting and reacting jets were significantly less at high momentum flux ratios [26, 27].

1.2.2 Flame stabilization in reacting jets

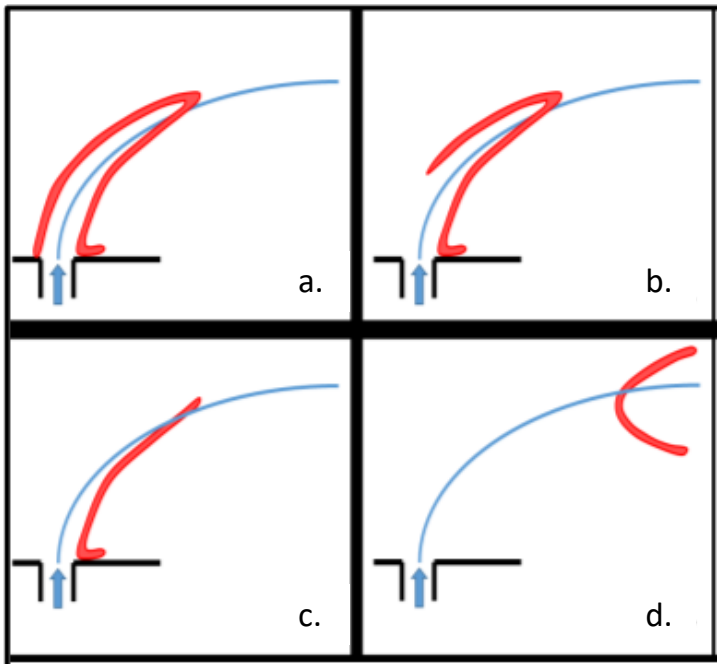

Figure 1.6: Schematic showing the different types of flame shapes/stabilization regions in RJICF flowfields; a) fully attached, b) windward lifted/leeward attached, c) lee stabilized flames, and d) fully lifted flames [29].

The wide variation and somewhat contradictory findings in RJICF studies suggest that even with respect to global metrics like the jet trajectory, combustion cannot be assumed to simply have a global effect in all reacting cases. To consider the effects of combustion on a case-by-case basis, it is important to understand the different ways that the flame can stabilize in the flowfield. This can depend on many factors including – the premixed or non-premixed nature of the jet, the chemical timescales involved, and the flow timescales. Figure 1.6 describes the different flame shapes or attachment locations, in the windward (upstream) and leeward (downstream) side, that have been observed by previous studies including both premixed and non-premixed jet compositions. The flow timescales (i.e. strain rates) on the windward side tend to be considerably shorter due to the sharp

shear gradient between the jet and the crossflow, while in the leeward size, the wake region has a sufficiently large recirculating zone of low velocity and/or reverse flow. Studies using highly reactive mixtures, including H_2/N_2 mixtures (non-premixed) [28] and air/C_2H_4 (premixed) [30] have shown fully attached flames with stable leeward flame bases and unstable lifted/attached windward flames (Figure 1.6a, b). Other studies using non-premixed and premixed hydrocarbon mixtures (i.e. methane, ethane or propane) show flames that are either anchored on the leeward lip or fully lifted from the jet (Figure 1.6c, d). Factors such as the jet flow profile can have significant impacts on the local coherent structure behavior, and thus change the local flow timescales impacting the lifting behavior [29].

This 'degree of lifting' from the base of the jet is an important parameter in the combustor design problem, as studies have correlated the degree of lifting with global effects like NOx generation [9]. In addition, investigations into the liftoff behavior have shown the presence of both 'auto-ignition' governed stabilization, dependent on the flow and ignition time scales, as well as stabilization based on the turbulent flame speed (flame propagation based stabilization) [31]. Research into the different stabilization mechanisms is still relatively nascent and is beyond the scope of investigation of this thesis. The purpose of providing a brief background on the different types of flame stabilization mechanisms, and consequently flame shapes, is to demonstrate the highly coupled nature of this problem, where, analyzing the impact of combustion on global metrics (i.e. jet trajectory) or even local effects (i.e. coherent structure behavior) can often mean considering locally varying heat release distributions.

1.3 Coherent structures in JICF

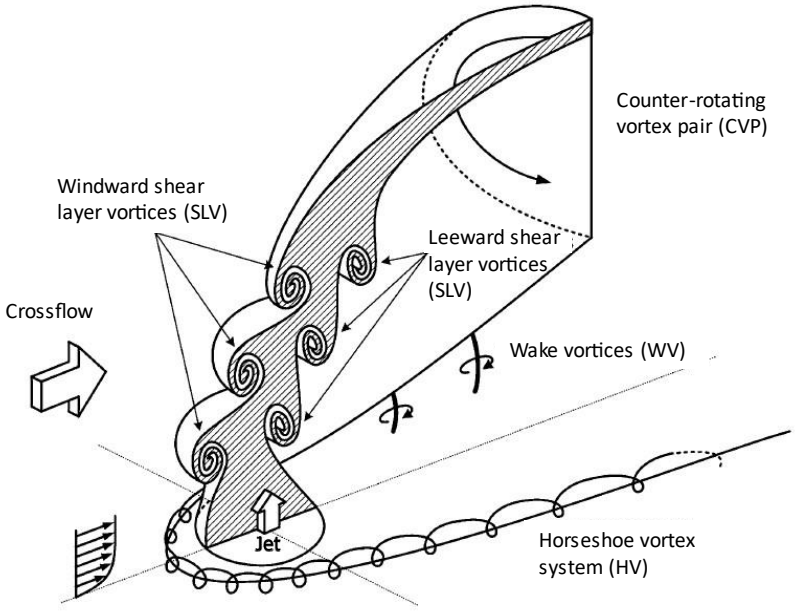

Figure 1.7: Schematic of the instantaneous JICF flowfield detailing the different coherent structures; adapted from New et al. [3].

One of the main reasons why the JICF has excellent mixing characteristics is because of its complex topology involving multiple coherent structures. The interaction between the jet and the crossflow generally gives rise to the following four structures (Figure 1.7) as noted by Fric and Roshko [32]: 1) the horseshoe vortex system (HV), 2) the upright wake vortices (WV), 3) the counter rotating vortex pair (CVP) and, 4) the shear layer vortices (SLV). While these structures are seemingly distinct and have a range of different time and length scales, they are strongly correlated. The primary sources of vorticity, especially for non-reacting flows with negligible stratification, is the jet boundary layer and the crossflow boundary layer [32]. Thus, all the structures observed are formed by the redistribution of vorticity from the same sources. The differences in the time scales ultimately stems from the range of time scales encountered in the flowfield ~ δ_∞/u_∞ (for

the crossflow) and d_j/u_j or θ/u_j (for the jet), where θ is the momentum thickness of the shear layer.

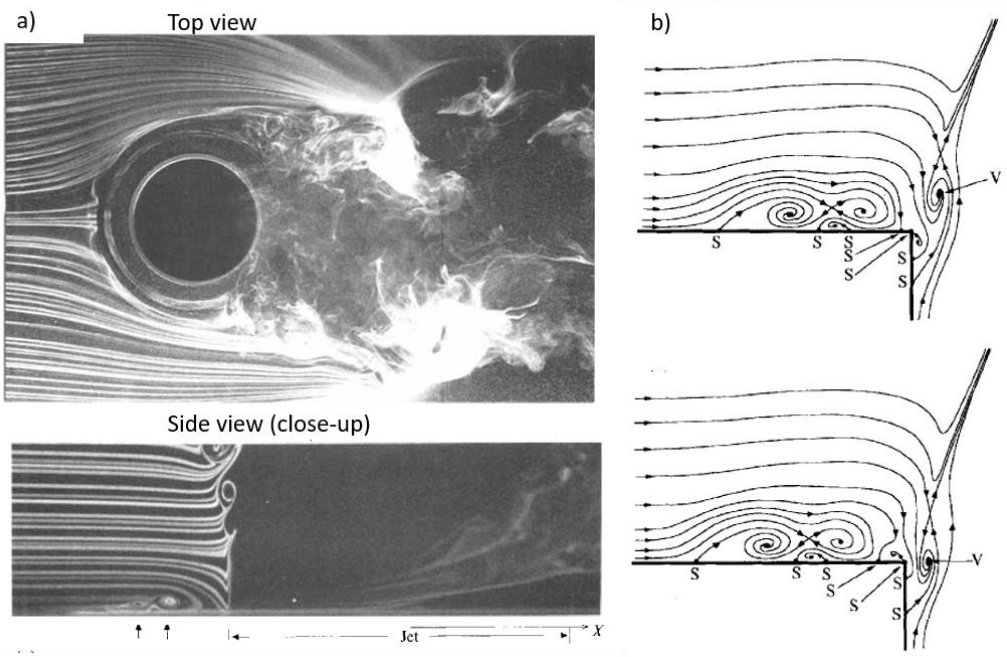

Figure 1.8: a) Smoke visualization experiments showing the top and side view of the HW system [32]; b) Streamlines showing the structure of the HW system as proposed by Kelso and Smits [33].

The two vortex systems that can be directly related to the crossflow boundary layer are the horseshoe vortex system and the wake vortices respectively. The horseshoe vortex system is a well-studied flow structure typically seen in juncture flows where the natural boundary layer is interrupted by a flow blockage [34]. Here, the adverse pressure gradient created by the blockage due to the jet creates a recirculation region where the boundary layer separates and rolls up. The structure of the vortex system can be seen in the smoke visualization experiments (Figure 1.8) to form a double looped structure upstream of the jet near the wall [32]. Kelso and Smits have suggested that the structure of the HV is primarily steady while also noting that small fluctuations were induced by the shedding of

the shear layer structures [33]. Krothapalli et al. [35] noted that for a rectangular jet the frequencies exhibited by the HV were similar to observations made in the 'wake' region of the jet. These observations further support the evidence that most of these coherent structures strongly interact and influence one another.

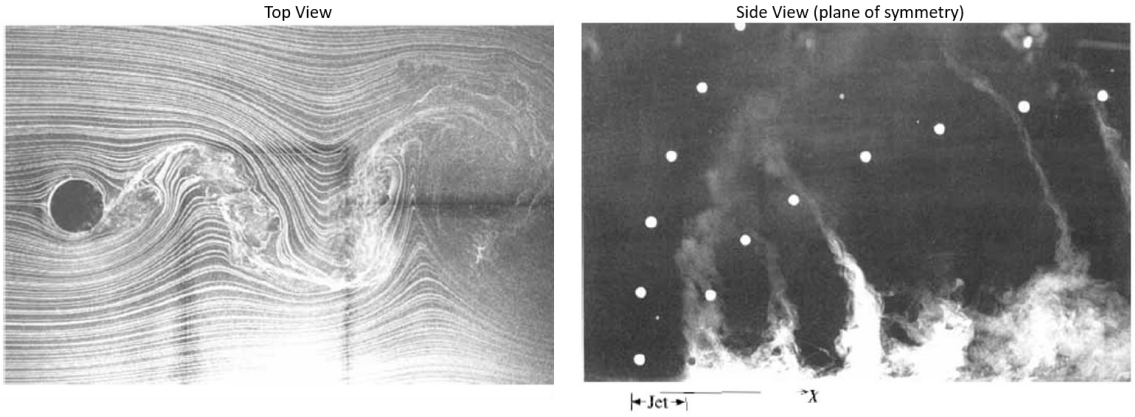

Figure 1.9: Smoke visualization experiments from [32] showing wake vortex structure from a top plane of view and in the plane of symmetry; white dots denote the location of SLV structures.

With the wake vortices, the relationship between the vorticity contained in these tornado-like wisps in the wake of the jet and the crossflow boundary layer is more ambiguous. The structure, as observed by multiple researchers, often resembles the Bernard-Von Karman (BVK) instability pattern known to form in the wake of a cylindrical bluff body thus, suggesting some analogies between those problems. But, as mentioned earlier, in a barotropic flow, vorticity cannot be created at the jet-crossflow interface unlike the solid boundary of the bluff-body. Moreover, the vorticity in the wake of a bluff body is oriented along the axis of the body (from a two-dimensional perspective), while the vorticity in the cylindrical shear region of the jet is oriented in the azimuthal direction. While it is possible that the vorticity from the jet shear layer is reoriented to form these

structures, this has only been suggested for the case of asymmetric jets in crossflow [36]. The most widely accepted theory, as proposed by Fric and Roshko [32], is that the vorticity originates from the crossflow boundary layer, which is entrained into the region of low pressure in the 'wake' of the jet. This can be seen in Figure 1.9, where the smoke injected into the crossflow boundary layer can be seen to form wisps that are entrained as these structures. More recent studies that have shown wake vortex behavior very similar to BVK type instabilities, in contrast to the traditional hypothesis, have shown this for non-isothermal and non-barotropic flows [37, 38].

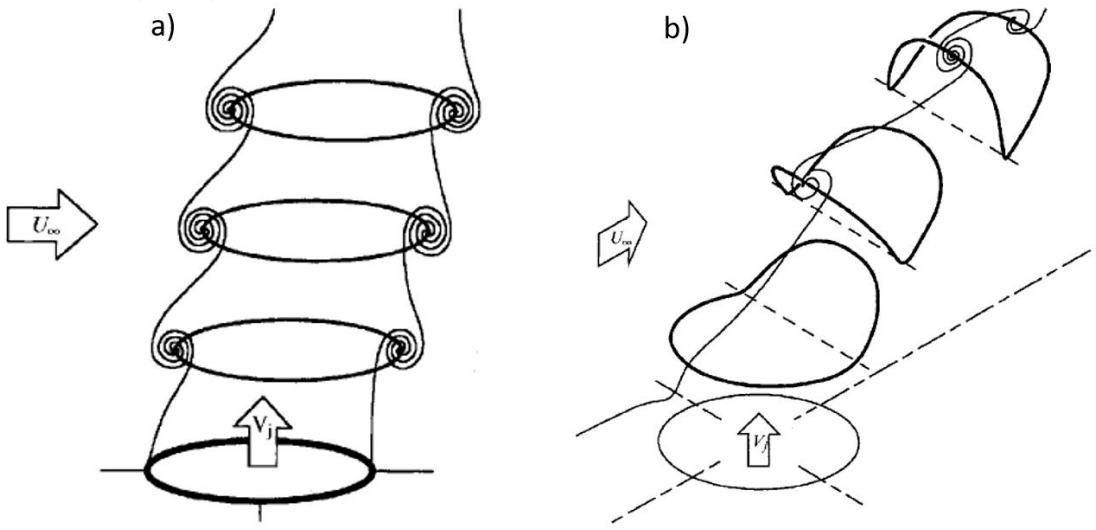

Figure 1.10: a) Description of ring like SLV structures in the near field of the jet; b) the process of rollup and folding of the rings as they advect with the flow. Adapted from Kelso et al. [1].

The shear layer structures (SLV) form from the roll up of the jet shear layer where the vorticity is transported primarily from the jet boundary layer. The shear layer rolls up through a Kelvin-Helmholtz like instability [39] which, in the case of axisymmetric jet, leads to the formation of vortex rings from the annular shear layer [40]. In the case of a JICF, the asymmetry in external flow condition, i.e. the presence of the crossflow, causes

these vortex rings to be stretched and reoriented. As a result most studies focusing on the plane of symmetry of the flowfield tend to capture the asymmety by slicing these rings through the centerplane, thus, separating the vortices into two sets - 'windward' vortices upstream of the jet exit and 'leeward' vortices downstream of the jet [1] (see Figure 1.7).

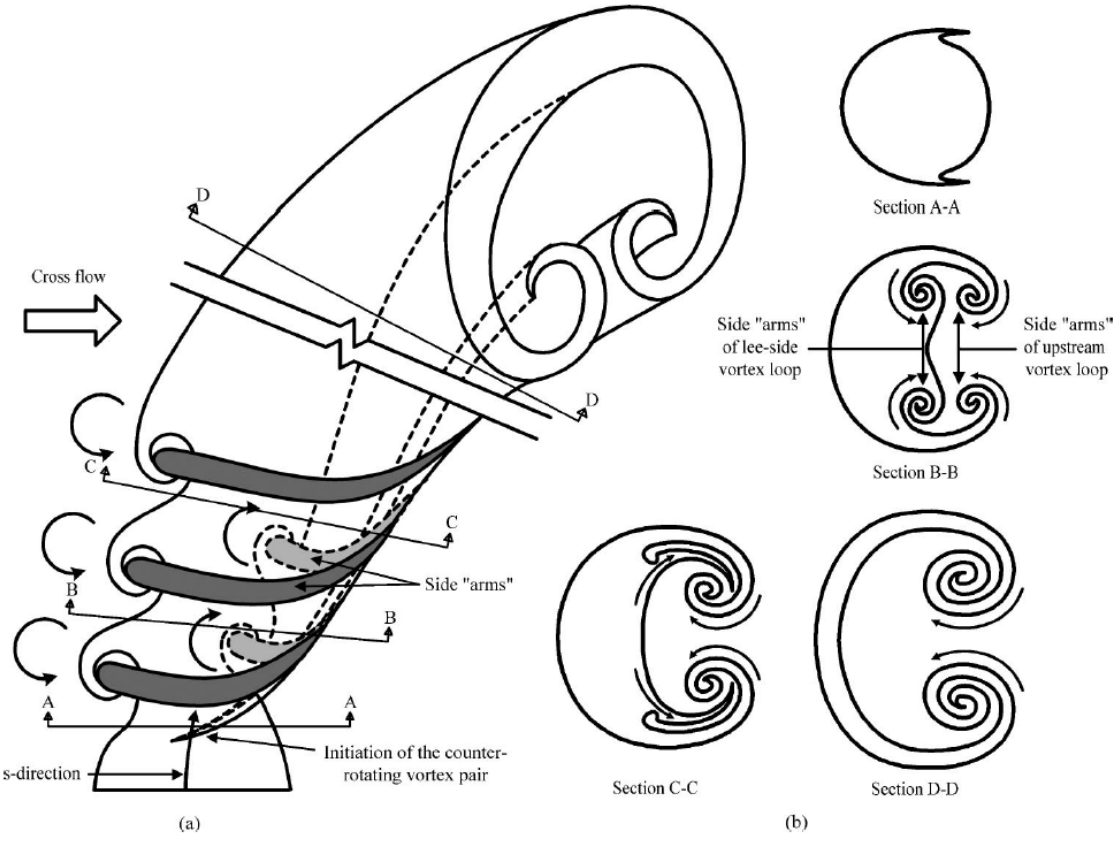

Figure 1.11: Reorientation of SLV structures by the bulk rotation of the CVP [41].

To first order, effects like the boundary layer thickness of the jet, and consequently the shear layer thickness (jet velocity profile shape), have a major impact on the structure of these vortices, especially in the near field [42]. This allows for instability results from simpler configurations, such as mixing layers or axisymmetric jets, to be used to understand the formation process of these vortices. The ring like topology that connects both these sets

of vortices ensures that their interaction is much more complex and cannot be ignored. As these rings evolve, their topology becomes increasingly complicated, a consequence of the highly three-dimensional nature of the flowfield as well as dissipation due to viscous forces and other non-linear effects. In the near-field, the vorticity contained in these vortices is reoriented into the spanwise direction and is thought to merge into the counter-rotating vortex pair [1, 41] (see Figure 1.11).

The counter-rotating vortex pair is the most dominant flow structure which is primarily present in the far-field of the jet. But, there is much debate regarding its characterization as a flow structure, since for most cases, instantaneous snapshots of the field show a complex set of structures that do not represent the large counter-rotating structures of the CVP, as is typically depicted in schematics (Figure 1.1). Early studies that sought to characterize the vorticity of a transverse jet observed this flow structure, as two regions of opposite vorticity, primarily in the time-averaged flow field and not on an instantaneous basis [16, 43]. Theoretical models of the transverse jet often use the CVP structure in entrainment-based trajectory models (Section 1.2) that have shown good agreement with empirical scalings and experimental data, justifying the characterization of this flow structure. In addition to this, there is further uncertainty regarding the source of the vorticity of the CVP. One school of thought suggests that the vorticity is redistributed from the shear layer structures as proposed by Kelso et al. [1] and Lim et al. [41], and further supported by vortex filament simulations performed by Cortelezzi and Karagozian [44]. But, studies such as the early work done by Broadwell and Briendenthal [17], and the two-dimensional model problem proposed by Muppidi and Mahesh [45] focus primarily on the pressure effects of the bending of the jet due to the crossflow and do not require the

jet shear layer to explain this structure. Despite the ambiguity of its existence on an instantaneous basis and the source of its vorticity, understanding its structure is essential in evaluating global metrics like the mixing performance of a JICF configuration [46].

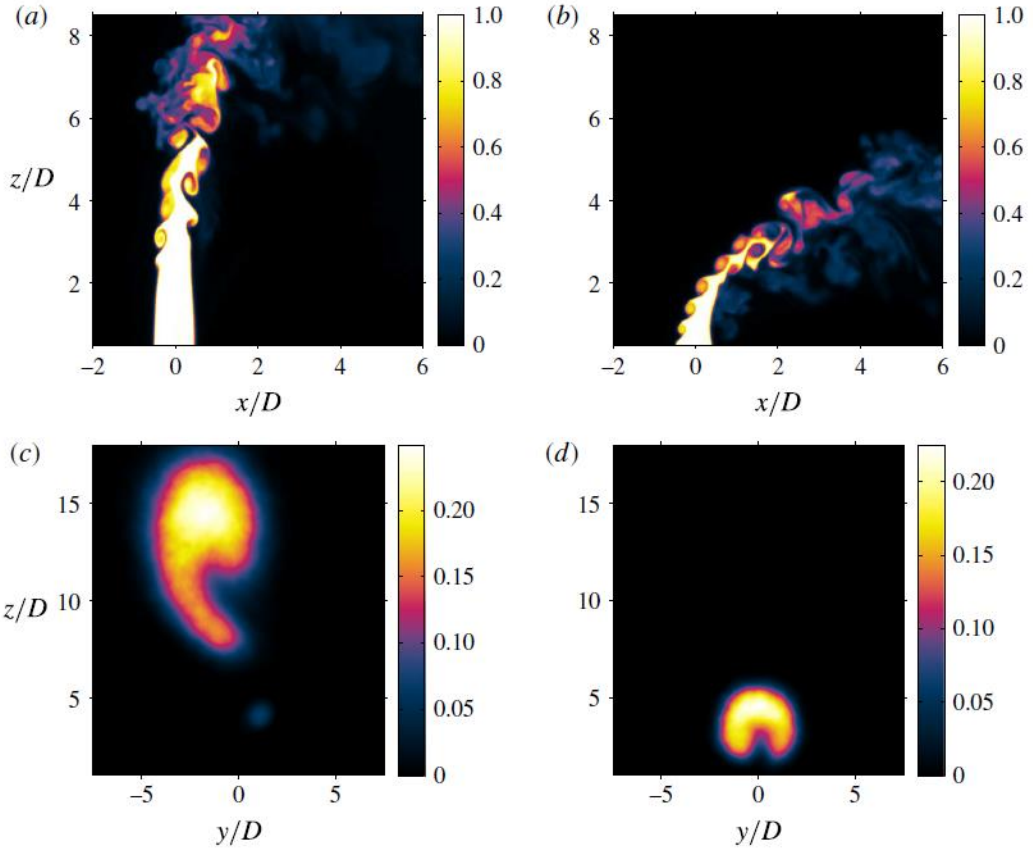

Figure 1.12: Acetone PLIF measurements for a non-reacting JICF at two momentum flux ratios, J = 41 (a, c) and J = 5 (b, d) and across two different interrogation planes - instantaneous centerplane (a,b) and time-averaged transverse plane (c,d) [46].

This thesis will focus primarily on the dynamics of SLV structures and the impact of heat release/density gradients on their behavior. From a practical standpoint, they account for a large percentage of the near field mixing and entrainment, i.e. enhanced vortex shedding in the near field corresponds to faster mixing of the jet with the crossflow [46]. This can be seen in acetone PLIF experiments done by Gevorkyan et al. [46], showing

qualitative changes in near field mixing based on the SLV structures. In addition, these measurements demonstrate that there is correlation in the mixing behavior of the CVP and the SLV structures (Figure 1.12). Thus, the impact of reactions on the behavior of the SLV structures has an important consequence on mixing and jet dynamics, both important design challenges in practical systems employing this configuration.

SLV structures, being formed through instability mechanisms in the near field shear layer, can also be analyzed from a hydrodynamic instability perspective considering it is a part of the general class of free-shear flows, i.e. jets, wakes and mixing layers. Thus, while the impact of heat release and significant density variation, specifically on JICF coherent structure topology, is relatively poorly understood, the large wealth of literature on the effect of reactions/heat release on hydrodynamic instability in canonical free shear configurations can be leveraged to understand RJICF behavior. Details of existing literature analyzing JICF behavior as shear layer instabilities is contained in the next section and the general impact of heat release on instability behavior for both canonical flows and JICF type configurations is given in Section 1.5.

1.4 Shear layer instabilities in JICF

The field of hydrodynamic stability provides a basis to analyze the behavior of these flow structures from a quantitative and fundamental point of view. While analyzing the behavior of these coherent structures in a linear framework has limitations, it has been shown to provide insight into how different flow parameters influence the stability behavior and characteristic frequencies for a large class of canonical shear flows [47]. The SLV structures discussed in the previous section are essentially formed from a Kelvin

Helmholtz type instability mechanism in the near field shear layer, between the jet and the crossflow. Many free shear flows, like jets, wakes or mixing layers, often encountered in practical combustor systems, demonstrate instability behavior under certain parameter regimes [48]. Essentially, small amplitude disturbances like acoustic noise or even turbulence can be amplified by these shear flows through linear as well as non-linear mechanisms. The coherent structures observed are a consequence of vorticity interaction and organization that follow instability growth.

Linearly unstable flows can further be classified as convectively or globally unstable flows [49]. A flow that can be represented as a parallel base flow profile (invariant in the streamwise direction) can be further classified as convectively unstable or absolutely unstable. Convectively unstable flows act as wave amplifiers, amplifying incoming disturbances to create spatial growth. They require a constant source of excitation to continue to grow as the wave packed is being advected from the point of origin. Absolutely unstable flows tend to behave like self-excited oscillators. The envelope of disturbance that originates from a point tends to grow both spatially and temporally. As a result, once perturbed they tend to continue oscillating and, if a sufficiently large region of absolute instability exists spatially in a flow, it drives global instability [50]. Flows that show convective or globally unstable behavior often have qualitative differences in the behavior of coherent structures.

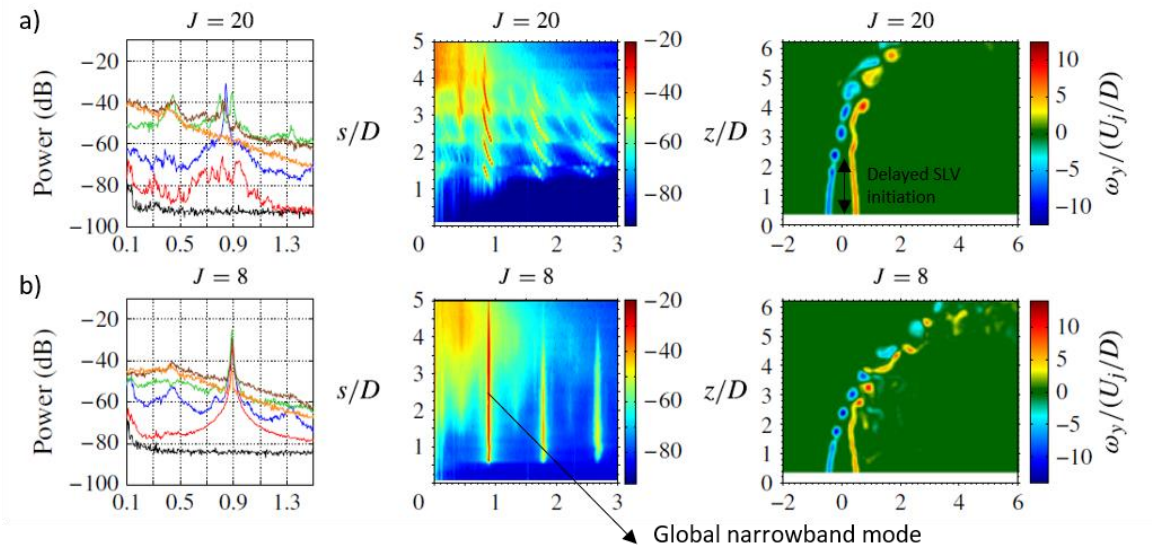

Figure 1.13 Characteristic plots for non-reacting iso-density JICF showing shear layer spectra at specific locations (left); spectral contour plots (center) and representative instantaneous vorticity measurements from PIV (right) for two conditions – a) J = 20 and b)) J = 8. Adapted from Getsinger et al. [51].

Similar to jets [52] and wakes [49], the primary flow parameters that alter local stability behavior for non-reacting JICF is the velocity ratio R (or the momentum flux ratio J) and the density ratio S. Experimentally, Megerian et al. [21] studied the transverse velocity spectrum for a range of R values at iso-density conditions (S = 1) and for flush and elevated injectors. The hot wire measurements were taken at locations in the windward shear layer to track the growth of these disturbance as a function of the jet-streamwise coordinate (s). They observed a transition in the stability behavior at $J \sim 10$ where, for smaller velocity ratios, the shear layer spectrum showed significant 'global' narrowband oscillations (Figure 1.13a), while at higher velocity ratios the spectrum was a lot less coherent and shows evidence of subharmonics along the jet (Figure 1.13b). In addition, PIV measurements [51] on the same configuration provided qualitative characterization of vortex behavior between the instability regimes. The globally unstable cases showed

significant vortex growth near the jet exit while, for convectively unstable conditions, this was suppressed and subharmonics corresponding to vortex pairing events were observed (Figure 1.13). Getsinger et al. [53] further extended the above work to investigate low-density jets and found evidence of a similar transition to global stability at density ratios S < 0.45. This is in line with observations for hot (low-density) jets [54] as well as stratified wakes [55]. Collectively, these observations can be combined into a stability map of the transitional boundaries with respect to the non-reacting jet parameters – J, S (Figure 1.14).

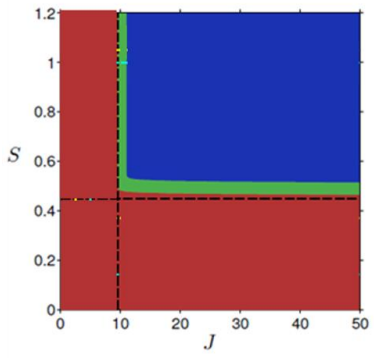

Figure 1.14: Stability boundaries from previous non-reacting studies (Megerian et al. [21], Getsinger et al. [53]), Red - Globally unstable, Blue - Convectively unstable, Green - Transition.

In addition to J and S, recent experiments by Shoji et al. [56] demonstrated that the viscosity can play a role in changing the critical momentum flux ratio for transition (J_{crit}). Theoretically, the curvature of the velocity profile plays little role in the transition to global instability for the case of thin shear layers ($D/\theta < 230$) [57]. Since a JICF tends to have a thicker θ compared to a free jet [21], they hypothesized that the transition to global instability was sensitive to the value of θ, which was modified by changing the absolute viscosity ratio between the jet and crossflow μ_j/μ_∞.

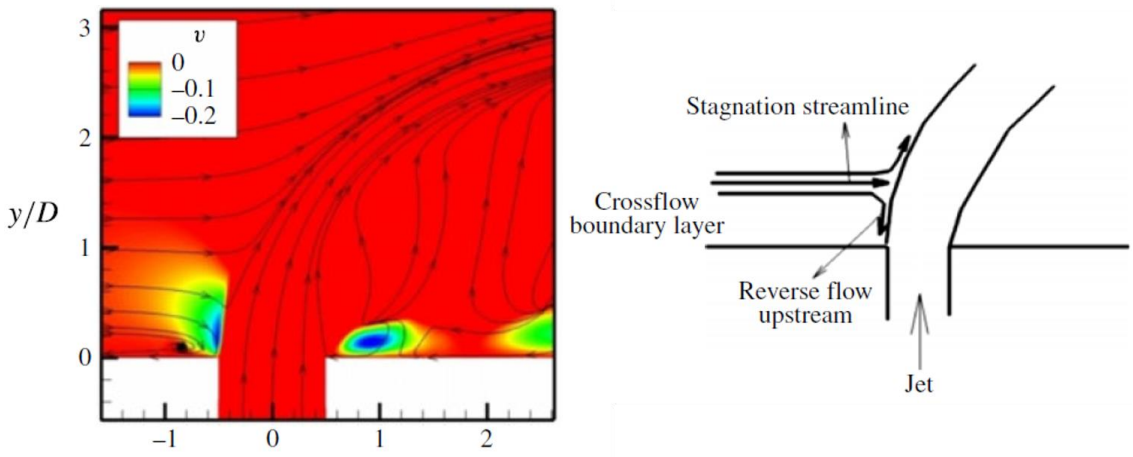

Figure 1.15: (left) Streamline plots showing regions of reverse flow ahead of the windward shear layer, J = 4; (right) schematic denoting the region of reverse flow formed from the recirculation of the crossflow boundary layer.

The observations on jet behavior and spatio-temporal stability transition above were primarily made on an empirical basis. Iyer and Mahesh [58] utilized detailed direct numerical simulation (DNS) data acquired at convectively and globally unstable conditions, based on experimental data [21], to provide a more quantitative analysis. They observed similar spectral behavior and mode structure predicted through dynamic mode decomposition (DMD) [59]. They noted the presence of reverse flow in the region upstream of the windward shear layer (Figure 1.15) – a condition necessary for absolutely unstable behavior in mixing layers [49]. In addition, the counter-current mixing layer ratio $\Lambda = {(V_1 - V_2)}/{(V_1 + V_2)}$ calculated for the windward shear layer showed that, for each case (convective/globally unstable), its value lay on either side of the convective-global transitional velocity ratio as predicted by Huerre and Monkewitz [49]. But this formulation would suggest that the magnitude of reverse flow, and by extension the crossflow boundary layer profile, is an independent parameter as well since the value of Λ is not unique for a given J value.

Understanding these shear layer instabilities is also essential in enabling the active control of jets [4]. Forcing, or pulsing the jet has been demonstrated to increase jet penetration as well as enhance mixing [60-62]. The exact mechanism by which this occurs, as proposed by Sau and Mahesh [63], involves the creation of toroidal vortex rings at the jet exit that interact with the unsteady shear layer. But, convectively and globally unstable JICF have been shown to have significantly different responses to forcing. Globally unstable cases do not respond to low-amplitude forcing distinct from the fundamental frequency [21] while convectively unstable cases proved to be highly sensitive to the externally driving frequency. Forcing studies focused on the crossflow have noted that crossflow forcing does have a significant effect on jet penetration and mixing [64]. While this effect was a consequence of jet shear layer manipulation and growth when forcing the jet, here, there is significant 'jet flapping' motion which is caused by the asymmetric nature of the unsteady crossflow that contributes to better spatial mixing. The study of crossflow forcing on JICF dynamics is of particular interest when considering staged combustion type architectures where acoustic/combustion instabilities from the main burner are bound to have an effect on the jet hydrodynamics and flame behavior [25, 65].

Although this thesis does not attempt to extend the investigation of forced JICF dynamics to reacting cases, understanding the effect of reactions on the hydrodynamic stability behavior of the flowfield provide important insight into possible forcing strategies. In addition, the effect of crossflow oscillations through combustion instability on jet flapping is of primary concern based on the facility used for this study (see Section 2.1) and must be considered while analyzing the results.

1.5 Effect of combustion on hydrodynamics

Researchers have grappled with the question of how exactly heat release and combustion alter the behavior of other canonical shear flows for over half a century [66]. There is also much debate on whether the qualitative observations stem primarily from combustion altering the base flow characteristics - through the introduction of density gradients locally, through vorticity creation/destruction by baroclinic torque and volume dilatation and the local viscosity changes.

Early work often focused on reacting mixing layers – a simpler, more idealized, canonical flowfield that is a part of a large number of practical systems. Hermanson and Dimotakis [67] demonstrated the suppression of entrainment and reduction in shear layer growth rate (calculated as a function of the spreading rate and vorticity length-scale) with increasing heat release for a H_2/F_2 mixing layer. They sought to explain these observations by demonstrating a decrease in the shear stress in the core regions of the large-scale structures, which is consistent with reduced growth. Similarly, McMurtry et al. [68], using a low-Mach number DNS framework to study a temporally growing mixing layer, showing lower turbulent shear stress and consequently, a reduction in the mean-flow production of the turbulent kinetic energy. But these observations were applied *ex post facto*, correlating the observed variances in the reacting flowfield with the local turbulence intensity and thus, insufficient to provide the exact mechanism of how combustion affects hydrodynamics.

1.5.1 Linear stability analysis of reacting flows

Linear stability theory, despite its limitations, has been used to try to explain bulk effects of heat release/combustion on flow dynamics [69, 70]. One method to do this is to

ignore the effects of gas expansion, narrowing the effect of combustion to its influence on the base flow density variation. While this would mean that there is no difference between the existence of a flame and a non-reacting density stratification, some of the results suggest that qualitative stability trends can be captured. A large body of the literature on stability behavior considering the effects of combustion-induced density stratification have employed the Boussinesq approximation - effectively separating effects due to inertia and buoyancy [71]. While combustion invariably affects the hydrodynamics of buoyant flows, only inertial effects will be considered here due to their relevance in high Froude number environments.

McMurtry et al. [68] modeled a diffusion flame in a mixing layer as a piecewise linear velocity and density profile where the spatial growth rate of the instability mode decreased for higher heat release (i.e. lower density in the flame region compared to the flow). Continuous (tanh type) velocity and density profiles show similar effects with respect to increasing the bulk heat release or its proxy - the temperature ratio [69]. This general trend of growth rate suppression from the density variation can be explained by considering a more generalized form of Rayleigh's stability equation [47]. Similarly, as Rayleigh's criteria for inviscid instability in homogenous flows is dependent on the vorticity distribution, a modified version of this criteria can be derived for the case of a stratified flow and is given below.

$$\int \frac{1}{\left|u_{x,0} - c_{ph}\right|^2} \frac{\partial}{\partial y}\left[\rho_0 \frac{\partial u_{x,0}}{\partial y}\right] |\hat{v}_1|^2 dy = 0 \qquad 1.6$$

Equation **1.6** is valid for a parallel flow having only a axial base flow component ($u_{x,0}$) and a base flow density variation (ρ_0) which is invariant in the streamwise (x) direction. The linearized disturbances are imposed by assuming solutions of the nature $v(\vec{x},t) = \hat{v}_1(y)e^{i(\alpha x+\beta z-\alpha c_{ph}t)}$ where, c_{ph} is the phase speed and α,β are the streamwise and spanwise wavenumbers [47]. For the above integral to vanish over the domain of integration (spanwise limits), since all the other terms are strictly positive, $\frac{\partial}{\partial y}\left[\rho_0 \frac{\partial u_{x,0}}{\partial y}\right]$ has to change signs over the domain. For a two-dimensional base flow, the only non-zero vorticity component can be represented as - $\Omega_0 = \frac{\partial u_{x,0}}{\partial y}$.

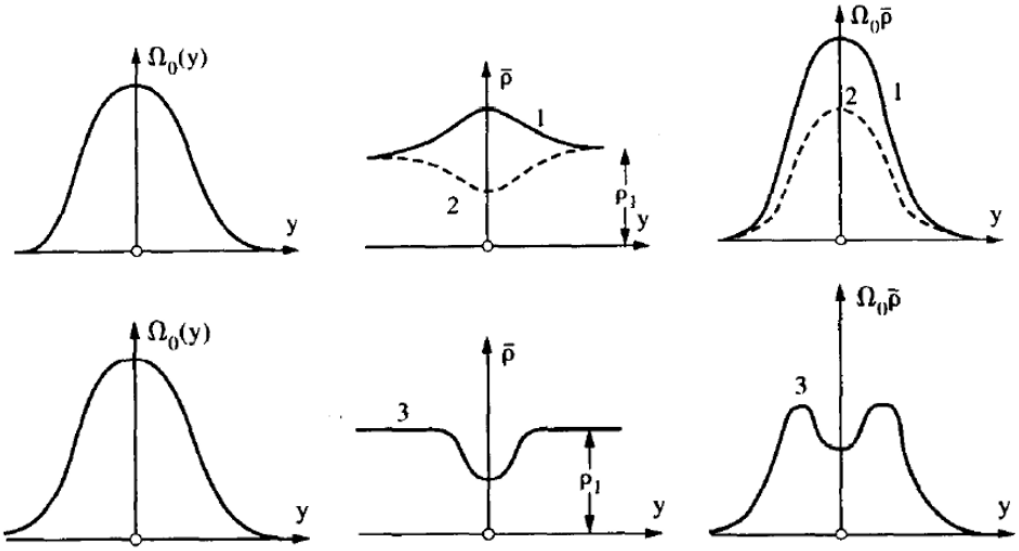

Figure 1.16: Base flow profiles of vorticity (left), density (center) and density-weighted vorticity (right) for three arbitrary density variations (marked 1,2-above and 3-below) adapted from Coats [66].

Thus, a necessary condition for instabilities in such stratified flows is the existence of extrema for the function $\rho_0\Omega_0$ - the density weighted vorticity (z-component) profile [72]. When density variations are introduced through flames or simply non-uniform gas properties, the inertial instability magnitude, being proportional to the magnitude of the

density weighted vorticity, is lower than in the case of a homogenous shear flow of similar vorticity distribution (see Figure 1.16). In addition, the existence of multiple extrema in the density weighted vorticity profile shows the evidence of multiple unstable modes [73].

Researchers have also attempted to extend the scope of local parallel flow stability analysis by linearizing the continuity, momentum, energy and species transport equations and thereby allowing density and heat release fluctuations for different canonical problems including, diffusion flames - Mahalingam et al. [70], low speed reacting mixing layers - Shin and Ferziger [69] and compressible reacting mixing layers - Day et al. [74]. While all these studies note the suppression of spatially growing disturbances in the case of reacting flows, Day et al. [74] showed that this was primarily for the case of the 'central' mode while the two 'outer' modes (stemming from the three extrema in the density-weighted vorticity profile) tend to destabilize with increasing heat release. These studies also note that the effects on stability primarily lay with the modification in the base flow profile due to heat release and neglecting the heat release term in the linearized equations had a negligible effect.

1.5.2 Flame-shear layer offset effects

Since the density weighted vorticity profile plays an important role in interpreting stability behavior for stratified/reacting flows, another way to qualitatively alter it is to introduce an offset between the density gradient (i.e. the flame) and the shear center (i.e. location of max vorticity).

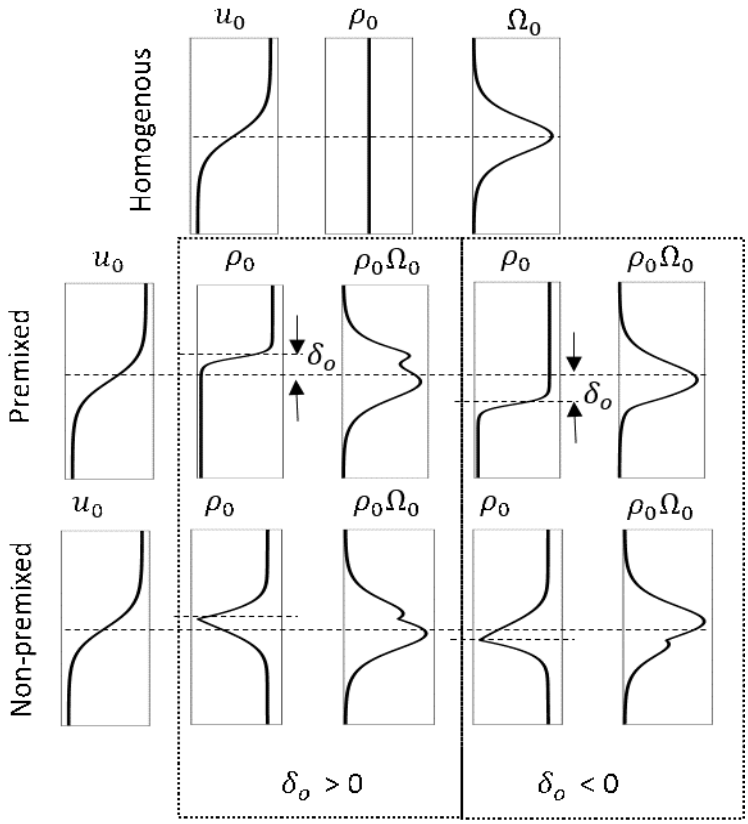

Figure 1.17: Schematic of the spanwise variation of base flow velocity (u_0), density (ρ_0) and density weighted vorticity ($\rho_0\Omega_0$) for three cases – homogenous mixing layer; mixing layer with density jump modeling a premixed flame with an offset δ_o; mixing layer with density variation modeling a non-premixed flam with an offset.

To illustrate this, consider a model mixing layer profile with an idealized smooth (tanh) velocity distribution (Figure 1.17). Three flame-induced stratification configurations involving different density stratification profiles are demonstrated - a homogenous (non-stratified) profile, a diffusion flame-like profile and, a premixed flame-like profile. While most cases with density stratification show the presence of multiple maxima, this also appears to depend on another parameter - an offset length-scale (δ_o). This parameter models compositional or flame stabilization effects, which tend to move the flame radially with respect to the shear layer in many practical configurations. While non-premixed case shows three extrema irrespective of the offset value, the premixed case with a negative

offset ($\delta_o < 0$), shows a single peak (similar to a homogenous profile). Thus, the offset between the flame and shear location is an important parameter capable of producing effects of a similar magnitude as gas expansion.

Introducing the flame-shear position offset as a parameter further complicates the question as to whether local stability analysis can accurately capture trends for all shear flow configurations. Few studies have explicitly considered the change in stability behavior while varying the offset as a parameter of interest, and those that do, often have varied conclusions. Emerson et al. [75] evaluated the effect of an offset for sinuous and varicose disturbances in a piecewise linear model problem representing bluff body flames, concluding that the offset was destabilizing in nature. Intuitively this supports their observation that, in the limit of maximum separation the solution defaults to a homogenous case that is more unstable than the reacting case. Hajesfandiari and Forliti [76] modeled a simple diffusion flame-like smooth density variation in a planar shear layer, and noted that the offset tends to be asymmetrically destabilizing in nature. Interestingly, they observed that moving the flame (or in the case of their model - the density trough) into the faster stream results in enhanced instability growth, even higher than the homogenous case. Experiments conducted by Furi et al. [77] on a coflowing jet diffusion flame note the complete suppression of the K-H instability rollup on moving the flame inside the shear layer. If we consider the co-flowing jet flame as two interacting mixing layers, this case would be analogous to the condition that is predicted to have a significantly higher destabilizing behavior by the inviscid model problem [76]. Furi et al. also performed a viscous linear stability analysis to reconcile the experimental observations, concluding that the variation in spatial amplification rates could be captured by noting the larger

momentum thickness in the cases where the flame was inside the shear layer, a consequence of significantly higher viscosity.

Although Local parallel flow stability analysis using inviscid or viscous assumptions have had success capturing qualitative trends with respect to the effect of combustion induced base flow effects for some canonical shear flows, due to the nature of the assumptions, it is difficult to pinpoint which mechanism is responsible for the discrepancies observed between these models and experiments for the other cases. For most realistic flows, the effect of heat release is not small and violates the parallel flow assumption. In addition, these models inherently ignore non-local effects of combustion, for example, in bluff body flows where you have interacting mixing layers (see Section 1.5.3). Non-reacting jet in crossflow behavior has been primarily analyzed through the linear stability framework, where the concepts like convective and absolute instability have been related to the base flow velocity and density profile (Section 1.4). For the reacting cases, the highly three-dimensional and asymmetric flowfield compounded with the highly three-dimensional effects of heat release make relating observed stability trends to base flow variations through local linear stability analysis challenging, compared with other canonical flowfields.

1.5.3 Vorticity dynamics in reacting flows

Since most instability mechanisms can be considered to occur through the organization of vorticity, qualitative effects of heat release can also be understood through the vorticity transport equation.

$$\frac{D\omega}{Dt} = (\omega.\nabla)u - \omega(\nabla.u) + \frac{\nabla \mathrm{p} \times \nabla\rho}{\rho^2} + \nabla \times \left(\frac{\nabla.\tau}{\rho}\right) \qquad 1.7$$

I II III IV

In Equation **1.7**, the LHS is the material derivative containing the convective term. On the RHS the terms from left to right are – (I) vortex stretching, (II) dilatation (gas expansion), (III) baroclinic torque and, (IV) viscous dissipation. McMurtry et al. [68] observed that the peak vorticity in the coherent structures was lower in the reacting case, attributing this to the effect of dilatation (II-**1.7**), where, as the vortex expands due to heat release and entrainment of hot products, the maximum vorticity drops to preserve angular momentum. The effect of baroclinic torque is typically highly complex and not uniform since it depends on the local gradient direction in the flow and its relationship with the local pressure gradient direction [78]. For the case of coherent structures, the local pressure gradient is often dictated by the vortex structure itself and, when combined with the local flame induced density gradient, causes local extrema to show at the edges of the vortices, causing counter-rotating motions and distorting the vortex structure. While dilatation effects generally suppress local vorticity irrespective of the sign, baroclinic torque can create or suppress vorticity locally [78]. The local temperature gradients setup by the presence of a flame can also modify the local absolute viscosity and consequently the local Reynolds number. Depending on the Reynolds number of the flowfield, viscous effects can have a strong impact, especially in configurations where the temperature ratio between the flame and reactants/ambient conditions is large. Yule et al. [79] suggested that this mechanism was responsible for the 'relaminarization' of a jet diffusion flame due to the locally lower Reynolds number.

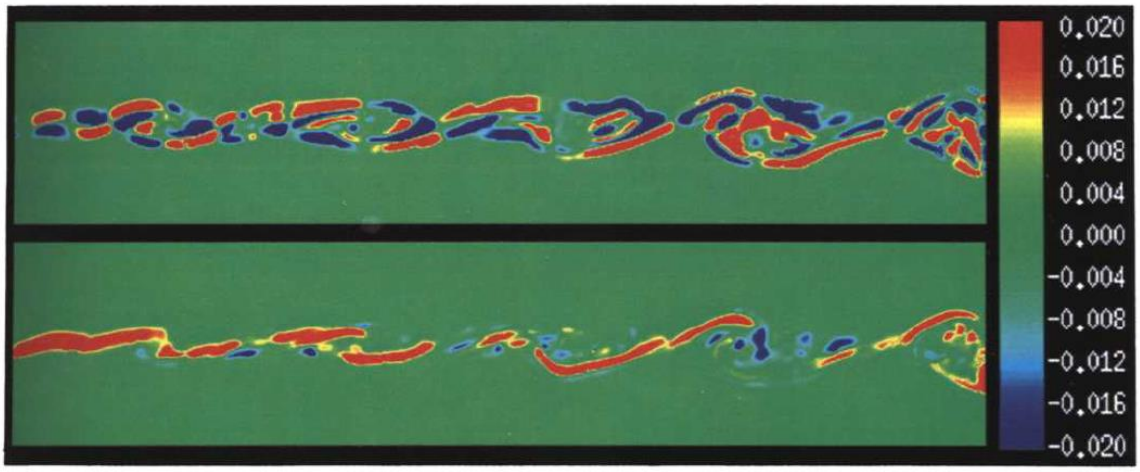

Figure 1.18: The distribution of the baroclinic (top) and dilatation terms (bottom), terms II and II of the vorticity transport equation (1.7**), for a two-dimensional mixing layer [80].**

The general nature of combustion effects on each term of the vorticity budget can be understood from the Lagrangian vortex element simulations of Soteriou and Ghoniem [80]. Their methodology allows them to individually 'turn-off' terms from the transport equation (Eq. **1.7**) and thereby isolate the effects from the heat release and baroclinic torque term. Spatially, the baroclinic torque distorts the eddy shape and inhibits entrainment, while gas expansion serves to thicken the vorticity distribution while reducing the peak in the near field. In the far field, both the processes act to inhibit mixing and interaction between the vortex structures. The same framework was used to analyze a bluff-body flow where, for the reacting cases, the BVK type sinuous instability was absent. Mehta and Soteriou [78] found that, while the baroclinic term has a strong effect on reversing the sign of vorticity in the far-field, it was solely the exothermicity that suppressed the mixing layer organization into the wave like non-reacting wake. The interaction between the two mixing layers was suppressed as vortices that advected through the flame tended to expand

outward and reduce their vorticity, reducing their ability to induce motion on vortex elements of the opposite sign.

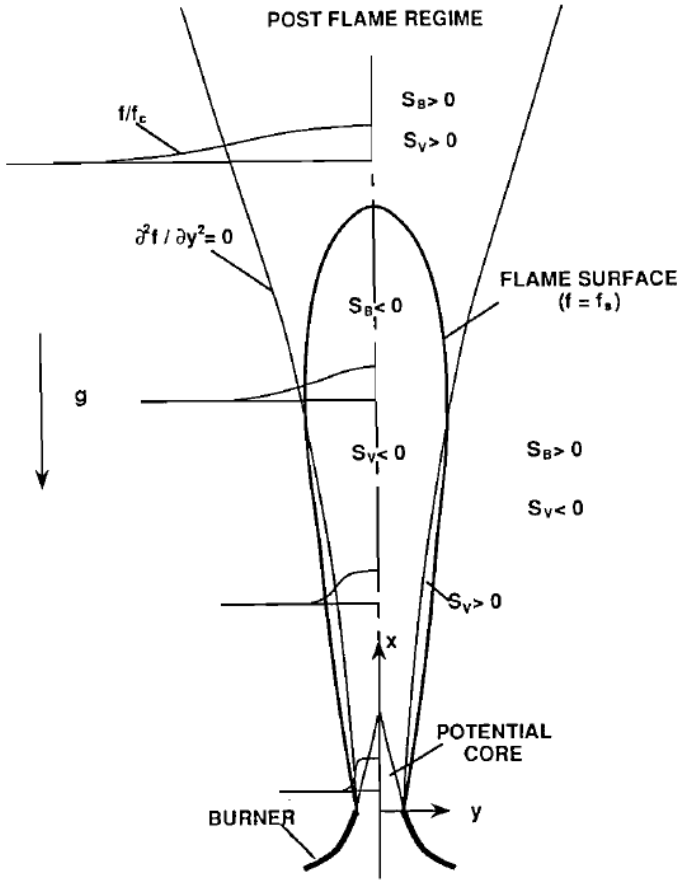

Figure 1.19: Mean variation of terms from the vorticity transport equation (1.7**), S_V – gas expansion and S_B – baroclinic torque.**

Analysis of individual terms of the vorticity transport equation on an instantaneous basis from experimental data is often challenging due to the need to extract three-dimensional pressure, density, and velocity fields. Chen et al. [81] used mean flow properties to scale the different terms of the vorticity transport equation in order to analyze their contribution in different parts of the flow (Figure 1.19). The ratio of the baroclinic contribution to gas expansion was noted to significantly drop as the flame was moved to

collocate with the shear center suggesting that the absence of K-H instability was a consequence of suppression through dilatation.

Modern advances in experimental data acquisition and the accessibility to optical diagnostic techniques has led to attempts to quantify these terms through Particle Image Velocimetry (PIV) and a number of techniques for species/thermometry measurements. Geikie et al. [82] used PIV and CH* Chemiluminescence measurements to extract flow-field and heat release information in bluff-body flames. Their measurements suggest that in the reacting cases, baroclinic torque enhances the vorticity in the shear layer, but, with the caveat that their analysis was primarily two-dimensional while the transport effects are highly three-dimensional. Kazbekov et al. [83] utilized tomographic PIV measurements and CH_2O PLIF to demonstrate that the baroclinic torque is a significant source of enstrophy (a scalar representation of vorticity) production in a swirling jet flame, possibly due to the mean pressure gradient of the swirl.

1.5.4 Hydrodynamics of reacting JICF

Studies quantifying unsteady effects of combustion on the JICF flowfield are relatively few. The general trend of observations has been that flames, both premixed and non-premixed, generally play a role in altering the qualitative vortex shedding behavior of the shear layer vortices. Nair et al. [84] used velocity data from PIV to track the strength of coherent vortices in the shear layer for non-premixed reacting and non-reacting cases noting that the growth rate was suppressed for reacting cases – similar to the observations for jet flames. While the strength here was calculated primarily from a two dimensional metric, follow-on work utilized tomographic PIV data [85] to characterize the three

dimensional topology and strength distribution, and demonstrate that the centerplane data sufficiently captures the growth in vortex strength. Pinchak et al. [38] focused on the effect of heat release on wake behavior for the case of a high-aspect ratio jet. By tracking the distribution of vortical structures, and using the mean vorticity field, they demonstrate a qualitatively different wake for the reacting case concluding that the heat release extends the wake region by inhibiting mixing.

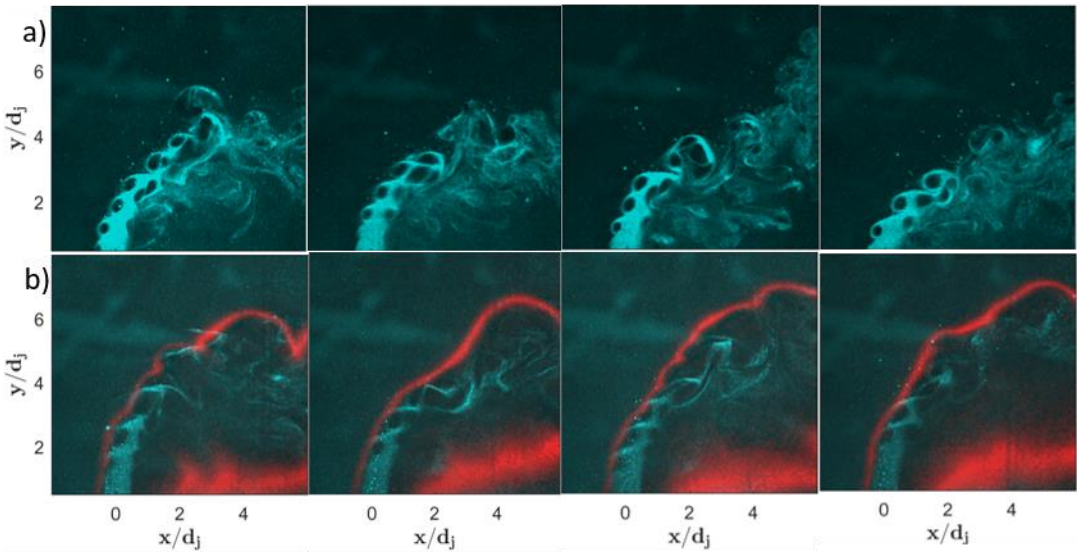

Figure 1.20: Mie Scattering (cyan) and OH-PLIF (red) instantaneous images for a) non-reacting and b) reacting cases, Nair et al. [84], showing suppressed vortex rollup in reacting cases.

The JICF is a complex three-dimensional flowfield with multiple interacting coherent structures and therefore obtaining a comprehensive understanding of the effect of reactions on flow dynamics is challenging. While evaluating the effect of baroclinicity or heat release, there is still uncertainty if the mean pressure variation, as described by Iyer and Mahesh [58], or the unsteady variation within coherent structures will play a major role in suppressing heat release. In addition, the sheer number of possible flame

configurations and stabilization mechanisms (Section 1.2.2) results in highly varying local heat release effects from case to case, making comparisons challenging.

1.6 Motivation and thesis outline

The primary goal of this thesis is to extend our understanding of the impact of combustion on the behavior of coherent structures and flowfield dynamics of a single reacting jet in crossflow.

Chapter 2 presents details of the experimental facility and the test matrix used in this study, along with a discussion on why those specific conditions were chosen. The focus is to extend the parametric space, in J and S, investigated by previous studies [25] and include an additional parameter of interest – the flame-shear layer offset through compositional modifications. As elaborated in Section 1.2, two applications for a reacting jet in a crossflow include staged combustion configurations and RQL-type combustion systems. Incidentally, both these cases have a vitiated crossflow, and the compositional differences between the jet and the crossflow in each case lead to theoretically different flame-shear layer offsets. As a result, adjusting the flame position, in addition to providing limiting cases to gauge the effect of combustion on flow dynamics, provides valuable practical information regarding the potential behavior of RQL type systems compared to its much better studied counterpart – the fuel jet into an oxygen rich crossflow.

A variety of non-intrusive optical diagnostic techniques were employed to extract data from the plane of symmetry of the JICF flowfield. High-speed Stereoscopic Particle Image Velocimetry (SPIV) was used to extract velocity data, to characterize the flow topology and hydrodynamic instability behavior under different conditions. Simultaneously, OH

Planar Laser Induced Fluorescence (PLIF) was used to extract information on the spatial distribution of OH radical concentration, a good proxy for the temperature and distribution of hot products and can be used to infer the flame position. This was supported by OH* Chemiluminescence to obtain the spatially averaged heat release through the span of the flowfield. Details regarding the diagnostic setup and post processing techniques used to extract information for the data generated by these techniques is provided in chapter 3.

The first research question tackled by this study is – *Does moving the flame inside the shear layer fundamentally change the structure and dynamics of a reacting jet in crossflow?* A fundamentally different structure here implies that existing scaling based on non-reacting and reacting jet parameters would not be able to capture the behavior and dynamics. Chapter 4 is therefore devoted to characterizing the differences in flow features for the non-reacting and the reacting cases with special emphasis on the qualitative differences in flow/flame topology. The results presented show significant differences in the flow structure on moving the flame inside the shear layer.

The second research question attempts to quantify these observed differences – *How does the measure spatial growth rates vary across different S, J and flame configurations?* Chapter 4 further details the characterization of vortex strength and extraction of spatial growth rates based on this quantity. These growth rates are further correlated with other structural and stability characteristics observed in JICF including non-linear saturation as well as turbulent breakdown. Due to the nature of the unsteady crossflow, a phenomenon characteristic of vitiated crossflows [25, 65], a discussion on the effects of this unsteady crossflow in interpreting the time-averaged and ensembled metrics presented in the rest of the paper is included.

The third research question addresses the gap in literature dealing with the characterization of the natural spectral response of reacting jets in crossflow – *How does the shear layer spectrum change with respect to the parameters of interest of this study (S, J and flame-shear offset) and can this help classify the global/convective instability behavior for RJICF configurations?* Chapter 5 presents velocity spectrum data along with ensembled metrics tracking characteristic vortex length and time scales. The appropriate scaling for these extracted frequencies is further investigated by considering appropriate normalizing length and velocity scales. In addition, while the viscosity is not a controlled parameter in this study, given that the reacting cases will tend to have a lower absolute viscosity, its impact on the global to convectively unstable transition will be discussed in this section.

Finally, noting that the traditionally used JICF parameters (S, J) cannot uniquely describe the stability behavior for RJICF configurations, the final question is posed as – *What parameters can be used to quantify the stability effects for RJICF configurations and can this be used to identify the mechanism by which combustion alters stability behavior ?* The counter current shear layer (CCSL) model is evaluated as a possible method of extracting parameters that better describe the stability behavior.

Chapter 6 summarizes the results and highlights the major contributions of this work while charting a possible direction for future work.

CHAPTER 2. EXPERIMENTAL SETUP

This chapter describes the experimental facility used for this study. The experimental facility was modified from a previous Reacting Jet in Crossflow study [25].

2.1 Experimental facility

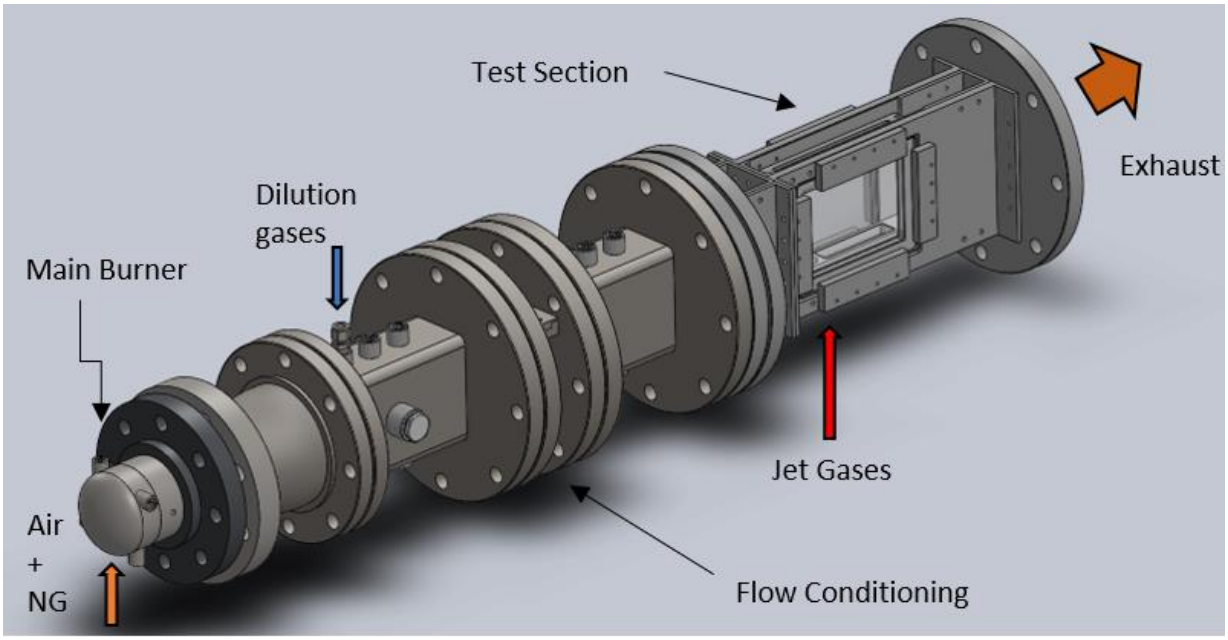

Figure 2.1: Schematic of overall experimental rig.

An overview of the experimental reacting jet in crossflow facility is provided in Figure 2.1.The blow-down facility is open to the atmosphere at the exit and thus, the test section operates at atmospheric pressure. A vitiator is used to control the temperature and composition of the main flow and allows for continuous operation at high temperature conditions.

2.1.1 Main burner

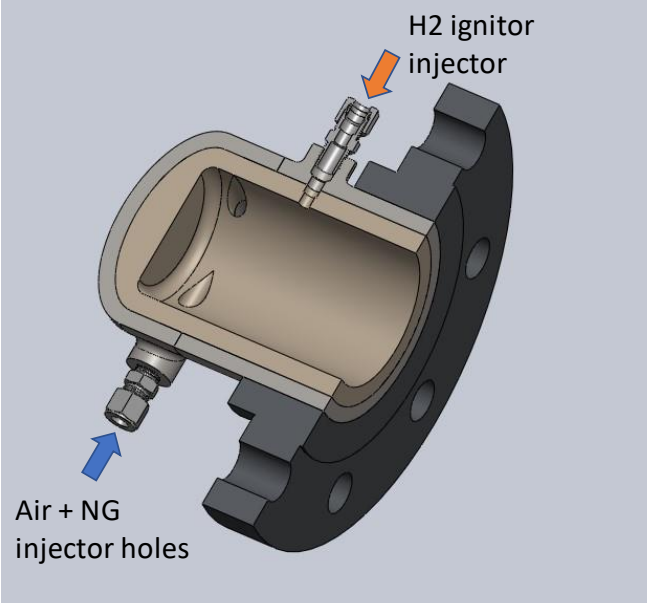

Figure 2.2: Main burner schematic

The main burner consists of a swirl-stabilized natural gas burner where the products are injected tangentially via four injection ports (Figure 2.2). The air coming into the main burner passes through an electric heater which can preheat up to a temperature of 600K. The combustion chamber has a length of 11mm, has an inner diameter of 76 mm and is lined with castable ceramic (Cotronics Corp. Rescor 780). Ignition is enabled through a hydrogen- torch injected through a ceramic coated electrode.

2.1.2 Flow conditioning section

The flow conditioning section consists of a two 30 cm settling chambers with two ceramic honeycomb flow straighteners separated by 10 cm. The honeycombs consist of 2.5 cm thick Mullite Versagrid units consisting of 6.35 x 6.35 mm^2 passages. The first settling chamber houses a ceramic sheathed R-type thermocouple for crossflow temperature

measurements. The bypass stream is injected into the first settling chamber through two injection holes (Figure 2.3) on the bottom and top of the test section. The first settling chamber is lined with two layers of castable ceramic, roughly 0.5 inches in thickness, in order to mitigate heat loss. The outer layer consists of a ceramic compound with extremely low conductivity (Rescor 740) but insufficiently high operating temperature for the crossflow temperature. In order to protect this layer, the inner layer (Rescor 760) has a much higher operating temperature while being slightly more conductive. The second settling chamber has a similar two-layer setup, but the thickness is approximately 0.25 inches thick.

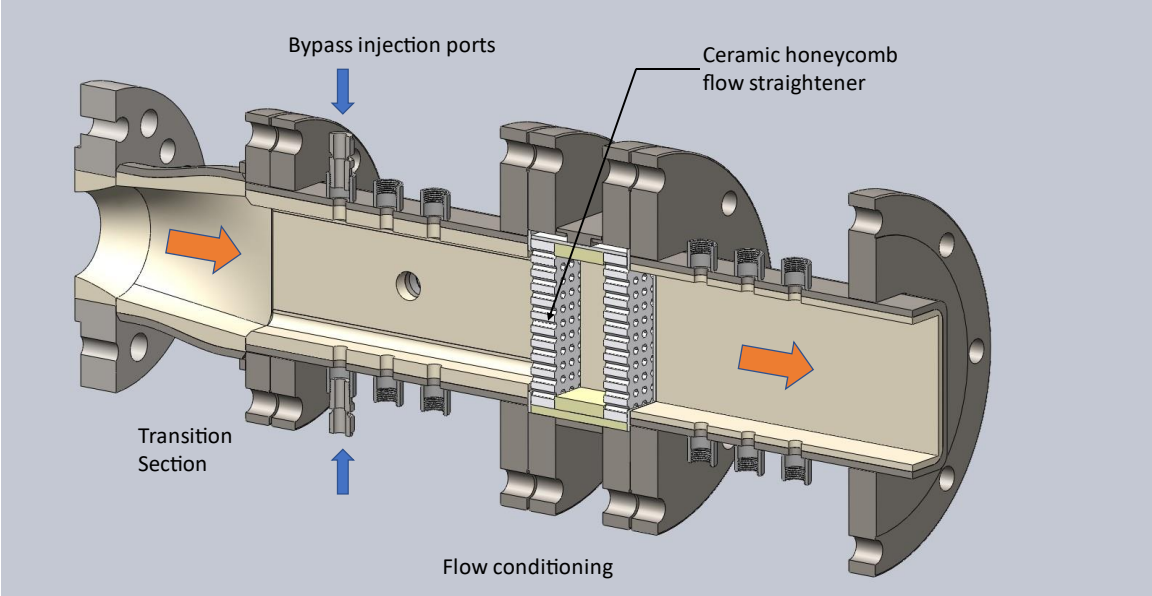

Figure 2.3: Flow conditioning section

2.1.3 Test Section

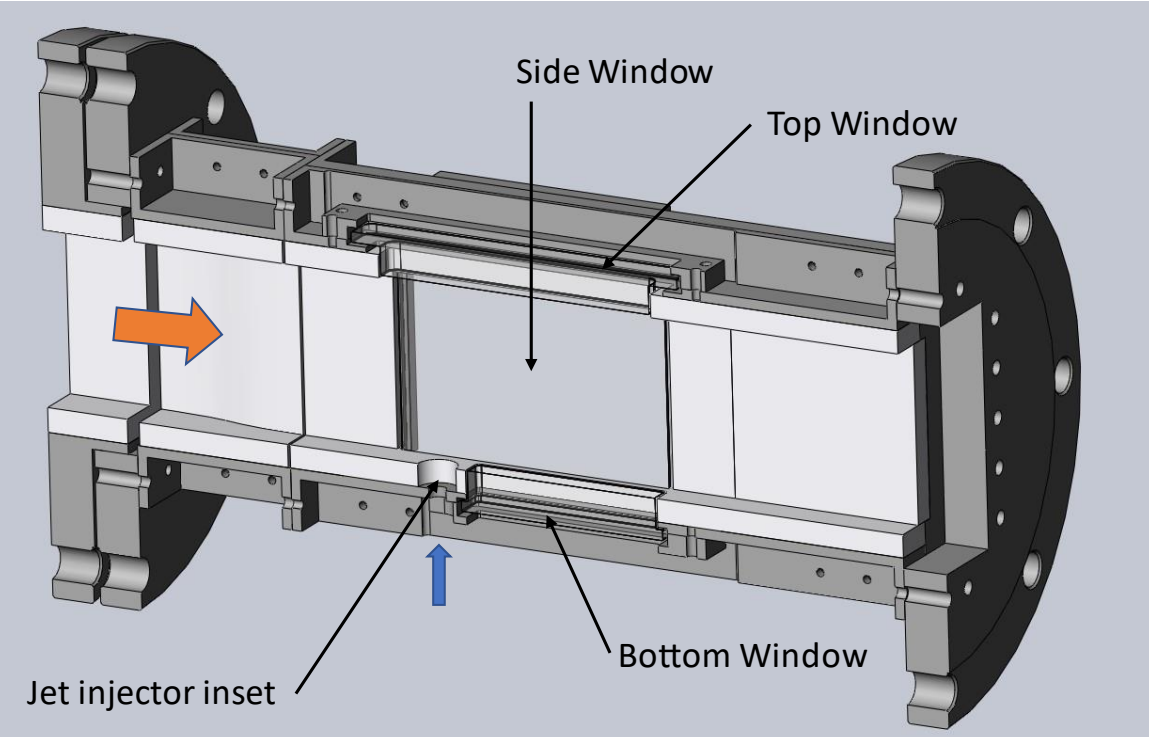

Figure 2.4: Test section schematic

The test section includes an area contraction (5th order polynomial contour) which transitions the cross section from dimensions of 76 × 114 mm^2 to 38 × 114 mm^2. This was done in order to increase the crossflow velocity and range of test conditions reachable by the vitiator. The interior walls of the test section were lined with machinable ceramic plates roughly 6.35 mm in thickness. Confinement effects are minimal in the near filed due to the width of roughly 12 d_j, while the height is sufficient for jet momentum flux ratios of J = 40 without interacting with the top wall. The test section provides optical access via two side windows and one top window, made from optical grade quartz, providing a viewable region of around 12 d_j × 44 d_j downstream of the jet. All the windows are designed to protrude into the test section so as to ensure that the inner surface is flush with the ceramic layer.

The bottom window extends a region of 20 d_j behind the nozzle insert and helps to reduce the noise from laser reflections off the bottom surface. The test section is also clamped to the base of the experimental test stand while the other sections float freely on castors to minimize the misalignment of the optical setup due to thermal expansion of the rig

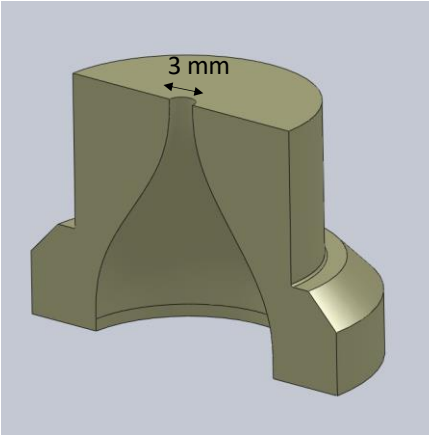

Figure 2.5: Ceramic nozzle insert

The jet insert is fabricated from machinable ceramic (Cotronics Rescor 960-9) with the nozzle machined on the inside and flush with the bottom wall of the test section. The nozzle is contoured using a 5^{th} order polynomial contraction in order to obtain a nearly top-hat velocity profile (Figure 2.10) similar to previous studies [21, 25]. The base of the nozzle contains a large plenum of diameter 22.9 mm and a length of 127 mm and is connected to the jet supply via a choked critical orifice. This helps in reducing the flow non-uniformities as well as fluctuations in the jet flow during intermittent seeding.

2.1.4 Flow Metering and Measurement

The gases used in the JICF facility can be primarily categorized based on whether the flow path involves the main flow, the dilution flow or the jet flow. The vitiator (main

burner) is supplied with air from the building's 125 psig supply, which is regulated down to 70 psig. The air is then routed through an electrical heater, which can increase the temperature of the air to a maximum of 600 F. The air supply is metered through a sub-critical orifice assembly that includes a static pressure transduced (Omega PX-209) upstream of the orifice, a K-type thermocouple and a differential pressure transducer (Omega PX-771A). The flow rate is controlled by means of a needle valve downstream of the subcritical orifice assembly. The natural gas for the vitiator is supplied from the building's 25 psig system. The natural gas line is also metered through a similar subcritical orifice assembly with a differential pressure transducer and metered through a needle valve.

As mentioned before, the dilution system is used to control the temperature and composition of the main flow while allowing for seeding. The flowpath for the dilution system allows for two dilution gases to be independently metered and mixed before passing through the seeding system and entering the crossflow. Each dilution gas stream is controlled via a needle valve and metered through a critical orifice assembly which consists of a K-type thermocouple, a static pressure transducer (Omega PX -209) upstream of the orifice to measure the supply pressure, and a static pressure transducer (Omega PX-209) at the mixing junction to ensure that the two streams are choked. The seeding system consists of an agitated swirl seeder with a solenoid valve upstream of it to enable seeding. An attached bypass system with a needle valve controls the pressure drop across the bypass to set the mass flow of dilution gases that will pass through the seeder. The gases for the dilution system are either sourced from the building supply, in the case of air, or from gas bottles. The air supply is regulated down to 150 psig to eliminate fluctuations from the building supply. The other gases that can be connected to the dilution system, sourced from

gas bottles and regulated to a supply pressure of 150 psig, are H_2 and He which are used for the rich crossflow conditions (details of the test conditions will be covered in the next section).

The jet flow system can supply a mixture of two gases that are sources from gas bottles. The gases used in this experiment include H_2, N_2, He and the premixed gas mixtures which will be used in the rich crossflow cases. Fuel gases like H_2 are connected to the gas supply system through a solenoid valve. The two gases that form the mixture for any particular test condition are metered independently through two critical orifice assemblies, similar to the system described above, and are controlled through needle valves. A static pressure transducer is located at the point of mixing to ensure the orifices are choked. After the point of mixing, the jet gases pass through the jet seeder system, which consists of a swirl seeder with a solenoid valve upstream to control the seeding. A bypass system allows for control over the mass flow going into the seeder through the use of a needle valve which allows for variable pressure drops to be set.

The jet flow then passes through a variable power heating element, which consists of piping wrapped with heat tape controlled with a variable voltage DC converter and insulated with fiberglass. As mentioned in the previous section, a critical orifice is located before the jet plenum, which serves to prevent acoustic coupling with the jet supply as well as prevent transients in the jet supply during seeding. In order to ensure that this orifice is choked, a static pressure transducer is located upstream of the orifice on a standoff tube. Downstream of the orifice, a four-way junction that allows for a thermocouple to measure the temperature of the gas entering the plenum, as well as a connection to a H_2 seeding line used for the rich cases. The seeding gas, H_2, is metered via a critical micro-orifice assembly

which includes a K-type thermocouple and a pressure transducer upstream of the orifice. The supply is connected to the dilution H_2 stream that is controlled via a solenoid valve for safety reasons and allows for the flow of H_2 into the dilution flow as well as the jet flow to be enabled simultaneously for safety reasons and ease of control.

The flow measurement instrumentation is monitored and recorded using a Labview application which displays the measurements at a sample rate of 10 Hz. The raw signals from the devices are sampled at a rate of 1 kHz on the FPGA device (NI-cRIO) which consist of multiple modules. The differential pressure transducers and static pressure transducers at the sub-critical orifice assembly are connected to 4-20 mA circuits via the NI 9208 module. The remaining pressure transducers are all connected to the chassis through 5V DC measurement circuits via the NI 9215 module and the thermocouples are measured using an NI 9213 module.

2.2 Design of experiments

This section describes the design of the test matrix and test conditions necessary for the investigation of the research questions posed in Section 1.5.4. The experimental conditions can be broadly separated into three categories – non-reacting (NR), reacting condition with the flame lying outside the shear layer (R1) and reacting with the flame lying inside the shear layer (R2).

For each category mentioned above, the test matrix involves varying J and S, the primary non-reacting jet parameters. Both J and S can be controlled by changing the conditions of the crossflow or the jet. As the vitiator can operate stably only for a limited range of mass flow rates and equivalence ratios, the crossflow velocity (u_∞) and

temperature (T_∞) cannot be varied to obtain a sufficiently large range of J values. In addition, changing the temperature through changing equivalence ratio cannot vary S sufficiently, as it is limited by the adiabatic flame temperature and heat loss through the facility. Thus, for each category of experiments, the crossflow conditions are kept fixed while J and S are varied by changing the conditions of the jet. In addition to the larger operability range, this also keeps the background natural acoustics of the facility relatively constant across the test conditions.

Table 2-1: Crossflow properties

	Lean		**Rich**	
Vitiator Properties				
$\dot{m}_{vitiator,fuel}$	0.617 g/s		1.39 g/s	
$\dot{m}_{vitiator,air}$	18.4 g/s		18.1 g/s	
$\Phi_{vitiator}$	0.575		1.3	
$T_{ad,vitiator}$	1635 K		1705 K	
Dilution flow Properties				
$\dot{m}_{total}$	3 g/s		0.812 g/s	
Composition	χ_{N_2}	0.79	χ_{He}	0.64
	χ_{O_2}	0.21	χ_{H_2}	0.36
T_{bypass}	300 K		300 K	
Crossflow Properties				
T_∞	1178 K		1150 K	
U_∞	14.5 m/s		21.5 m/s	

Table 2-1 (continued)				
$\boldsymbol{\rho_\infty}$	0.298 kg/m^3		0.189 kg/m^3	
$\boldsymbol{\mu_\infty}$	0.0475 mPo		0.045 mPo	
$\boldsymbol{Re_\infty}$	9960		10400	
Composition	χ_{O_2}	0.101	χ_{He}	0.075
	χ_{H_2}	0.0	χ_{H_2}	0.269
	χ_{H_2O}	0.098	χ_{H_2O}	0.146
	χ_{CO_2}	0.049	χ_{CO_2}	0.010
	χ_{CO}	0.0	χ_{CO}	0.065
	χ_{N_2}	0.75	χ_{N_2}	0.435

Between the three categories, the NR and R1 conditions require a high-temperature oxygen rich crossflow. For these cases, the vitiator is operated at a lean equivalence ratio and the choice of dilution gas is air. For the R2 cases, the vitiator is run at a rich equivalence ratio. But, operating the swirl burner at an equivalence ratio necessary for obtaining a sufficiently high fuel concentration in the crossflow is challenging. The primary reason is that the high-swirl NG burner cannot operate stably at an equivalence ratio, $\Phi_{vitiator} \geq 1.5$. In addition, the vitiator can only be ignited at a lean equivalence ratio and the fuel flow increased to get to the rich equivalence ratio, which exerts a sudden thermal shock on the ceramic liner. Thus, to get to the necessary rich crossflow conditions, the vitiator is run at an equivalence ratio of 1.3 and a mixture of H_2 and He is injected through the dilution ports to further increase the H_2 concentration in the crossflow. Detailed conditions for both the lean and rich crossflow are given in Table 2-1.

The compositions listed in Table 2-1 is assumed to be the equilibrium products of combustion considering the composition of the vitiator and the dilution streams. This is a reasonable assumption, with respect to the major species, based on the residence time of the flow stream post vitiation – 50 ms. For the same reason, given the residence time and the heat loss from the rig, the adiabatic flame temperature (T_{ad}) calculated from the composition does not provide a good estimate of the flow properties entering the test section. To estimate the temperature, the mass averaged velocity calculated from the mass flow measurements was compared with the average velocity calculated from the crossflow velocity profile. In addition, an R-type thermocouple was inserted through the jet and the readings used in correlation with this temperature. This allows for a more accurate estimate of the thermodynamic properties of the crossflow prior to entering the test section. The temperature estimate (T_∞), along with the measured mass-averaged velocity (u_∞), is used to calculate the resulting crossflow Reynolds number, $Re_\infty = \rho_\infty u_\infty h / \mu_\infty$, which is similar for both the rich and lean conditions. The uncertainties in this process are listed in Appendix A (Uncertainties in calculation of parameters). The mass flow conditions listed in Table 2-1 were chosen with two considerations: to obtain a velocity and Reynolds number value closer to those observed in most industrial staged combustion/RQL systems than other fundamental studies while ensuring that the appropriate time scales can be captured by the diagnostic systems.

The three primary parameters of this study – S, J and the flame position are manipulated primarily by changing the composition, temperature (T_j), and velocity (u_j) of

the jet. Since both the crossflow conditions involve vitiation, mixtures of low molecular weight gases such as H_2 and He are necessary to obtain a low-density jet. The thermophysical properties of the jet fluid for each case is listed in Table 2-2. The targeted range of density ratios for each case is chosen based on the observed change in hydrodynamic stability behavior for a non-reacting JICF [53] as stated in Section 1.4. For the non-reacting conditions, a mixture of inert gases – N_2 and He is used to obtain the required density ratios. The viscosity is obtained by using the transport properties for the gas mixtures calculated in Cantera.

For the reacting case, R1, as the crossflow is oxygen-rich, the jet contains H_2 as the fuel of choice for two reasons. Primarily, as elaborated in Section 1.2.2, there are many different types of RJICF flame topologies depending on local chemical time-scale considerations which can have significantly different effects on flow-dynamics. Here, it is desirable to decouple the problem of flame stabilization from the study of the effect of heat release on hydrodynamics. Given the temperature of the crossflow, approximately T_∞ = 1150 K, H_2 is the most practical choice for a fuel as its fast kinetics ensure auto-ignition and a fully attached flame configuration for all flow conditions. In addition, the low molecular weight of H_2 allows for gas mixtures with density lower than the transitional value. From Table 2-2, H_2 is mixed with N_2 or He and the jet fluid temperature, T_j is adjusted to obtain the specific density ratios. The lower target S = 0.35 is chosen as lower density ratios are not practically possible given the low density of the vitiated crossflow. At the upper end, the limit of S = 1.75 was chosen as the presence of H_2 as the fuel significantly decreased the density of the mixture and obtaining higher density ratios

through increased dilution levels (with N_2) resulted in suppressed chemistry and a loss in flame stability.

Table 2-2: Jet fluid properties

	S	T_j (K)	Composition				ρ_j (kg/m^3)	μ_j (mPa-s)	T_{ad} (K)
			χ_{N_2}	χ_{H_2}	χ_{O_2}	χ_{He}			
NR	0.35	475	0.0	-	-	1.0	0.103	0.027	-
	1.0	300	0.12	-	-	0.88	0.295	0.02	-
	1.75	300	0.4	-	-	0.6	0.51	0.02	-
R1	0.35	300	-	0.72	-	0.28	0.104	0.012	2153
	1.0	400	0.3	0.7	-	-	0.29	0.02	2176
	1.75	300	0.4	0.6	-	-	0.51	0.017	2135
R2	1.1	550	-	0.02	0.2	0.78	0.209	0.033	2120
	2.2	550	0.38	0.04	0.2	0.38	0.41	0.033	2199

The conditions listed above involve using a fuel rich jet to create a non-premixed flame on interaction with the oxygen-rich crossflow. Due to the vitiated nature of the crossflow, and the significantly large amount of air required to burn a fixed mass of fuel at stoichiometric conditions, the mixture fraction for combustion (f_{st}), and subsequently the

flame position, will tend to lie in the crossflow side of the shear layer of the jet. As stated in the research goals, one of the main objectives of this study is also to investigate the effect on RJICF hydrodynamics while manipulating the flame position. This is accomplished in this study by running the head end at a rich equivalence ratio while using a jet containing an oxidizer. The specifics for the composition of the fuel-rich crossflow was covered in the previous paragraphs and in Table 2-1, and further details on the calculations used to establish the nominal flame position for each case are detailed in Appendix A.3. The choice of oxidizing gas is limited to O_2, which creates some challenges in matching crossflow density conditions due to its relatively high molecular mass. To obtain the targeted density ratios, O_2 is combined with inert gases such as He and N_2.

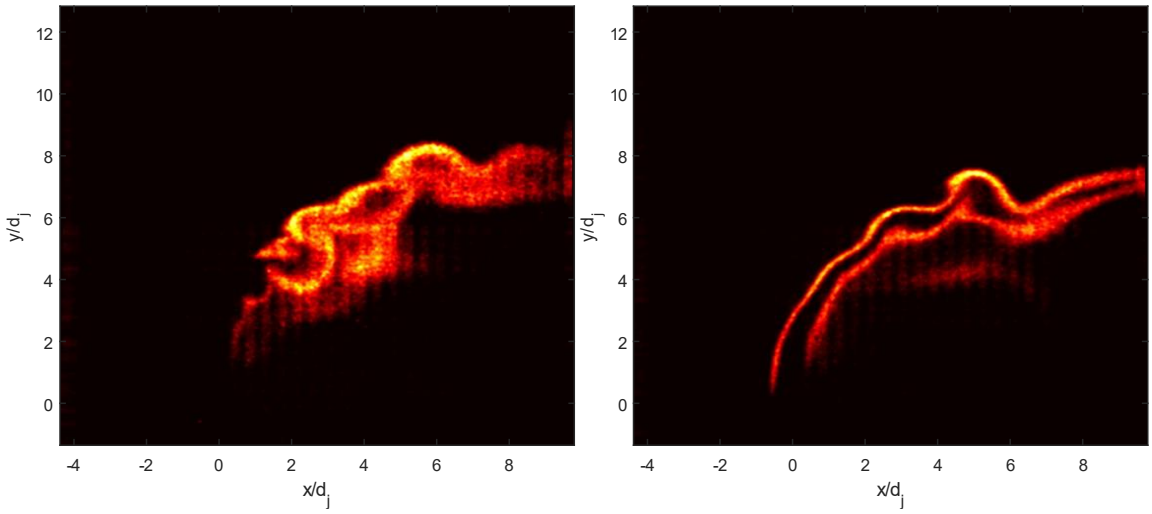

Figure 2.6: OH-PLIF intensity fields for R-2 case with H_2 doping (right) and without (left).

The second challenge in the R-2 case is the feasibility of obtaining a stably attached flame under these configurations. Most previously investigated RJICF configurations involve fuel injected into an oxygen-rich crossflow, which like case R-1, have a flame that

is stabilized outside the jet shear layer. In such a configuration, the flame stabilization point lies within the crossflow boundary layer where the high-temperature crossflow (i.e. fast kinetics) and the low velocity scale of the boundary layer contribute to a favorable attachment point. But, in the R2 configuration, moving the flame inside the shear layer requires that the point of stabilization lies in the relatively colder jet fluid with a much faster local velocity timescale. To mitigate these issues, the jet is heated to a temperature T_j = 550, which helps to reduce the density of the mixture further and increase its reactivity. In addition to this, a small amount of H_2 (2 – 4% by volume) is added as a doping agent to further increase the reactivity of the jet mixture, allowing for a flame to stabilize under the unfavorable conditions inside the jet shear layer. This can be seen from the flame position inferred from the OH-PLIF intensity fields in Figure 2.6. For all the reacting cases, R1 and R2, the composition and temperature is adjusted to ensure the net exothermicity, measured here as the adiabatic flame temperature (T_{ad}) at f_{st}, is similar in all the cases.

Table 2-3: List of cases with corresponding properties

Case	Type	J(target)	S (target)	u_j (m/s)	Re_j
1	NR	6	1.75	27.03	2225
2	NR	12	1.75	38.23	2986
3	NR	18	1.75	46.82	3607
4	NR	30	1.75	60.45	4650
5	NR	6	1	35.76	1560
6	NR	12	1	50.58	2141
7	NR	18	1	61.94	2426
8	NR	30	1	79.97	3392
9	NR	6	0.35	60.45	727
10	NR	12	0.35	85.49	980
11	NR	18	0.35	104.70	1096
12	NR	30	0.35	135.17	1542
13	R-1	6	1.75	27.03	2373

Table 2-3 (continued)					
14	R-1	12	1.75	38.23	3487
15	R-1	18	1.75	46.82	4323
16	R-1	30	1.75	60.45	5546
17	R-1	6	1	35.76	1564
18	R-1	12	1	50.58	2184
19	R-1	18	1	61.94	2801
20	R-1	30	1	79.97	3353
21	R-1	6	0.35	60.45	1557
22	R-1	12	0.35	85.49	2138
23	R-1	18	0.35	104.70	2738
24	R-1	30	0.35	135.17	3518
25	R-2	6	2.2	35.92	1434
26	R-2	12	2.2	50.79	1719
27	R-2	6	1.1	50.21	1077
28	R-2	12	1.1	71.01	1500

To investigate the variation in RJICF dynamics with the other primary non-reacting parameter – J, the mass flux through the jet is adjusted for a fixed composition to target the specific momentum flux as described in Table 2-3. While the Reynolds number, and consequently the momentum thickness θ/d_j, varies between cases at fixed J and S, previous studies have shown that Re_j does not have a significant effect on jet dynamics under these constraints [21].

2.3 Baseline measurements

This section will present measurements made to establish the inlet conditions of the crossflow and the jet.

2.3.1 Crossflow Characterization

The crossflow velocity profile was characterized using PIV measurements. Details of the setup and experimental details are provided in Section 3.2. To prevent any influence

from the jet, the ceramic nozzle was replaced by a filled plug. In this study, there were two distinct crossflow conditions used – lean and rich based on the category of experiment. Figure 2.7 compares the axial velocity profile (u) normalized with the outer flow velocity, u_e, for each case. The transverse coordinate (y) is normalized with respect to the half channel height, h. The shape profile is similar in both cases and, as listed in Table 2-1, the crossflow Reynolds numbers are similar in both cases based on the mass-averaged flow velocity.

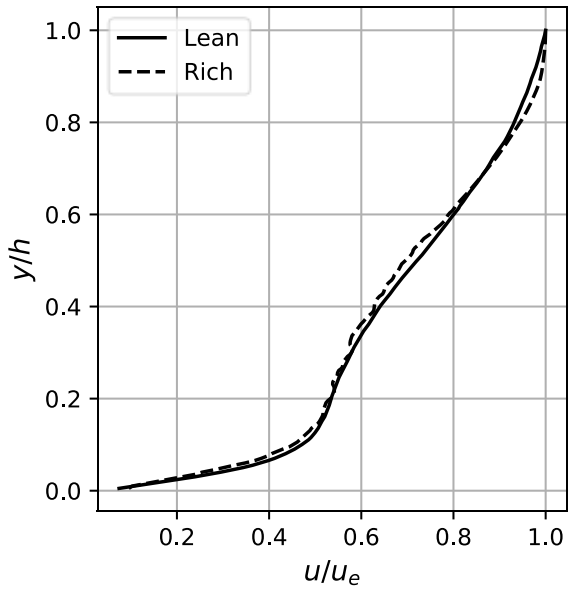

Figure 2.7: Comparison of measured axial velocity profile between the two conditions.

The measured mean velocity profile is compared with theoretical laminar and turbulent profiles in Figure 2.8a. The calculated free-stream Reynolds number (Re_∞) was estimated using the measured mean velocity at the mid plane and is used to estimate C_f [86] and calculate the friction velocity, u_τ = 1.01 m/s, and the viscous length scale, δ_v = 0.16 mm. These values are used to construct the theoretical laminar and log-low turbulent

profiles based on the same integrated mass-averaged velocity - $u_\infty = \frac{1}{h}\int u(y)dy$. The crossflow Reynolds number ($Re_\infty \sim 11000$) , suggests that the flow regime is turbulent, but the measured profile deviates from the theoretical fully-developed outer velocity scaled profile [86]. In the region $y/\delta < 0.1$, the profile is close to the theoretical log-law profile while in the region $y/\delta > 0.5$, the shape of the profile resembles the theoretical laminar profile. This suggests that flow is in a somewhat transitional regime.

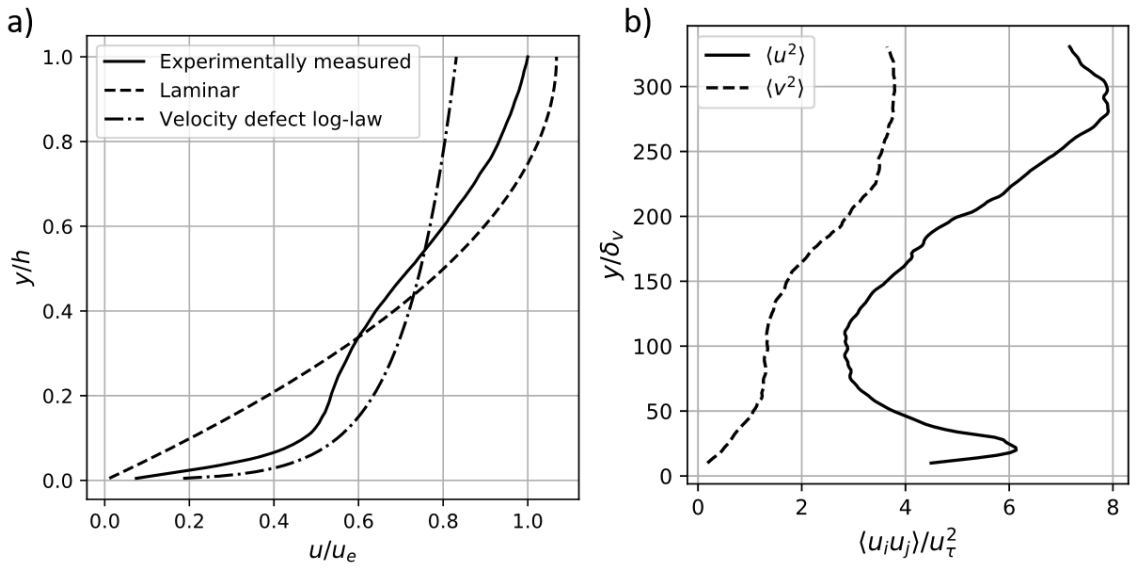

Figure 2.8: a) Comparison of experimentally measured profile with theoretical profiles; b) comparison of spanwise variation of fluctuating components.

The flow path upstream of the test section and the design of the test section might contribute to this deviation. Based on previous theoretical studies on channel flows [87], the minimum development length for a fully-developed channel flow is often significantly longer than the distance between the honeycomb flow-straightener and the test section (Section 2.1.2). This is supported by the PIV data near the test section centerline, which suggests that U_e decreases up to 5 % over a length of 10 d_j in the vicinity of the jet. The

5th order polynomial contoured nozzle upstream of the test section with an area contraction of approximately 2:1 leads to a favorable pressure gradient, which can further explain the deviation for the theoretical turbulent profile [88]. In addition, the aspect ratio of the test section here is less than 1, while most studies [89] have suggested that a minimum aspect ratio of 6 is necessary to neglect three-dimensional effects.

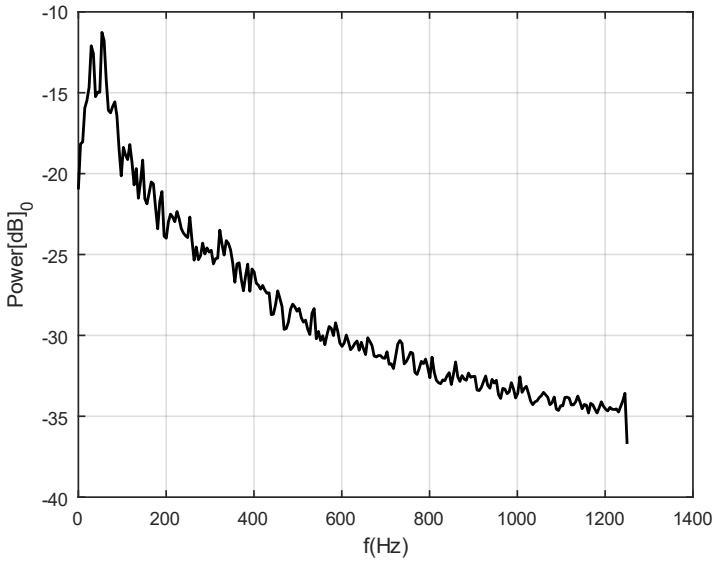

Figure 2.9: Power spectrum of the crossflow axial velocity.

The fluctuating velocity field, including the streamwise and spanwise components, are plotted for the lean crossflow case in Figure 2.8b. The peak in the measured fluctuations at y_+ = 20 is due to the high level of energy production due to the mean shear in the near wall region [86]. While the experimentally measured fluctuations deviate from the theoretically expected value in the outer flow region (y_+ > 100), the Reynolds stresses represent both random turbulent fluctuations as well as coherent fluctuations due to acoustics. While care was taken to not operate the rig at thermo-acoustically unstable parameter spaces, background acoustic has a strong influence on coherent structures in the

crossflow. The spectral content of these coherent structures in the crossflow velocity field can be seen in Figure 2.9, where the peak fluctuations occur at frequencies f = 58 Hz and 29 Hz. The power spectrum is averaged over the time varying velocity measurements made at each point above the jet exit.

2.3.2 Jet Characterization

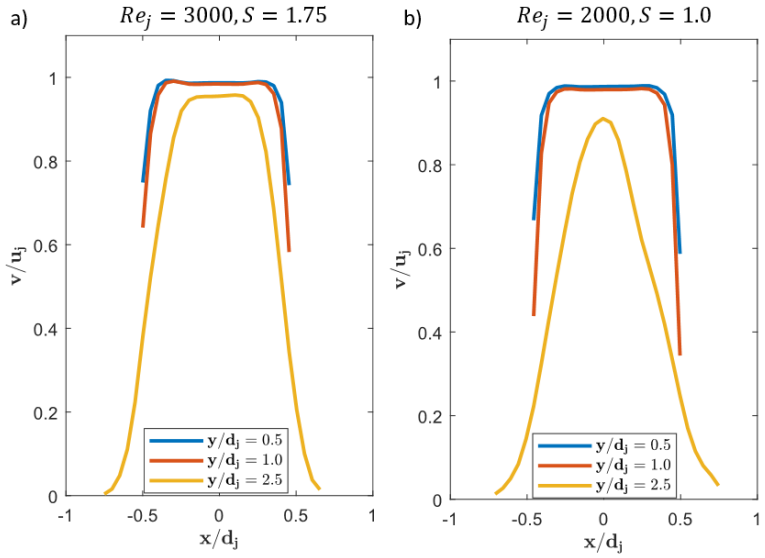

Figure 2.10: Jet velocity profile across two different Reynolds numbers and *S* values.

The jet velocity profile was characterized using the SPIV measurements using the setup detailed in Section 3.2 while seeding only the jet and with no crossflow present. The transverse velocity profile for two cases with different Re_j and S were presented here to characterize the shape of the velocity profile. For both the cases measurements taken near the jet exit show that the velocity profile (Figure 2.10) resembles a top-hat like shape similar to profiles observed by Megerian et al. [21] and Wilde [25] for a similar nozzle

contour. The lower density case ($S = 1.0$) shows a shorter potential core as is characteristic of low-density free jets.

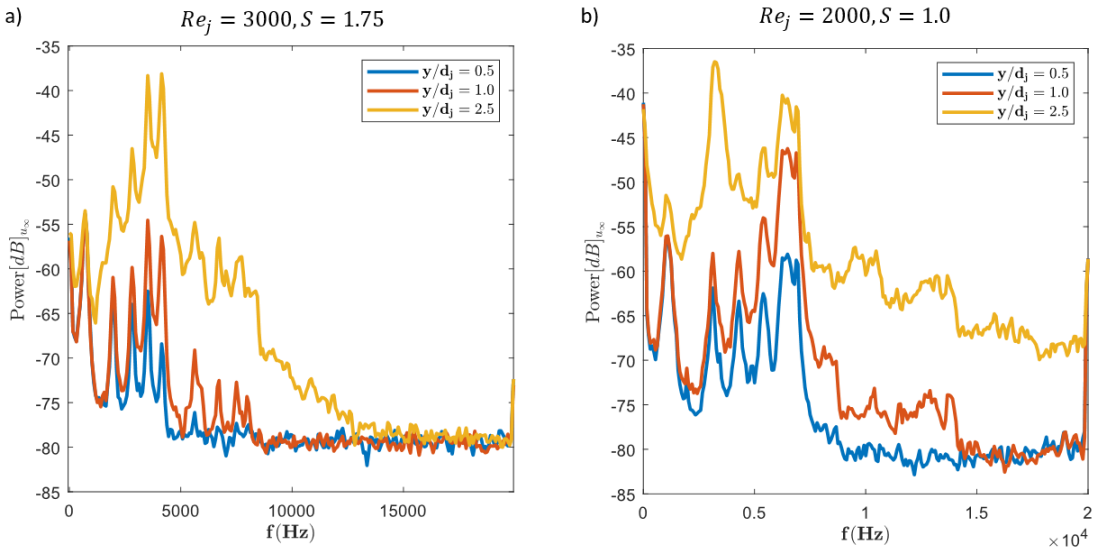

Figure 2.11: Transverse velocity power spectrum probed at three locations along the centerline for two different Reynolds numbers and *S* values.

The transverse velocity spectrum along the jet centreline at three probe locations was also used to validate that the jet supply system does not introduce strong tones. Figure 2.11 shows that the spectral amplitude of the transverse velocity fluctuations, referenced with respect to the crossflow velocity scale, is very weak at locations near the jet exit. The observed tones likely correspond to the vortex shedding from the free jet which is likely influenced weakly by acoustics in the jet plenum. Between the two cases no common narrowband frequencies were observed confirming that the jet supply system does not act like an acoustic forcing source during operation and thereby impose its resonant frequencies on the dynamical content of the JICF configurations. The observed frequencies were also lower than the fundamental frequencies characterized for the convectively unstable JICF configurations in Chapter 5.

CHAPTER 3. DIAGNOSTIC TECHNIQUES AND POST PROCESSING METHODOLOGY

This chapter details the diagnostic techniques and data processing methodologies utilized in the rest of this thesis. Non-intrusive laser and optical based diagnostic techniques were primarily used due to the high-temperature environment in the reacting flow. Planar techniques allowed for simultaneous acquisition of flowfield information in the centerplane of the JICF flowfield. To this end, stereoscopic-particle image velocimetry (SPIV) was used to obtain velocity measurements in the centerplane while OH* chemiluminescence and OH-planar laser induced fluorescence (OH-PLIF) were used for the purpose of studying the flame behavior in the reacting cases.

Particle image velocimetry is a non-intrusive laser diagnostic technique where small 'seed' particles are introduced into the flowfield. A high powered, typically monochromatic coherent light source (here, a laser) is used to illuminate the seed particles and a digital camera or similar imaging device records these illuminated 'snapshots' of the flowfield. These images are a consequence of Mie scattering by the particles, since they are typically larger than the wavelength of the light source. The velocity data is obtained by correlating two snapshots of the Mie-scattering images, analogous to the position of particles in the flowfield, which are taken with a small (with respect to the flow time-scales) time-lag. While there are numerous variants of PIV techniques based on the application and data requirements [90], for this study we employ high-speed SPIV, a variant where three-components of the velocity can be obtained from a 2D interrogation plane in the flow domain.

To supplement the flow information with information on the flame position and reaction zone characteristics, OH-PLIF and high-speed chemiluminescence were used simultaneously with SPIV. PLIF can probe the concentration of target species by exciting molecules using a monochromatic light and imaging the subsequent emissions. In this thesis, the region of interest is a plane concurrent with the PIV region of interrogation and the molecule of interest is the hydroxy radical (OH). OH has an important role to play in the combustion process and thus can be correlated to the flame position based on the flame characteristics [91] – this relationship is further explored in Section 3.4.2. Chemiluminescence is a passive technique where the natural light emission of combustion processes is captured with a camera. Often the emissions can be filtered to target a specific activated radical. Here, the emissions are filtered to target the light released by OH*, the activated hydroxyl radical, which is an intermediate species in the combustion chemical pathway. The quantum of light released by OH* is often a good marker for the local thermal energy release [92].

3.1 Combined diagnostic setup

The capabilities of most optical diagnostic systems (PIV, PLIF or chemiluminescence) are often limited by the acquisition technology, in this case high-speed CMOS camera technology. As this study is primarily focused on the behavior of SLV structures and its impact on flame dynamics, which generally have a small length scale (d_j) and a fast time-scale, the choice of acquisition frequency and region of interest incur a trade-off between the resolvable temporal scales and spatial (length) scales, i.e. acquiring data at high sequential repetition rates is often at the cost of reduced camera resolution. To overcome these limitations, two separate series of experiments were

conducted, non-simultaneously but at analogous flow conditions (Table A-2 and Table A-3).

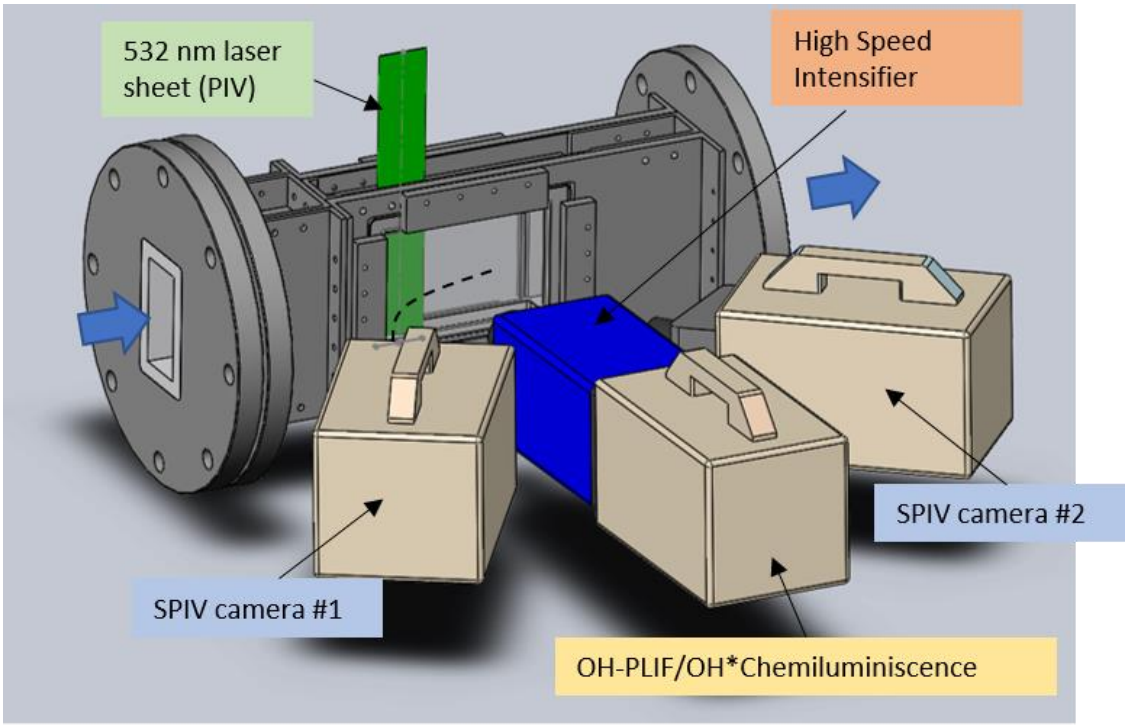

Figure 3.1: Schematic of the camera arrangement for the HS-SPIV and OH-PLIF/OH*Chemiluminescence experiments.

The experimental series focusing on high repetition rate measurements to temporally resolve the shear layer structures consisted of simultaneous 40 kHz SPIV and OH* chemiluminescence. The diagnostics were focused on a small region of interest close to the jet to obtain the required spatial resolution while accounting for the limitation of lower Mie scattering image resolution at high frame rates. This pairing was also chosen as past studies have shown that the heat release information in the near field of a JICF can be corelated with hydrodynamic structures [93]. The other experiment, SPIV was paired with OH-PLIF and run at 4 kHz probing a larger region of interest to obtain flowfield information and

understand the reaction zone structure in both the near and far field of the jet. The next few subsections will detail the specific diagnostic settings and parameters used.

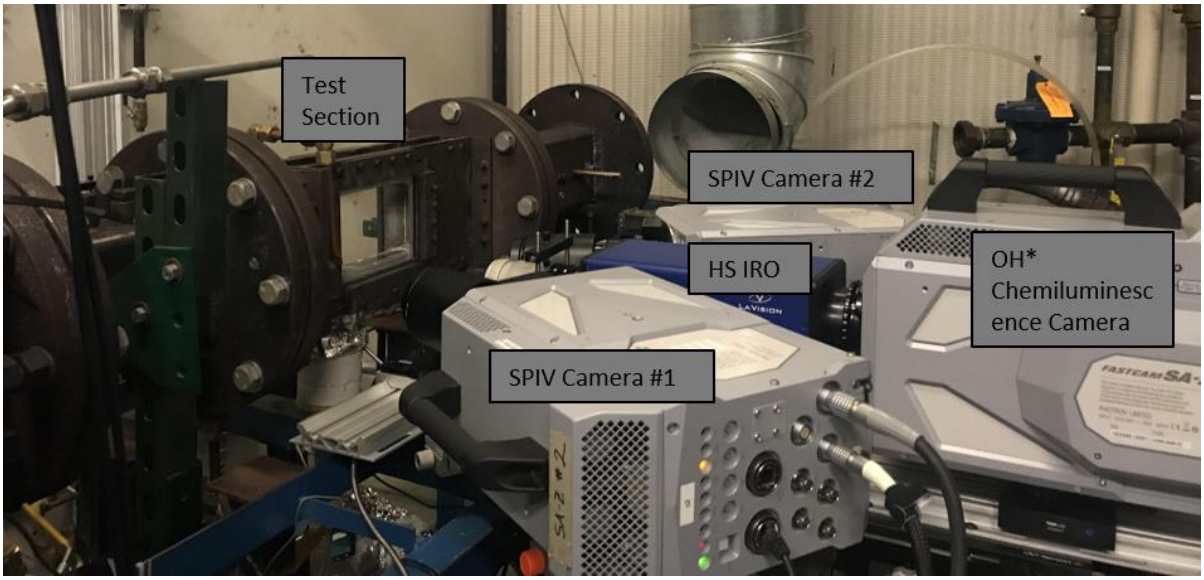

Figure 3.2: Picture of 40 kHz diagnostic setup involving SPIV and OH* chemiluminescence.

3.2 Stereoscopic-particle image velocimetry parameters

3.2.1 Optics and acquisition settings

Illumination for both series of experiments was provided by a pulsed Nd:YAG laser (Continuum Mesa PIV 80W), which has an operational range between 2 kHz and 40 kHz. The laser contains two laser heads which can be controlled independently, allowing for custom time delays between the two pulses used for PIV image pairs. The pulse duration of each head was 150 ns and the maximum power was 40 W at 10 kHz. As each experiment was focused on a different sized field of view, the sheet optics used to obtain the region of illumination were different. For the larger field of view, a cylindrical concave lens was used to expand the beam and a cylindrical convex lens was used to collimate it to the

required span of 55 mm. To obtain the laser sheet for the smaller field of view, the natural divergence of the laser beam was sufficient to obtain a laser sheet of span 10 mm in the test section. In both cases a high focal length, f = 750 mm cylindrical concave lens was used to focus the beam along the transverse axis (z – axis) at a height of approximately $6d_j$ from the bottom of the test section. The collinearity of each pulse was checked after forming the laser sheet and found to have an overlap of around 75% suggesting minimal errors due to differential spatial illumination between pulses. In both cases the thickness of the sheet was measured to be roughly 0.5 mm by using a knife edge.

For the 40 kHz experiments, the net power produced by each laser head was reduced to approximately 26 W, resulting in a pulse energy of 0.65 mJ/pulse. The pulse energy density of the laser sheet, as well as the required spatial resolution, constrained the field of view for the 40 kHz experiment to a region spanning $4\,d_j \times 3.5\,d_j$, located approximately 1.3 d_j from the base of the jet (Figure 3.3) to avoid the specular reflection of the laser sheet from the base of the test section as well as probe the jet flowfield at this location. This region was imaged using two Photron SA-Z high speed CMOS cameras angled approximately 25 degrees with respect to the normal of the centerplane (Figure 3.1). The pulses were captured in frame straddling mode at a repetition rate of 80 kHz resulting in a raw Mie scattering image resolution of 512 × 484 px^2. The cameras were fitted with 180 mm Tamron Macro lenses allowing for sufficiently high magnification (~ 0.8) at a distance of 150 mm from the centerplane of the test section. The aperture was set at $f/\#$ = 8.0 to increase the diffraction limited particle size as well as control the focal depth through the laser sheet. Two 3-inch Semrock Brightline filters, centered at a wavelength of 532 nm

with a transmissive bandwidth of 10 nm, were used to filter out ambient light as well as PLIF emission.

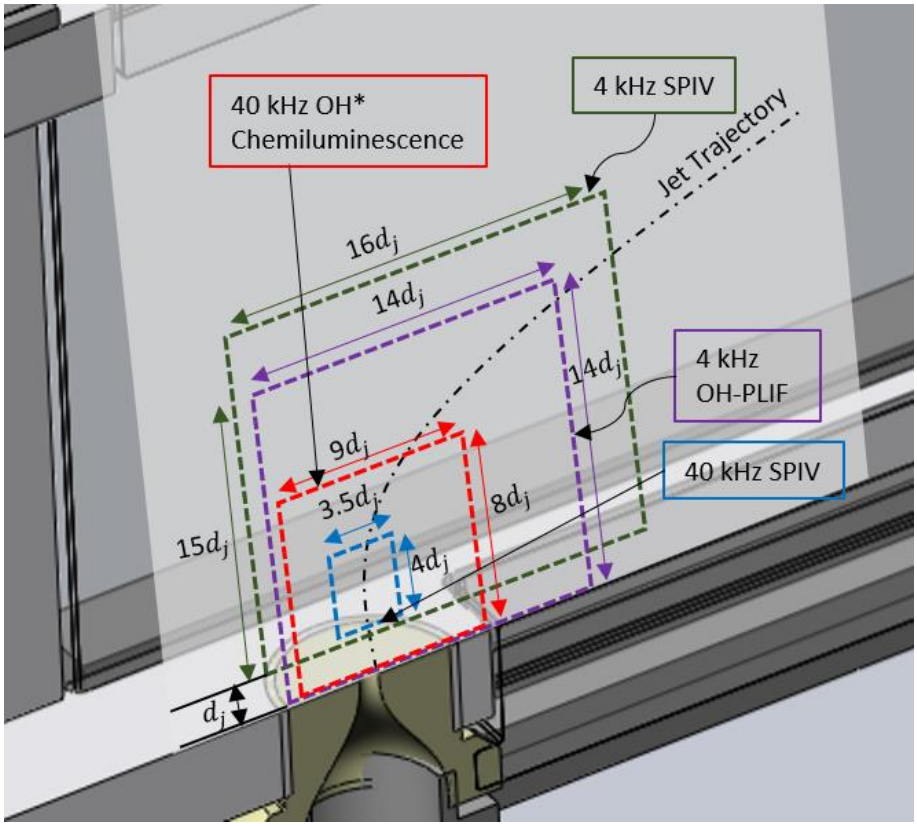

Figure 3.3: Diagnostic field of view (FOV) for all the 4 diagnostics listing the dimensions for each FOV; Generic jet trajectory is drawn for reference.

The lower repetition rate SPIV measurements utilized the same laser setup, while running the two laser heads at a frequency of 4 kHz. At these settings, the pulse energy obtained was approximately 9 mJ/pulse, sufficient to illuminate the 15 d_j × 14 d_j wide region of interest (Figure 3.3). The region was imaged using two Phantom v2610 high-speed CMOS cameras angled at 35 degrees with respect to the centerplane normal in side-scatter configuration. While operating in frame straddling mode, the lower repetition rate of 8 kHz allows for a captured image resolution of 1792 × 1792 px^2 for the raw Mie

scattering images. The cameras were fitted with 100 mm Tokina macro lenses with the aperture set at $f/\# = 5.6$ to optimize the brightness and diffraction limited particle size. A 2-inch Brightline Semrock 532 nm green filter with a bandwidth of 3 nm was fitted at the end of each lens to minimize extraneous reflections. Two 55 mm quarter-wave polarizing filters were adjusted to minimize the saturation from the specular reflection off the bottom of the test section. For both the experimental setups, the combination of focal lengths and aperture settings ensure that the diffraction limited particle size is larger than the CMOS pixel size in each camera to minimize the possibility of peak locking.

The delay between the two PIV pulses was adjusted based on the flow conditions and estimated by considering the time taken to produce an optimal pixel displacement of roughly 12 pixels [90], considering the resolution of the particle images and the jet velocity. The resultant pulse separation times varied from 3.5 μs to 12 μs for the 40 kHz experiments and 5 μs to 14 μs for the 4 kHz experiments. The out of plane (z-axis) velocity is not considered to be the limiting velocity scale here due to the measurements lying very close to the plane of symmetry, implying no bulk out of plane motion. A custom-made calibration stand, using a micrometer translation stage, was used to angle the front face of the calibration target - a Lavision Type 10-0.5 μm target - with the plane of symmetry was used to calibrate the smaller field of view, whereas the larger field of view was calibrated with a Lavision Type 058-5 3D target. The laser was then aligned with the plane of symmetry using the edge of the calibration target.

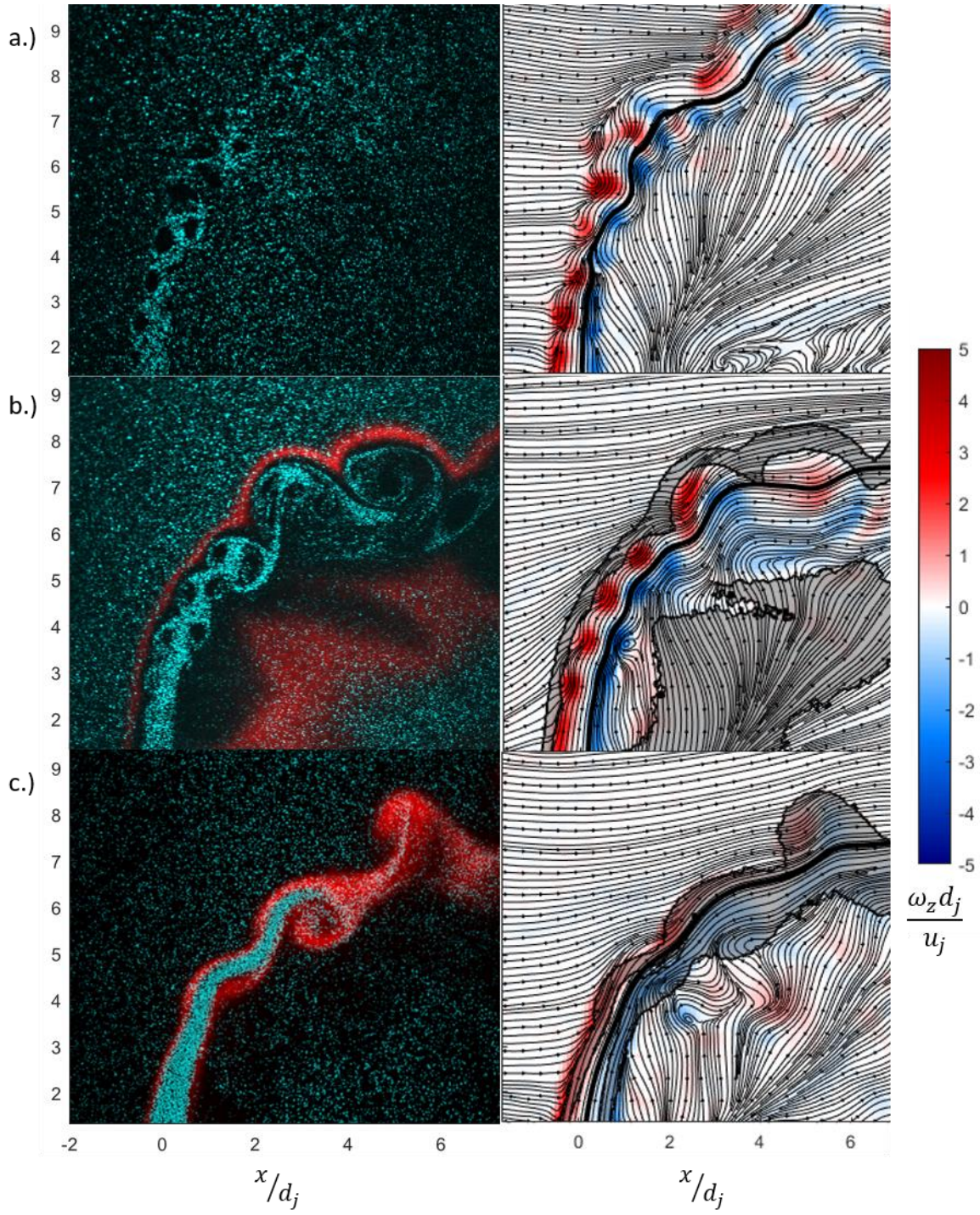

Figure 3.4: Instantaneous composite Mie field (4 kHz) – cyan, and OH-PLIF signal - red (left); Corresponding instantaneous velocity fields (streamlines) superimposed on the vorticity with elevated OH-PLIF signals demarcated by shaded regions; The instantaneous jet center-streamline is denoted by the darker streamline.

3.2.2 Seed particle considerations

The seed particles used for these experiments are commercially available TiO_2 (rutile) powder due to its ability to survive in high temperature oxidizing/reducing environments and its relatively large scattering cross section compared to other ceramic oxides. The seed particle size was reported as between 200 – 300 nm as per the manufacturer's specifications. The effective size can be assumed to be larger due to the tendency of the seed particle to clump together in the presence of moisture. To minimize clumping effects, seed was dried in an oven prior to each day of experimental testing to reduce the moisture content but without the presence of predetermined flow structures with a fixed time-scale, like a shock, it is challenging to estimate the true mean diameter based on the response time. The ability of a seed particle to accurately follow the flow field can also be captured by using the non-dimensional Stokes number $St = t_0 u_0 / l_0$. Here, t_0 is the characteristic time-scale of the particles and l_0/u_0 can be considered to be the flow time-scale. The particle time-scale depends on the material properties and density difference with the fluid and can be estimated by considering the maximum frequency that provides a 50% energy response [94]. Using this technique, the mean fluid properties are estimated to be approximately equal to the crossflow conditions, and the range of cut-off frequencies for the particle response lie between 90 kHz and 200 kHz (for particle sizes ranging from 200 – 300 nm). This reduces the effect of clumping on potential aliasing effects to some extent. Assuming a particle response of 90 kHz, the stokes number lies between 0.11 – 0.5 based on the maximum and minimum jet flow velocity. Thus, to prevent aliasing and due to the limitations on the smallest possible interframe delay of the cameras, the highest J cases were excluded from the test matrix for the 40 kHz experiment series.

3.2.3 Vector processing

The vector processing on the raw Mie scattering images is done using LaVision DaVis 8.3.1 software. Prior to processing, the raw Mie scattering data is pre-processed using a sliding background filter of length 11 to remove any persistent reflections from the laser. The raw data is then smoothed using a 3×3 px^2 Gaussian filter to remove uncorrelated noise and to increase the size of the imaged particles (although this will not provide any benefit in the event the data is highly peak-locked). The particle field images are normalized by adaptively mapping the local dynamic range (adaptive histogram equalization) which helps reduce any bias errors due to the difference in seeding levels between the jet and the crossflow. Prior to correlation, a 5 pt rectangular minimum spatial filter helps isolate particles from their neighbors providing a relatively disperse field and min-max normalization helps to further improve the contrast.

For both cases of data (4 kHz and 40 kHz SPIV), velocity vectors were computed using multi-pass processing with circular (Gaussian-weighted) interrogation windows. For the 40 kHz data, the velocity fields were calculated using a total of 5 passes where the first two passes were made with an initial interrogation window size of 48×48 px^2 and the final 3 passes were made with 12×12 px^2 sized windows with 50% overlap. For cases 25 – 28, all the R2 configurations, the final interrogation window size was 16×16 px^2 with 50 % overlap due to lack of seeding density (Section 3.5.1). For all passes, the normalized correlation function was used. Between passes, outlier vectors were iteratively removed and replaced using DaVis' median filter algorithm. The missing vectors were interpolated on the final pass. For vector post processing, the universal outlier detection algorithm based on the median filter was applied twice and gaps in the data interpolated. Finally, a 3×3

px^2 Gaussian filter was used to smooth the post-processed vector fields. The final interrogation window size was approximately 150 μm, sufficient to capture the length scales of interest in the flowfield.

For the 4 kHz data, the initial circular (Gaussian weighted) interrogation window size used was 48 × 48 px^2 for 2 passes and the final interrogation passes used a 24 × 24 px^2 window twice, to get sufficiently good correlation values. Similar to the process described for the 40 kHz data, the multi-pass steps removed and iteratively replaced outliers as well as smoothed the obtained vector data. The final post processing steps included applying the outlier detection algorithm and smoothing with the 3 × 3 px^2 Gaussian filter. The final interrogation window size was approximately 280 μm. While this was sufficient to capture the scale of the coherent structures in the flowfield, a finite grid size causes bias in gradient calculations through the truncation error which is discussed in Section 3.7.2.

3.3 OH* chemiluminescence

3.3.1 Acquisition system

The filtered OH* chemiluminescence acquisition system was synchronized to the high repetition rate SPIV system. The data was imaged using a high-speed CMOS camera, a Photron SA-Z running at 40 kHz. Due to the small temporal integration time to acquire each snapshot, and the low OH* emission intensity from H_2 – Air flames, a LaVision IRO high-speed intensifier was used to greatly increase the brightness of the signal. The intensifier gate was kept open for the entire acquisition time-period (25 μs) to maximize the collected light signal. The light from the imaging plane was collected using a 100 mm

$f/\#$ = 2.8 UV transmissive Cerco lens mounted with roughly 22 mm of focal extender rings to allow for a higher magnification at the fixed focal length. Background light, including the green light from the PIV system, was blocked by using a Semrock UV bandpass filter centered at 320 nm with a bandwidth of 40 nm.

3.3.2 Data processing

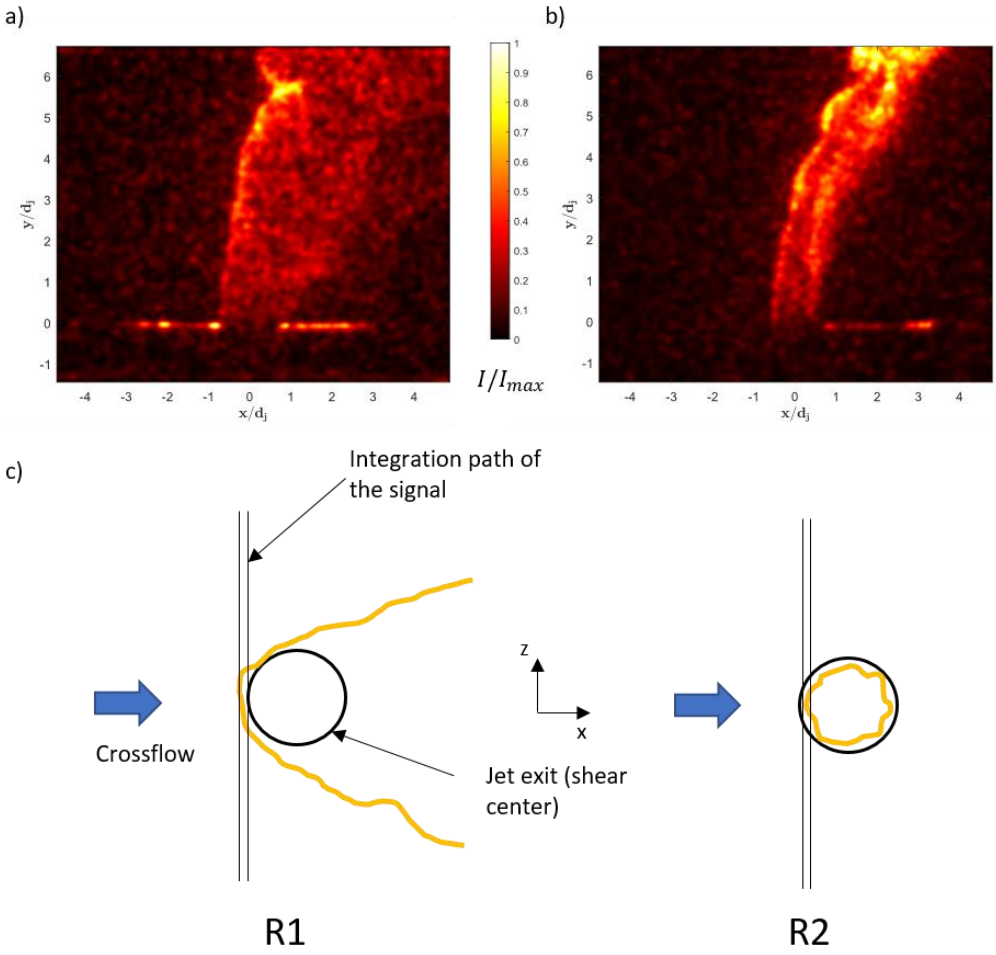

Figure 3.5: Instantaneous OH* Chemiluminescence images for a) Case 14: *J* = 12, *S* = 1.75, R1; b) Case 27: *J* = 6, *S* = 1.1, R2; c) Schematic demonstrating the impact of the flame structures on the resultant signal through the path of integration for the R1 and R2 flame configurations (top view of the configuration).

The emissions captured by the OH* chemiluminescence diagnostic are essentially intensity measurements of the region of interest line integrated through the transverse axis with respect to the jet. Given the flame shape, which tends to be narrow along the windward edge but spreads out towards moving away from it, the signal can only resolve large scale features along the windward flame edge (Figure 3.5). In the current study, the OH* Chemiluminescence data is primarily used to analyze the time-domain heat release behavior to compare the observed dominant mode shapes of the heat release data. The signal to noise ratio (SNR) is only sufficiently high (~ 15-20) along the windward flame region and therefore can only be used for qualitative comparison with the windward shear layer spectra presented in Chapter 5.

3.4 OH-planar laser induced fluorescence

3.4.1 Optics and image acquisition

OH-PLIF is used in this study to infer the flame characteristics in the centerplane of the RJICF flowfield. Illumination is provided using a Sirah Credo Dye laser system which includes a EdgeWave Innoslab 120 W pump laser which pumps a Credo tunable dye laser containing Rhodamine 6G. The laser system has an output power of 4W of 283 nm UV light at a repetition rate of 4 kHz (synchronized with the lower rate SPIV) corresponding to an average pulse energy of 1 mJ/pulse. The output wavelength was tuned to the $Q_1(9)$ transition of OH in the between the $\nu'' = 0$ to $\nu' = 1$ vibrational state in the $A^2\Sigma^+ - X^2\Pi$ system, and optimized to obtain the strongest emission signal from the flame. The output beam was expanded using cylindrical concave lenses and collimated to set the span of 40 mm. Following which, the beam was reflected into the test section using a

Dichroic mirror and focused into a sheet, coplanar with the PIV sheet, in the center-plane of the test section using a cylindrical converging lens. The final sheet thickness of the OH-PLIF system was approximately 0.5 mm.

A high-speed CMOS camera, Photron SA-5, was used to acquire the emission signal from the OH radicals. In order to enable acquisition of a sufficiently strong UV signal, a Lambert Instruments 25 mm HiCatt V2 was used, fitted with a 100 mm, $f/\# =$ 2.8 UV transmissive Cerco lens. The camera and intensifier setup were arranged between the high-speed SPIV cameras and position normal to the imaging plane (centerplate). Similar to the OH* chemiluminescence setup, the background light including the green light from the PIV system was blocked by using a Semrock UV bandpass filter centered at 320 nm with a bandwidth of 40 nm. To minimize the light from passive sources (i.e. chemiluminescence), the gate of the intensifier was limited to provide exposure for only 150 ns and was verified to maximize the captured OH transition emission signal while minimizing the light due to OH* chemiluminescence. The gain on the intensifier was set to 780V to get a sufficient dynamic range of intensities in the raw PLIF images. The timing was adjusted to ensure the UV pulse bisected the green laser pulse doublet (PIV).

At the frame rate of 4kHz, the high-speed camera was able to acquire images at full resolution 1024 × 1024 px^2. Considering a viewable area of $14\,d_j \times 14\,d_j$, this corresponded to a raw image resolution of 0.041 mm/pixel. A total of 3696 images were taken at each test condition synchronously with the SPIV system. The imaging plane was aligned and calibrated using a Davis 058-5 3D target synchronously with the SPIV cameras. To account for variation in the laser sheet strength, baseline measurements were made while plugging the test section and filling it with acetone vapor. The acetone

emissions from over 200 pulses were captured and averaged to obtain the net variation, which was used to correct the raw images. As the focus of this study is primarily the qualitative flame behavior, the discrepancies in acetone sheet profile compared to the shot to shot intensity variation are thought to have a small impact on data interpretation.

3.4.2 OH-PLIF image processing

The corrected OH-PLIF images were processed by using a time-domain background subtraction filter, followed by a 3×3 px^2 Gaussian filter to smooth out sensor noise. An edge preserving filter is further used to smooth out high-frequency noise while retaining the flame shape especially along the windward flame branch. When the temperature and pressure field is known, the signal intensity from the OH-PLIF measurements effectively measures the OH concentration ($[OH]$) locally. For the current study, assessing this intensity variation on a qualitative basis is sufficient to understanding the regions of high temperature combustion products, across the different configurations. While the flame position is not directly correlated with the OH-PLIF signal, under certain conditions, it is possible to infer the flame position. For example, observing the OH-PLIF emission structure for the R1 type flame configurations (fuel jet into an oxidizing crossflow - Figure 3.6a), the windward flame is relatively thin and shares a lot of similarities to H_2 – Air diffusion flames [91]. If we consider the variation in mixture fraction space (f), detailed studies [95] have shown that the $[OH]$ concentration peaks on the oxidising side of the stoichiometric mixture fraction (f_{st}) as can be seen in Figure 3.6c. Thus, based on this we can approximate the flame position as lying along the contour of maximum slope (white - Figure 3.6a) on the side of the jet (fuel side).

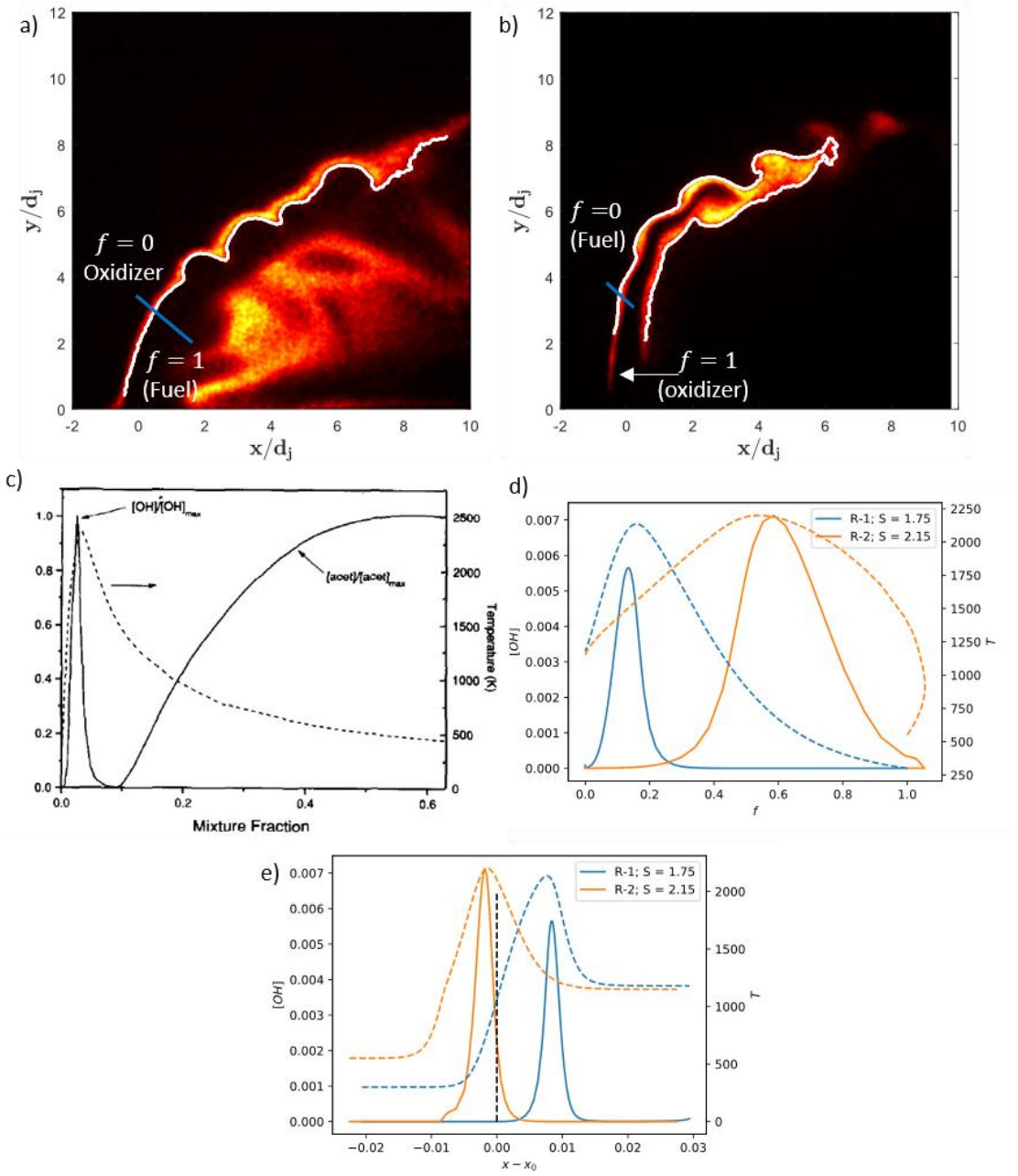

Figure 3.6: Instantaneous OH-PLIF intensity field for a) Case 14: *J* = 12, *S* = 1.75, R1; b) Case 26: *J* = 12, *S* = 2.15, R2; c) Relationship between [OH], *T* and mixture fraction (*f*) from one-dimensional opposed diffusion flame computations for a H_2-N_2 diffusion flame (Clemens and Paul [91]); d) Relationship between [OH], *T* and *f* from OPPDIFF computations for the two cases considered here; e) Spatial variation of [OH], *T* from OPPDIFF computations for the two cases considered here, 'dashed line' denotes approximate shear center.

Now, for the R2 type configuration (Figure 3.6b) the jet contains diluted oxidizer and the crossflow is now fuel rich. As a result, the flame will probably lie on the crossflow side of the OH-PLIF intensity distribution for both the windward and leeward branches. This assumption is further supported by one-dimensional opposed diffusion flame model calculations, performed using CANTERA [96], for the different jet compositions considered in this study. Figure 3.6d shows the variation in $[OH]$ and T distributions with respect to the mixture fraction (f). The peak $[OH]$ value lies on the oxidizer, or crossflow side of the flame (defined here as peak T) for the R1 configuration while for the R2 configuration it lies on the jet side with respect to the flame. In addition to f, the variation of $[OH]$ and T is presented with respect to the spatial coordinates and the shear center - Figure 3.6e. This provides an estimate of how well the spatial distribution of $[OH]$ can support the claim that the flame lies inside the shear layer in the case of the R2 configuration while the $[OH]$ and T peak clearly lie on the other side of the shear layer for the R1 configuration.

While the one-dimensional model results provide some insight into possible flame locations from the OH signal, this is true primarily in regions that the diffusion flame has a thin laminar flamelet like structure. This is because OH is a relatively long-lasting species with a relatively long recombination time (~ 3 ms) and, consequently, can be convected away from the flame proximity [97]. This is especially true in the leeward reaction zone branch of the R1 type configuration, where OH effectively accumulates in the recirculation region, complicating the estimation of the flame position. For the R2 case, this effect complicates the identification of the flame structure along the jet, as convected OH is entrained into the wrinkles caused by advecting vortices in the far field and thus the region

of elevated OH becomes more diffused. Despite these limitations, given that the flame nature is well established for these diffusion flame type configurations, the OH-PLIF signal will be further used to contrast flame and reaction zone characteristics between the considered cases in Chapter 4.

3.5 Sources of error – PIV

3.5.1 Seeding density

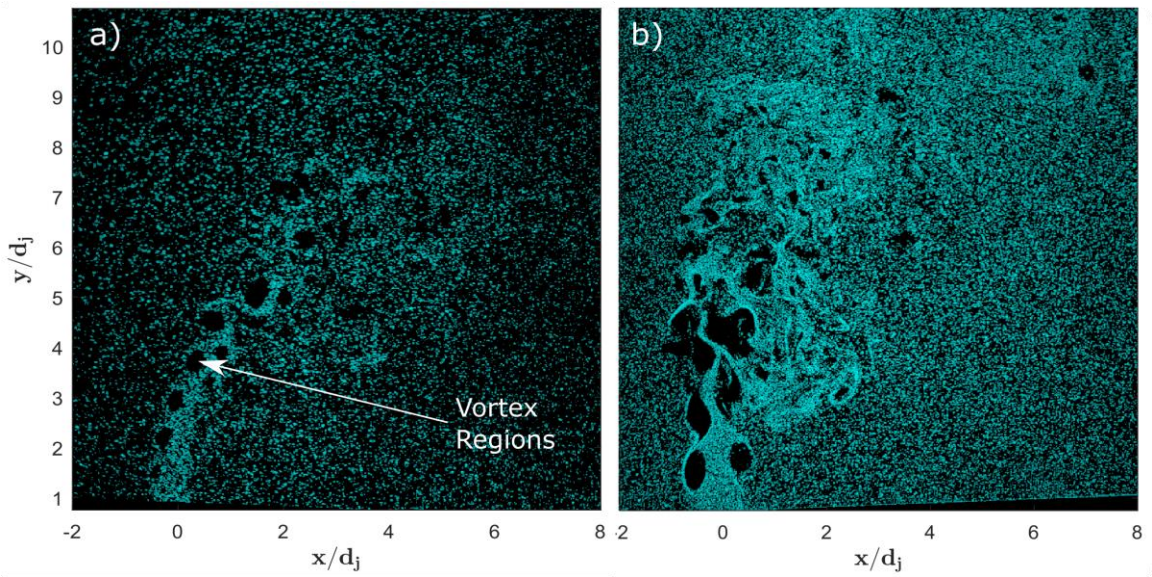

Figure 3.7: Instantaneous Mie scattering images for the 4 kHz SPIV experiments - a) Case 2: J = 12, S = 1.75, NR; b) Case 11: J = 18, S = 0.35, NR.

While care was taken to ensure uniform and sufficient seed density in the jet and the crossflow, seeding density in turbulent reacting flows depends strongly on the local flow conditions. In the current set of experiments, non-uniformities in the seeding levels are observed due to three primary sources – 1) centrifuging of seed particles due to the vortical structures, 2) dilatation induced density reduction in regions of high temperature and heat release and 3) lower seeding in the wake of the jet.

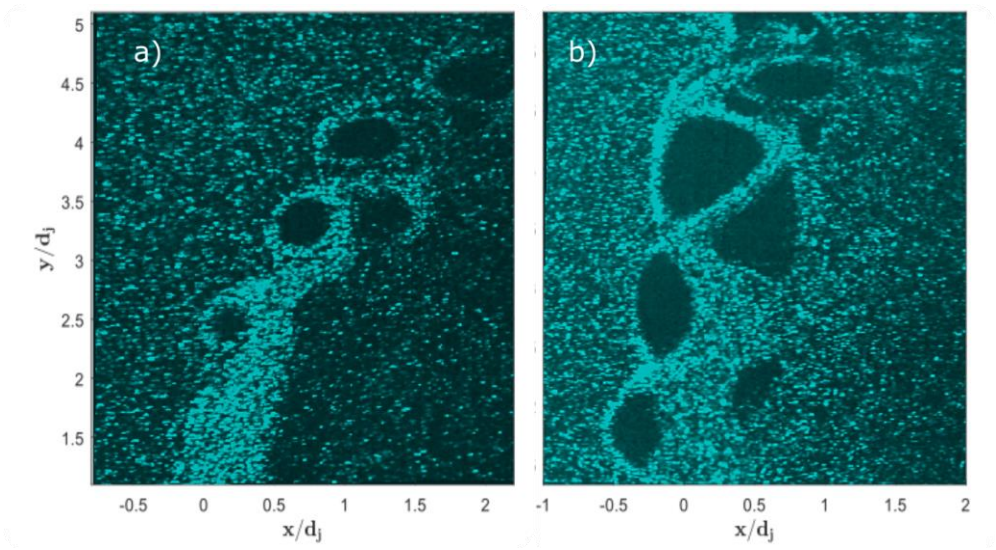

Figure 3.8: Instantaneous Mie scattering images for the 40 kHz SPIV experiments - a) Case1: J = 6, S = 1.75, NR; b) Case 10: J = 12, S = 0.35, NR.

The shear layer vortices which rollup on the windward and leeward shear layers of the jet in the near field have a very short time-scale $\sim R_0/u_j$ defined by their characteristic size as well as the velocity scale. Lecuona et al. [98] demonstrated how the centrifugal force induces a radial velocity to these particles, which is dependent on the stokes number (St_k) and the density and diameter of the particles. In the limit of large residence times, measured in their case from the start of the simulation, the particles tend to aggregate outside the vortex core over a time scale $\sim St_k^{-1}$. This explains some of the differences between the centrifuged regions of different cases with slower (Figure 3.7a) and faster timescales (Figure 3.7b). While this time was found to be $O(10\,ms)$ for the flow parameters investigated by Lecuona et al. [98], the stokes number for the current study is significantly higher resulting in a time-scale $\sim O(0.1\,ms)$. In addition, this timescale can be compared to the convective time scale of the vortices.

$$\frac{s}{U_c} \sim \frac{1}{St_k} \tag{3.1}$$

Where s can be considered to be a streamwise coordinate and U_c is the convective velocity. Since $St_k \sim U_C$, across the different jet velocity scales the level of centrifuging will be relatively constant and considering the real values of time scales, the convective length scale $s \sim O(10^2 d_j)$ which essentially means it is unlikely that the particles are completely centrifuged out from the vortices within the domain. Thus, while the centrifuged region grows as the vortices advect (Figure 3.8), it is unlikely that the centrifuged region will exceed the core diameter before viscous effects breakdown the vortices or slow down the swirl thereby providing some confidence that the vorticity/circulation calculations that are used to estimate the vortex boundary. Additionally, the induced radial velocity does not bias the calculation of swirl or vorticity due to its direction. Thus, the primary source of uncertainty is due to the loss in particle density [98].

The second cause of lower seed density is due to the flame induced dilatation. This can occur in the direct vicinity of the flame – such as the windward flame branch (Figure 3.9a) or due to drop in density in the entrained combustion products in the wake of the same flowfield. In both cases, it is clear there is a strong correlation between the low seed density and the regions of high OH-PLIF signal (red).

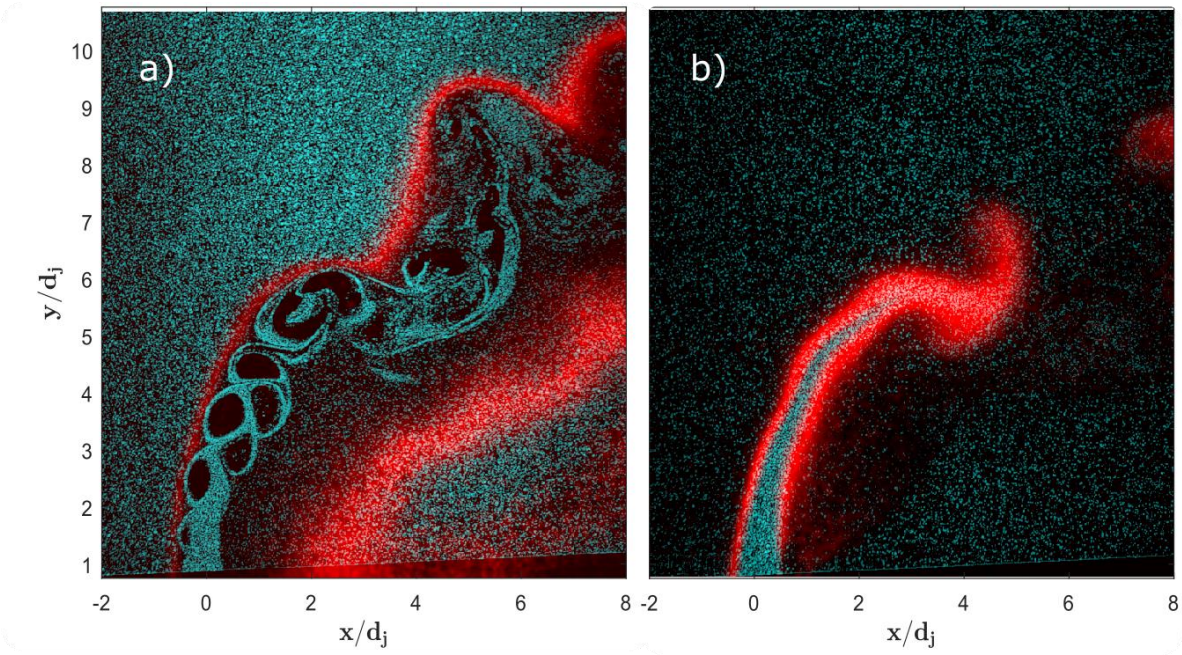

Figure 3.9: Instantaneous Mie scattering images with superimposed OH-PLIF intensity fields for the 4 kHz SPIV experiments - a) Case 18: *J* = 12, *S* = 1.0, NR; b) Case 26: *J* = 12, *S* = 2.2, R2.

For the second reacting configuration (R2), the seed density was low in the crossflow due to challenges in seeding the H_2 rich crossflow. Seeding of the crossflow was carried out using Helium, due to the safety risks of passing the dilution gas - H_2 through the seeding system. The high volumetric flowrate of H_2 and the limitation of the amount of He that could be mixed with the crossflow, to preserve the enthalphy and prevent the density from going extremely low resulted in a limitation to the maximum amount of seed that could be mixed in the crossflow despite the higher volumetric flow rate compared to the other reacting condition (R1). In addition, the wake region of the jet showed substantially lower particle counts (Figure 3.9b) - a consequence of hot combustion products being entrained into the wake as well as the reduced entrainment of the crossflow into the recirculation region .

3.5.2 Combustion induced bias effects

The uncertainty in PIV measurements made through the algorithm were obtained through DaVis, which estimates the random component of the instantaneous measurement error by using the correlation statistics [99]. Thus, regions of low correlation value naturally correspond to higher computed uncertainty. This technique does not consider errors due to stronger sources of bias such as peak locking, seed density and size and combustion effects. The particle sizes in all cases across both experiment series were large enough to ensure that there was no peak locking and was verified by observing the histogram of particle displacements for each case.

In order to understand the effects of the combusting flowfield on the sources of error for PIV measurement, two effects are considered. The effect of flame induced particle density reduction is dealt with qualitatively in the previous section and results in higher uncertainty due to the reduced correlation value. The second effect involves the thermophoretic effect which causes the particle to drift along the temperature gradient as opposed to the velocity field [100]. Sung et al. [101] estimated the thermophoretic velocity using the expression:

$$\nu_{TP} = -D_{TP}\frac{\nabla T}{T} \tag{3.2}$$

where D_{TP} represents the thermophoretic diffusion which was experimentally determined by Gomez and Rozner [102] to be approximately $D_{TP} \approx 0.5\nu$, which is applicable to the particle sizes used in this experimental study. While utilizing these expressions to correct for the local velocity on an instantaneous basis is challenging due to the inability to extract

instantaneous temperature information, the OH-PLIF data provides a reasonable estimation for the flame length scales on average, as well as, the contour of maximum temperature in jet diffusion flames [95]. To estimate the worst-case drift velocity, we consider the temperature gradient along the windward flame branch where the flame thickness has an approximate the thickness of ~ 0.3 mm based on the observable thickness of the OH-PLIF signal. For the R1 flame configuration (Figure 3.9), the temperature gradient on the oxidizer (crossflow) side can be estimated using the adiabatic flame temperature and the crossflow temperature as ~ 1800 K/mm. On the fuel side, the OH-PLIF signal does not track the temperature field and therefore we use the value obtained from a turbulent jet diffusion flame as 2000 K/mm at 1300 K. This provides an estimate of the thermophoresis induced velocity as $v_{TP} = 0.14$ m/s. This velocity is relatively small compared to the characteristic velocity scales in the jet and the crossflow. Spatially, the windward flame region lies outside the vortical structures which are a focus of this work and therefore would play a little role in creating biased velocity measurements in the region of interest. While the vortices do entrain high temperature fluid, the temperature is considered to be diffused through the structures [95] and the gradient length scale is on the order of the structure size creating a negligible effect. For the second flame configuration the gradients are found to be similar, resulting in a similar induced velocity except in this case the flame is entrained directly into the vortical structures based on the OH-PLIF data. The bias uncertainty in evaluating the vorticity, and swirl, is assumed to be low due to the radial direction of the thermophoresis induced velocity, which would not contribute to any bias to the vorticity or swirling strength measurement (Section 3.6.2).

3.6 Vortex identification and characterization

3.6.1 Vortex identification

To condition the data with respect to instantaneous coherent structures, vortex identification techniques are used to identify the regions of high rotation in the flowfield. There are numerous vortex identification techniques that have been developed and used across many turbulent flow applications [103] and the choice of technique is often highly specific to the given flowfield. Most Eulerian vortex detection techniques require the calculation of a vortex identification metric, calculated in the whole flowfield. Here, the compressible extension of the Q criterion [104], introduced by Hunt et al. [105], is used as the metric to gauge the level of local rotation while neglecting the gas expansion effects. The criterion is defined as -

$$Q = \frac{1}{2}(\|\Omega\|^2 - \|S_D\|^2) \tag{3.3}$$

where $\|\Omega\|$ is the rotational rate of the velocity gradient tensor and $\|S_D\|$ is the deviatoric component of the strain tensor. Vortical regions are defined as regions where the rotation exceeds the strain locally as $Q > 0$, but for the case of turbulent flows with noise, a threshold is generally applied.

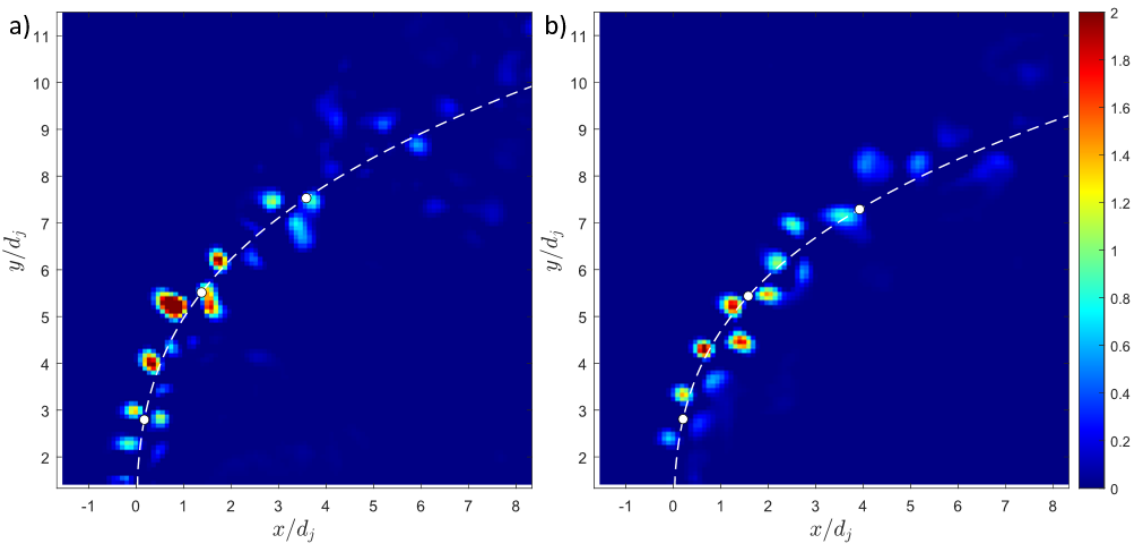

Figure 3.10: Instantaneous Q criterion field for two different cases for the 4 kHz SPIV data a) Case 7: J = 18, S = 1.0, NR; b) Case 14: J = 12, S = 1.75, R1.

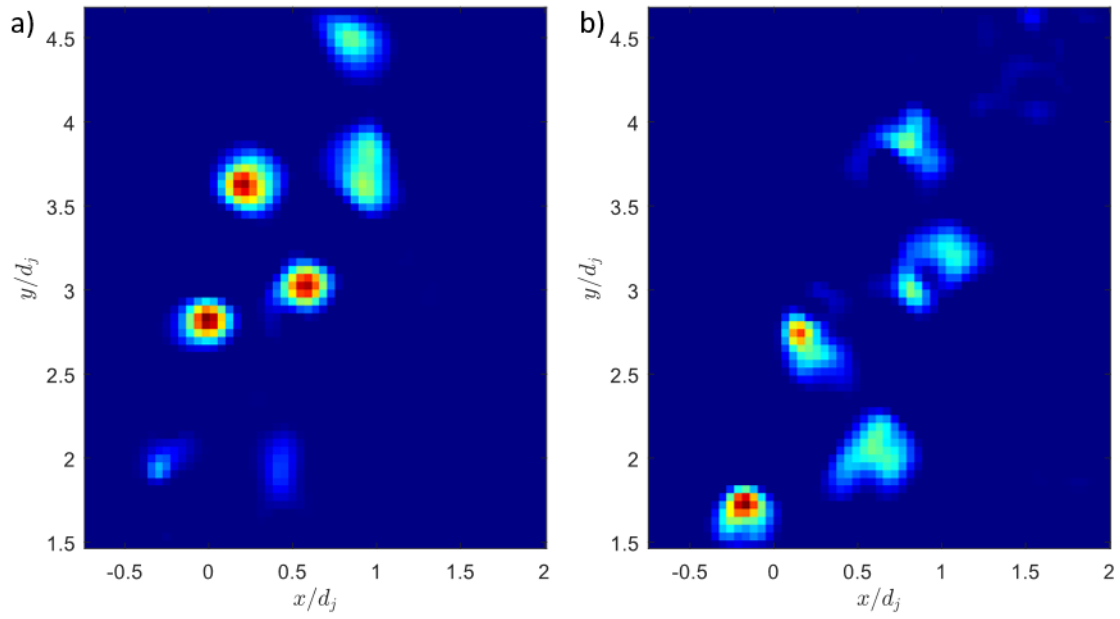

Figure 3.11: Instantaneous Q criterion field for two different cases for the 40 kHz SPIV data a) Case 2: J = 12, S = 1.0, NR; b) Case 9: J = 6, S = 0.35, NR.

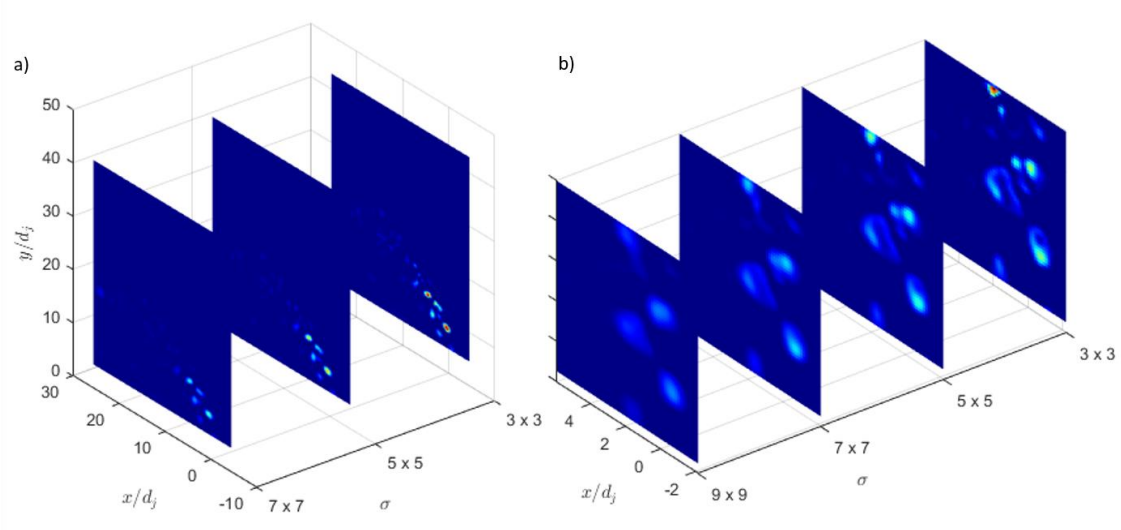

Figure 3.12: Scale space smoothing of the Q-criterion field a sample instantaneous field from the a) 4 kHz SPIV data and b) the 40 kHz SPIV data.

In order to increase the robustness of the vortex detection process, especially in cases where the data at the center of vortices is highly uncertain (particularly the high resolution cases), scale space theory [106] is used to extract only large regions of significant rotation while neglecting noise. For the 4 kHz data, three levels of smoothing were chosen in scale space with Gaussian kernel sizes increasing from 3×3 pt^2 to 7×7 pt^2. Four levels of smoothing were used for the 40 kHz data, going from 3×3 pt^2 to 9×9 pt^2. Significant regions of rotations that persist through all levels of smoothing were identified as the targeted vortices.

The choice of vortex boundary is another highly ambiguous metric but is critical to define metrics such as vortex size and circulation. Previous studies have attempted to provide a physical boundary by defining a fixed vorticity contour [107]. As the shear layer vortices can be approximated to Lamb-Oseen vortices, it is possible to define the boundary based on the vorticity value at the location of maximum angular velocity, typically

corresponding to the characteristic core size of the vortex (σ_c) but due to the limited resolution, the vorticity field of neighboring vortices can often be under resolved resulting in the contours merging at vorticity values greater than this threshold.

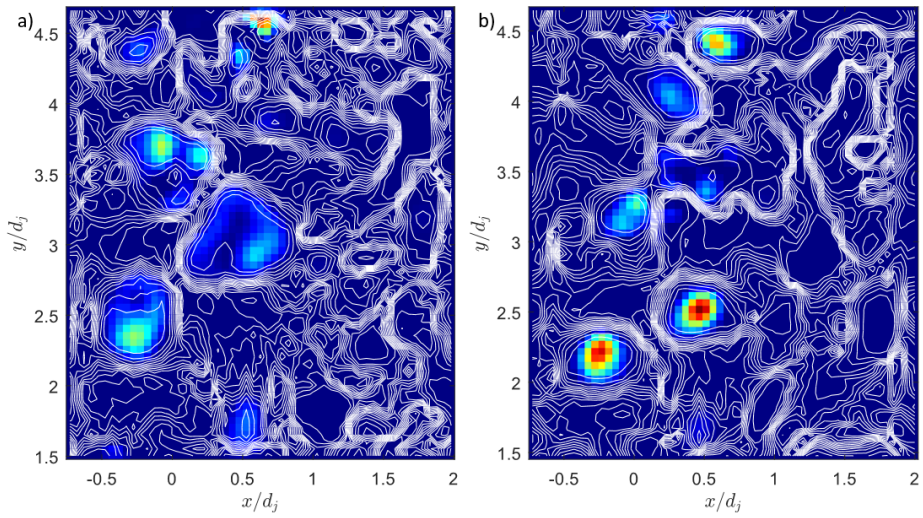

Figure 3.13: Q criterion field with contours ('white') corresponding the the Γ_2 criterion field for the 40 kHz SPIV data- note the aggregation of contours along boundaries of the coherent structures.

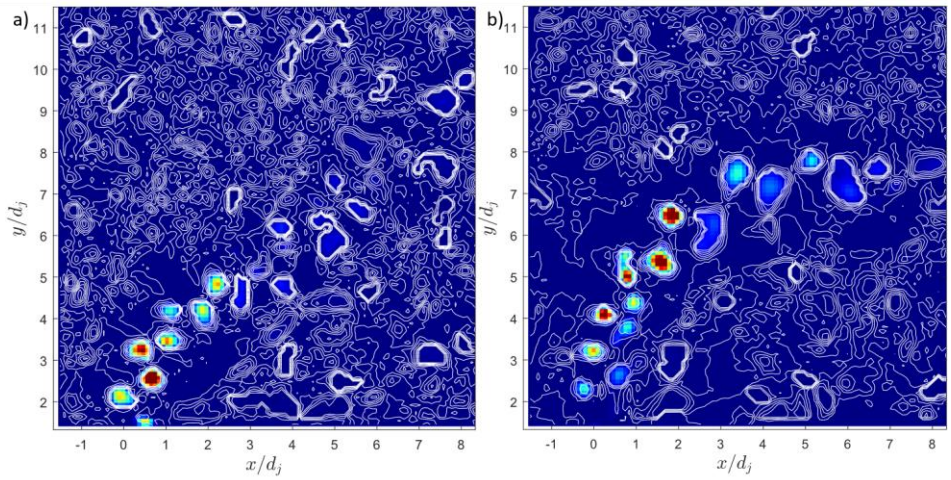

Figure 3.14: Q criterion field with contours ('white') corresponding the the Γ_2 criterion field for the 4 kHz SPIV data.

Graftieaux et al. [108] introduced the Γ_2 criterion, a non-local Eulerian approach that measures the pseudo-circulation around a defined circuit for a point. This technique is relatively robust to measurement error since, unlike the other techniques, the Γ_2 criterion do not involve calculating derivatives. In addition, the data presented by Graftieaux et al. [108] suggests that this metric is has a sharp slope near the boundary of a lamb vortex across multiple vortex sizes. Thus, the boundary here for each vortex is chosen based on the contour which maximizes the spatial derivative magnitude of the Γ_2 criterion – regions of clustering in the Γ_2 as seen in Figure 3.13 and Figure 3.14. An initial contour is created using a local threshold of the Q criterion and this contour is grown to the final size of the vortex, along the boundary of the Γ_2 structures, by using Chan-Vese method of calculating active contours [109]. Since the final step involves the growth of a contour to its final state based on the Γ_2 field, this methodology is quite insensitive to the arbitrarily chosen initial Q threshold chosen. The MATLAB implementation of active contours is an iterative process that requires the definition of two parameters which control the energy weight of the contour itself - the contraction bias, and the energy of the potential field it sits in (Γ_2) which are tuned based on the average vortex sizes for each case (a larger contraction bias will result in faster growth of the contour, running the risk of overshooting the boundary).

3.6.2 Vortex metrics

This vortex identification technique is essentially used to extract certain metrics from each of the vortices on an instantaneous basis and ensemble these metrics based on the instantaneous vortex position (as measured by its centroid) across all the obtained flowfield

snapshots. The ensembling and binning process is further elaborated in Chapter 4, while this section will provide the definition and methodology of calculation of these metrics.

The vortex swirling strength λ_{ci} has seen widespread use as a vortex identification metric since it was introduced by Zhou et al. [110]. Essentially it measures the local 'swirl' of the instantaneous streamlines through the complex conjugate eigenvalues of the velocity gradient tensor ($\nabla\vec{v}$).

$$\nabla\vec{v} = \begin{bmatrix} \frac{\partial u}{\partial x} & \frac{\partial u}{\partial y} \\ \frac{\partial v}{\partial x} & \frac{\partial v}{\partial y} \end{bmatrix} \tag{3.4}$$

If we only consider the two-dimensional gradient tensor, Eq. **3.4**, since only these components are resolvable from SPIV data, then λ_{ci} effectively measures the time period for completing one revolution of the streamline $\sim 2\pi/\lambda_{ci}$. As a consequence, it provides a physically relevant measure of the strength of rotation for a given vortex core along a defined plane (here the centerplane). In addition, the metric is unbiased in regions of compressive or expansive dilatation [104] as is present in reacting (or even non-reacting) PIV data. In this study, we argue that the instability strength that contributes to the growth of K-H vortices along the shear layer can be estimated quantitively by using this measure of local rotation as a surrogate. For each vortex identified, the maximum swirling strength contained within the boundaries, which will be identified as $\lambda_{ci,max}$ henceforth, is chosen to represent the strength of the vortex and therefore the defined vortex boundary effectively acts as a mask to choose the relevant maximum from the distribution of local λ_{ci} values identified for each vortex. While the metric is calculated at each point, practically due to

the finite size of the numerical stencil used for gradient calculation, this is effectively an average measure over an area (spanned by the stencil points).

The other two metrics calculated are the vortex area and the vortex circulation (Γ). Both these metrics require the accurate estimation of the vortex boundary. Since the data is discrete the vortex area is defined by adding the number of points contained within the boundary region and multiplying it with the grid size of the domain as -

$$A = \sum_{i \in Vortex} \Delta x \Delta y \qquad 3.5$$

The circulation utilizes the velocity values calculated at the boundary of the identified structures to integrate the velocity along with the circuit defined with the boundary:

$$\Gamma = \sum_{i \in Boundary} \overrightarrow{v_i}.\overrightarrow{\Delta s_i} \qquad 3.6$$

The quantity $\overrightarrow{\Delta s_i}$ is estimated cyclically along the boundary through forward difference approximation as $\sim 0.5 \times (x_{i+1} - x_i, y_{i+1} - xy_i)$. A discussion of the uncertainty in estimating these metrics on an instantaneous basis is provided in Section 3.7.2.

3.6.3 Lagrangian vortex tracking

For the 40 kHz data, the above vortex identification technique is further extended to track vortices across successive snapshots of the flowfield which is possible due to the high

temporal resolution. Starting with an masked image based on the detected vortices for a field at time $F(t)$, a guess for the future orientation of these vortices is obtained by perturbing each vortex structure based on the mean velocity field $(\bar{u}, \bar{v})$ to obtain the guess field $F'(t)$. Now this field, $F'(t)$, is compared with the obtained vortex detection field for the subsequent time step $F(t + \Delta t)$ and the structures correlated based on their overlap with their predicted positions. This essentially allows for the identification and tracking of a vortex i in space and time as it advects through the measurement region of interest.

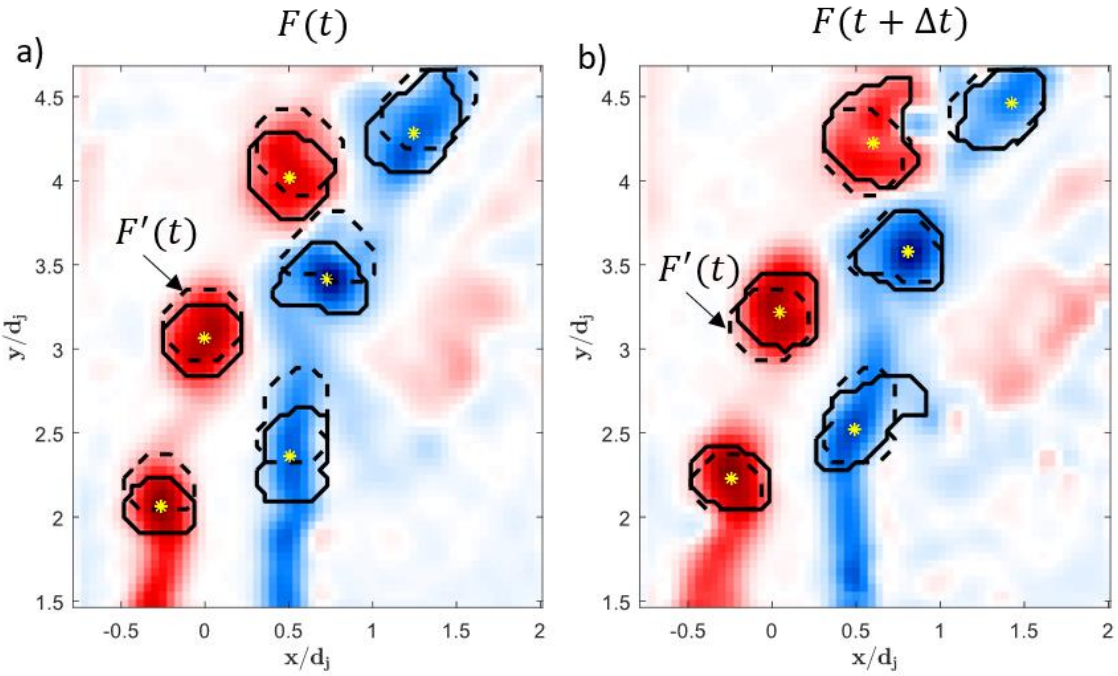

Figure 3.15: a) Detected vortex field for an instantaneous snapshot $F(t)$ and predicted subsequent field $F'(t)$; b) Detected vortex field for an instantaneous snapshot at the subsequent time step $F(t + \Delta t)$('solid line') with the predicted field $F'(t)$ ('dashed line').

3.7 Uncertainty quantification and propagation

The SPIV processing software (DaVis 8.3.1) also provides an estimate of the uncertainty in the measurement of each velocity component at each vector location (U_u, U_v, U_w). This is done largely in accordance with technique elaborated by Wieneke [99] where the PIV uncertainty is estimated from the correlation statistics. This estimate is calculated purely based on the random component of the uncertainty which can be obtained through the correlation value at a point but does not provide any estimate of bias errors such as peak locking or errors due to the physical phenomena outlined in Section 3.5. In addition, Wieneke [99] comments that the random error from the correlation statistics tends to be significantly stronger when quantifying the uncertainty of an instantaneous vector measurement. Despite the fact that the algorithm doesn't actively calculate any bias errors related to flow phenomenon, uncertainty in the measurements made in regions subject to strong combustion effects or vortical motion will naturally be higher due to a lower seed density resulting in a lower or 'more uncertain' correlation. This section will further discuss the propagation of this measured metric into derived quantities including vorticity, swirling strength, etc …

3.7.1 Gradient estimation

As most of the quantitative analysis is performed on metrics based on the calculation of in-plane velocity gradients, it is important to quantify the uncertainty and bias related to this calculation. Since it is necessary for the gradient to be numerically evaluated from the PIV data, the choice of numerical stencil is an important consideration with respect to the resolvable scales. Here, we use the Richardson 4th-order extrapolation

stencil suggested by Lourenco and Krothapalli [111] to balance the effect of the truncation error as well as the noise amplification coefficient (elaborated in the next section). The formulation of the stencil along with the associated leading term of the truncation error (T.E) and noise amplification term (R.E.) -

$$\left(\frac{df}{dx}\right)_i \approx \frac{-f_{i+2} + 4f_{i+2} - 4f_{i+2} + f_{i-2}}{3\,\Delta x} + 4\frac{\Delta x^4}{5!}\frac{\partial^5 f}{\partial x^5} + 0.95\,\frac{\sigma_f}{\Delta x} \qquad 3.7$$

T.E. R.E.

The spectral behavior of the filter was further investigated and contrasted with other commonly used gradient stencils by Foucaut and Stanislas [112]. They provided a high and low cut-off wavenumber based on the PIV grid spacing as $k_{cl}\Delta x = 0.0811$ and $k_{ch}\Delta x = 1.923$. The current grid spacing for the 4 kHz PIV data is $\Delta x = 280\ \mu m$ which results in cut-off wavenumbers of $k_{cl} = 0.289\ mm^{-1}$ and $k_{ch} = 6.867\ mm^{-1}$. Converting this into a length scale this implies that the smallest resolvable gradients will be of the order of $\sim 0.145\ mm$ or roughly $\sim d_j/20$. In-addition to the cut-off wavenumbers, Focaut and Stanislas [112], further analyzed methods of optimizing the choice of derivative filter in measuring vorticity by estimating the error in measuring the vorticity at the center of an Oseen vortex ($\Delta\omega_0/\omega_0$), a suitable idealization for the vortices observed in turbulent flowfields. They commented that the Richardson 4th order filter presented a minimum error of ~ 10% for vortex length scales $R_0 = 5\Delta x$. If we use the characteristic flow length scale instead, this implies $R_0 \sim 0.5 d_j$ and the error can be as large as 20% for $R_0 \sim 0.25 d_j$ which would increase the bias in the vorticity estimate for very small vortex structures in the flowfield. This has implications on the measurement of gradient based vortex metrics.

3.7.2 Uncertainty propagation of vortex metrics

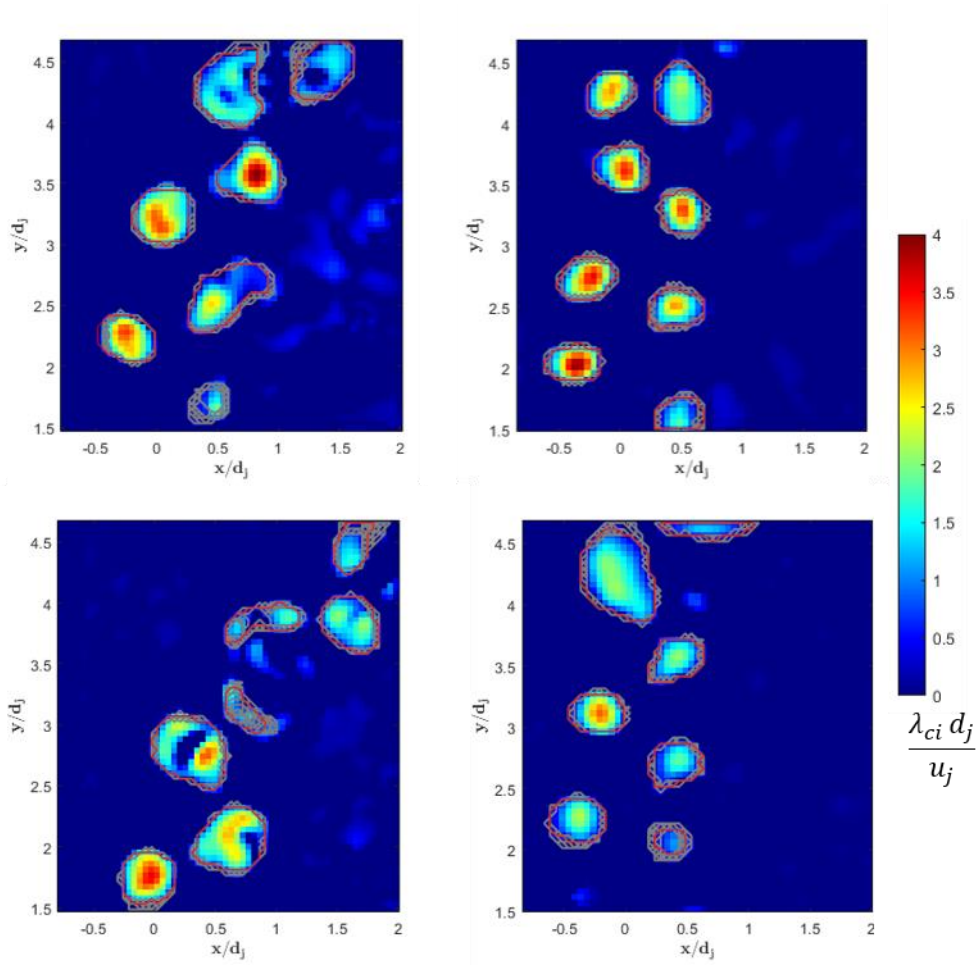

Figure 3.16: Instantaneous flowfield snapshots from different 40 kHz SPIV cases with identified vortex boundaries from the Monte Carlo Samples (grey) ($N_{samp} = 1000$) and identified boundary from the measured velocity data (red).

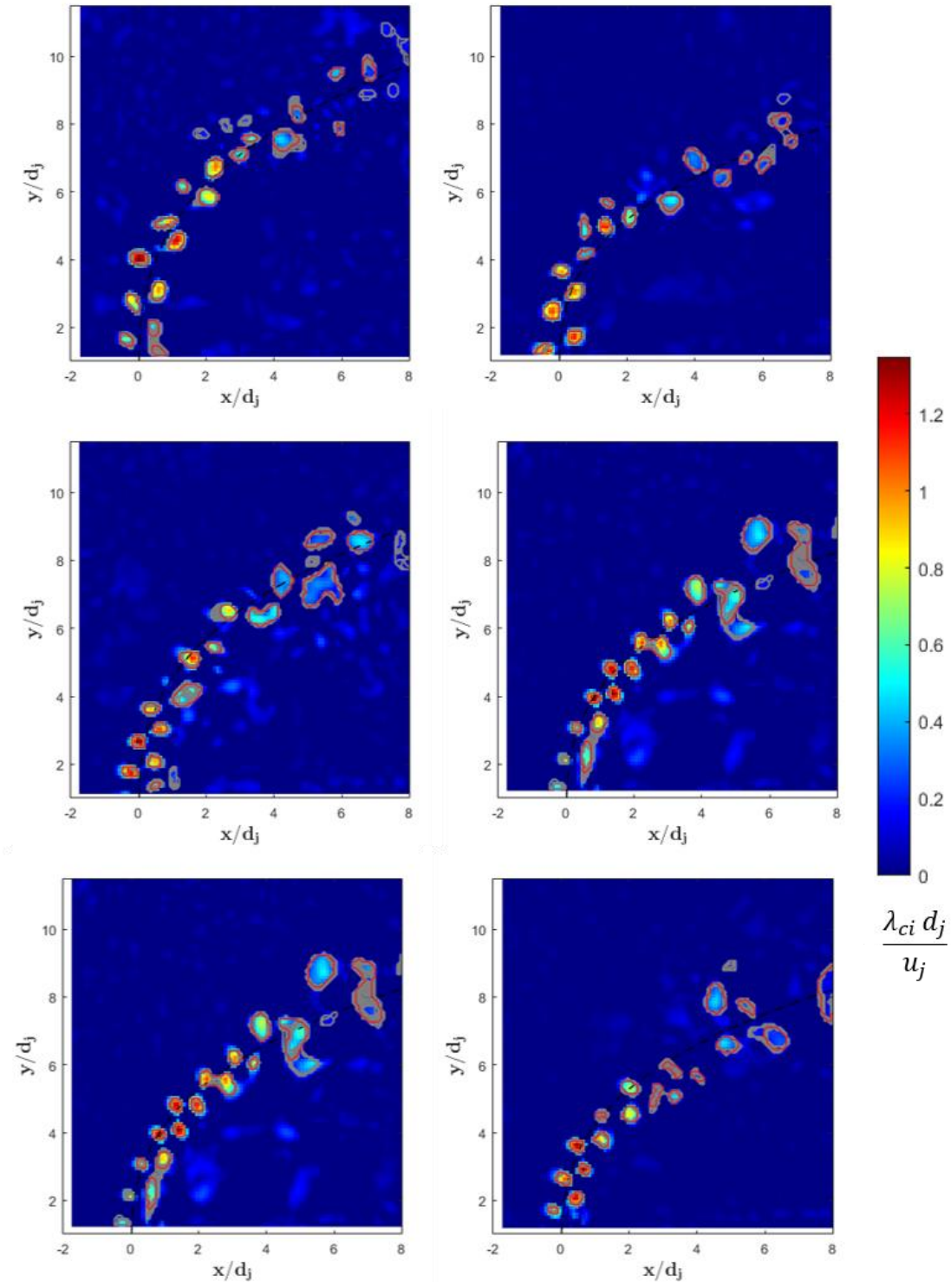

Figure 3.17: Instantaneous flowfield snapshots from different 4 kHz SPIV cases with identified vortex boundaries from the Monte Carlo Samples (grey)($N_{samp} = 1000$) and identified boundary from the measured velocity data (red).

The uncertainty estimates of the in-plane components of the velocity field (U_u, U_v) were used to estimate the uncertainty in calculation of the vortex metrics. Since these metrics are calculated with respect to the boundary defined, the propagation procedure is not straightforward, as the vortex identification process cannot be represented as an analytical function. Monte Carlo sampling was used in order to get an estimate of this uncertainty. For a given instantaneous snapshot of the flowfield, a fixed sample of flowfield realizations (N_{samp}) were created by drawing from a normal distribution at every location of mean (u, v), and standard deviation (U_u, U_v). All N_{samp} vector fields were then passed through the vortex identification process to obtain a set of detected boundaries. The result of this process can be observed for the 40 kHz data (Figure 3.16) and 4 kHz data (Figure 3.17).

The grey contour effectively provides some qualitative measure of the uncertainty of the vortex identification process by demonstrating the 'spread' for a given instantaneous set of vortices. As expected, vortices that are weaker tend to have a more diffused boundary and therefore exhibit higher uncertainty with respect to the identification technique as observed by the larger variability in detected boundaries. For stronger vortices, the identified boundaries does not vary by more than a grid point for most of the locations along the circuit. While Figure 3.16 and Figure 3.17 provide some qualitative estimate of the uncertainty in vortex boundary definition, propagating this uncertainty into the calculated metrics would require running the vortex identification algorithm N_{samp} number of times for every single vector field in each case, which is computationally prohibitive. But, on closer inspection, it is apparent that the uncertainty in the detected maximum swirling strength $\lambda_{ci,max}$ is relatively insensitive to the boundary of the detected vortices

since the maximum value tends to lie closer to the center of the detected region. In addition, the analysis of both the circulation and vortex area, as presented in chapter 4, is done primarily with respect to capturing the qualitative behavior of these metrics and therefore performing Monte Carlo sampling to estimate each of these metrics was deemed unnecessary. The physical correlation between the more uncertain vortex boundaries (weaker vortices) also manifests in the ensembling process by which Γ or A is calculated at a given spatial location and this variability is assumed to be more dominant, especially in regions with high flow uncertainty, and is therefore sufficient in gauging the uncertainty of the ensembled metric.

While the uncertainty in the maximum swirling strength $U_{\lambda_{ci,max}}$ does not require the uncertainty of the vortex boundary to quantify, it is still sensitive to the uncertainty in the underlying velocity field U_u, U_v. This uncertainty can be propagated using standard error propagation formula first, to the estimation of the velocity gradient tensor $\nabla\vec{v}$, and further onto the eigenvalues of this tensor λ_{ci}.

The above process only captures the error due to the random error in the velocity measurements but does not provide an estimate for the bias that is caused by the gradient estimation, as covered in the previous section. This gradient bias will be higher for smaller vortices due to the larger effect of the truncation error. Like the vorticity bias estimate $\Delta\omega_0/\omega_0$, a similar approach can be used to relate any bias in the peak swirling strength - $\Delta\lambda_{ci,0}/\lambda_{ci,0}$ (likely the swirling strength at the center of the vortex $\lambda_{ci,0}\sim\lambda_{ci,max}$). If we consider a field of an Oseen vortex defined by an azimuthal velocity scale –

$$u_\theta = \frac{u^*}{R}(1 - e^{-b_0 R^2}) \tag{3.8}$$

where, u^* is the characteristic velocity scale of the vortex, b_0 is a length scale parameter (~1.256) and $R = r/R_0$ is the radial distance (r) normalized with the characteristic radius (R_0). The swirling strength at the center is effectively the time taken to complete a circuit with the velocity $u_\theta(r)$ in the limit $r = 0$. This can be written as –

$$\lambda_{ci,0} = \lim_{R=0} \frac{\frac{u^*}{R}(1 - e^{-b_0 R^2})}{RR_0} \tag{3.9}$$

If we use the limited expansion for the denominator as given by Focaut and Stansilas [112] and only take the terms of $O(R)$ this expression effectively reduces to the same expression derived for the vorticity at the center of the vortex ω_0 since the Oseen flow has no shear and consequently $\lambda_{ci,0} = \omega_0$. Now, in the actual turbulent flowfield $\lambda_{ci,0} \neq \omega_0$ because of both shear and rotation will contribute to the local measure of vorticity. Nevertheless, given that $\lambda_{ci,0}$will still be strongly correlated with ω_0, we obtain, for the case of the Richardson 4th order filter (Eq. **3.7**)-

$$\frac{\Delta\lambda_{ci,0}}{\lambda_{ci,0}} = \frac{\Delta\omega_0}{\omega_0} = \frac{4b_0^2}{3!}\left(\frac{\Delta x}{R_0}\right)^4 \frac{\partial^5 u}{\partial x^5} + \frac{0.95}{\sqrt{2}u_* b_0}\frac{\sigma_u}{\Delta x} \tag{3.10}$$

For small vortices, $R_0/\Delta x$ is small and consequently the truncation error term (first term on the RHS) is dominant. For larger vortices, the noise term becomes dominant but is already estimated through the direct propagation of the uncertainty of the velocity field U_u, U_v and therefore the second term in this expansion is neglected. The truncation error is

therefore added to the uncertainty estimate of each instantaneous vortex realization to provide an estimate of the bias, which is bound to occur while capturing small vortices with a numerical stencil. To further motivate the choice of the Richardson 4th-order filter, the vortex peak swirling strength ($\lambda_{ci,max}$) measured across all the detected vortices in the windward shear layer for a given case (case 3) was plotted (Figure 3.18) with the gradient calculated using the Richardson 4th order filter as well as the Least Squares filter (Raffel et al. [90]). Although the Least Squares filter has a smaller noise amplification factor compared to the Richardson filter, for small vortex sizes $R_0/\Delta x < 3.0$, the effect of the truncation error (Eq. **3.9**) causes a bias of nearly 25 – 50% from the measured value using the Richardson filter.

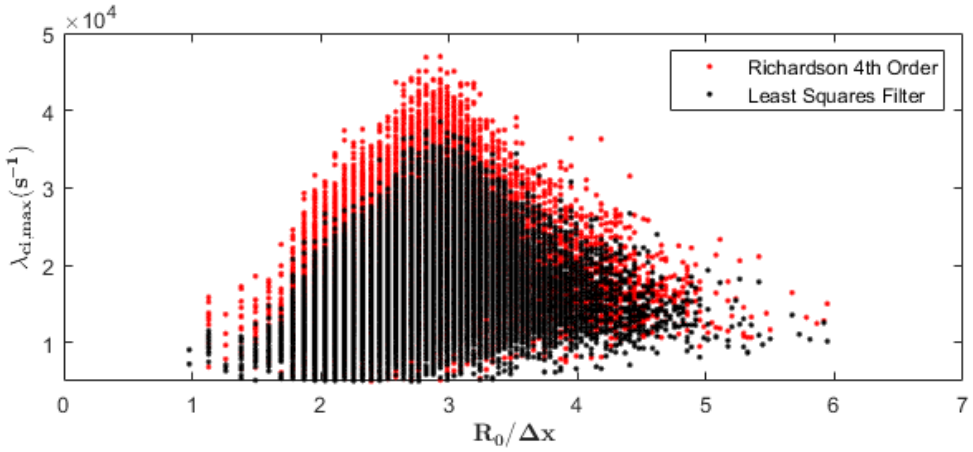

Figure 3.18: Comparison of the measured peak swirling strength versus the characteristic size of the vortex – gradients were calculated using Richardson 4th order stencil (Red) and Least Squares Filter (black)

Based on Figure 3.18, it appears a large number of the detected vortices lie in this smaller size regime, thus, optimizing the gradient stencil to minimize the truncation error is more critical than the noise amplification factor. Based on the formula for the swirling strength bias given by Eq. **3.10**, for $1.5 < R_0/\Delta x < 3.0$ the bias estimates range from 20%

to 1% which is small compared to the bias for the Least Squares filter while also having a noise amplification coefficient ~ 0.95.

3.7.3 Velocity data fidelity in vortex cores

To assess the impact of the low seed density on the processed vector data in the vortex cores, the data can be contrasted across different regions of the flowfield. Figure 3.19a shows an instantaneous Mie scattering image where the centrifuged vortex cores from the leeward and windward SLV structures can be clearly seen. The processed, unsmoothed vector data is plotted in a smaller region of interest containing the regions of centrifuged seed as in Figure 3.19b. The different vector choices provide some perspective on the local quality of the vector data, since the PIV algorithm will choose the vector corresponding to the n^{th} correlation peak based on whether the first $n-1$ vector choices are outliers with repsect to their neighborhood. Consequently, in regions where the seeding density is poor, such as in the vortex cores, the algorithm clearly evaluates and chooses vectors corresponding to secondary or tertiary correlation peaks. A majority of the alternative vectors appear to be the 2nd choice (yellow), while in the center of some cores the 3rd (green) or 4th (blue) choices are used. Most of the vortex cores, for the most part, do not have interpolated vector fields (red). In addition, the vector fields appear to be relatively smooth without vector post-processing using an averaging filter. Since the velocity field inside of a Lamb-Oseen vortex core has no extrema, linearly interpolating the vector fields would likely yield small errors. The exact vorticity value obtained in these regions would be limited by the truncation error as discussed in Section 3.7.2.

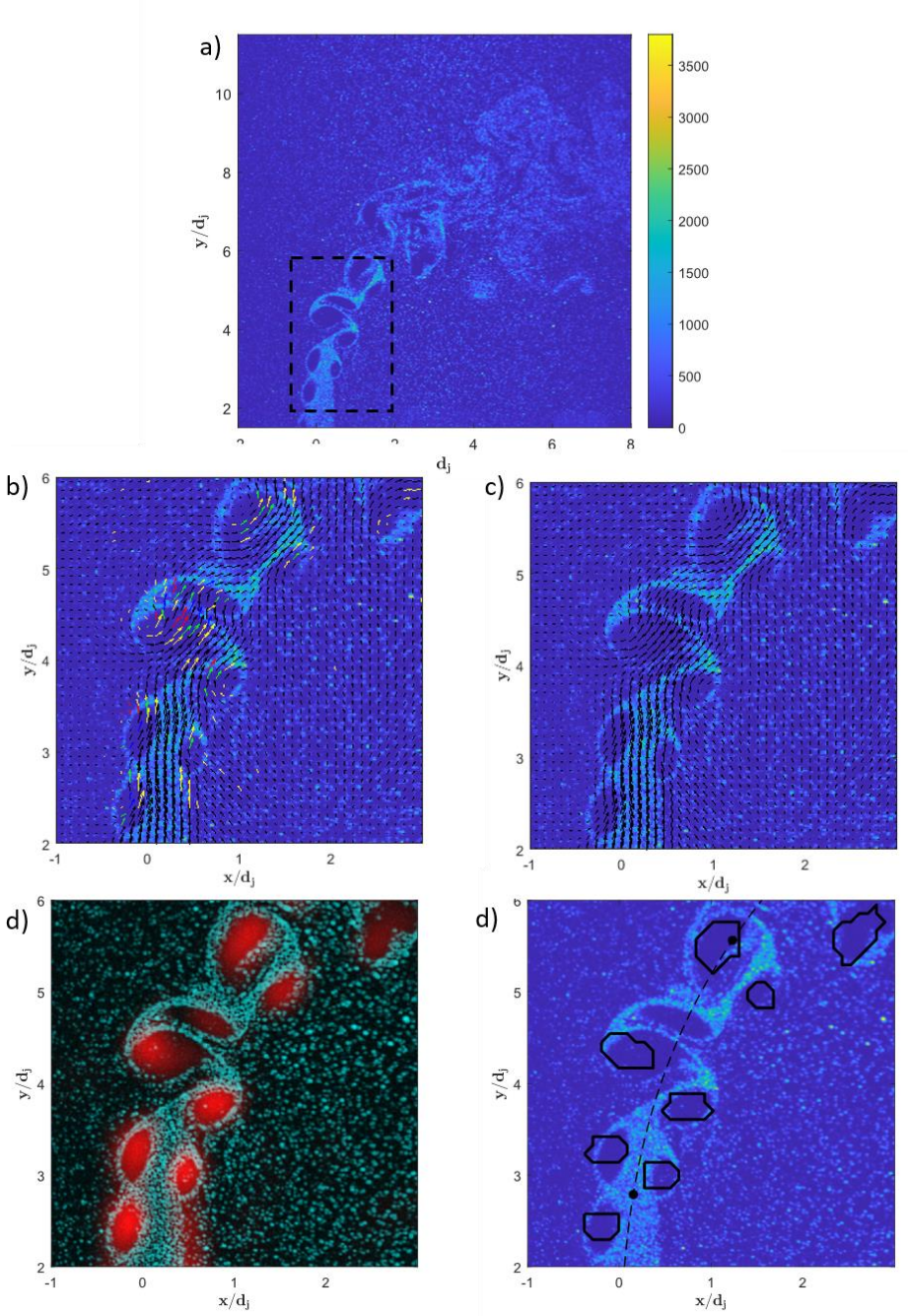

Figure 3.19: a) Instantaneous Mie scattering image from Case 6 with near field region marked; b) Vector plots superimposed on the raw Mie scattering field, color corresponds to vector choices from algorithm - 1st choice/final (black), 2nd choice (yellow), 3rd choice (green), 4th choice (blue) and interpolated (red); c) Smoothed vector data; d) Out of plane vorticity data ($|\omega_z|$) is plotted superimposed on the raw Mie scattering data; e) Detected vortex cores on the raw Mie scattering data.

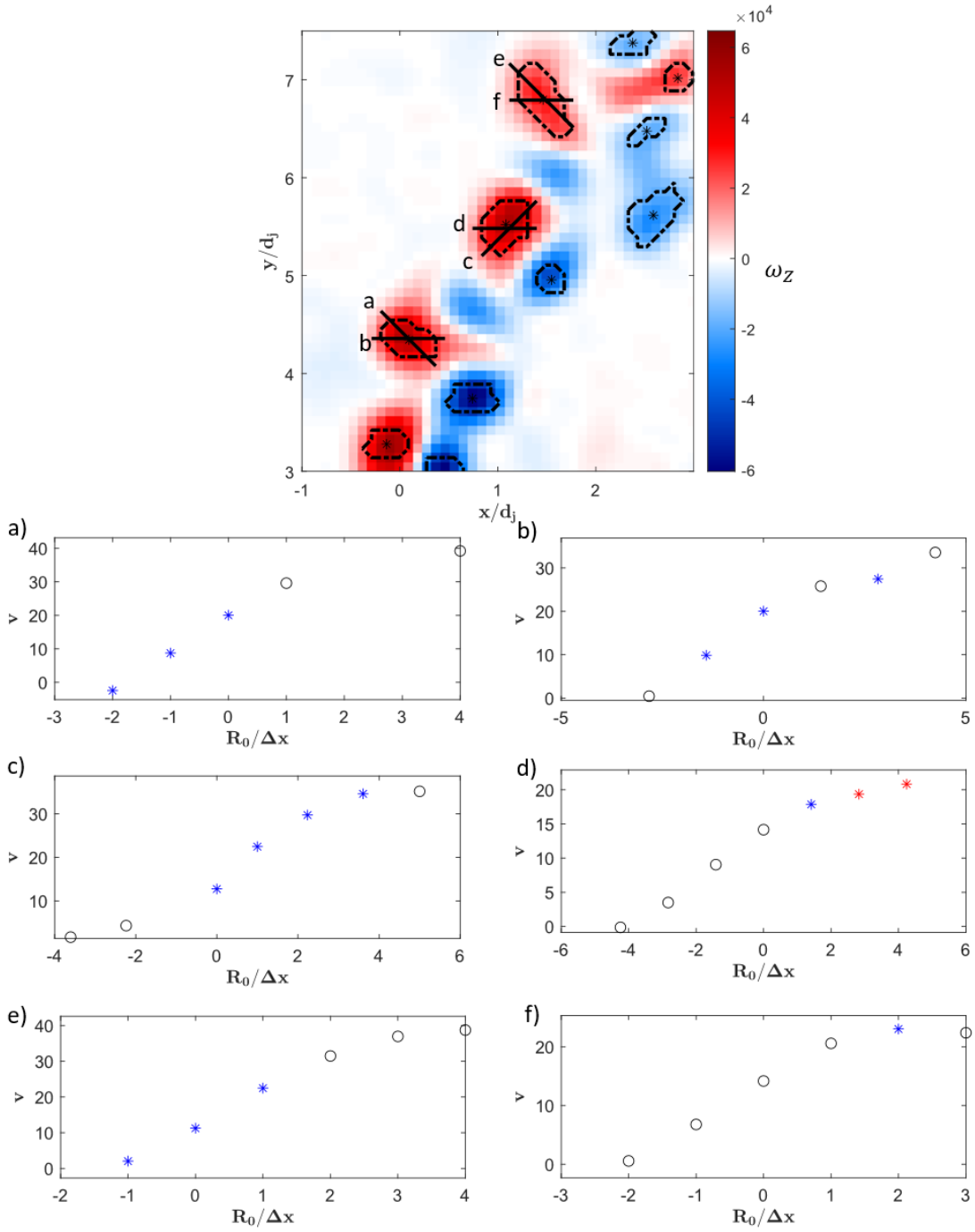

Figure 3.20: Out of plane vorticity plot denoting vortex boundaries ('-.') and vortex centroids ('*'); Scatter plots represent transverse velocity probed along the marked lines ('-') labeled accordingly; black 'o' – 1st choice, blue '*' – 2nd/3rd/4th choice and, red '*' – interpolated value.

The final velocity data can be observed in Figure 3.19c, where the velocity vectors from Figure 3.19b have been smoothed using a 5×5 pt^2 denoising filter. The resultant calculated vorticity field from the final vector data can be observed in Figure 3.19d. The absolute magnitude of the vorticity data aligns well with the regions of rotation observed from the Mie scattering data suggesting there is reasonable data fidelity in most of the vortical regions. The smoothness of the vector data can be gauged from Figure 3.20. The scatter plots probe slices for three vortices, showing the smoothness of vectors obtained from alternate (not 1st choice) correlation peaks. Few data points at the center of the vortical structures are interpolated, while the majority have weaker correlation peaks.

To further assess the quality of the vector data in the vortex cores, the Stokes theorem is used to calculate the circulation around the defined vortex boundary (Figure 3.19e). Stoke's theorem states that the flux of the curl of velocity vectors through a defined surface is equal to the line integral defined along the circuit. Thus, the circulation can be calculated using two different methods given in Eq. **3.11** and **3.12**.

$$\Gamma_1 = \oint_{dS} \vec{v}.dl \tag{3.11}$$

$$\Gamma_2 = \iint_S \nabla \times \vec{v}.dS = \iint_S \vec{\omega}.dS \tag{3.12}$$

Here, Γ_1 is calculated by using the circuit defined by the vortex tracking algorithm using, for the most part, the velocity vectors present in regions with good seeding and consequently high fidelity (Figure 3.19b). On the other hand, calculating Γ_2 requires the contributions from the vorticity calculated in regions close to the center of the vortex cores,

where the velocity is usually obtained from weaker correlation peaks and in some cases, from interpolated data (Figure 3.20).

Figure 3.21a compares the circulation calculated both ways for all the cores identified using the vortex tracking algorithm in Case 6 – the other cases all show similar trends. Remarkably, the circulations match extremely well over a large range of detected circulations. For smaller vortices where the truncation errors associated with the discretization are bound to be larger, there is a bias in the calculation of Γ_2 (Figure 3.21b), which is nominally low (< 10%) for even moderately large vortices ($R_0/\Delta x$ > 2.5). The effective radius of the vortex ($R_0/\Delta x$) is calculated in a similar manner as presented in Figure 3.18. The agreement of these two metrics provides additional encouragement regarding the fidelity of the velocity data processed from the Mie scattering images.

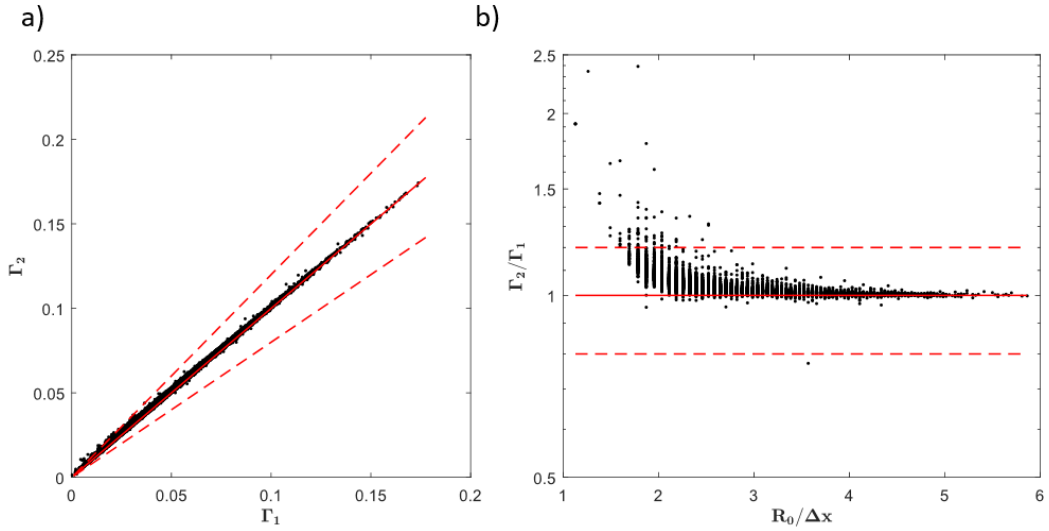

Figure 3.21: a) Line integral based circulation (Γ_1) versus the surface based definition (Γ_2) for all the vortex cores identified in Case 6; b) ratio of calculated circulations versus the normalized vortex radius; Three reference lines represent $\Gamma_2 = \Gamma_1$ ('solid') as well as $\Gamma_2 = 0.8\,\Gamma_1$ and $\Gamma_2 = 1.2\,\Gamma_1$ ('dashed').

3.8 Large Eddy Simulation (LES) details

3.8.1 Description of problem

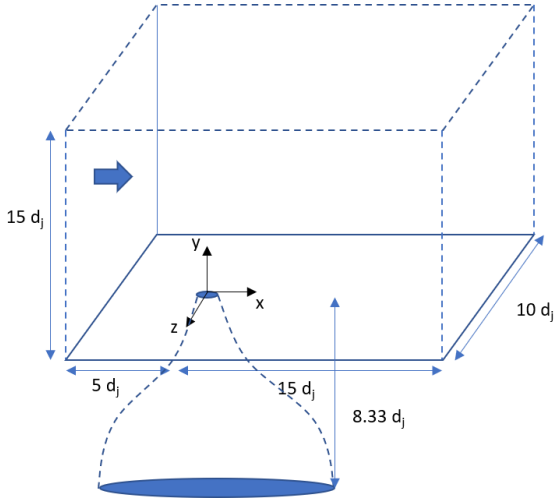

Figure 3.22: Schematic of the computational domain.

The computational domain is described in Figure 3.22 and is essentially a cuboid of dimensions 15 d_j (height) × 20 d_j (length) ×10 d_j (width) with an attached nozzle contoured with a 5th order polynomial. The diameter of the jet, d_j, is fixed at 3mm and is located at a distance of 5 d_j from the crossflow inlet. The mesh consists of 8 million structured hexahedral elements with the smallest element size of ~0.03d_j near the jet exit. The mesh structure and refinement (Figure 3.23) was chosen to best resolve the shear layer, similar to the computational mesh used by Iyer and Mahesh [58]. A grid independence study was performed by contrasting the turbulent kinetic energy (TKE) spectrum obtained from 3 probes in this mesh as well as a coarser mesh (1 million cells) and a finer mesh (12 million cells) to assess the adequacy of the current mesh.

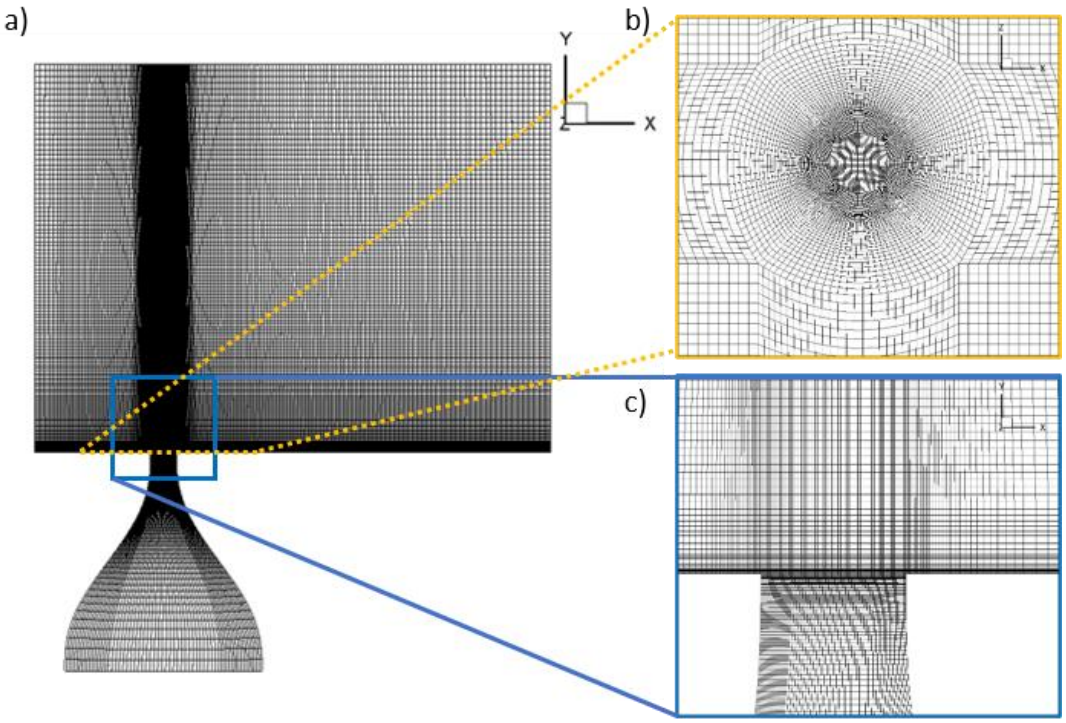

Figure 3.23: Computational mesh in the a) centerplane (*x*-*y* plane), b) close up of the *x*-*z* plane (at *y* = 0) and c) closeup of the domain at the lip of the nozzle.

The inlet velocity is fixed at 20 m/s and the synthetic turbulence intensity is set at 10%. The jet velocity is fixed based on the momentum flux ratio and the turbulence intensity is set at 5%. The influence of jet inflow conditions has been detailed experimentally by Megerian et al. [21] and numerically by Iyer et al. [58], where they found that a top hat profile enhances the shedding of SLVs due to the narrow shear layer thickness. Thus, a nozzle was used to simulate a top-hat profile, which would provide the strongest vortex shedding characteristics and allow us to assess the suppressive effect of the reacting cases. The wall boundary conditions were setup as no-slip for velocity and Neumann condition for pressure and species and temperature, modeling an adiabatic boundary. The crossflow boundary layer is captured by an inflation layer spanned by 20 points where the first point is at $y^{+}_{=1}$.

Table 3-1: Flow conditions for the different computational cases

Case	NR	R1	R2
Crossflow Composition	$Y_{O_2} = 0.233$; $Y_{N_2} = 0.767$	$Y_{O_2} = 0.233$; $Y_{N_2} = 0.767$	$Y_{O_2} = 1$
T_∞	511 K	511 K	550 K
Jet Composition	$Y_{CH_4} = 1$	$Y_{CH_4} = 1$	$Y_{CH_4} = 0.075$; $Y_{N_2} = 0.925$
T_j	300 K	300 K	472 K
$T_{ad}(f_{st})$	-	2315 K	2315 K

The composition and temperatures for the jet and crossflow are listed in Table 3-1. The composition was modeled around the experimental conditions used by Furi et al. [77] to obtain two reacting cases where the flame lies in different positions with respect to the shear layer. The temperatures of the crossflow and jet are chosen to keep the density ratio fixed to iso-density conditions, S = 1 and to maintain the same adiabatic flame temperature of the reacting mixture at f_{st}.

3.8.2 Computational methodology

The computational solver is implemented using the C++ toolbox OpenFOAM (Open-Field-Operations-And-Manipulations). The *reactingFoam* compressible finite-volume solver was used to solve the governing-equations using the Pressure Implicit Splitting of Operators (PISO) algorithm to enforce velocity-pressure coupling. To avoid the interaction of longitudinal acoustics, the *wave transmissive* characteristic boundary condition was used to enforce a pressure outflow condition. For turbulence closure, the Smagorinsky turbulence model was used.

Since of the goal of this study is to primarily assess the hydrodynamic effects of the flame induced density gradient and heat release on the flowfield, an infinite rate single-step chemistry model was chosen to model the flame while keeping computational costs low and decoupling the issue of flame stabilization from the problem. The spatial discretization was implemented using a fourth-order scheme and temporal integration used a second order backward Euler scheme with a time-step of around 10^{-8} s to limit the maximum local Courant number to 0.5.

CHAPTER 4. GLOBAL STRUCTURE AND SHEAR LAYER BEHAVIOR

This chapter discusses the generally structure of the reacting jet in crossflow while contrasting its behavior with different J, S and flame-offset values. As the primary objective is to capture the overall structure – near field and far field, the 4 kHz SPIV and OH-PLIF data is used to obtain the characteristics across a large field of view (compared to the 40 kHz SPIV data). The measured test conditions that are evaluated in this chapter are listed in Table A-2 and each case will be referred to by its case number and classified using the target J, S value and flame behavior (NR, R1 and R2). In addition to the experimental data, the centerplane data from the three CFD cases investigated are also presented to provide insight into properties not necessarily extractable from the experiments. The details of the CFD simulation conditions are provided in Table 3-1.

The chapter begins by presenting the qualitative features of the RJICF as observed from the Mie scattering data, as well as OH-PLIF intensity fields. These visualizations demonstrate that the shear layer behaves qualitatively differently under different J, S values and when the flame is moved inside the shear layer, providing motivation for characterizing these effects by studying the shear layer dynamics. The second section attempts to use the OH-PLIF data to infer flame position across the different jet compositions for cases where the flame lies inside and outside the shear layer. Subtle differences in flame location across different S values and its sensitivity with respect to the jet composition is further investigated by using the passive scalar information from CFD cases at analogous conditions. The following section attempts to capture the shear layer dynamics by tracking

the streamwise variation in coherent structure metrics. An appropriate metric is proposed to capture the effect of the different jet parameters on the instability growth rate. The fourth section covers effects of mixing and entrainment and further demonstrates how streamwise variation in coherent structure metrics can be used to understand the turbulent breakdown process in JICF. Finally, the effects of the unsteady nature of the crossflow are analyzed with respect to its impact on the trajectory and other measured parameters and results quantified earlier.

4.1 Qualitative features of the reacting jet in crossflow

The Mie scattering data and OH-PLIF intensity fields can be used for qualitative flow visualization to understand the general structure of the jet in crossflow and flame location. Since the seed level between the jet and the crossflow was highly variable (with care taken to match the seed density for the PIV measurements), the seed density is not necessarily correlated with concentration measurements. This is especially true in flows with significant dilatation and local density changes. Other structural characteristics associated with turbulent JICF are visible including the regions of low seed density associated with the shear layer vortices. These vortices rollup from the shear layer through the K-H mechanism and as their rotational timescale becomes fast, the seed particle get centrifuged out. These coherent structures eventually breakdown at some location downstream which is apparent from the loss of coherent vortical structures from the particle fields. The qualitative features of these coherent structures, the transitional length and the flame characteristics for the reacting cases are the primary qualitative features which will be discussed here.

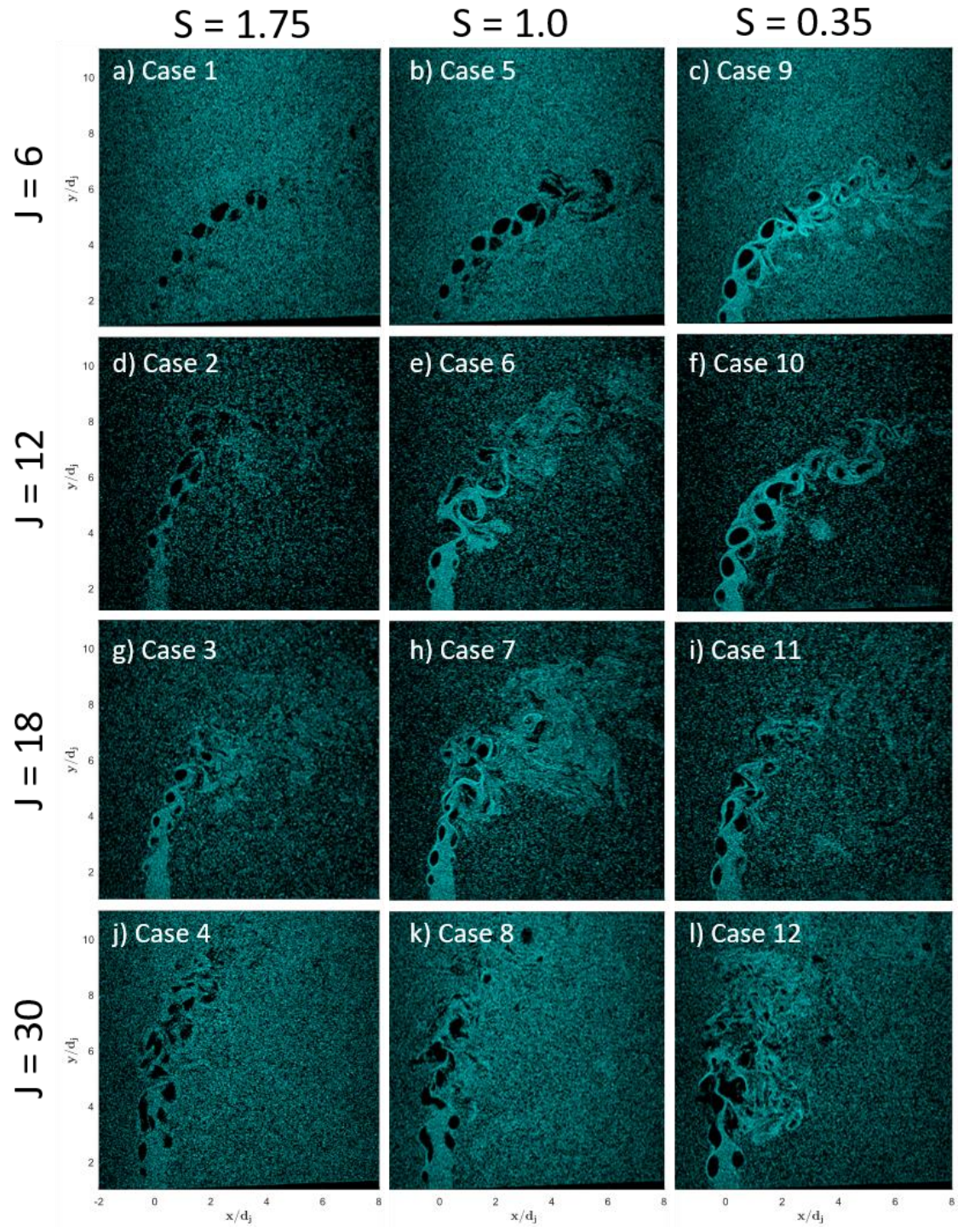

Figure 4.1: Instantaneous Mie scattering data snapshots across the different NR flow conditions with varying *S* (left-right) and *J* values (top-bottom).

Consider the NR cases first, the vortex rollup appears to occur very close to the jet exit for all the cases irrespective of J or S (Figure 4.1). The main differences between the cases are apparent with respect to the size of the coherent structures and transitional length of the jet – which is characterized as the point at which the vortices start becoming incoherent and transition to turbulence. The size of a vortex is defined with respect to the visual region devoid of seed particles and can be considered dependent on the swirling strength of the coherent structures since the level of centrifuging is dependent on the azimuthal velocity of these structures. The cases with lower S but same J have a higher swirling strength due to higher flow velocities u_j. Unfortunately, the time taken for these particles to completely centrifuge from the vortex cores is longer than the convective timescales for most cases (Section 3.5.1) and therefore the observed 'size' is also a function of the residence time of each individual vortex. In the high density ratio cases, with comparatively slower convective times, the vortex sizes appear to grow as they advect, but it is unclear whether the vortex sizes are getting larger due to a growing swirling strength or because the residence time of a given vortex is increasing. Interestingly, across all the density ratios considered, the dependence of J on the vortex rollup behavior was largely absent which is unlike the observations made in most NR studies [51] which show a higher growth rate and consequently a shorter rollup distance at lower J values. This will be investigated further in the following sections.

The second structural feature that appears to vary with S and J is the transitional length – the location at which the coherent behavior disappears to give rise to small scale turbulence. While the process of transition is highly complex and no simple scaling has been derived for most shear flows, including jets in crossflow, the general consensus is that

the process starts with the onset of three-dimensional instabilities [113]. Here the low density conditions appear to transition significantly faster (Figure 4.1c, f, i, l) similar to the observations made by Kyle and Sreenivasan [114] for low S axisymmetric jets. This is most likely a consequence of the globally unstable behavior of low density jets where strong limit cycle behavior promotes the growth of secondary instabilities along the vortical structures, increasing the strain and promoting the transfer of energy to smaller scales through vortex stretching [115].

For the reacting cases, the Mie scattering images are superimposed with the OH-PLIF intensity field. The compact OH-PLIF signal on the windward shear layer in all the cases allows the flame position to be inferred relatively easily (Section 3.3.2). For diffusion flames with similar compositions [91, 95], the peak in OH-PLIF signal tends to lie on the oxidizer side of the mixing interface due to the relative stoichiometric ratio of air to fuel required for complete combustion. In addition, the high temperature of the crossflow made for a favorable environment for flame stabilization. As a result of the radial (with respect to the jet) position of f_{st}, the flame tends to exist outside the shear layer and is wrinkled by the presence of coherent structures. Previous studies [25, 28] on diluted-H_2 jets in crossflow have noted local extinction in the windward branch in regions of high strain associated with the shear layer structures, which is likely absent here because of the 1) lower bulk flow velocity and consequently strain compared to those studies and 2) higher enthalpy of the crossflow. The instantaneous windward flame edge does tend to thicken with downstream distance, which can be attributed to a higher scalar dissipation – similar to H_2 jet diffusion flames [91].

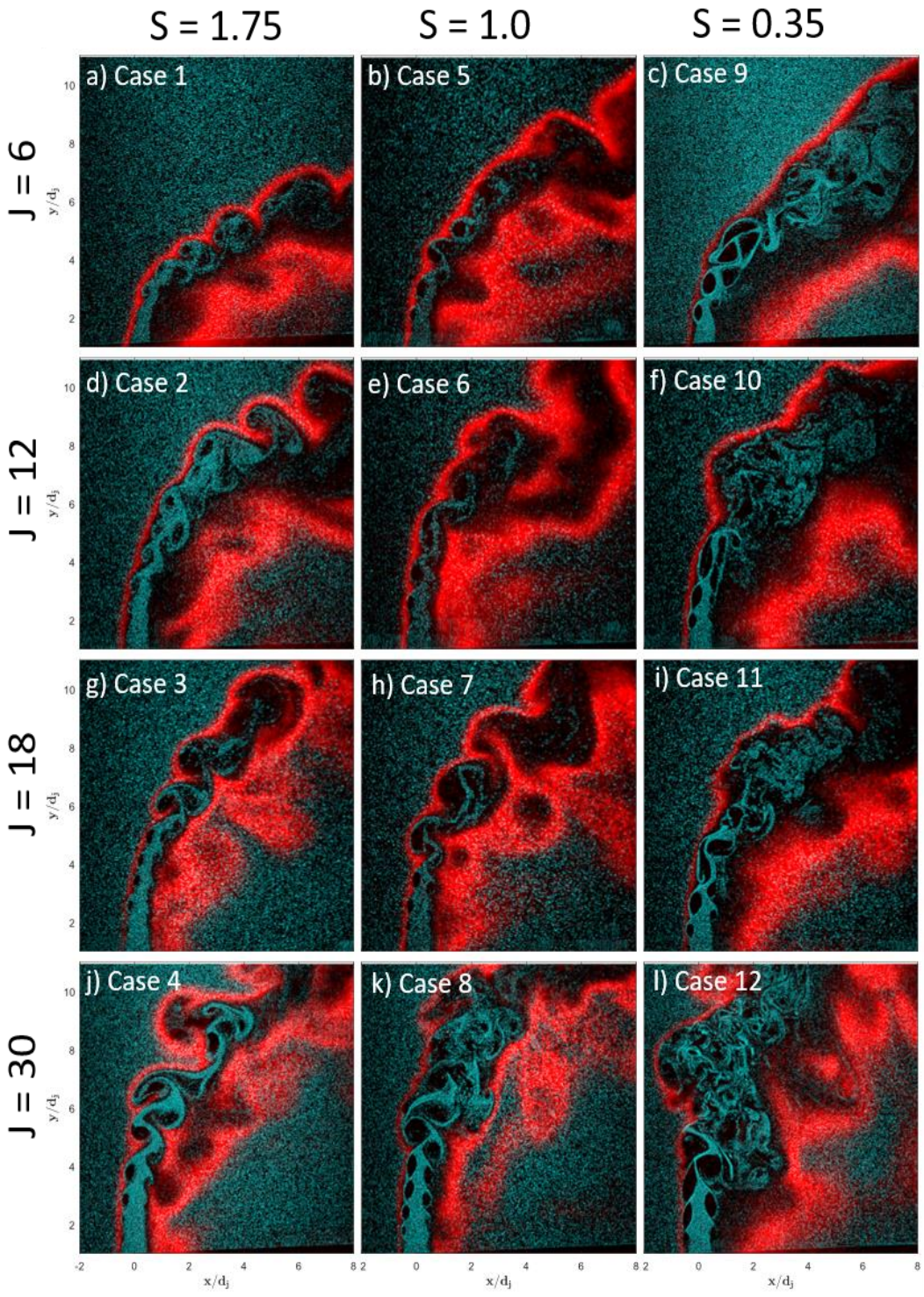

Figure 4.2: Instantaneous Mie scattering data snapshots across the different R1 flow conditions with varying *S* (left-right) and *J* values (top-bottom).

On the leeward size, inferring the exact flame location from the OH-PLIF signal is less clear due to the complicated flowfield involving the shear layer merging with the recirculation zone. Even though the jet flames are attached at the leeward base of the jet, the recirculation region sometimes shows evidence of flame quenching, through the absence of OH-PLIF signal, especially for the $J = 6$ cases. It is likely that the instantaneous flame position varies significantly in the leeward region due to variation in the instantaneous mixture fraction. Distinctions in the flame position for all the different jet compositions are explored in more detail in Section 4.2. In most of the cases, the presence of pockets of fluid with no OH-PLIF signal can be seen convecting in the leeward region, suggesting that periodically non-flammable mixtures are entrained into the leeward recirculation zone, similar to observations made by Wilde [25].

The Mie scattering data in the reacting cases (R1) does not show significant differences compared to the NR cases. While the presence of centrifuged seed particles in the windward and leeward shear layer suggest similar qualitative vortex rollup behavior as the NR cases, combustion does have an effect on the magnitude of swirl and the strength of the vortices, as demonstrated by earlier studies [84]. This can be observed in some of the high density cases (Figure 4.2a, d, g, j) where the level of particle centrifuging appears to be weaker compared to analogous NR cases (Figure 4.1). In addition, the coherence of the vortices appears to persist further downstream for the R1 cases compared to the corresponding NR cases. The effect of combustion on delaying transition to small scale turbulence has been noted by Yule et al. for jet diffusion flames [79], where combustion was hypothesized to suppress the onset of the secondary instabilities responsible for the turbulent breakdown process. The lack of OH-PLIF signal in the jet core post breakdown

suggests that even after breakdown the jet fluid has not mixed out into the crossflow. Quantitative metrics, including the strength and characteristics of the observed coherent structures are used to help capture these effects and contrast them with the observations for NR jets in Section 4.3.3.

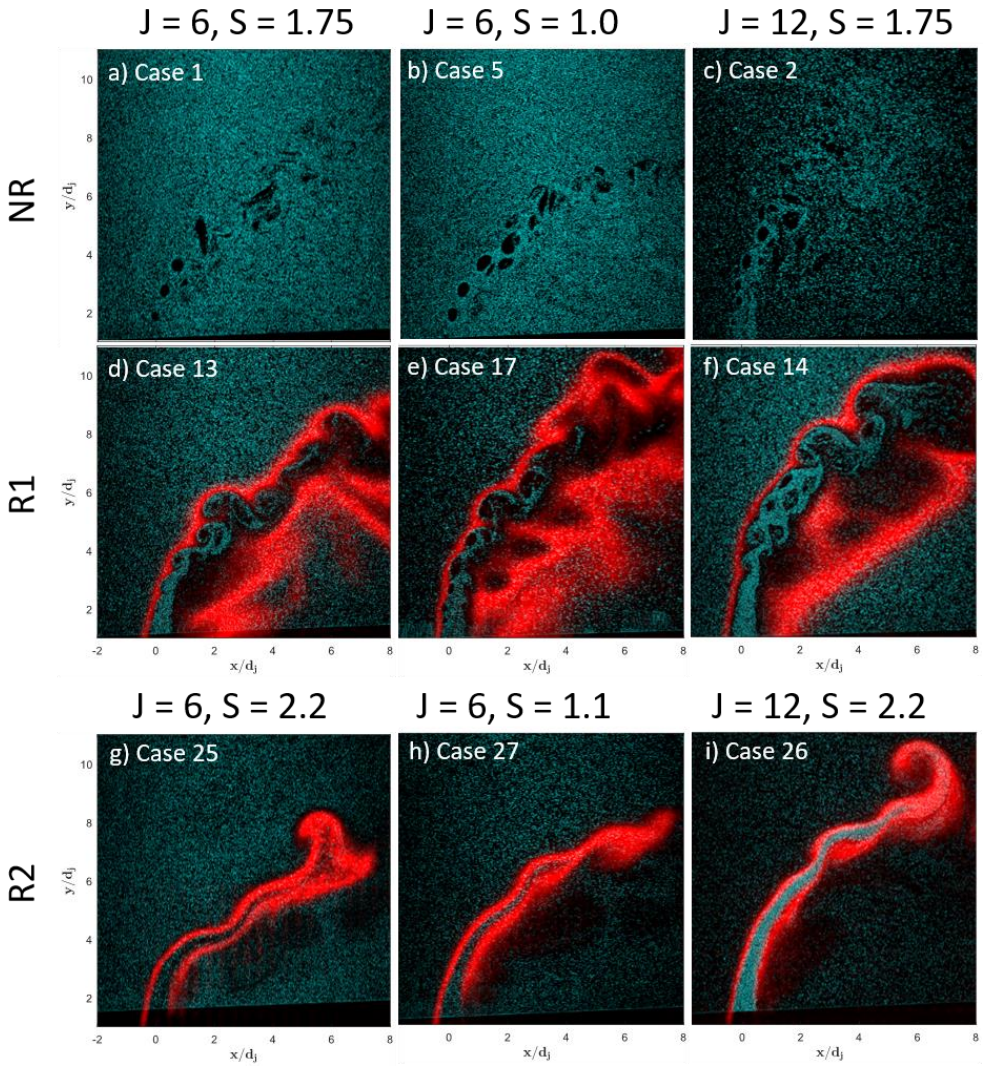

Figure 4.3: Instantaneous Mie Scattering and OH-PLIF data for cases with analogous *S*, *J* values with different flame configurations – NR, R1 and R2.

Finally, the qualitative features of the second reacting condition (R2) are contrasted with NR and R1 cases of similar *J* and *S* values. The OH-PLIF images show that the

dynamics of reaction zone for the R2 cases are significantly different from the other reacting configuration (Figure 4.3). The near field of the reaction zone is less wrinkled, which can be attributed to the almost complete absence of shear layer vortices in the near field. In the far field, there is evidence of shear layer rollup due to the moderately wrinkled flame and regions where the combustion products appear to be entrained into the shear layer vortices. The absence of regions of high swirl suggests that these structures have significantly lower rotational timescales compared to the vortices in the other two configurations.

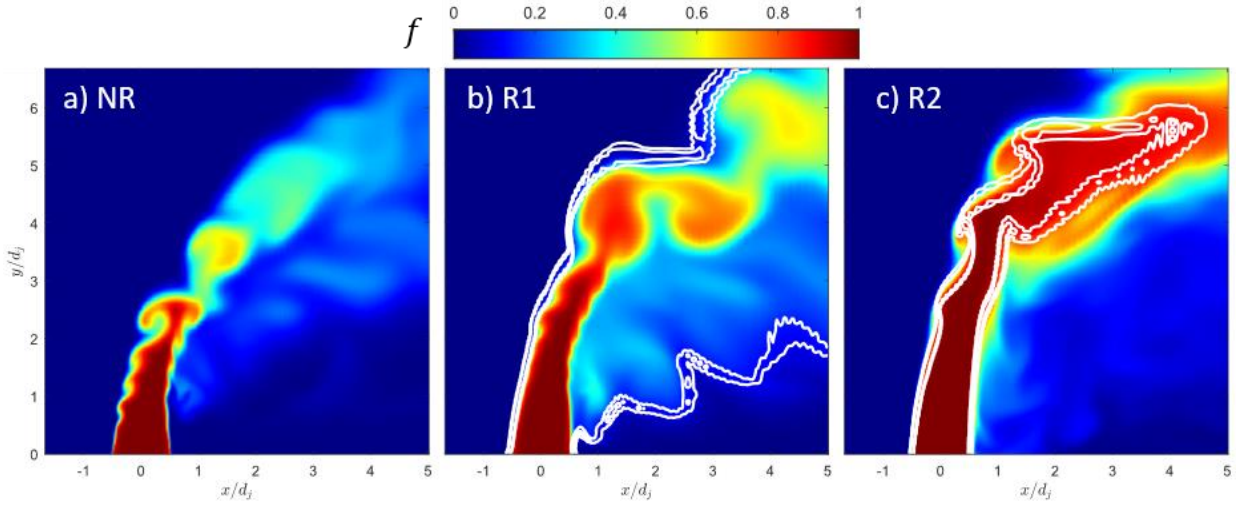

Figure 4.4: Centerplane data (CFD) showing mixture fraction with contours ('white') corresponding to $[\dot{Q}]/[\dot{Q}]_{max}$ = 0.1 and 0.001 for the two reacting conditions – b,c.

Qualitative features of the computational data can contrasted with the experimental observations by looking at the mixture fraction distribution for the three cases (Figure 4.4). The NR case shows strong rollup behavior in the near field and quickly mixes out into the crossflow. The R1 case shows the region of heat release wrapping around the jet column

on the windward side and significantly into the recirculation region on the leeward side, similar to the observations made from the OH-PLIF data. The near field rollup also qualitatively appears weaker, and consequently, there is a higher concentration of jet fluid further downstream. Similar to the experimental data, the R2 CFD case shows very weak rollup and mixing behavior, the flame appears to lie at a relatively higher value of f_{st} (by design) and consequently the dynamics appear significantly different compared to the NR and R1 cases at analogous conditions.

4.2 Flame dynamics

This section presents data on the reaction zone structure for the different jet compositions and flame configurations considered in this thesis. Two broad class of reacting flows are considered here – R1 cases where the flame lies outside the shear layer and R2 cases where the flame lies inside. While care was taken to obtain an attached flame across all conditions, the diffusion flame position has been shown to be sensitive to jet composition as it changes the value of f_{st}, and consequently, the position at which the flame stabilizes with respect to the jet shear layer. Thus, while the differences in flame position between the R1 and R2 cases can be clearly observed (Figure 4.3), the differences between the different S values within each configuration are more subtle but can have a significant impact on the general flow and flame structure.

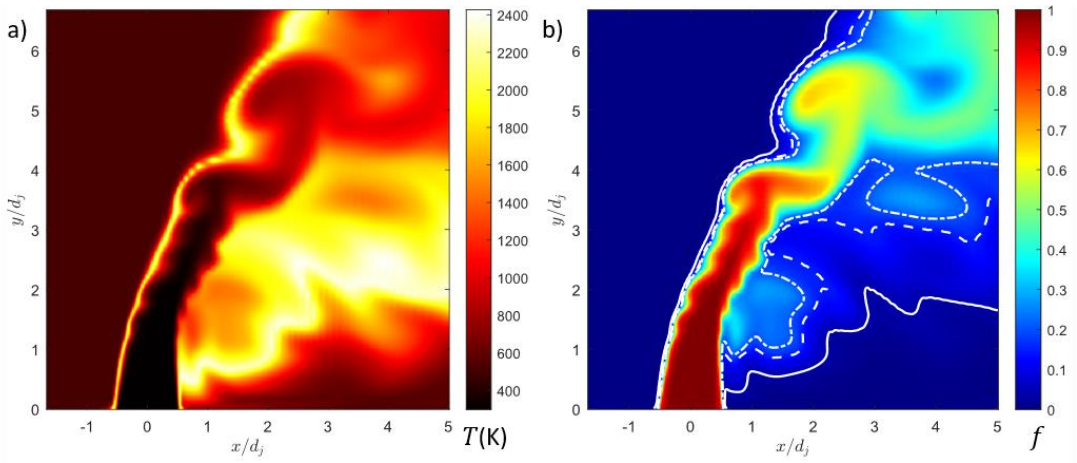

Figure 4.5: R1-CFD case showing a) *T* field and b) *f* field with contours corresponding to $f = f_{st}$ for the different experimental *S* values (see Table 4-1): (--) 0.04, (- -) 0.16 and (-.) 0.20.

Table 4-1: Theoretical f_{st} values (experiment) for different reacting jet compositions

	R1			R2	
S	1.75	1.0	0.35	2.2	1.1
$\boldsymbol{f_{st}}$	0.20	0.16	0.04	0.58	0.39

To illustrate the sensitivity of the flame position on f_{st}, we will consider the flowfield and species information from the CFD data, specifically the R1 case. The flame structure for this case (Figure 4.5) was similar to the flame structure inferred from the experimental OH-PLIF data for the R1 cases. In addition, the attached flame behavior shows similar qualitative structure to the DNS data presented in Lyra et al. [10]. Assuming that the flowfield structure and mixing behavior is similar, the mixture fraction field provides an estimate of the flame position sensitivity to changing f_{st}. Figure 4.5b demonstrates that the mixture fraction field, specifically the spatial gradient, is significantly

different on the windward and leeward side of the jet. Additionally, the three contours marked correspond to the theoretical f_{st} values for the R1 cases with different jet compositions (Table 4-1) demonstrating that, while along the windward shear layer, all three theoretical flame position will vary by small amounts, in the leeward region there can be considerable differences.

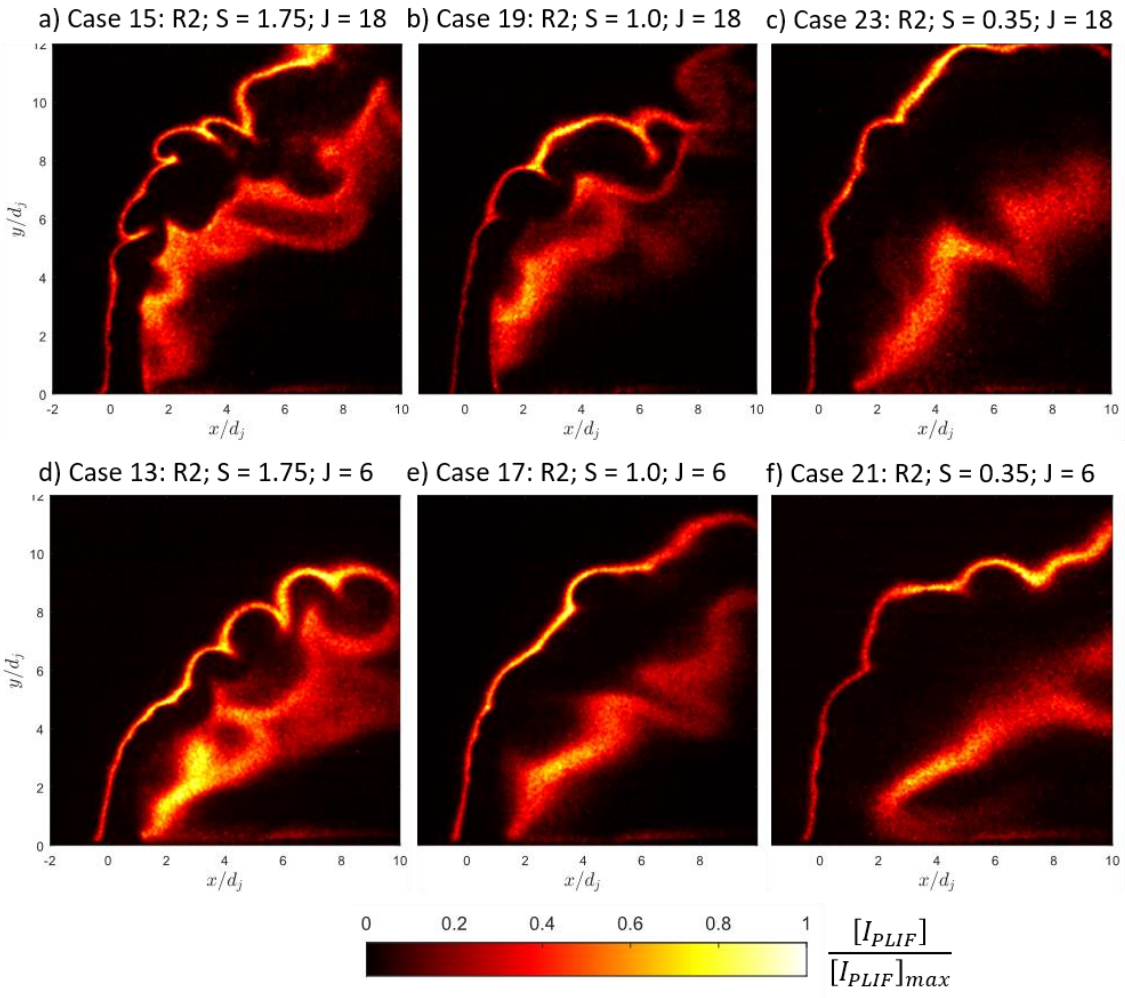

Figure 4.6: Instantaneous OH-PLIF snapshots for the R1 flame configuration across different *S* values (left to right) for *J* = 18 (top) and *J* = 6 (bottom).

This is further corroborated by the OH-PLIF signals (Figure 4.6) for the low density cases (with the lowest f_{st}) where the leeward reaction zone structure seems to be

considerably detached from the leeward shear layer compared to the other two jet compositions. Since the mixture fraction distribution depends on the general structure of the flowfield changing the value of J is bound to have an impact on the location of f_{st}. Figure 4.6d-f show that for the J = 6 cases, the relative detachment is larger and there is no clear flame structure near the leeward shear layer.

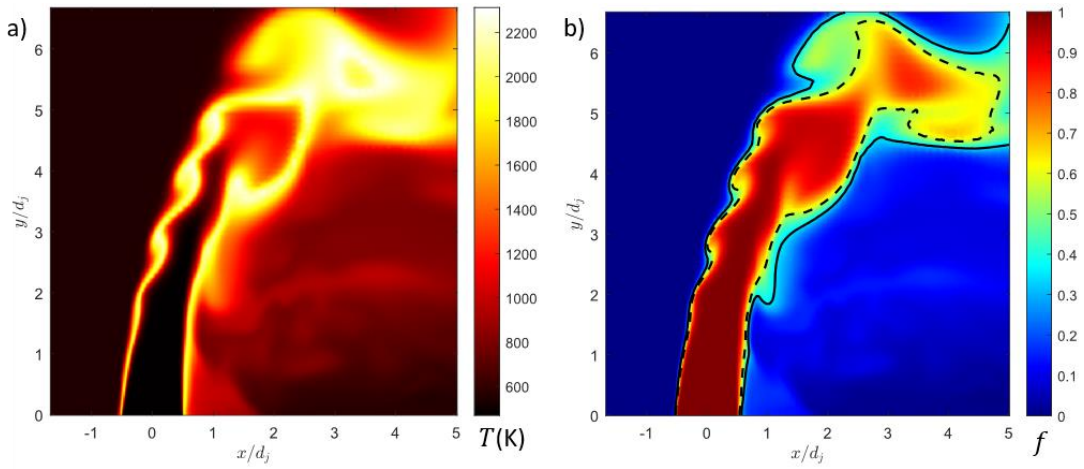

Figure 4.7: R2-CFD case showing a) T field and b) f field with contours corresponding to $f = f_{st}$ for the different expeirmental S values (see Table 4-1); (- -) 0.58 and (-) 0.39.

Now consider the effect of the two jet compositions used to for cases that move the flame inside the shear layer. Once again, the CFD data provides a reasonable estimate for understanding the distribution of jet material since it qualitatively captures the flame structure observed experimentally. The value of f_{st} corresponding to the two conditions is plotted on an instantaneous mixture fraction snapshot and demonstrates that since they both lie closer to the jet core, the sensitivity is low and the practical difference between the two theoretical contours is unlikely to be discernable from OH-PLIF data. This is can also be due to the dependence of the flame position on the most reactive mixture fraction (f_{MR}).

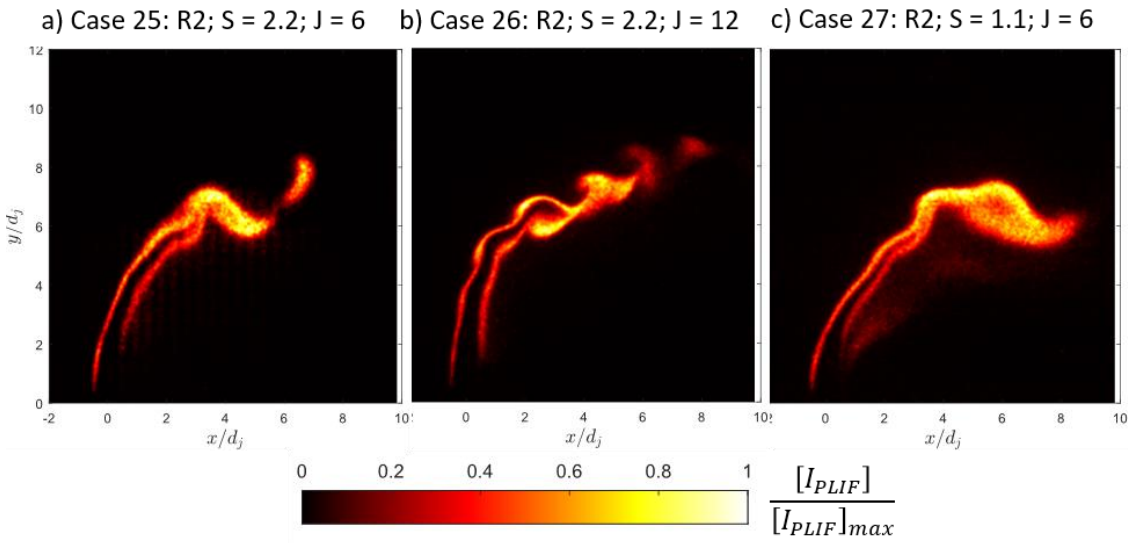

Figure 4.8: Instantaneous OH-PLIF snapshots for the R2 flame configuration across different conditions.

The presence of high-temperature combustion products, captured by the OH-PLIF signal, for the R2 cases has, to this authors knowledge, not been documented previously. Since the OH-PLIF signal has been shown to peak on the oxidizer side of the flame, the exact flame location here lies on the crossflow side of the contour describing the peak signal. But, given the compactness of the flame the deviation is assumed to be very small. The general structure resembles the flame structure captured by the R2-CFD case with some differences, including lifted flames on the leeward side, which can be attributed to finite rate chemistry effects. As discussed in Chapter 2, stabilizing the flame in the shear layer is particularly challenging due to the fast flow timescales and lack of slow velocity regions such as boundary layers or recirculation bubbles. The doped H_2 in the jet creates a radical pool which stimulates the attachment process but, as is observable from the OH-PLIF signals, both the windward and leeward branches of the reaction zones tend to be slightly lifted from the jet exit (Figure 4.8), for all three cases. The windward branch

appears to be weakly connected with the lip of the nozzle suggesting that the flame initiation occurs within the boundary layer of the jet nozzle while the OH-PLIF signal is discernable only downstream at some distance corresponding to the flow-timescale at the lip. On the leeward side the anchoring point appears to be more unsteady and further downstream of the nozzle lip and stabilized through auto-ignition since there are no discernable regions of low velocity magnitude in its vicinity.

The results presented in this section demonstrate that for the R1 cases, comparing the effect of combustion on the flow dynamics is less sensitive to the compositional changes when considering the windward shear layer. The instantaneous leeward flame structure is more intermittent and highly dependent on local variation of the mixture fraction, and consequently its effect on suppressing instabilities in the leeward shear layer is bound to be weaker. For the R2 cases similarly, the windward branch appears to extend close enough to the nozzle exit that it will have an effect on the shear layer dynamics right from the base of the jet. The leeward branch here is more intermittent and tends to be stabilized 1.5 – 2 d_j above the nozzle and consequently its effect on the rollup of leeward structures is bound to be weaker. These hypotheses will further be investigated in the following sections.

4.3 Shear layer dynamics

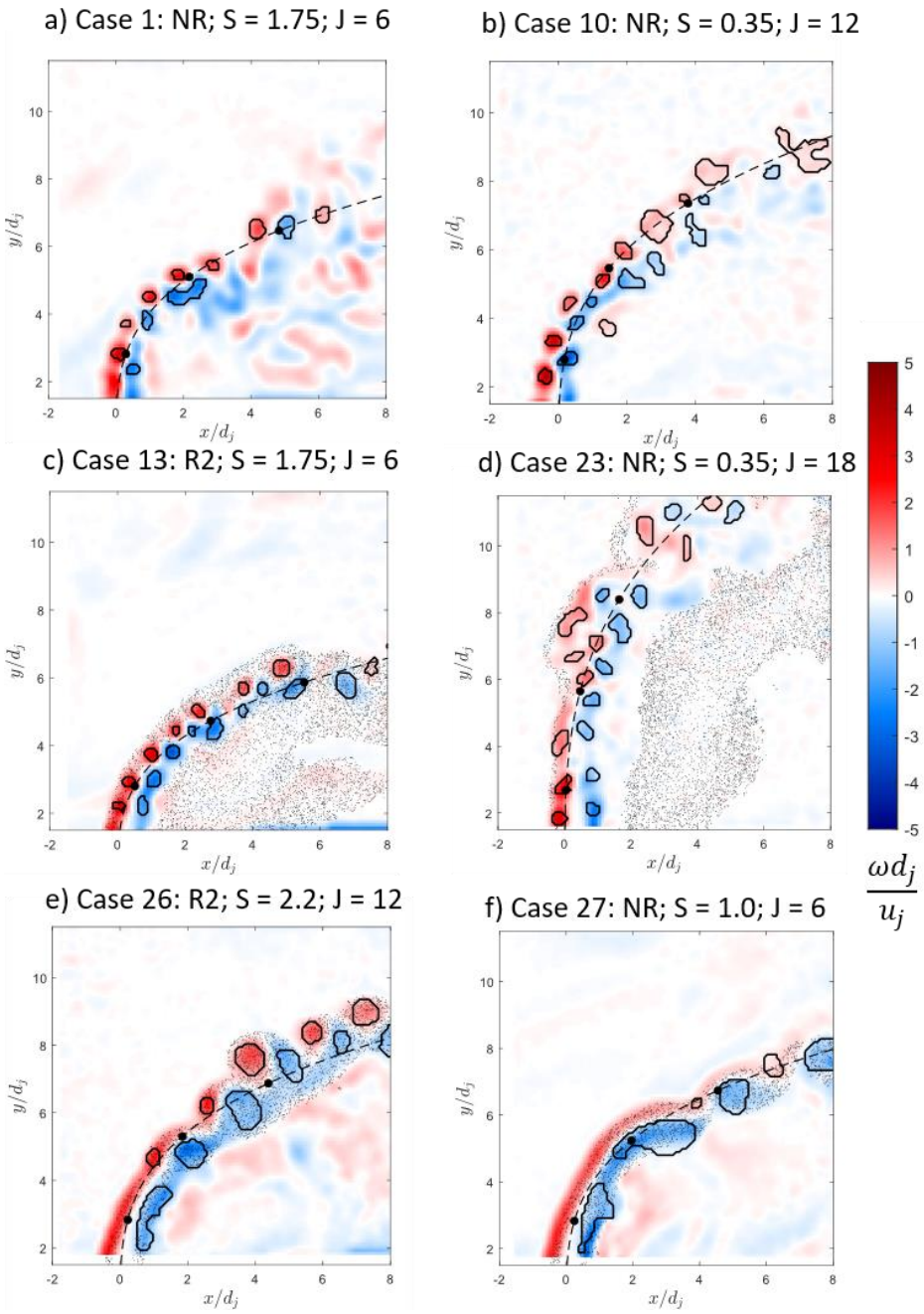

Figure 4.9: Instantaneous snapshots of normalized out of plane vorticity (ω_z) with detected vortical regions ('black') and speckled regions denoting elevated OH-PLIF signal.

The shear layer dynamics can be better visualized by looking at the out of plane vorticity component (ω_z). Figure 4.9 shows instantaneous vorticity values with the vortex boundaries, as identified through the process outlined in Section 3.6, and the instantaneous approximate jet trajectory. Windward and leeward shear layer vortices are clearly observable in the near field formed from the rollup through the K-H instability mechanism. The rollup process is similar for both the NR and R1 cases in general as observed from Figure 4.9a-d. In the near field, the vorticity contained outside these structures corresponds to shearing motion, while the vorticity contained within these structures is rotation but as the vortices rollup and accumulate strength the vorticity of the shear layer tends to accumulate in the cores through irrotational entrainment. This is more discernable in the R2 cases (Figure 4.9e, f), where the rollup process is highly suppressed, as a result, the vorticity in the near field can clearly be seen to correspond to shearing motion while in the far field the vorticity appears to be entrained into the vortical structures. For the R2 cases the windward and leeward structures tend to interact in the far field resulting in intermittent weakening of the windward shear layer which can be seen in case 27 (Figure 4.9f). This is likely a consequence of competing induction process by which the stronger vortical structures tend to stretch out the other vortex cores and dissipate them.

In the far field, the relative 'coherence' of these structures can be estimated by percentage of vorticity originating in the shear layer that is contained within the boundary of the defined coherent structures and is a good indication of the transitional length. The vortex size appears to increase while the average vorticity decreases with downstream distance because of turbulent dissipation, as hypothesized by Moore and Saffman [116]. For the low density cases, both NR (Figure 4.9b) and R1 (Figure 4.9d), this can be seen as

the vortical structure both contains weaker out of plane vorticity and there is a significant amount of vorticity present in the shear layers that is not associated with the identified structures. Between the lower J, NR (Figure 4.9a) and R1 (Figure 4.9b) cases, the presence of reactions appears to allow these coherent vortices to retain their shape and coherence for a longer duration, most likely a consequence of combustion suppressing the transition process. For the R2 cases, the rollup process has not completely entrained the vorticity in the shear layer and therefore, inferring the transition length is challenging, but the relatively circular shape of the coherent structures in the far field suggest that this transition process is also significantly suppressed.

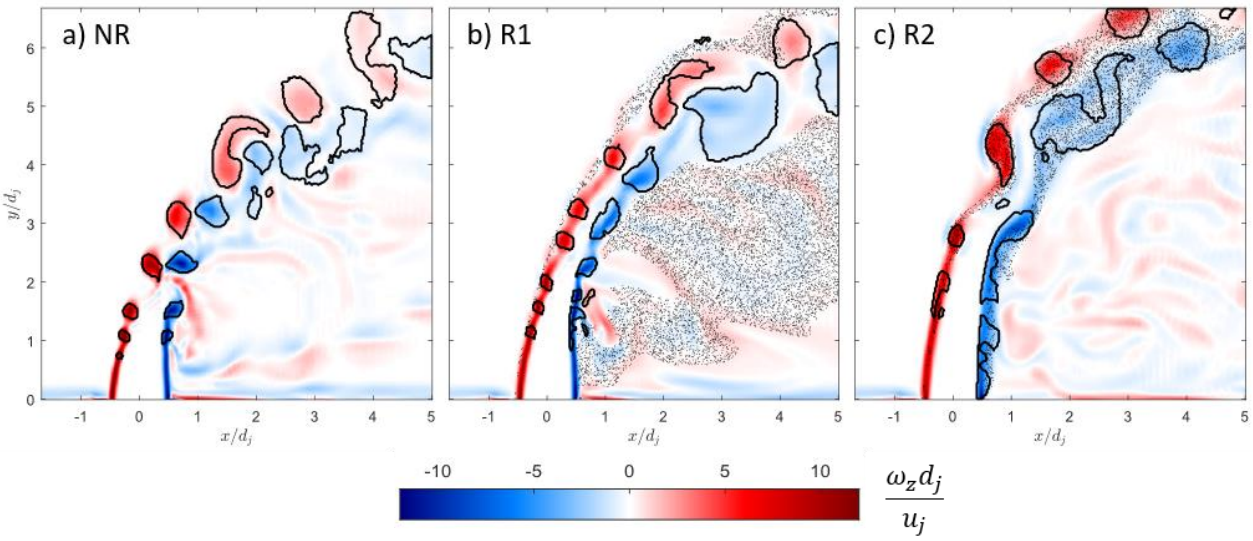

Figure 4.10: Instantaneous snapshots of the out of plane vorticity (ω_z) sampled at the centerplane of the CFD data for the three conditions – NR, R1 and R2; The speckled regions correspond to regions of elevated temeprature T > 1500 K.

The CFD data captures the broad qualitative observations of the vortex shedding behavior between the three different flame configurations (Figure 4.10). The NR and R1 cases show relatively strong vortex rollup behavior in the near field unlike the R2 case

where the shedding is weaker and the timescales associated with it are slower. In addition, the NR case shows strong vortex pairing behavior as it convects which has been observed for convectively unstable jets in crossflow. These non-linear effects and the possible role of combustion in inhibiting it will be explored in detail in Chapter 5.

Statistically, these observations demonstrate that the rollup and transition process depends on J, S and the flame offset. But the highly turbulent nature of the flowfield results in variability in the shear layer vortex behavior making observations using instantaneous images subject to a high degree of uncertainty. Thus, identifying individual structures allow for the calculation of the ensembled streamwise variation of vortex metrics and can be used to provide a more quantitative method of contrasting the behavior of different cases.

4.3.1 Streamwise variation of vortex metrics

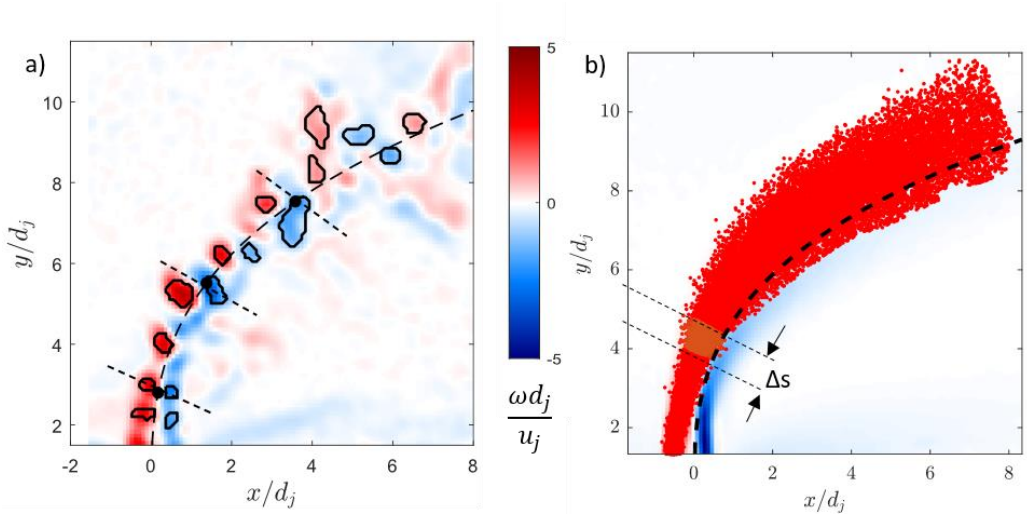

Figure 4.11: a) Instantaneous normalized out of plane vorticity (ω_z) for Case 2: J = 12, S =1.75 with identified structures and the instantaneous jet trajectory; b) Ensembled windward shear layer vortex centroid locations superimposed on the mean vorticity field with streamwise binning.

The individual vortices defined through the vortex identification process provide an effect way to condition the ensembled metrics associated with vortex strength (Figure 4.11a). Each metric associated with a coherent structure can be assigned a streamwise (s) and spanwise spatial coordinate (n) based on the centroid of each vortex, weighted by the local rotation magnitude. The total number of vortex centroids associated with the windward shear layer across all 3880 instantaneous flowfield snapshots is plotted in Figure 4.11b. Streamwise properties of vortex metrics are obtained by averaging the vortex centroids that lie within each streamwise bin. Since the vortex identification process does not impose any constraints on the spatial location of detected vortices, simply considering vortices with a positive circulation is not sufficient since these structures can exist outside the shear layer and in the wake. To consider only the vortices that can be categorized as shear layer vortices in each streamwise bin, the spanwise centroid locations are assumed to fit a gaussian distribution similar to the observations by Hernan and Jiminez [117] for a mixing layer. A probability threshold is set to eliminate vortices that are outliers to this distribution. Streamwise properties are extracted by using the mean value for all the vortices that lie within a bin (Figure 4.11b). The uncertainty of the mean peak swirling strength ($\lambda_{ci,max}$) is estimated as -

$$\sigma_{err}^2 \cong \sigma_{rand}^2 + \overline{U_{\lambda_{ci,max}}^2} \qquad 4.1$$

where σ_{rand}^2 is the variance of all the swirling strength values in each bin, and $\overline{U_{\lambda_{ci,max}}^2}$ is the root mean square (RMS) of the individual uncertainty values of each swirling strength estimate $U_{\lambda_{ci,max}}$ (obtained from the UQ process outlined in Section 3.7.2).

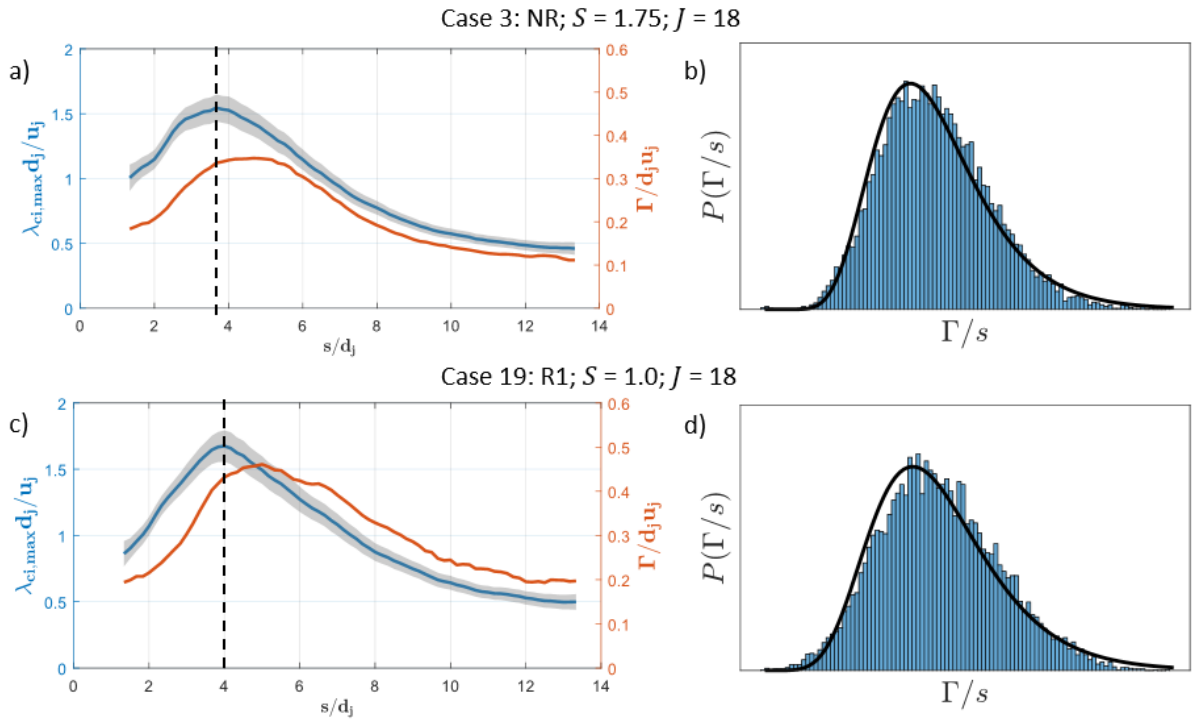

Figure 4.12: (a, c) Streamwise variation of normalized swirling strength ($\lambda_{ci,max}$) and normalized circulation (Γ) for two cases NR, R1 with analogous *J* and *S* values; (b, d) Histograms capturing the self-similar vortex circulation considering all vortices which lie below the streamwise location marked with '- -' line in (a, c) respectively.

To illustrate the process of streamwise binning, the streamwise variation of vortex circulation (Γ) and swirling strength ($\lambda_{ci,max}$) normalized with the characteristic length (d_j) and velocity scales (u_j) for two NR and R1 cases with similar J and S values is plotted in Figure 4.12a, c. The uncertainty was represented by the width of the greyed out region representing the 95% confidence interval with a standard deviation σ_{err} (Eq. 4.1). The vortex circulation grows in the near field as more of the vorticity contained within the shear layer is entrained into the vortex cores while the swirling strength grows as the strength or degree of rotation intensifies. As the instability strength saturates, so does the magnitude of swirl and consequently the circulation tends to plateau. For the reacting case (Figure

4.12c) the increase in circulation beyond the saturation point is likely the effect of entrainment of hot combustion products from the windward flame branch resulting in expanding vortex area due to low density entrainment. A more in-depth discussion in the streamwise variation of these metrics across different jet conditions is provided in Section 4.3.2.

Few studies in the past have used similar vortex identification methodologies to look at vortex statistics associated with a mixing layer but have typically been applied through direct visualization of schlieren images [67, 117]. Consequently, the metrics extracted, such as the core area [117] and distance between successive braids [118], were purely geometric and were not defined based on flow field measurements. Bernal [118] formulated a statistical theory of vortex circulation proposing that the self-similar probability distribution of vortex circulation, in their case the distance between successive vortices, was a log-normal distribution with σ = 0.28, independent of velocity and density ratio. While the jet in crossflow flowfield is highly three dimensional and significantly more complex than a two dimensional mixing layer, the near field of the windward shear layer tends to behave similar to a mixing layer in the vicinity of the jet potential core. This streamwise location is generally associated with the saturation of the circulation and marked for the two cases in Figure 4.12a-c. Considering an equivalent self-similar circulation (Γ/s) for all vortices that lie upstream of this location, the probability distribution for the two considered cases is shown to follow a log normal distribution with a σ = 0.30 and 0.31 respectively. This value are similar to the standard deviations noted by Brown and Roskho [119] (σ = 0.30) as well as Hermanson and Dimotakis [67] (σ = 0.31) for both reacting and non-reacting mixing layers. For cases where the saturation

occurs upstream, close to the jet exit, i.e. globally unstable cases, the standard deviation tends to be low and the circulation will not follow the statistical distribution derived for a convectively unstable mixing layer.

4.3.2 Characterizing vortex strength

To establish an appropriate metric to best represent the instability growth process, the streamwise variation of the extractable vortex metrics – circulation, swirling strength and vortex area are analyzed for different conditions. First consider the streamwise vortex behavior across NR cases of different S values with a fixed J. Figure 4.13 a, c and e, contrasts the streamwise variation of peak vortex swirling strength ($\lambda_{ci,max}$) between the windward and leeward shear layer. Physically, the swirling strength provides an estimate of the time-scales of rotation of the vortical structures and has been used on similar data to capture the growth rate of shear layer structures [84]. For the cases considered in Figure 4.13, the windward shear layer appears to have a higher initial swirl and peak faster than the leeward swirl. Previous studies [25, 51] have noted this asymmetry in the vortex rollup behavior since there is a sharper velocity gradient associated with the windward shear layer compared to the leeward shear layer, due presence of the recirculation region. This, in addition to the flame position along the windward shear layer, suggests that the windward shear layer vortex metrics are more likely to capture the variation of stability characteristics of the flow imposed through changes in J, S and combustion. This is demonstrated by considering the growth of the vortex swirling strength among the cases with different S. where the windward shear layer shows a relatively stronger increase in growth, compared to the leeward swirl, as the density ratio is reduced. This is in line with previous

observations showing higher instability growth rate for low density jets in crossflow [53] sampled along the windward shear layer.

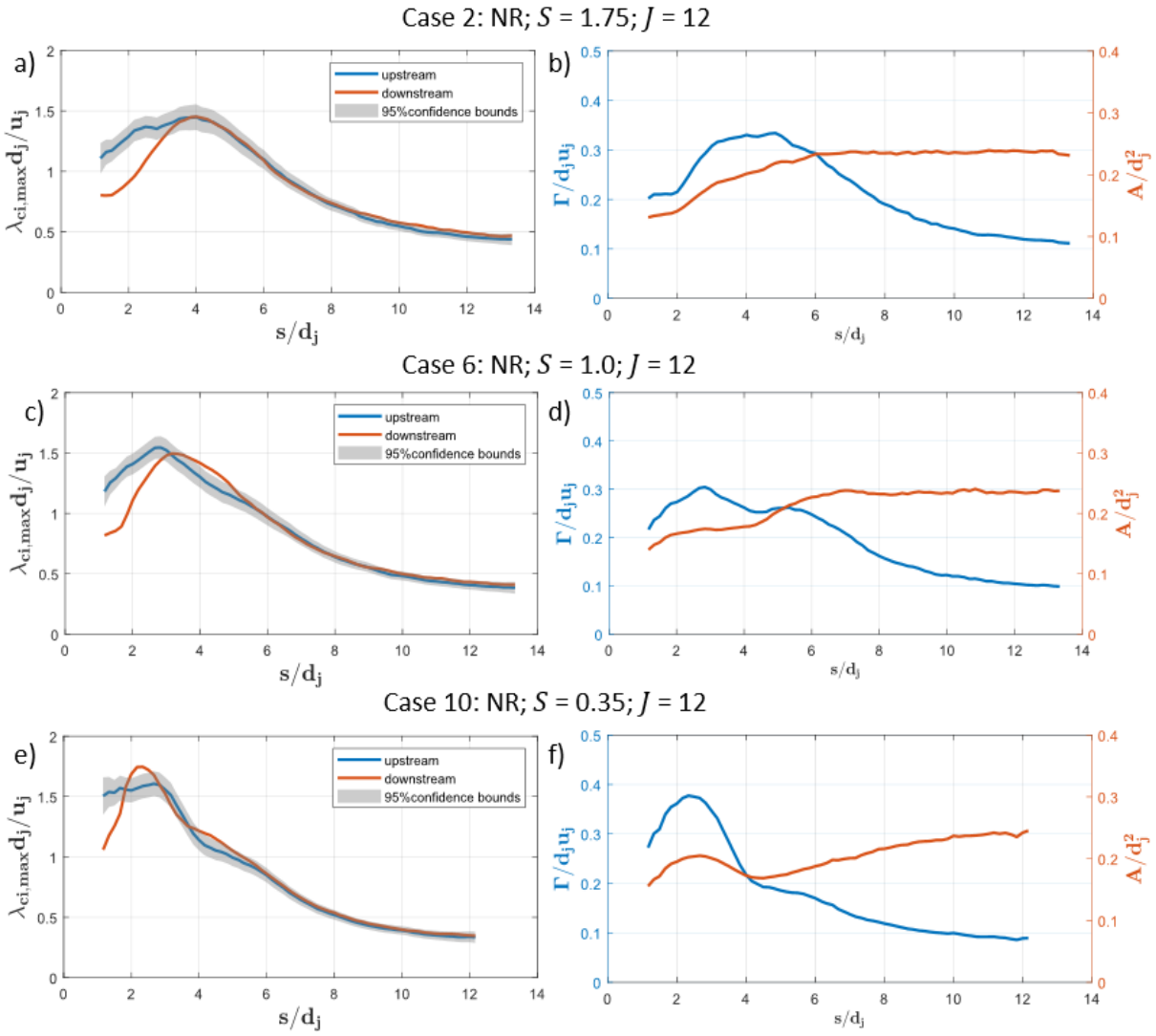

Figure 4.13: Streamwise variation in peak swirling strength ($\lambda_{ci,max}$) for windward and leeward vortices (left) and the streamwise variation in circulation and coherent structure size (right) for three different NR cases with different S and J = 12.

The streamwise variation of circulation and vortex area for the windward shear layer vortices are also described in Figure 4.13 to understand how the growth, rollup and transition process is represented through these metrics. The circulation tends to

increase in line with the swirling strength as described in the previous section since the vortices continue to accumulate the vorticity contained in the shear layer primarily through irrotational entrainment. Similar to free jets, the circulation tends to saturate as the potential core, and consequently the driving momentum of the jet, disappears. For the high S case, Figure 4.13a, the circulation tends to saturate but doesn't dissipate immediately unlike the swirl suggesting that, while the vortices have slower rotation, they continue to entrain irrotational low density fluid from the crossflow. This is in line with the relatively steady increase in streamwise coherent structure size as demonstrated by the normalized area. The point at which the circulation starts decreasing coincides roughly with the point at which the growth rate of the area drops.

The second mechanism by which the vortex circulation can double is through vortex pairing [113], which would double the circulation even if the swirl of the resultant vortex decreases. While this would necessarily be a step like increase in area and circulation, the intermittency of the location at which this occurs results in a relatively smooth increase of the ensembled vortex area. While both these mechanisms, continuous growth through entrainment and step-like growth through pairing, are responsible for the streamwise variation in circulation and area before the transition point, it is challenging to separate the dominant effect. This led to a lot of ambiguity regarding the source of coherent structure growth in early mixing layer studies [66], since both these processes occur simultaneously. Post transition, the vortices lose their coherence and while coherent structures can still be identified, their growth is attributed to turbulent dissipation by transferring energy to smaller scales. From the cases considered, this transition point can be estimated by looking at the point where the circulation drops and the slope capturing

the growth in vortex area decreases. Between case 2 and case 6 (Figure 4.13b, d), this transition point occurs further downstream as the density ratio decreases. The low-density case 10 (Figure 4.13f) initially shows a large area likely associated with saturated globally unstable vortices which breakdown quickly. The lack of vortex pairing and growth in globally unstable mixing layers was noted by Strykowski [57] and the rapid transition to turbulence was noted in low-density jets in crossflow by Getsinger et al. [51]. These metrics therefore help capture the qualitative behavior noted from the Mie scattering visualizations (Section 4.1).

For the reacting cases considered here (Figure 4.14), the windward and leeward swirling strength variation are similar in growth and magnitude. This is likely due to the suppressive effect of combustion on the windward shear layer and the low growth rate on the leeward shear layer due to the recirculation induced weaker velocity gradient. Between the R1 and NR cases the general structure of the shear layer growth and saturation process appear to be similar. Additionally, it appears that combustion tends to shift the peak swirling strength downstream and consequently reducing the initial value implying a slower growth rate.

The coherent structures on average appear to have a larger size and growth in area compared to the NR cases due to the entrainment of hot combustion products from the windward reaction zone branch. The entrainment of lower density material has an effect of increasing the circulation through the conservation of angular momentum, which would tend to keep the circulation elevated even while the coherent structures are losing rotational coherence. As noted from observing the Mie scattering data (section 4.1) the role of combustion in delaying the transition process is a consequence of the suppression of

secondary instabilities. Here, this can be noted by contrasting the downstream location at which the area growth of coherent structures changes for both NR (Figure 4.13) and R1 (Figure 4.14) cases. Similar to the NR cases, reducing the density of the jet causes the transition location to move further upstream.

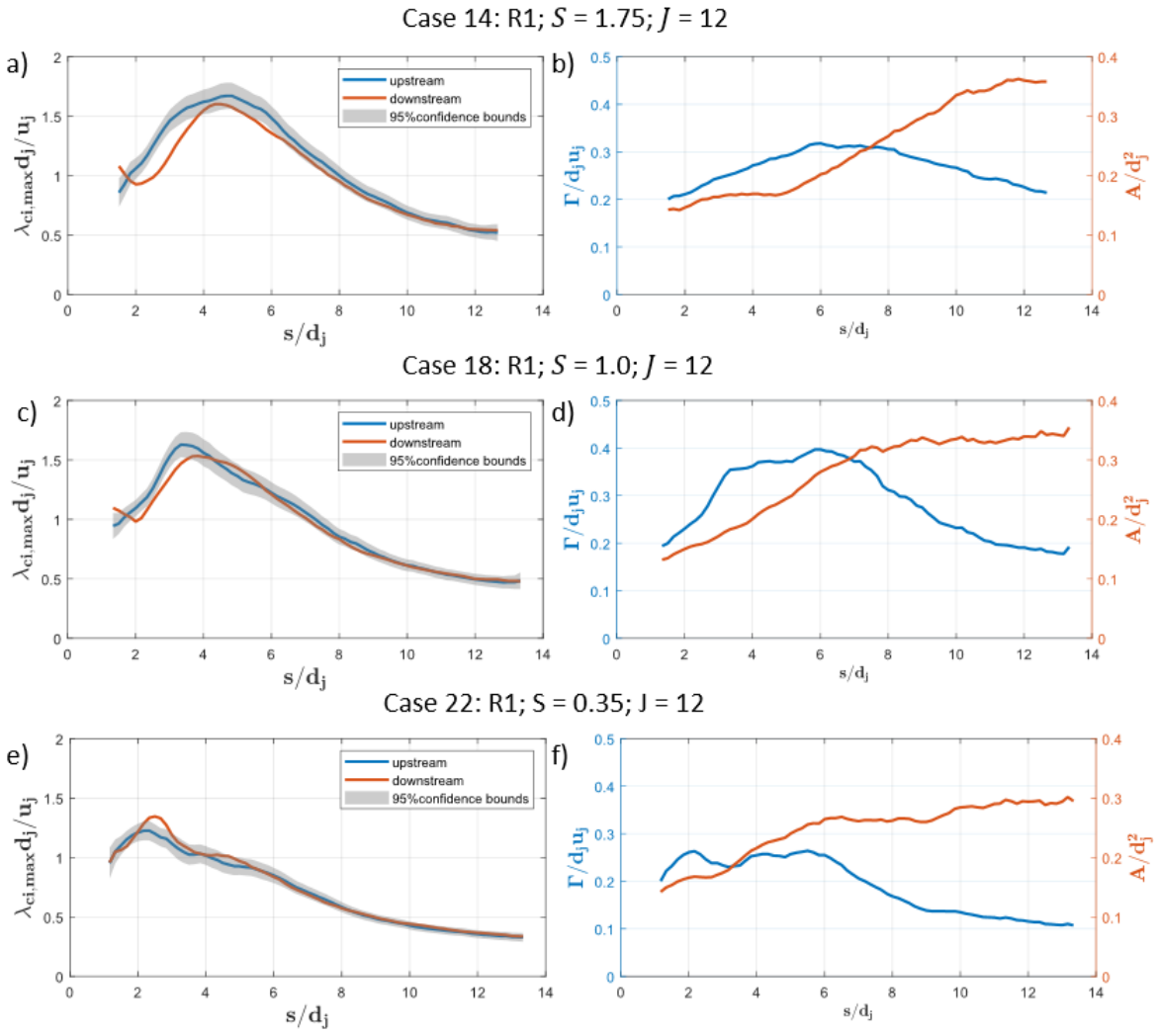

Figure 4.14 Streamwise variation in peak swirling strength ($\lambda_{ci,max}$) for windward and leeward vortices (left) and the streamwise variation in circulation and coherent structure size (right) for three different R1 cases with different S and J = 12.

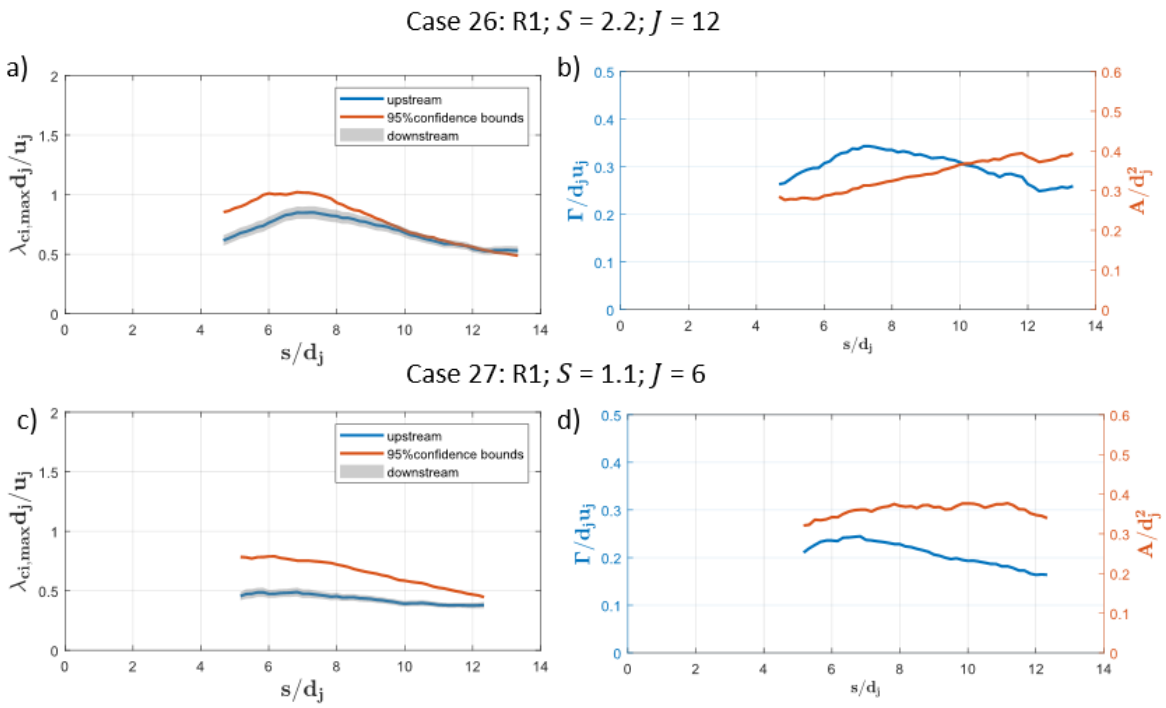

Figure 4.15: Streamwise variation in peak swirling strength ($\lambda_{ci,max}$) for windward and leeward vortices (left) and the streamwise variation in circulation and coherent structure size (right) for two R2 cases.

Finally, considering that the visual dynamics of the R2 cases appear significantly different compared to the other cases, the streamwise variation in their properties is captured in Figure 4.15. For these two cases, the streamwise averages start further downstream due to the lack of coherent structures detected in the near field, resulting in unreliable statistics for these bins. For both the cases, the windward swirling strength appears to be more suppressed compared to the leeward regions which may be a consequence of the absence of the leeward reaction zone branch for $s/d_j < 2$ (Figure 4.8). In general, the swirling strength appears to be substantially reduced, both in magnitude and growth, compared to the NR and R1 conditions suggesting that the time-scales associated with the vortices, when they eventually rollup downstream, are slower.

The circulation contained in the windward structures appears to be considerably larger, compared to the NR and R1 cases, due to the entrainment of the hot combustion products directly into the vortex cores as demonstrated in by the presence of elevated OH-PLIF signal (Figure 4.9e). Consequently, the area is nearly double compared to the NR and R1 cases (note the right y-axis scaling is different in Figure 4.15b, d). As a result, the average vorticity contained within these structures tends to be of similar magnitude between all the three configurations except for the R2 cases, where, the entrainment of hot combustion products results in the larger sized vortical structures. The growth in area of the coherent structures also appears to be continuous with no clear transition to smaller scale behavior, further supporting the hypothesis that the growth of secondary instabilities is suppressed when the primary instability growth is suppressed.

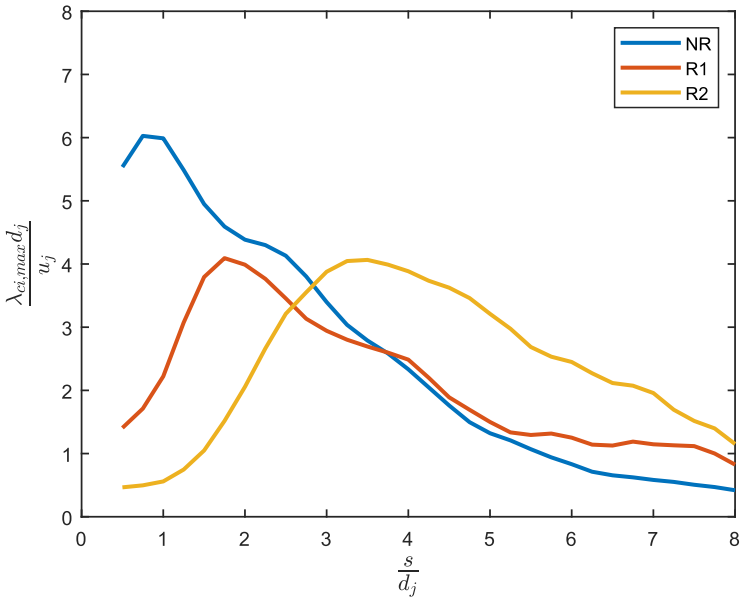

Figure 4.16: Streamwise variation of the peak swirling strength ($\lambda_{ci,max}$) for windward shear layer vortices across the different CFD cases NR, R1 and R2.

4.3.3 Defining the growth rate

The previous section established that the swirling strength is the most appropriate metric that captures the growth and saturation of the shear layer instabilities. To contrast the behavior across all the cases it would be convenient to define a 'growth rate' that captures the qualitative differences in the swirling strength variation with S, J and combustion. Pozirikidis and Higdon [120] demonstrated that even for the simple case of a finite vortex layer, the shape of the overall growth curve is a complex combination of a linear growth process followed by a non-linear saturation process. Fitting such a curve to the swirling strength data would be challenging because there is no empirical scaling available for a complex flow such as this and no simple way to quantify and separate the factors – vortex stretching, turbulent dissipation, etc., that contribute to the non-linear saturation process.

Close examination of the swirling strength variation suggests that the linear and non-linear effects can be captured by observing the initial swirling strength (point 1) and the peak swirling strength (point 2) from the streamwise variation of the normalized swirling strength (Figure 4.17). Since the uncertainty of the data at initial points tend to be high for some cases, a uncertainty threshold is applied to ensure that the initial point (point 1) is chosen from a streamwise location (s) where the uncertainty lies below the threshold.

For example, consider the normalized swirling strength variation for a NR and a R1 case at analogous J and S values (Figure 4.17). The non-reacting case has a higher initial swirl (point 1) which would suggest that the linear growth, here captured by the parameter γ_1, is stronger. For cases that show globally unstable behavior the validity of defining γ_1

is not clear because global instability is associated with no clear spatial amplification and the instability is shown to saturate right from the jet exit [21] corresponding to a theoretically infinite growth rate. Given the limitation of capturing data that far upstream, any extracted growth would be sensitive to the non-linear saturation process since that would govern the initial value of swirling strength measured for this data. Thus, the γ_1 measured for low J and low S conditions represent a conservative lower limit, since these parameter values have been shown to exhibit global oscillations for non-reacting flows [21, 53].

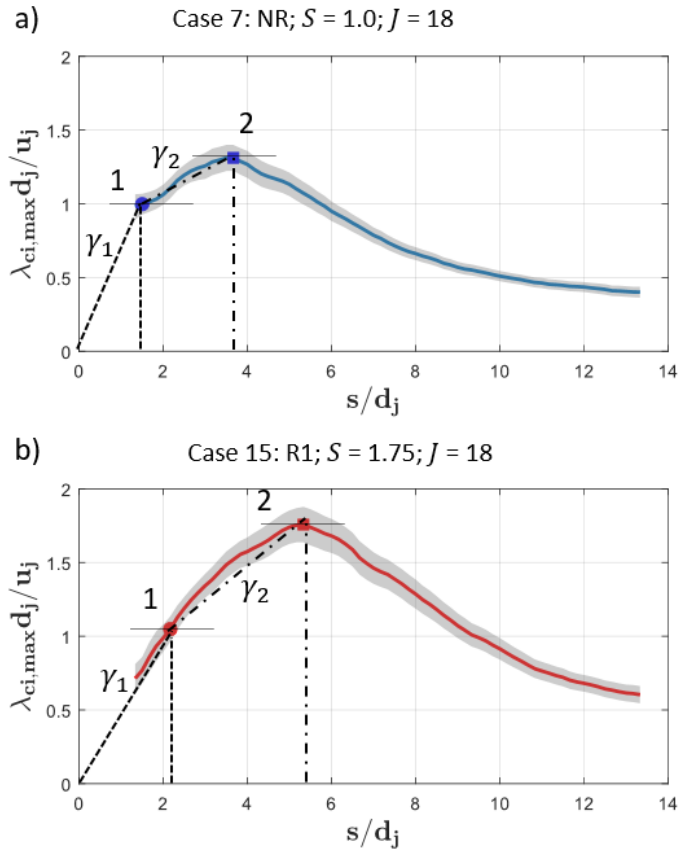

Figure 4.17: Streamwise variation of swirling strength ($\lambda_{ci,max}$) for windward shear layer for a) Case 7: S = 1.0, J = 18, NR; b) Case 19: S = 1.0, J = 18, R1.

Saturation effects can be understood by considering the growth from point 1 to point 2, essentially capturing the degree of nonlinear saturation. For the NR case where the instability quickly saturates, the growth rate associated with this phase - γ_2 would be slower implying stronger saturation effects. The reacting cases on the other hand show slower linear growth but weaker non-linear saturation effects resulting in $\gamma_2 \sim \gamma_1$, which would suggest that the linear growth phase saturates further downstream in the reacting cases.

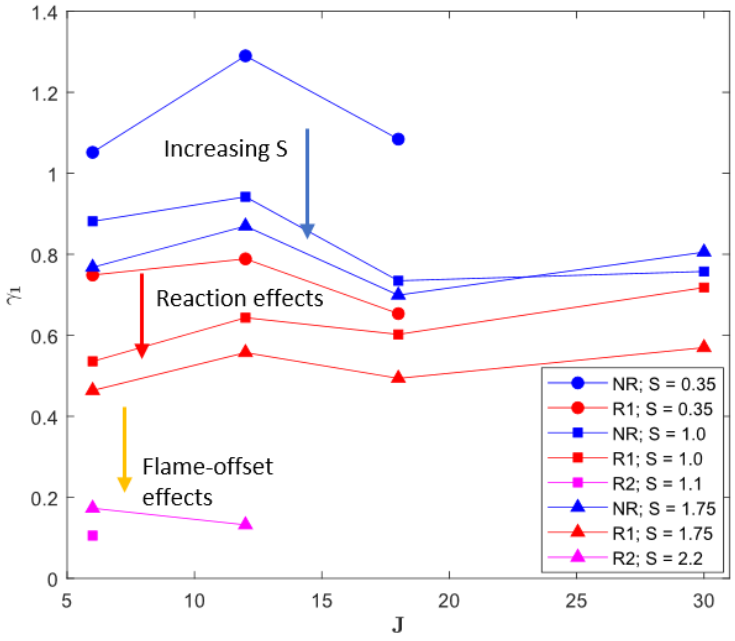

Figure 4.18: Linear growth parameter (γ_1) variation with J; Colors correspond to the flame configuration – NR (blue), R1 (red) and, R2 (purple); Lines connect cases with constant S values as indicated in the legend.

Figure 4.18 captures the variation in the linear growth parameter (γ_1) with S, J and flame-offset. The largest impact on growth rate is the presence of combustion, more specifically, moving the flame inside the shear layer. Between the NR and the R1 cases the effect of combustion is also discernable as all the R1 cases have suppressed growth rates compared to NR cases of corresponding parameters. Lowering S also appears to increase

the growth rate for both NR and R1 cases. This is expected since the linear growth rate in systems where the low-density stream is faster (here the jet), is much higher than for iso-density shear layers. Due to the limited sample set of R2 cases, it is not possible to evaluate whether S has a significant effect on linear growth and, for the cases considered, it is not discernable.

One striking observation is the relative lack of variation of the linear growth rate with J. As discussed earlier, previous studies have demonstrated that reducing J has a strong effect on increasing the spatial growth rate as well as promoting global instability below a critical value. Getsinger et al. [53] further noted that for all cases where $J < J_{crit}$, the jet shows strong global stability but for $S < S_{crit}$, if the value of J is increased significantly the jet can transition back to convectively unstable behavior. Based on the current data, the relationship between the growth rate and J appears to be weak and non-monotonic with a majority of the cases peaking at $J = 12$. For the current study, the variation with S is significantly stronger and is also consistent across all J values, as well for both NR and R1 cases.

This would suggest that J and S, the commonly used jet parameters, cannot uniquely describe JICF stability for both NR and R1 type configurations and a different set of parameters might be required to predict the growth rate. From the perspective of the stability and growth rate of instabilities in mixing layers, the two primary parameters are the density ratio S and the mixing layer velocity ratio Λ [49]. The results here suggest that the relationship between J and Λ is clearly more complex and configuration dependent and is explored in more detail in Chapter 5.

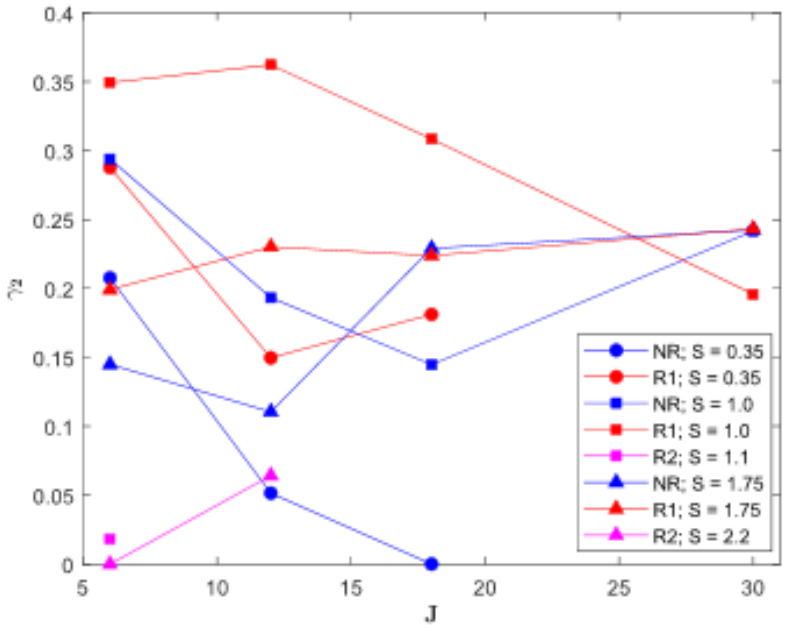

Figure 4.19: Saturation growth parameter (γ_2) variation with J; Colors correspond to the flame configuration – NR (blue), R1 (red) and, R2 (purple); Lines connect cases with constant S values as indicated in the legend.

The variation in the saturation growth parameter, (γ_2) across the different conditions is captured in Figure 4.19. The R1 cases here show a higher growth in this highly non-linear phase compared to their corresponding non-reacting conditions, except for the $J = 30$ cases. Considering the sources of non-linear saturation – the main driving factor in a turbulent flowfield is the saturation due to turbulence driven vortex stretching and the onset of secondary instabilities which destabilizes the primary vortex core. Considering that combustion suppresses both the primary and secondary instability process, the onset of destabilizing secondary instabilities is likely inhibited as well. In addition, the local turbulence level can be correlated with the local Reynolds number, which would be considerably lower in the presence of high-temperature, low-viscosity fluid in the vicinity of a flame. Considering the R1 flame structure, the shear layer is enclosed with a layer of

hot combustion products which promote weaker energy transfer to smaller scales. This effect has been described as a combustion induced 'laminarization' process by some studies based on observations for jet diffusion flames [79].

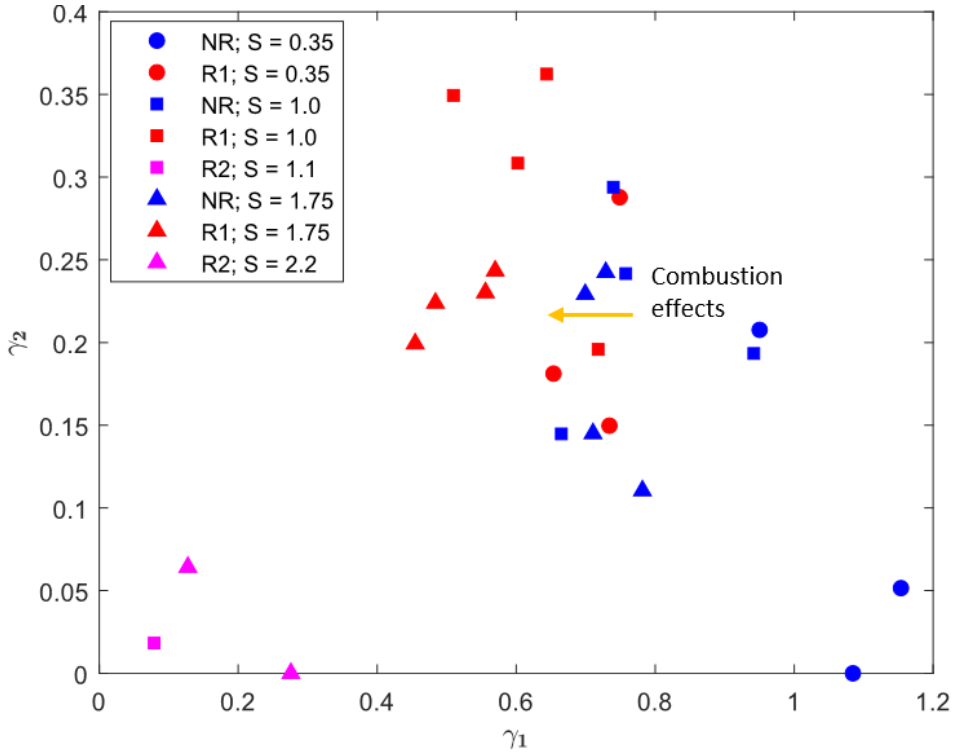

Figure 4.20: Saturation growth parameter (γ_2) scaled with the jet Reynolds number (Re_j) variation with the linear growth parameter (γ_1); Colors correspond to the flame configuration – NR (blue), R1 (red) and, R2 (purple).

The exact contribution from either of these effects is ambiguous since for lower densities, stronger saturation is noted for the NR cases, which can be primarily an effect of stronger growth of the secondary instabilities. While for the R1 cases, where the presence of combustion likely suppresses the onset of secondary instabilities, low density cases show weaker suppression effects, likely a consequence of lower local Reynolds number since here $Re \sim 1/S$. To further investigate whether this saturation effect is driven purely by inviscid mechanisms, i.e, driven by the primary growth rate, or whether the local Reynolds

number plays a role, the non-linear growth parameter (γ_2) is plotted against the linear growth parameter (γ_1) (Figure 4.20). For both the NR and R1 cases it is apparent that γ_1 does have a major effect on the saturation strength since cases with stronger linear growth saturate faster and will have a weaker γ_2. It is interesting to note that there is some clustering among R1 and NR cases. This would imply that there is some impact of the local Reynolds number on this saturation strength and consequently the value of γ_2 for reacting cases. The R2 cases, on the other hand, show lower γ_2 compared to the R1 and NR cases not due to strong non-linear suppression, but due to the highly suppressed linear growth.

4.3.4 Mixing transition and turbulent breakdown

The mixing process in most shear flows can be separated into three phases as postulated by Dimotakis [121] – irrotational entrainment driven by coherent structures (*induction*), turbulent breakdown into smaller scales (*diastropy*) and finally mixing at the molecular level (*infusion*). Typically, most JICF studies which have focused on quantifying these mixing effects have used some concentration metric obtained experimentally (Acetone-PLIF) or by analyzing a conserved scalar in computational studies. The mixing process in the near field is driven primarily by the entrainment of crossflow products into the shear layer vortices while post the mixing transition the coherent structures diffuse, and mixing occurs at a smaller scale. Although concentration measurements are not available for the experiments performed, as the coherent structure play an important role in the mixing process, variations in the mixing process with jet conditions can be inferred from the calculated vortex metrics. The coherent structure area, a metric described in Section 4.3.2, should theoretically capture effects of both the entrainment as well as the transition process.

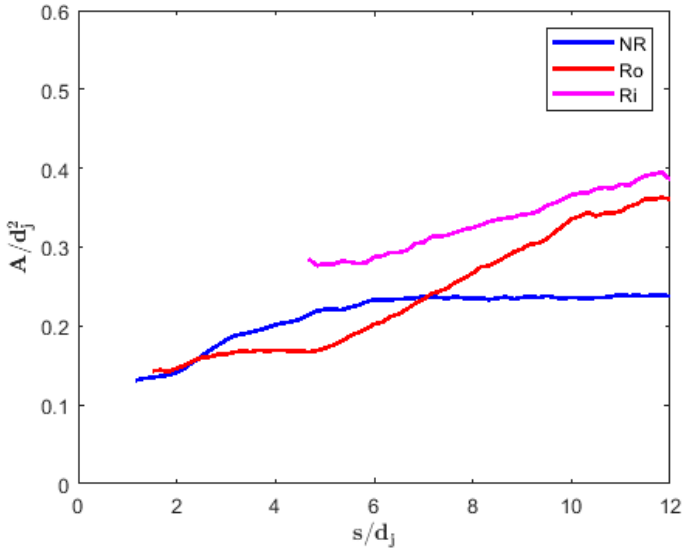

Figure 4.21: Variation of coherent structure area between cases with different flame configurations (NR, R1 and R2) and S = 1.75 (2.2 for R2) and J = 6.

Consider the coherent structure area for three cases (NR, R1 and R2) with analogous J and S values as described in Figure 4.21. Studies [117, 122] have used the area of these structures as a measure of the visual thickness of the shear layer (δ_{vis}) and consequently the area can provide some insight on the local length-scales since $\delta_{vis} \sim \theta$ (momentum thickness). Consequently, since the time-scales associated with the vortex rollup for the NR and R1 cases are similar and considerably faster than the vortex shedding in the R2 cases, the coherent structures are smaller in the near field compared to the larger initial structure size for the R2 cases. While the R1 and NR cases start from similar length scales, as they both grow, the NR case appears to saturate in terms of the area growth around $s/d_j = 7$, while for the R1 case the area increases significantly before the saturation occurs further downstream. The relative differences in coherent structure growth can be tied to the entrainment process in both cases. While the NR case entrains crossflow products and grows, the R1 case entrains hot combustion products from the windward

reaction zone branch and consequently the volume entrainment is significantly higher causing the vortical structures to expand as they advect. In addition, the point at which the area growth abruptly slows for both the cases corresponds to the point at which turbulent breakdown occurs – the mixing transition which as hypothesized before is delayed in the presence of combustion.

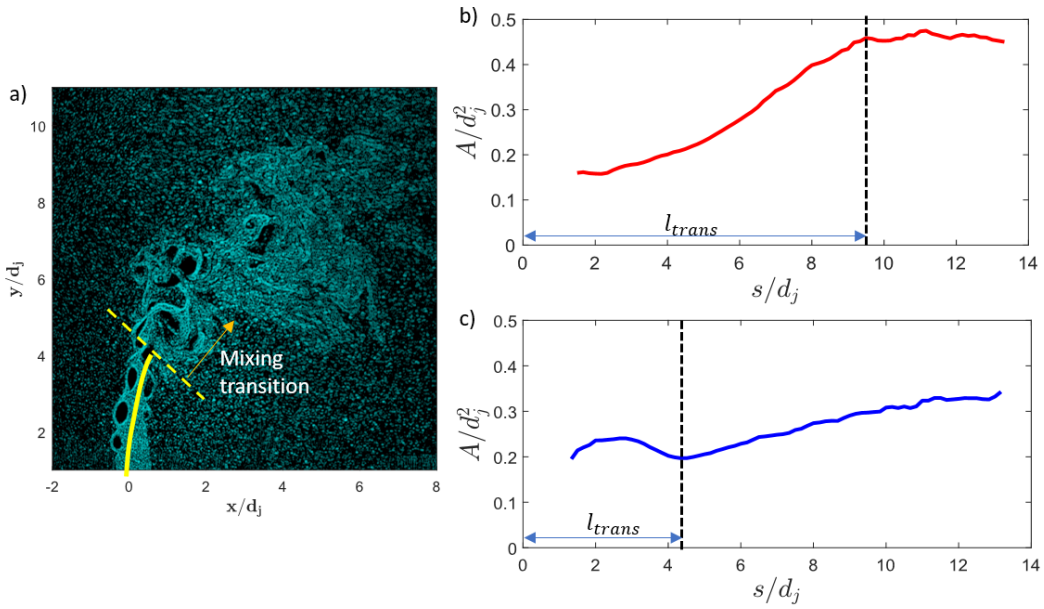

Figure 4.22: a) Instantaneous Mie scattering snapshot showing mixing transition; Streamwise variation in coherent structure area for b) Case 15, *S* = 1.75, *J* = 18, R1 and c) Case 10, *S* = 0.35, *J* = 12, R2.

The mixing transition process can be observed visually (Figure 4.22a) as associated with the breakdown of coherent structures. The streamwise variation of the vortex area, and consequently the change in area growth can be seen to be associated with the rough position at which the breakdown process occurs. Seemingly, post breakdown the vortices no longer grow through irrotational entrainment and as a result form larger coherent structure regions through dissipation or smaller fragments through vortex tearing [113]. As a result, the variability of the vortex size at a streamwise location post transition increases

considerably and the mean growth in area reduces since vortices no longer grow 'on average' in this region. For a vast majority of the cases considered here, which can be categorized as convectively unstable, the spatial amplification of the structure causes the area growth to be higher upstream of the transition region as seen in Figure 4.22b and this point was visually identified to establish the streamwise transition location. For few of the cases which exhibit global instabilities, the vortex area in the near field is large due to the saturation in the size of the shear layer vortices. Here, the breakdown process can be identified as the point at which these saturated structures breakdown from secondary instabilities (Figure 4.22c), and the resultant post transition coherent structures continue to grow through turbulent entrainment and diffusion.

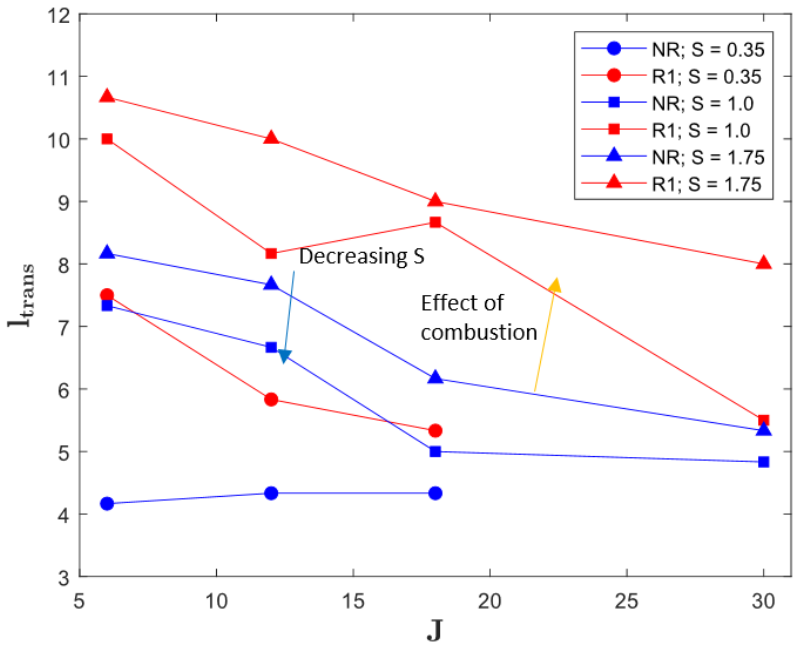

Figure 4.23: Mixing transition length (l_{trans}) variation with J; Colors correspond to the flame configuration – NR (blue), R1 (red) and, R2 (purple); Lines connect cases with constant S values as indicated in the legend.

On visual inspection of all the cases, the transition point can be extracted using the arguments presented in the previous section and the streamwise transition locations (l_{trans}) are presented in Figure 4.23. The R2 cases are not considered as there is no visual mixing transition associated with these cases within the domain. l_{trans} appears to depend on the effect of combustion as well as shows sensitivity to S and J. The figure demonstrates that combustion plays a role in delaying the onset of transition, which as discussed earlier, has been demonstrated in jet diffusion flames. In addition, decreasing the value of S promotes faster transition to turbulence with the globally unstable $S = 0.35$ cases showing the shortest transition lengths.

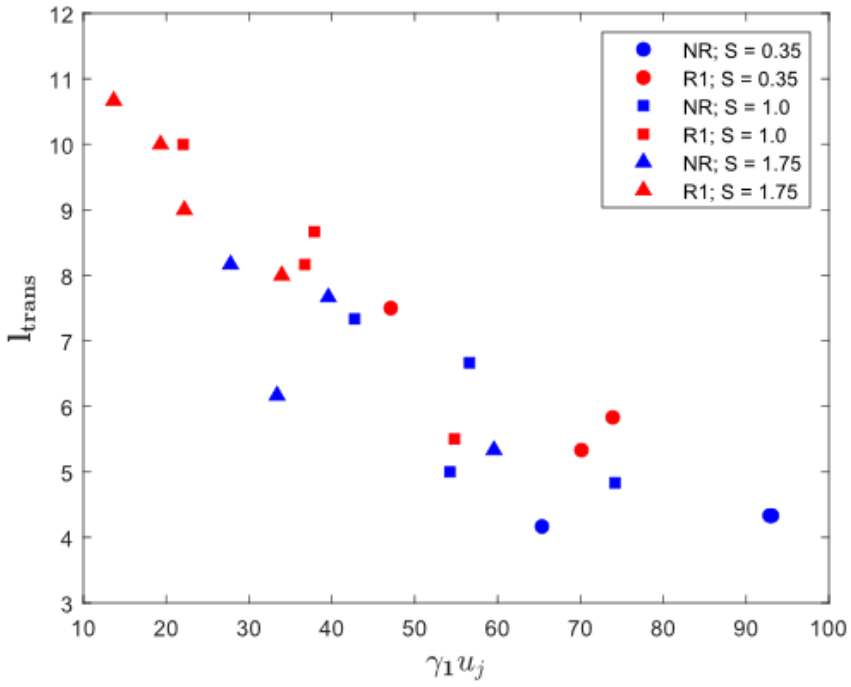

Figure 4.24: Mixing transition length (l_{trans}) variation with $\gamma_1 u_j$; Colors correspond to the flame configuration – NR (blue), R1 (red) and, R2 (purple).

Ultimately, the variation in instability transition length appears to mirror the behavior of the linear growth parameter (γ_1) - Figure 4.18. Cases where the primary instability shows faster linear growth (decreasing S, increasing J and non-reacting) also promote the growth of secondary instabilities. But, since this transition distance would depend on a convective time scale as well, we use the non-normalized (or absolute) growth rate $\gamma_1 u_j$ to demonstrate this correlation (Figure 4.24).Thus, stronger shear layer instabilities promote stronger secondary instabilities, which ultimately stretch out the vortices by moving the energy into smaller scales until they finally reach the viscous scales. This demonstrates that the breakdown process in this scenario depends primarily on inviscid instability mechanisms.

4.3.5 Density gradient driven secondary instabilities

In addition to the shear driven Kelvin-Helmholtz instability (KH), flows with substantial density stratification can exhibit buoyancy driven instabilities like the Rayleigh-Taylor instability (RT) [47]. The strength of buoyancy driven instabilities compared to shear driven instabilities can be captured by computing the Richardson number (Ri).

$$Ri = \frac{-g\left(\frac{\partial \rho}{\partial y}\right)}{\rho\left(\frac{\partial u}{\partial y}\right)^2} \qquad 4.2$$

Observing Eq. 4.2, it becomes clear why these effects were largely ignored from the discussion in this thesis. Firstly, the direction along which the density gradient exists (Spanwise through the shear layer in the near field) is orthogonal to the direction of gravity-induced hydrostatic pressure variation (gravity) and consequently $\nabla\rho.\nabla p = 0$. In addition, a simple order of magnitude estimation of the characteristic velocity and length scales

yields a very small Ri value for most flow velocities considered here, when contrasted with the gravity driven buoyancy effects.

But, on an instantaneous basis, the locally rotating fluid elements in the vortex cores provide a source of centrifugal acceleration which can behave analogously to gravity, creating a radially varying hydrostatic pressure variation [123, 124]. To be able to capture the behavior for a centrifugal Rayleigh-Taylor instability (CRTI), an analogous Richardson number can be obtained by replacing the acceleration due to gravity with the centrifugal acceleration [125] given by the Eq. 4.3.

$$Ri^* = \frac{-\langle\lambda_{ci,max}\rangle^2 r_0 \left(\frac{\Delta\rho}{r_0}\right)}{\rho\left(\frac{u_j}{d_j}\right)^2} \qquad 4.3$$

Here, the centrifugal acceleration can be represented using the rate of rotation of the vortex structure, i.e. its ensembled swirling strength, as well as the radius of the coherent structure ($\langle\lambda_{ci,max}\rangle^2 r_0$). The density gradient is approximated over the vortex core considering the density difference between the fluid contained in the vortex cores with the fluid outside the vortices with the characteristic length scale defined as the vortex core size (r_0). Finally, the inertial scales are obtained using the characteristic velocity and length scales – (u_j/d_j). Interestingly, this is independent of the characteristic vortex size and the centrifugal effects can be captured by considering just the vortex swirl variation. The maximum saturation swirling strength is related to the inertial scales since $\lambda_{ci,max} = cu_j/d_j$ (Section 4.3.2) where c is a constant with a value ~ 1.3 – 1.6. Thus, these scalings

can be used to simplify the expression for the Richardson number, $Ri^* = -\frac{c^2 \Delta\rho}{\rho}$, which provides a conservative estimate of the effect of centrifugal acceleration.

Based on the expression for Ri^*, the Richardson number is primarily dependent on the density difference between the vortex core and the external fluid ($\Delta\rho$). First, we consider the NR conditions where the two density scales can be isolated as the density of the jet (ρ_j), and the density of the crossflow (ρ_∞). This model is complicated by the fact that the vortices continuously entrain fluid from both the jet as well as the crossflow making the density in the vortex core variant with the vortex location along the jet centerline. In addition to this, the fluid surrounding the vortex is not necessarily uniform since they form in the interface between the jet and the crossflow fluid, much like a mixing layer and by the non-isothermal conditions where the temperature gradient can complicate this analysis.

In general, cases where $Ri^* > 0$ will be stable, corresponding to vortices with light cores [124] since $\Delta\rho \sim \rho_j - \rho_\infty$. Thus, the low-density NR cases, $S = 0.35$ will likely be stable to RTI since the vortex cores contain mostly lighter, jet fluid (based on observations by Gevorkyan et al. [46]). For the high-density jet cases, $S = 1.75$, $Ri^* \sim -0.8$ using a similar approach to estimating the density differences as above. It is challenging to use this number to infer whether the flow exhibits any substantial RTI characteristics as there is no clear condition for a vortex with radial stratification and, as noted by Dixit and Govindarajan [123], for a gaussian vortex core shear and density stratification are present everywhere which further complicates the definition of Ri^*.

Now considering the reacting cases, R1, the presence of the flame surrounding the vortex cores complicates the analysis since it provides a local stratification surround the

vortex core with low density high temperature fluid – a naturally unstable configuration. For the R2 cases, the OH-PLIF data suggests that the vortices, when they do rollup in the far field, contain mostly high temperature combustion products, along with the relatively weak swirling strength suggest that this configuration would likely be stable to any RTI instabilities. The peak effect of the centrifugal acceleration is likely at the edge of the vortex cores, for a Lamb-Oseen vortex field this is the radius of maximum azimuthal velocity v_θ. But, since the vortex cores and regions of OH-PLIF signal do not generally overlap in the near field, the region of low-density fluid is likely located immediately outside the vortex cores which was noted to be neutrally stable by Dixit and Govindarajan [123].

Ultimately, neither the density stratification level nor the Mie scattering data, capturing the vortex shapes, suggest any significant non-axisymmetric centrifugal or RTI type instabilities. In general, given the fast time-scales and the weak density gradients along with the presence of no base flow source of acceleration, these conditions are unlikely to exhibit RTI effects compared to the secondary shear driven instabilities caused by azimuthal modes developing on the vortex rings. In addition to this, density stratification cannot solely be used to estimate the significance of body force driven instabilities in a system with strong shearing effects [123]. Temperature/density fields of these instantaneous vortices would be required to make a more definitive conclusion.

4.4 Jet trajectory and unsteady crossflow effects

4.4.1 Mean jet trajectory

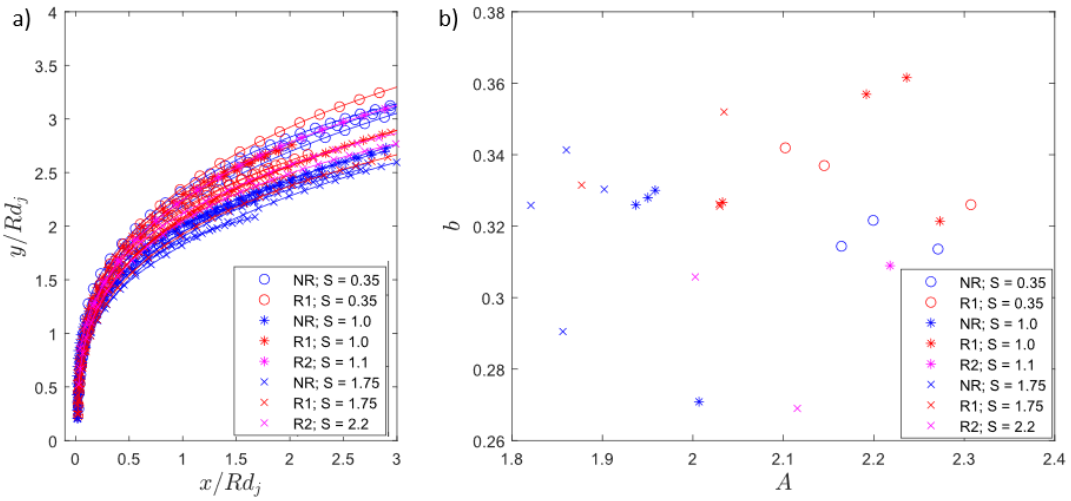

Figure 4.25 a) Scaled trajectories based on the Rd_j scaling across all cases; b) Scatter plot with the different trajectory scaling parameters.

This section focuses on characterizing the effects of 'jet flapping', a consequence of a naturally unsteady crossflow, with respect to the interpretation of the results. To characterize the unsteady effects, the mean jet trajectory is first captured with respect to commonly used scaling laws. Typically, the $J(= R^2)$ dependence of the jet trajectory can be accounted for by using the scaling:

$$\frac{y}{Rd_j} = A\left(\frac{x}{Rd_j}\right)^b \tag{4.4}$$

In the current study, the mean trajectory is defined based on the center streamline of the mean velocity field. Figure 4.25a, shows the jet trajectories across the different cases scaled by Rd_j. These trajectories are fit to the power law (Eq. 4.4) to get the scaling

constants A and b. The empirical form of this scaling essentially comes from modeling the horizontal momentum balance resulting from the entrainment of the crossflow into the jet [17] where the constant $b \sim 0.33$. Figure 4.25b captures the variation in the scaling constants with respect to the different jet density ratios considered.

While the variation in the parameters is quite significant, it is interesting to note that the most of the points lie within the range of observed values for the coefficients, $1.2 < A < 2.6$ and $2.8 < b < 3.4$, given in literature [6]. Muppidi and Mahesh [19] demonstrated that this scaling law ignores pressure and boundary layer effects and thus were insufficient to collapse the trajectories of non-reacting jets. While reacting cases were not shown to show considerably different trajectories compared to their non-reacting counterparts, a majority of the studies making this observation considered primarily high-density jets ($S > 1$) and jets with lifted flames. For iso-density and low-density reacting jets with a similar attached diffusion flame configuration, Wilde [25] demonstrated an increase in the trajectory of the reacting cases compared to the non-reacting ones. In the near field, since the effect of pressure on the trajectory scaling is more dominant [18], the impact of combustion were attributed to the modification of this pressure field in the presence of heat release and increased aerodynamic blockage.

Considering all the cases investigated, it is likely that both entrainment effect as well as the modification of the near field of the jet would have an effect on the validity of the Rd_j scaling law used. If we limit our observation to just the NR S = 1.0 and S = 1.75 conditions, this variation becomes considerably smaller. For the S = 0.35 NR cases, as well as most of the reacting (R1 and R2) cases, the obtained scaling constants suggest a deeper

penetration of the jet. Inferring the impact of density stratification and combustion on the near field pressure is not possible based on the data obtained in the current study. Considering entrainment effects is also challenging because of the lack of information regarding the local density or concentration. Therefore, a more rigorous quantification to develop more accurate scaling models for reacting conditions is beyond the scope of this study. The Rd_j scaling is sufficient to quantify the unsteady crossflow effects observed in this study as elaborated in the next section.

4.4.2 Unsteady crossflow effects

To quantify the effect of jet flapping, it is necessary to quantify the jet trajectory on an instantaneous basis. To do this, the scaling constants A and b, as obtained from the mean trajectory, are used along with Eq. 4.4. Since the instantaneous velocity fields are highly turbulent and the streamlines, being two-dimensional projections onto the plane of interrogation, would not be expected to follow the mean jet trajectory. Consequently, for a given flowfield snapshot t_i, the two preceding (t_{i-2}, t_{i-1}) and subsequent snapshots (t_{i+2}, t_{i+1}) are ensembled to obtain an averaged velocity field $(\tilde{x}(t_i), \tilde{y}(t_i))$. The instantaneous jet centerline is obtained by using the trajectory of the center streamline from this averaged field $(\tilde{x}(t_i), \tilde{y}(t_i))$ for a given snapshot t_i. The measure of the instantaneous jet trajectory (J_i') can be obtained through a linear fit of Eq. 4.4 using the coordinates of the center streamline. This averaging process is unlikely to smear out fluctuations significantly, since the time-period of flapping $(\sim 16\, ms)$ is over ten-times longer than the time-period over the current averaging process $(\sim 1.25\, ms)$.

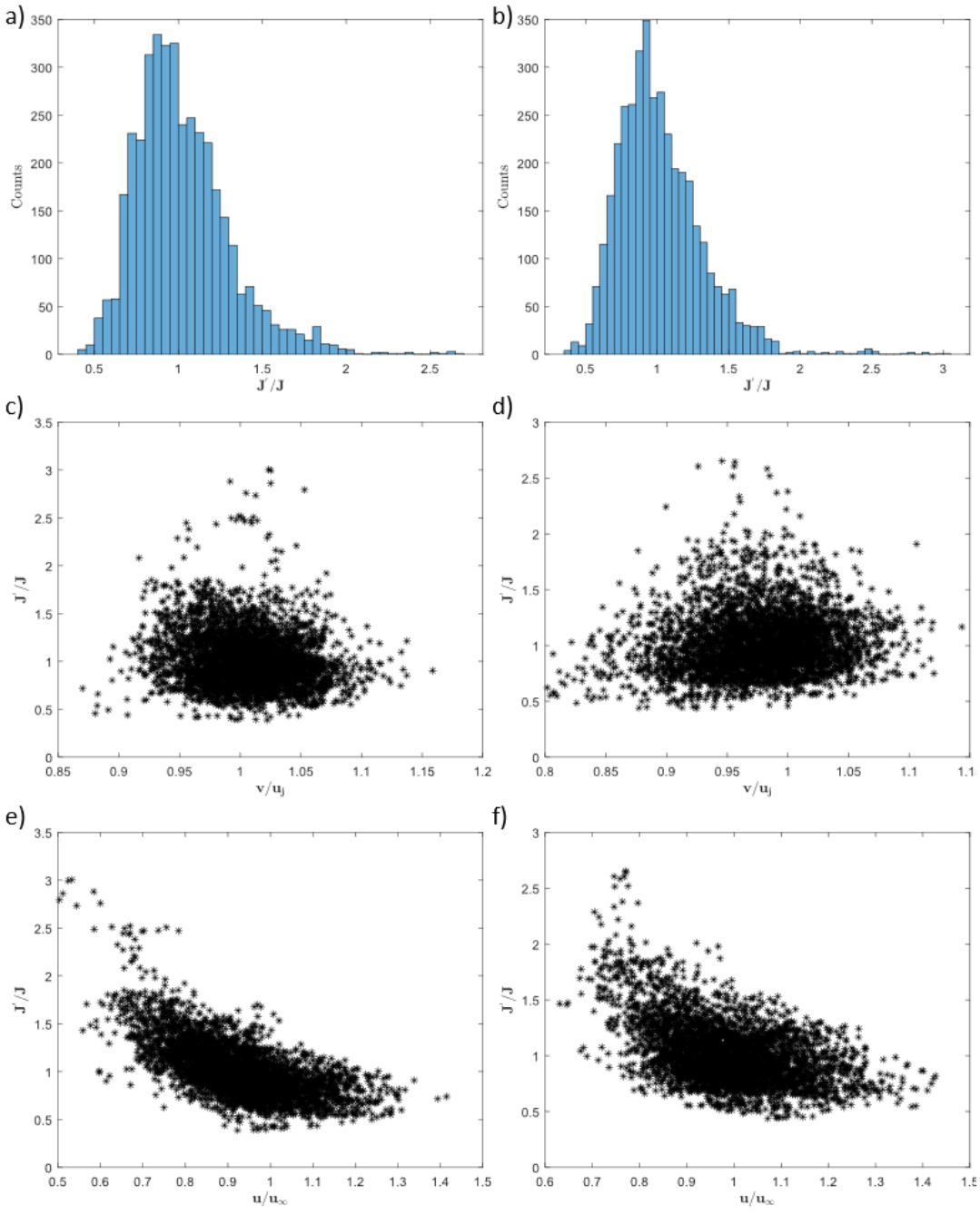

Figure 4.26 (a, b) Histogram of extracted J' showing variation of the instantaneous jet trajectory; (c, d) Correlation between J' and the vertical velocity in the jet core (v); (e, f) Correlation between J' and the horizontal velocity in the crossflow (u).

The resulting statistics of J', for two selected cases are plotted in Figure 4.26. The histogram depicts that the variation in J' resembles a log-normal type distribution which would be expected since $J' \sim u^2$. Since the parameter J' merely captures the effect of jet flapping by fitting the instantaneous centerline, a wide variation is expected in the current turbulent flowfield. To understand the factors that contribute to this jet flapping behavior, we plot the correlation between the instantaneous J' as well as the instantaneous vertical velocity $v(t)$, sampled from the probe location $y/d_j = 2.0$, as well as the instantaneous crossflow velocity $u(t)$, sampled from a location sufficiently downstream of the jet, in the core flow. The plots (Figure 4.26) indicated that the parameter J' is effectively uncorrelated with the horizontal velocity in the jet core but shows some correlation with the instantaneous horizontal velocity in the crossflow. Thus, the instantaneous horizontal velocity effectively sets the instantaneous shape of the jet trajectory, J'.

Although the crossflow here is not actively forced, the horizontal velocity scale shows a reasonably high amount of variation suggesting that combustion in the vitiator is augmenting the unsteadiness in the crossflow through some level of acoustic coupling. In such a scenario the injector velocity is directly coupled with the phase of the crossflow oscillations since the velocity through the injector is a function of the pressure drop across it. Wilde [25] demonstrated that, depending on whether the spatial location of the injector lies at a pressure node or anti-node, the effects of natural crossflow acoustics can exacerbate the flapping phenomena. In addition, assessing the dependence of the jet velocity on the flapping phenomena is further complicated by the convective timescale of the jet. This essentially means that a pocket of fluid with an instantaneous momentum exiting the jet nozzle will take a finite time to penetrate through the crossflow and

consequently, if there was an impulse change in the jet velocity, it would take a finite time for it to alter the entire trajectory. Assessing the dependence of this possible time-lag is not possible in this study as it would require carefully controlling the phase of both the jet and crossflow velocity fluctuations through acoustic modulation.

4.4.3 Impact on ensembled metrics

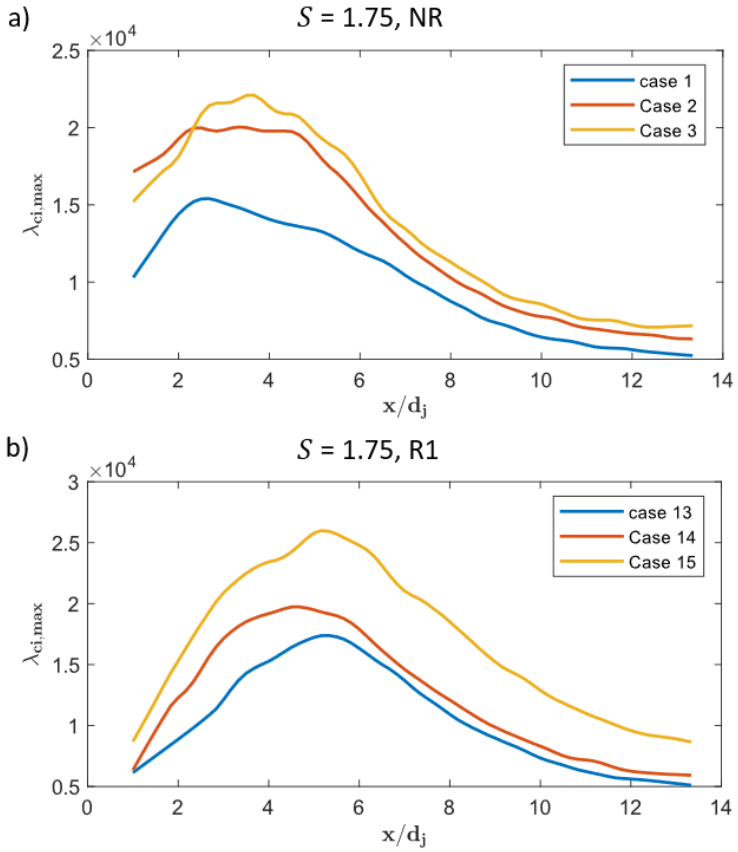

Figure 4.27 Vortex swirling strength variation for two jet compositions: a) *S* = 1.75, NR and b) *S* = 1.75, R1

The main purpose of quantifying the variability in the jet trajectory is to assess the impact it has on the calculated vortex metrics and the conclusions made in the previous sections. To assess the trajectory effect, for a given jet composition (for example: NR, *S* =

1.75), the swirling strength variation is calculated conditioned on the instantaneous J' value. In Figure 4.27, this conditioning was applied to all instantaneous snapshots with $10 < J' < 15$ for two different jet compositions. Note that the y-axis does not have the normalized swirling strength unlike all the other plots presented in this chapter. Consequently, the intensity of the captured swirling strength appears to scale only with the jet velocity scale $\lambda_{ci,max} \sim u_j$. This further supports the observations made in the previous section where the shape of the trajectory was not a function of the instantaneous u_j and therefore all the trajectory variation was causing, is essentially changing the path along which the generated vortices were advected.

Further, given that the instability strength and shear layer behavior is primarily determined by the shear in the near field of the jet, the shear strength variation would primarily depend on u_j. The flapping is not likely to significantly alter the instability characteristics, although a time-varying crossflow velocity scale might have an effect on vortex evolution in the far field. This idea that the stability behavior is primarily a function of the velocity characteristics, including the shear strength, only in the near field is an extension of the counter-current shear layer (CCSL) model which will be explored in more detail in Chapter 5.

4.5 Summary of key findings

This chapter focused on characterizing the structure and stability characteristics of reacting jets in crossflow across multiple J, S and flame configurations. The raw Mie scattering data and OH-PLIF intensity data was used to assess the differences between the structure of the NR, R1 and R2 cases by observing the qualitative behavior of the shear

layer vortices. The observations suggest that decreasing S stimulates faster rollup with stronger vortex cores for both NR and R1 conditions. The effect of combustion appears to have a different effect between the R1 and R2 cases. For the R1 cases, the shear layer dynamics appear to be qualitatively similar to the NR conditions, albeit slightly suppressed. For the R2 cases, the topology of the JICF appears to be significantly different with the complete absence of SLV structures in the near field shear layer.

Understanding the effects of combustion is aided by the discussion of the reaction zone structure for the different jet compositions and flame positions. While the reaction zone configuration between the R2 and R1 cases is radically different, since the flame is moved inside the shear layer, subtle variations in the jet composition can significantly change the stoichiometric mixture fraction (f_{st}). This leads to small changes in the windward reaction zone branch but can lead to significantly different stabilization locations in the leeward shear layer. Since the current study focuses on the windward shear layer characteristics, the subtle differences in the windward reaction zone branch can be ignored while interpreting the impact of combustion for the R1 or R2 cases.

Characterizing the stability characteristics of the different RJICF configurations is performed by identifying coherent structures and extracting ensembled metrics related to the strength of these structures - peak swirling strength, vortex circulation and vortex area. The vortex swirling strength provides a good estimate of the instability growth in the near field shear layer and consequently a growth rate can be defined based on its spatial variation in the near field (γ_1) as well as the location of peak swirl (γ_2). The extracted growth rate shows that decreasing *S* increases the spatial growth rate while the presence of combustion

suppresses γ_1 between analogous cases. The R2 cases further showed a significantly suppressed growth rate in line with the qualitative observations made.

In addition to the growth rate, the mixing transition can be characterized by tracking the coherent structure size as a function of the downstream distance. The location of the transition point, shown to be related to the growth of secondary instabilities, is shown to be well correlated with the growth rate of the primary instability growth rate for most cases and relatively insensitive to the local Reynolds number. This allows for further insight into the structural characteristics observed in low S jets. Finally, the unsteadiness in the crossflow and its impact on the jet trajectory are quantified and the relationship between the causes for 'jet flapping' investigated. The results show that flapping is driven primarily by variations in the crossflow velocity while shear layer stability characteristics are more sensitive to the jet velocity scales and consequently, the effect of flapping was deemed to have a small effect on the interpretation of the vortex metrics.

CHAPTER 5. FREQUENCY CHARACTERIZATION AND NEAR FIELD DYNAMICS

The previous chapter discussed the basic structure of the reacting jet and crossflow and extracted metrics related to the shear layer behavior such as the growth rate and transition to turbulence. This chapter attempts to characterize the temporal behavior across the different conditions considered to understand the frequency characteristics and instability behavior. Due to the high frequency nature of the shear layer instabilities, the 40 kHz time-resolved SPIV data is analyzed and the results presented in this section. While these experiments were conducted non-simultaneously with respect to the 4 kHz diagnostics, the test conditions evaluated as a part of these experiments are similar to the test conditions evaluated in the previous chapter except for the $J = 30$ data points, which are dropped due to potential aliasing effects. The measured test parameters for these experiments are documented in Table A-3.

The chapter begins with qualitative flow visualization demonstrating the shear layer behavior through sequential snapshots of the instantaneous Mie scattering data and corresponding vorticity fields. The next Section, 5.2, presents the transverse velocity spectra extracted from the windward shear layer and discusses the absolute/convective instability classification for these instabilities. Section 5.3 utilizes Proper Orthogonal Decomposition (POD) to extract the mode shapes and spatial coherence relevant to the dominant frequencies. Finally the counter current mixing layer model, as introduced by Iyer and Mahesh [58], is explored in Section 5.4 as a potential technique to map the

traditional JICF parameter space (J, S) to a different space governed by the mixing layer parameters and help reconcile the observed stability behavior.

5.1 Instantaneous velocity data

The shear layer vortices are formed from the rollup of the near field shear layer due to the K-H instability. This rollup process and the highly rotational strength of the formed vortex cores causes the particles to be centrifuged out and appear as regions devoid of seed particles in the Mie scattering images. Thus, flow visualization of these centrifuged vortex cores, along with the processed vector fields, can provide important insight regarding the nature of the shear layer instabilities. In Figure 5.1, a sequence of four snapshots of the flowfield for two non-reacting cases are contrasted. The flowfield snapshots show streamlines corresponding to the in-plane velocity components (u, v) and associated out of plane vorticity ω_z, normalized with respect to the flow time scale u_j/d_j, denoting windward (red) and leeward (blue) shear layer structures. Case 5 ($J = 6, S = 1.0$) shows strong vortex rollup behavior characterized by clear pattern of period structures and large vortex sizes –indicating stronger instability strength. Case 3 ($J = 18, S = 1.75$) shows relatively weaker rollup behavior as indicated by the smaller vortex size, despite the larger jet velocity scale, and shear layer growth through vortex pairing. This is in line with observations from previous studies on non-reacting jets which note that for $J < 10$, jets tend to show globally unstable behavior characterized by stronger instabilities while for higher J and S values, the shear layer instabilities tend to be convectively unstable – weaker and more susceptible to vortex pairing.

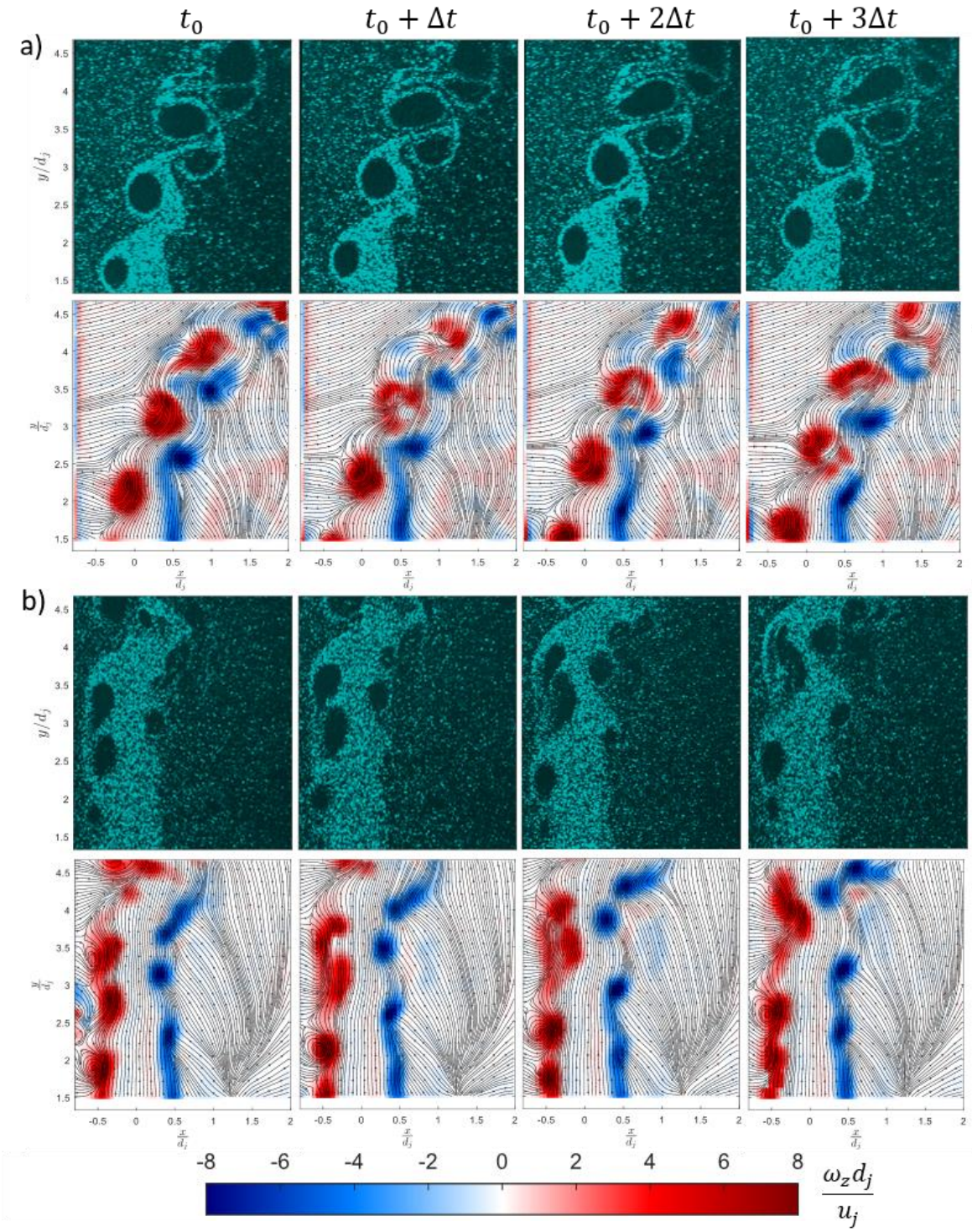

Figure 5.1: Sequential snapshots of Mie scattering (top) and Vorticity fields (bottom) for a) Case 5: J = 6, S = 1.0, NR and b) Case 3: J = 18, S = 1.75, NR.

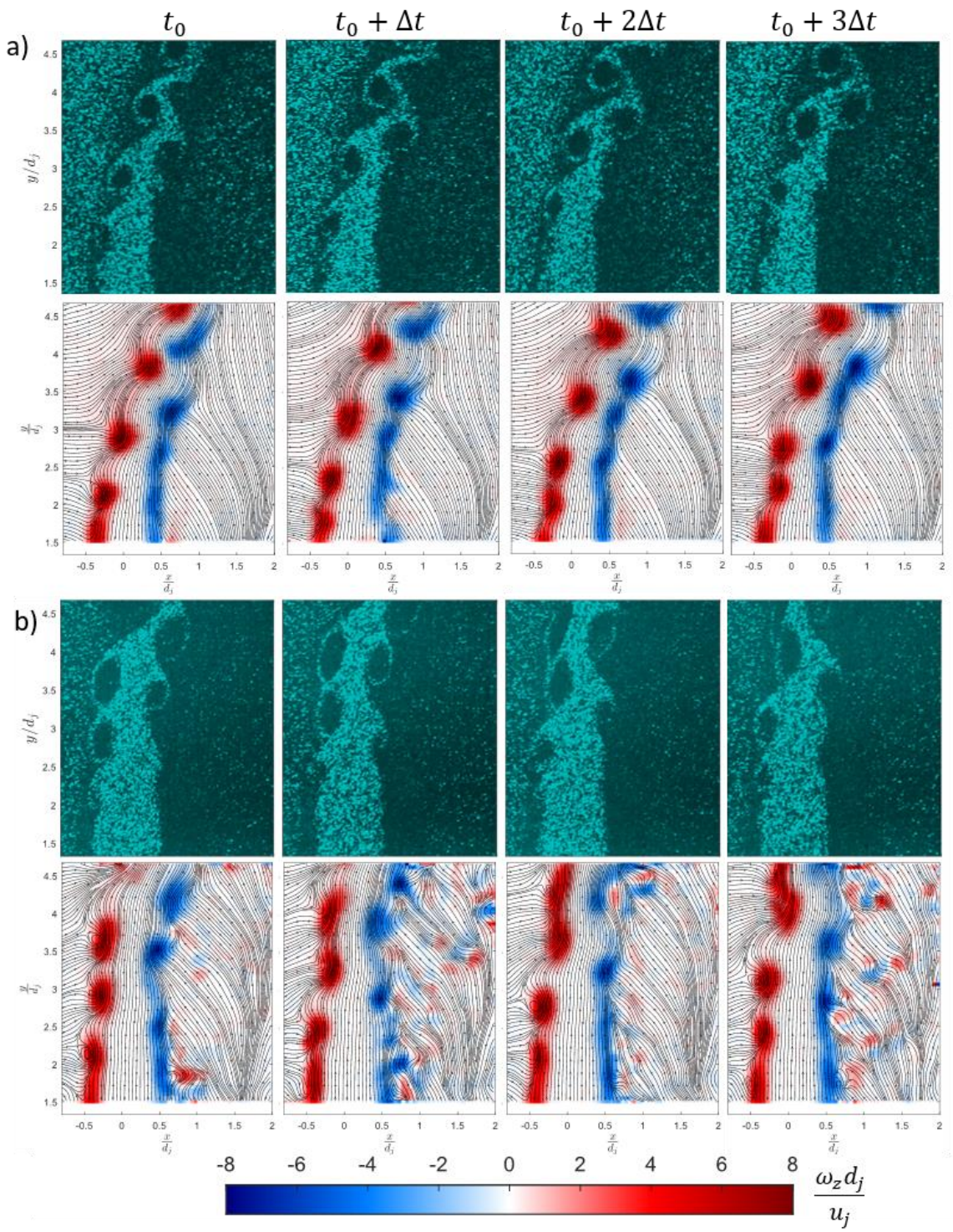

Figure 5.2: Sequential snapshots of Mie scattering (top) and Vorticity fields (bottom) for a) Case 14: J = 12, S = 1.75, R1 and b) Case 19: J = 18, S = 1.00, R1.

The reacting cases, R1 (Figure 5.2), show qualitatively similar shear layer behavior as demonstrated by the presence of vortical regions in the windward and leeward shear layers. As the flame position for this case lies outside the shear layer, the flame front is wrinkled by the advecting vortical structures. On average the strength of rotation for the reacting cases appear to be lower as characterized by smaller regions of centrifuged seed particles among cases with analogous velocity scales as NR cases. In addition, the onset of shear layer rollup is relatively suppressed as observed in previous reacting flow studies [84]. The wake of the jet shows significantly lower seed density due to the diffused nature of the leeward flame structure and presence of hot combustion products as indicated by the OH-PLIF measurements made on H_2/N_2 jets in similar JICF configurations [28, 84].

The second reacting configuration considered here, R2 (Figure 5.3) has a dramatically different shear layer structure compared to the other two cases - NR and R1. Here, the rollup of the shear layer structures appears to be completely suppressed on moving the flame inside the shear layer. The presence of vortical regions of high rotation are completely absent in the Mie scattering images and consequently the vorticity data indicates that it is comprised primarily of shearing motion and has not been aggregated into vortical structures. In addition to the relative suppression of the instability rollup mechanism these observations suggest that the flowfield has a significantly different flow topology. The vorticity magnitude also appears to be comparatively reduced which is due to the fact that it has not rolled up into vortical structures. These observations are similar to the flow visualization observations made by Chen et al. [81] who noted the absence of vortical structures where the flame was moved inwards with respect to the shear layer.

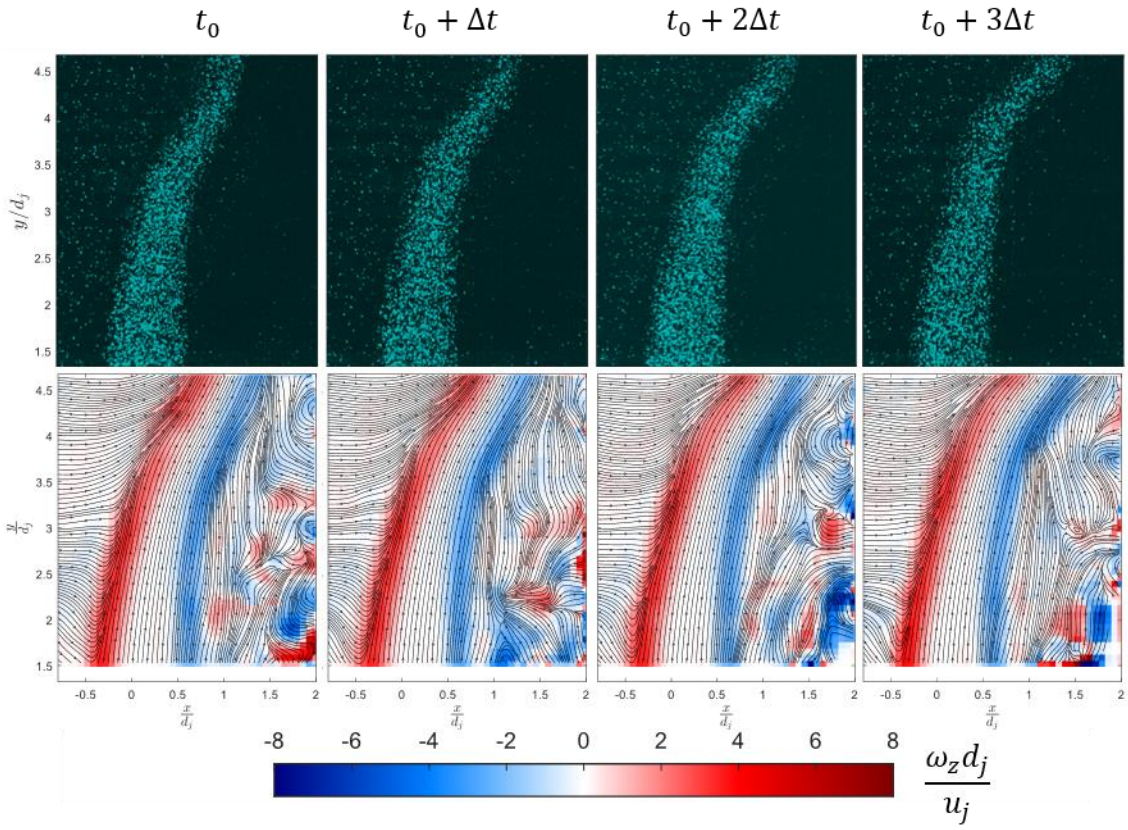

Figure 5.3: Sequential snapshots of Mie scattering (top) and Vorticity fields (bottom) for Case 27: J = 6, S = 1.1, R2.

While the Mie scattering and associated vorticity data provide important evidence of qualitative changes in shear layer behavior across different J, S and flame configurations and capture major topological changes, it is challenging to solely use flow visualization to comment on the instability nature (absolute/convective) and strength. The correlation between the vortex size and instability strength is also complicated further by the finite time-scale over which the particles are centrifuged from the vortex cores [98]. This results in ambiguity regarding whether the vortex cores are getting larger (with downstream

distance) due to a spatially growing instability or due to the residence time (from the onset of rollup) over which the observations are made.

5.2 Frequency dynamics

Analyzing the frequency characteristics of the velocity data in the shear layer is essential to extracting the dominant characteristic natural frequencies (*St*) as well as classifying the instability behavior (globally vs convectively unstable). Previous studies focusing on characterizing the behavior of non-reacting jets utilized hot-wire anemometry (HWA) to extract the natural frequencies across different J [21] and S [53] values. In addition to quantifying the spectra and obtaining the characteristic non-dimensional Strouhal numbers, $St = fd_j/u_j$, they also tracked the variation in the spectral behavior along the jet-oriented streamwise coordinate (*s*) and consequently demonstrated clear variations in the spectral behavior of globally unstable and convectively unstable shear layers. A similar approach is employed in this study where velocity data, obtained from SPIV, is extracted from the shear layer and is used to quantify the spectral behavior and characteristics.

5.2.1 Transverse velocity fluctuations

Due to the orientation of the shear layer along the plane of symmetry and considering the dominant direction of vorticity - ω_Z, the unsteady streamwise velocity (with respect to the crossflow) u' and the transverse velocity v' will both show strong spectral content corresponding to the SLV structures while w' will likely be significantly weaker. Here, the transverse velocity spectrum v' is chosen, as the choice of reference

velocity scale (u_j) straightforward since the measurements are made in the shear layer and $v' \sim u_j$.

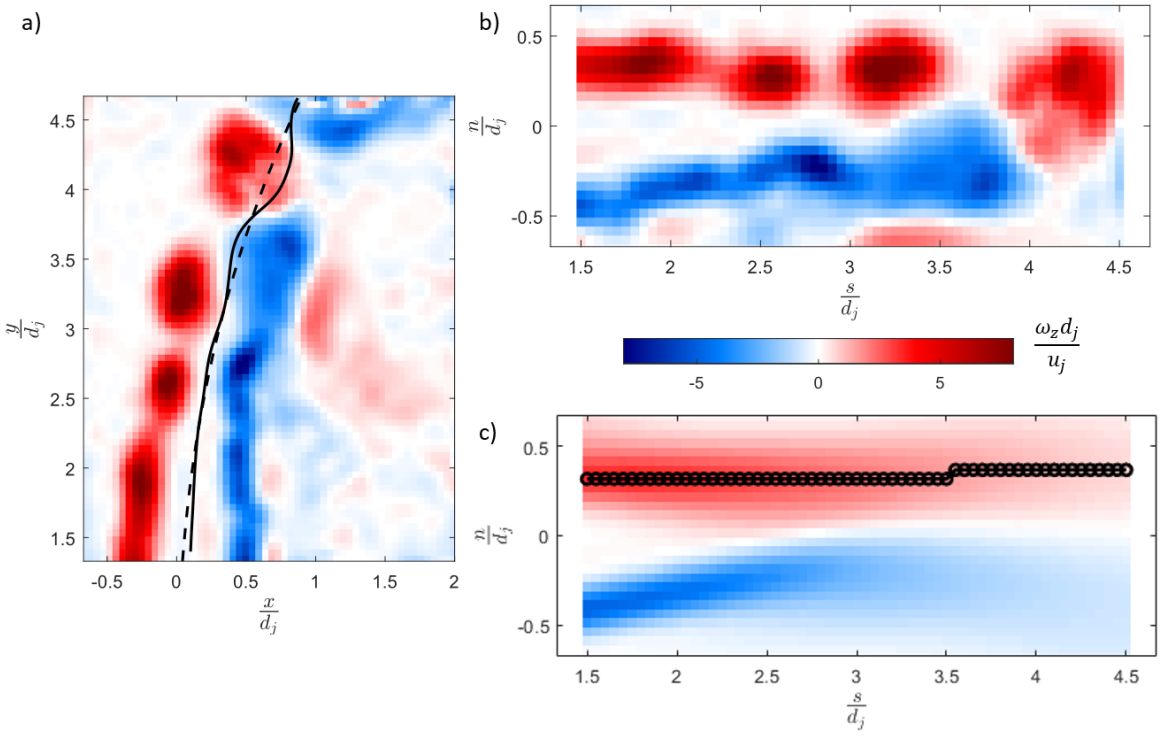

Figure 5.4: a) Instantaneous normalized out of plane vorticity field in cartesian (x, y) coordinate system with denoted center-streamline ('solid line'') and fit of approximate trajectory ('dashed line''); b) Instantaneous vorticity field in (s, n) coordinate system; c) mean vorticity field with markers ('o') demoting sampling points along the windward shear layer where the spectra is obtained – data from Case 6: J = 12, S = 1.0, NR

To compensate for large-scale jet flapping, the points extracted along the shear layer need to be conditioned with respect to the jet trajectory. This is especially necessary for reacting cases (R1), where jet flapping would result in probe points fixed in the laboratory frame of reference (*x*-*y*) to sample velocity data from inside the flame intermittently, despite the flame lying outside the shear layer. The instantaneous data in the cartesian coordinate system (*x*-*y*) (Figure 5.4a), is converted to a jet-oriented trajectory

system (*s*-*n*) (Figure 5.4b). As the instantaneous vector fields do not have a well-defined potential core and consequently, the center-streamline is not guaranteed to follow the 'mean' jet trajectory, a pseudo-instantaneous jet trajectory is computed from the mean velocity field taken from 7 sequential vector fields centered around each instantaneous snapshot. Due to the high time-resolution of the vector data, the time period across which this average is computed (~ 175 μs) is still significantly lower than the time-period of jet flapping (~ 12.5 ms) and therefore would still be effective in conditioning the instantaneous data with respect to the jet trajectory.

The sample points are chosen based on the mean trajectory of the windward shear layer in the (*s*-*n*) coordinate system (Figure 5.4c). The windward shear layer is chosen as its behavior, including the transition to global instability, is highly sensitive to changing J and S values [126].This can be attributed to the significantly sharper velocity profile at the windward leading edge, as opposed to the leeward shear layer where the velocity gradient is significantly weaker due to the recirculation zone in the wake of the jet. As a result, while the windward shear layer undergoes significant qualitative changes when transitioning to global instability, the leeward shear layer will continue to show rollup behavior similar to a convectively unstable shear layer. This is a likely consequence of the region of reverse flow that is present upstream of the windward shear layer, which can act as a driver for global instability [58], while no such region of counterflow exists in the leeward region. This idea of treating the windward shear layer as a counter-current mixing layer will be explored further in Section 5.4.

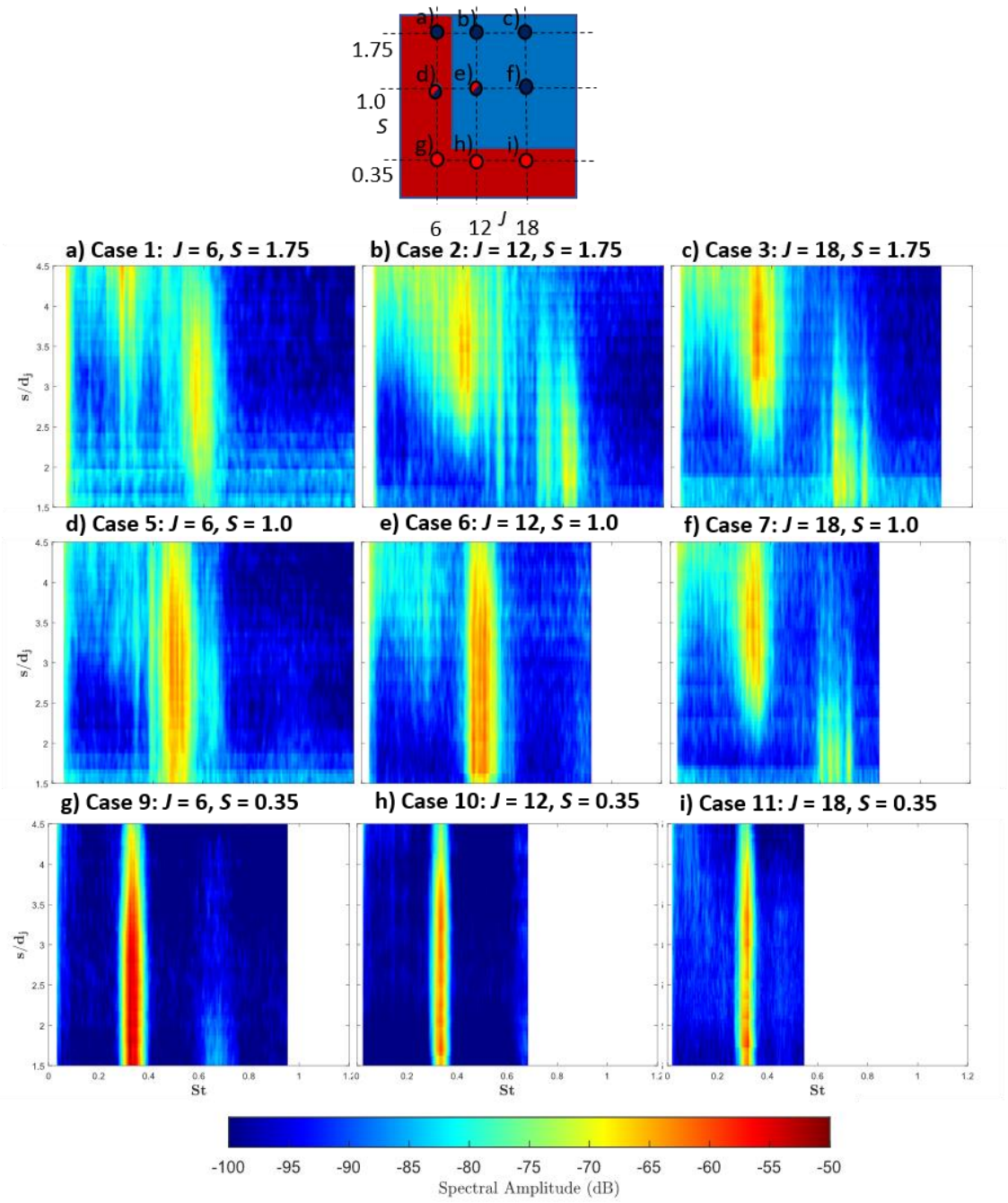

Figure 5.5: Transverse velocity spectra for the NR cases – plots show spectral amplitude (colorbar) tracking the dominant *St* values at different locations along the jet coordinate system (*s*); The schematic maps the parameters of the explored cases with the global – convectively unstable transitional parameter space with respect to (J, S) [21, 53]; Blue – convectively unstable behavior, Red – globally unstable behavior and Semi-filled (Red/Blue) transitional behavior

The spectral content is sampled along these probe positions and is presented as a contour plots of spectral amplitude (dB) where the abscissa contains the Strouhal number calculated with respect to the characteristic jet length and velocity scales, $St = fd_j/u_j$, and the ordinate represents the streamwise location along the jet. To provide some perspective on the expected shear layer behavior, the current study test matrix parameters are mapped onto a stability diagram based on the critical parameters (J_{crit} and S_{crit}) for absolute to convective stability transition from previous studies [21, 53].

First considering the non-reacting cases, the spectral behavior is presented in Figure 5.5. For cases 1,2,3 and 7, the initial shear layer mode in the near field ($s/d_j < 3$) shows a multiple broadband frequency peak around St = 0.7-0.8. The amplitude of this mode soon saturates and is replaced by a stronger subharmonic instability at half the frequency. This is in line with the characteristic behavior of convectively unstable cases noted in previous studies where the initial higher harmonic is weaker and the presence of the subharmonic indicates vortex pairing in the far field, a non-linear effect of vortex interactions in flows without strong global modes [57]. Within flows that show convectively unstable behavior, the relative comparison between the fundamental and the subharmonic is a function of the jet parameters as observed by contrasting the spectrum from Case 1 and Case 3 where for Case 1 the higher frequency fundamental persists much further along the jet before the subharmonic becomes dominant. This convectively unstable behavior has not been observed for jets with J < 10, but the previous non-reacting studies only explored S variations from low density to iso-density ($S \leq 1.0$) conditions suggesting that the stability criterion cannot be extrapolated for higher density cases ($S > 1.0$). Alternately, this suggests that JICF stability cannot be uniquely captured by only J and S.

The spectral characteristics of the convectively unstable cases is in contrast to the spectrum of case 9, 10 and 11, which show a strong singular tone through the entirety of the domain at a lower characteristic frequency (St = 0.35 - 0.4). The lack of subharmonics is a consequence of the lack of vortex pairing, an observation made by Strykowski and Niccum [57] for the case of low density jets showing globally unstable behavior and similarly demonstrated for non-reacting JICF [21]. These cases are classified based on the presence of global modes (red) or convectively unstable spectra (blue) and mapped onto the stability parameter space at the top of the figure to contrast the observed characteristics with early stability limits. The presence of higher harmonics caused by the strong global mode which were noted in the previous studies was largely absent here, except for case 9, due to the inability to capture frequencies higher than 20 kHz.

In addition to cases that can be classified relatively unambiguously, some cases – Case 6 and Case 5 (Figure 5.5d, e) show the evidence of a single fundamental tone, but the normalized amplitude is nearly an order of magnitude lower (compared to cases that can be classified as globally unstable), and the presence of broadband signal in the subharmonic region at high s/d_j , suggests intermittent behavior characteristic of points, which would lie in a transitional region between the stability maps and are denoted by semi filled circles.

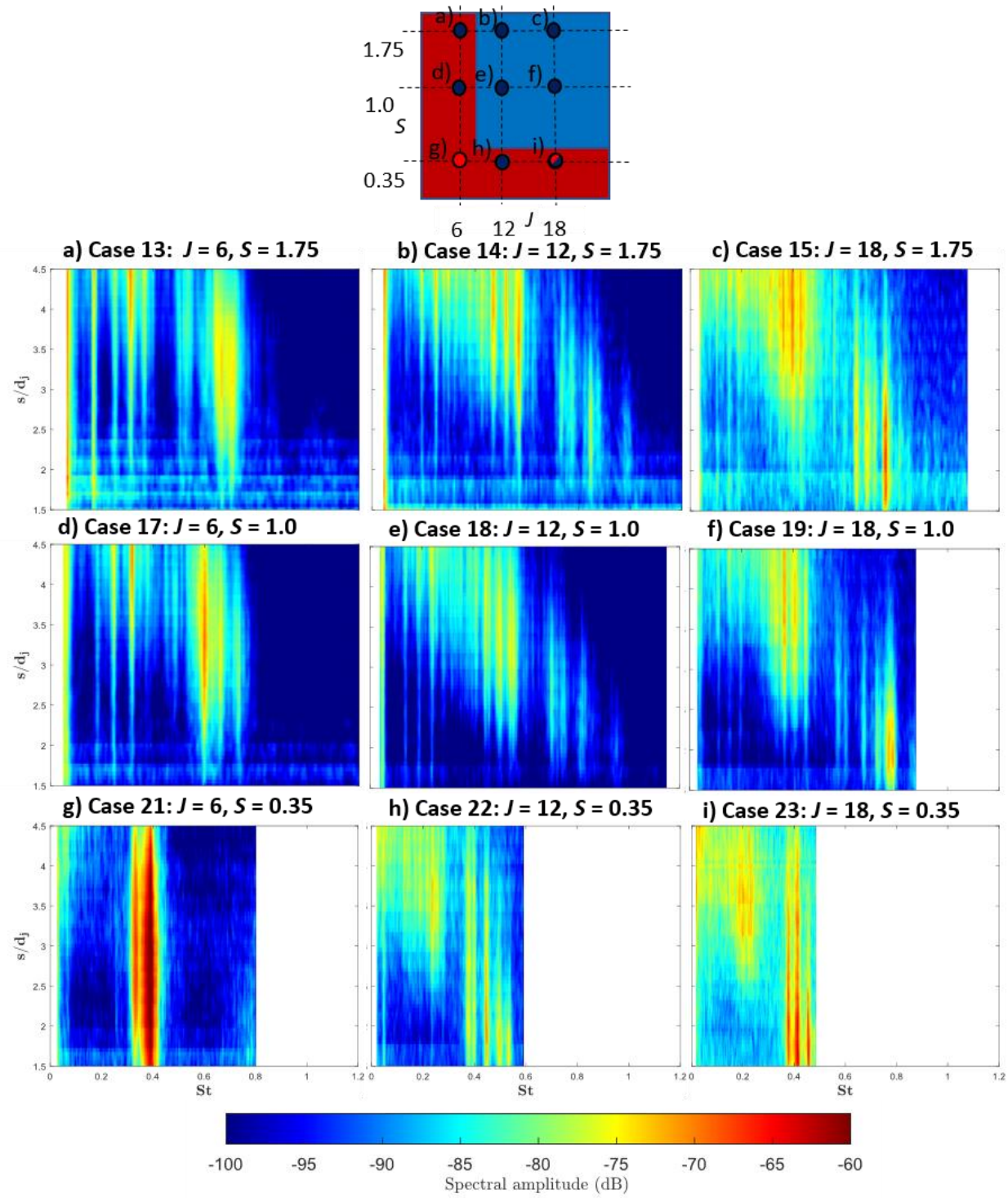

Figure 5.6: Transverse velocity spectra for the R1 cases – plots show spectral amplitude (colorbar) tracking the dominant *St* values at different locations along the jet coordinate system (*s*).

The reacting configuration R1 is considered next. Like the NR conditions, the Mie scattering images showed qualitatively similar high-frequency vortex shedding behavior (Figure 5.2) which is further represented by the presence of high-frequency content in the spectral plots. Comparison of similar cases shows the effect of combustion on broadening the spectra (Case 1 - Figure 5.5a vs Case 13 - Figure 5.6a) and in some cases altering the transition from a global narrowband mode to a more diffused 'convectively unstable' spectra with strong subharmonic content (Case 6 - Figure 5.5c vs Case 18 - Figure 5.6b). Of the reacting conditions considered here, only a single case (Case 21) showed the presence of a strong global narrowband mode, albeit at a lower normalized amplitude (Figure 5.6) compared to the equivalent NR mode. The other low density ($S = 0.35$) cases showed transitional (Case 23) and convectively unstable (Case 22) characteristic spectra. The remaining cases showed significant subharmonic content and weaker high frequency content in the near field including cases that based on non-reacting jet parameters (J, S) have shown global modes. In general, the reacting cases show systematically weaker spectral behavior which is expected based on the reduced growth rate of the coherent structures as covered in the previous chapters.

As mentioned in the introduction, the suppressive effect of combustion of combustion on instability rollup has been well documented. But, for most studies with a similar flame configuration – a diffusion flame outside the shear layer [70, 91] - this effect has been demonstrated to be primarily due to the density stratification caused by the high-temperature flame and not due to the direct interaction of heat release with vorticity (through the gas-expansion term). Consequently, the dominant parameter in addition to the velocity ratio, or in this case J can be considered to be the density ratio between the flame

and the jet, $S_f = \rho_j/\rho_f$ and not S. Since $\rho_f < \rho_\infty$, S_f will be larger for analogous jet and crossflow conditions between NR and R1 cases and will lie further into the convectively unstable region on the (S_f, J) parameter space. This hypothesis will be further explored in section 5.4 as a part of the counter-current mixing layer model.

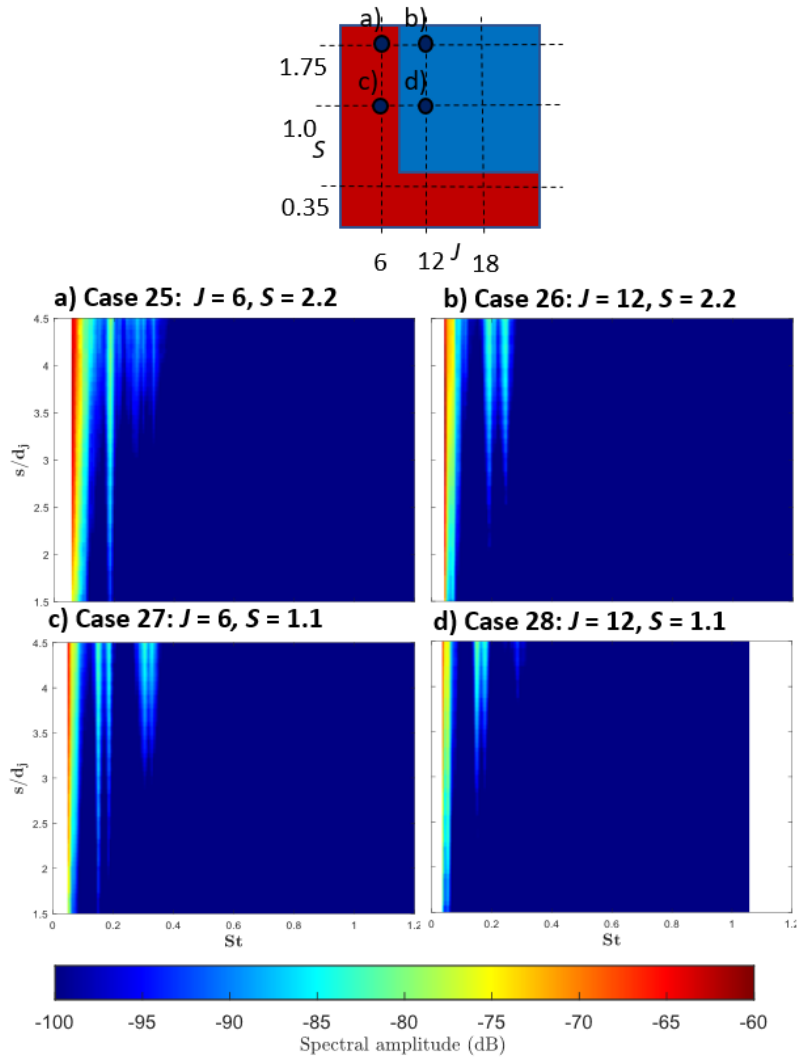

Figure 5.7: Transverse velocity spectra for the R2 cases – plots show spectral amplitude (colorbar) tracking the dominant *St* values at different locations along the jet coordinate system (*s*).

Finally, cases corresponding to the R2 flame configuration as expected showed significantly reduced instability magnitude for the detected tones as demonstrated in Figure 5.7. This is in line with the qualitative observations, which indicated a significantly suppressed shear layer rollup which is a function of the instability growth. In the far field, the vortex rollup length scale is significantly longer than that observed from analogous NR and R1 cases resulting in a significantly lower Strouhal number for cases with similar convective velocity scales (u_j). There is some uncertainty in determining the dominant frequency, as the presence of lines with comparable signal to noise ratio (SNR) are adjacent to one another.

The presence of sub-harmonic bands generally stronger than the fundamental suggest that the subharmonic modes likely form the dominant length scale of vortex spacing when they rollup in the far field. Another striking feature is the significantly lower noise floor for the spectra because while the lower threshold of the power spectra is set at a value of -100 dB, similar to the R1 and NR plots, there is significantly more noisy spectral content across all frequencies. One possible reason for this is that the R2 cases were processed with larger PIV interrogation window sizes, which would have an aliasing effect with respect to high-frequency instabilities (Section 3.2.1). While this might affect the energy contained in the high-frequency end of the spectrum it doesn't explain why there is why the noise floor at lower frequencies is also significantly lower.

The qualitative behavior and the spectral content suggest that the R2 cases that heat release has a significantly different effect apart from simply imposing a density stratification on the base flow. While there are likely multiple contributing factors of moving the flame inside the shear layer, one factor to consider is the closer collocation of

the flame region and the shear center compared to the R2 cases where the flame naturally lies outside and thereby behaves as a boundary condition to the shear layer. This idea was echoed by both the only other studies to manipulate the flame position. Chen et al [81], hypothesized based on qualitative flow visualization that the collocation of heat release with the shear center would result in the suppression of peak vorticity and consequently instability growth rate. Furi et al. [77] attempted to quantify the momentum thickness and suggest that the differences in the shape of the velocity profile can be related to the differences in local viscosity – with R1 analogous cases having lower temperature at the shear center than cases where the flame was moved inside (R2). This theory in particular has merit in supporting the idea of 're-laminarization' in the presence of combustion [115]. While this phenomena is likely present in the R1 cases as well, the closer collocation for the R2 cases will result in a much smaller equivalent Reynolds number $Re_\theta \sim 1/\nu$, since ν will be significantly higher if the flame is collocated with the shear layer. In addition the velocity in the inner edge of the shear layer is likely accelerated strongly due to hear release in the R2 cases as opposed to the R1 cases where the effect is more likely to be passive and due to the entrainment of hot gases into the shear layer. This mechanism, through heat release [127] or strong flow acceleration [128], has been hypothesized to cause 're-laminarization' as well for numerous flow configurations.

5.2.2 Subharmonics and vortex pairing

While the spectral information provides important insight into the dominant frequencies present in these flowfields, the exact source of these different instabilities in the flowfield and their manifestation is unclear. In addition, it is not apparent immediately if any of the spectral peaks are aliased due to the fundamental mode being present outside

the sampling range. To further gain insight into the frequency dynamics, characteristic length and time-scales of the flowfield can be obtained from vortex tracking (Section 3.6.3). Given the high level of time-resolution with respect to the convective time-scale, these vortical structures can be identified and tracked across consecutive flowfield snapshots until they advect out of the domain (Figure 5.8). The resultant data can be compiled in to *s*-*t* plots (Figure 5.8) to extract corresponding Strouhal numbers and vortex spacings across all the sampled vortex histories. Similar *x*-*t* plots have been used to evaluate the coherent structure behavior in mixing layers [117, 119] as well as axisymmetric quiescent jets [114]. The dominant Strouhal number will correspond to the most probable time-scale of vortex passing, which can be sampled at any streamwise location (Figure 5.8b, c) within the domain, providing physical evidence of the presence of frequency content extracted from the transverse spectra.

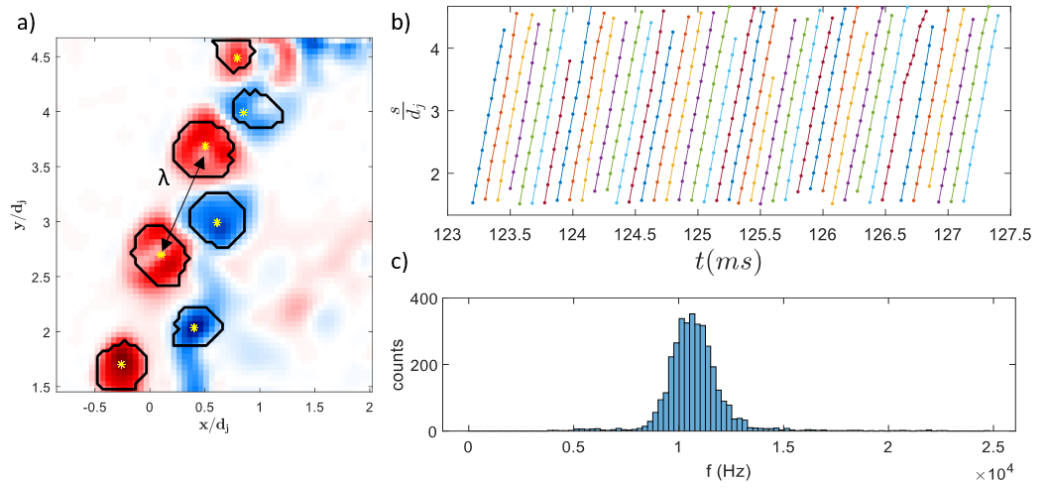

Figure 5.8 a) Instantaneous vorticity snapshot for Case 6: J = 12, S = 1.0, NR showing detected boundaries of vortical structures ('solid line') and characteristic vortex spacing (λ) b) *s*-*t* plots shown vortex time-histories and c) Histogram of characteristic time-scale of vortex passing as sampled at s/d_j = 3.

For example, consider the two cases contrasted in Figure 5.9. Case 3, which based on the transverse spectra, was classified as showing convectively unstable behavior and the *s*-*t* plots (over a small time-sequence) shows that a considerable number of trajectories end before the end of the domain which shows evidence of vortex pairing. For Case 9, nearly all the vortex trajectories end closer to the edge of the domain suggesting that most vortices that rollup persist through the domain without pairing. The probability distribution of vortex frequency scales, as calculated by the passing frequency at a given *s* coordinate, shows the relative intermittency of the vortex pairing process in Case 3, where although the subharmonic has a stronger peak (Figure 5.9e) the number of vortices passing at the fundamental is higher. For the cases with the global mode, the periodicity in the shedding process is apparent, since a majority of vortices are found solely at the fundamental global mode. Naturally the weak presence of higher harmonics, as indicated in the near field of the spectra Figure 5.9f, cannot be captured by looking at the vortex passing frequency since the higher harmonics do not manifest through physical interaction mechanisms. Exceptions to this would be vortex tripling [66], where two vortices interact to give three structures, and tearing [117], when a single vortex gives rise to two smaller structures. No evidence of either of these events has been documented within the domain of this data set, although it is only likely to occur during the turbulent breakdown process.

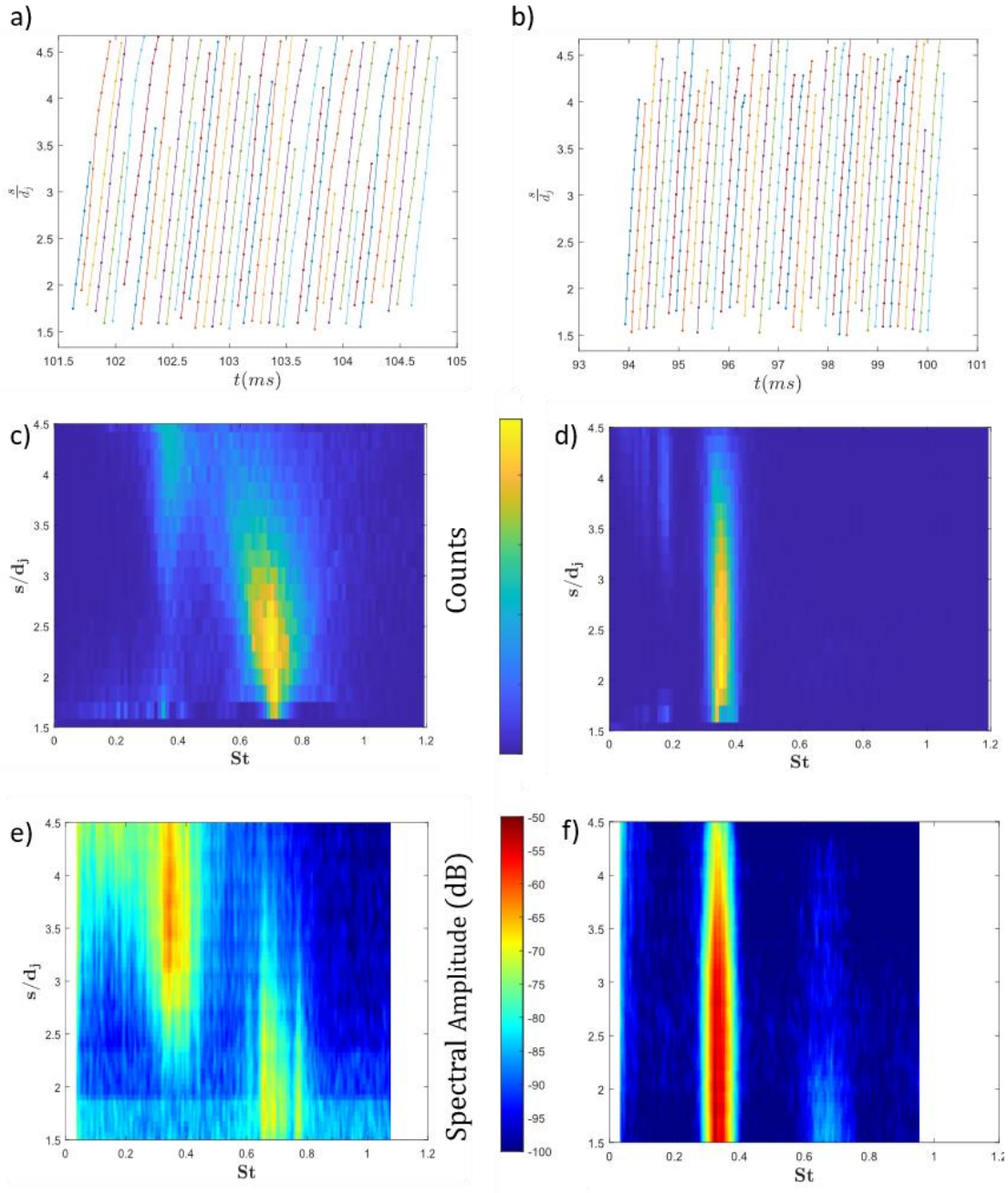

Figure 5.9: *s-t* plots (top), probability map showing vortex counts of each St number at different streamwise coordinates (s) (middle) and associated transverse spectrum (bottom) for (a, c, e) Case 3: J = 18, S = 1.75, NR and (b, d, f) Case 9: J = 6, S = 0.35, NR

5.2.3 *Strouhal number scaling*

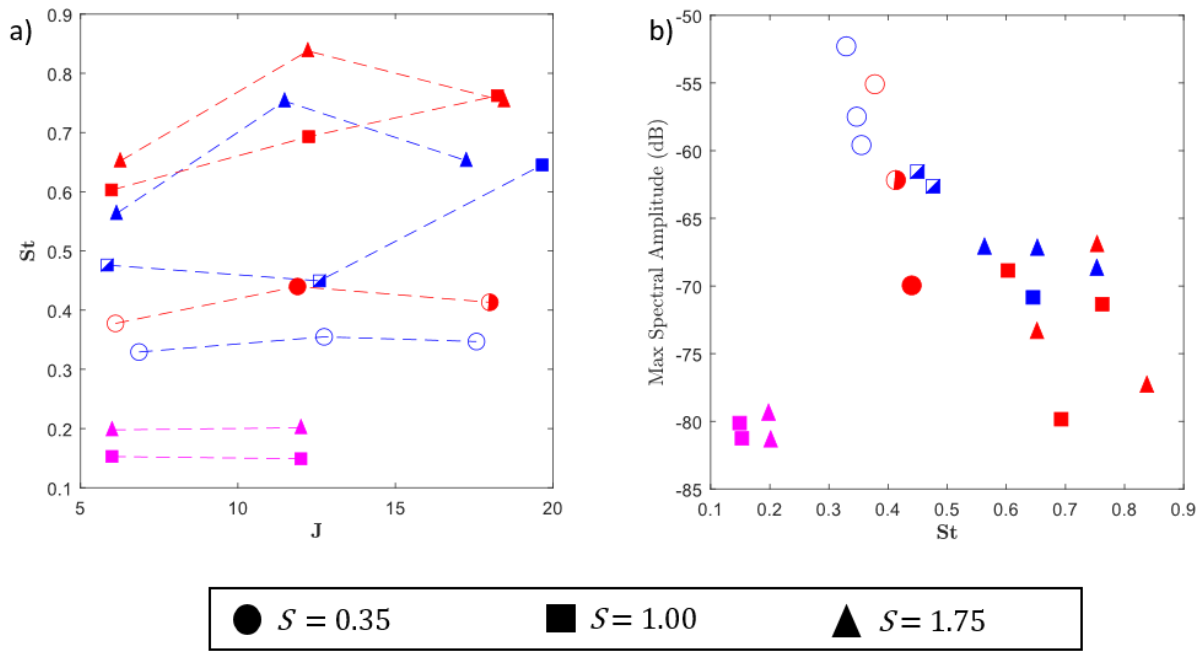

Figure 5.10: a) Characteristic Strouhal numbers plotted with *J*, line connect points at constant target *S*; b) Spectral amplitude plotted with respect to the Strouhal number of associated fundamental mode; Blue points – NR, Red points – R1 and Magenta points – R2. Filled markers indicate convectively unstable behavior, Empty markers indicate global instability while half-filled markers indicate transitional behavior. For R2 *S* = 1.0 markers were used to represent cases with *S* = 1.1 and similarly the markers for *S* = 1.75 correspond to *S* = 2.2

Using the most probable vortex passing frequency helps to estimate the characteristic timescales with relatively less ambiguity especially among cases that show multiple broad peaks – typically the convectively unstable cases. The fundamental St is extracted through inspection by choosing the dominant high-frequency mode in the spectra (Figure 5.9c, d) which corresponds to the most probable vortex frequency scale as determined from the histograms (Figure 5.9e, f). These extracted frequencies are plotted with respect to their measured J and S values in Figure 5.10a. For the high - S cases the NR and R1 cases show similar dependence on J that was documented by Getsinger et al. [53] for NR jets with

across different S values showing a peak in characteristic frequency (St) at approximately $J \sim 3.5$. Similarly, the decrease in St with reduction in S was qualitatively captured by observing that the $S = 0.35$ cases, NR and R1 have significantly lower St values. The lower observed frequencies for the R2 cases are a consequence of the suppression of vortex rollup. For these cases, the rollup occurs significantly further along the jet where the thickness of the vorticity layer is sufficiently diffused and θ, the momentum thickness, is consequently larger thereby controlling the governing time-scales of the vortex shedding.

Figure 5.10b provides further quantitative justification for the classification of instability behavior between the different cases based on the nature of the spectra as well as the instability strength. The cases that show global modes show the strongest amplitude of normalized instability and nearly an order of magnitude higher than cases which were classified as convectively unstable. The cases which were ambiguous based on their spectral characteristics also lay in between the globally and convectively unstable cases in terms of instability strength. The R2 cases show a significantly suppressed instability magnitude compared to the R1 and NR cases.

5.3 Modal decomposition

5.3.1 Mathematical formulation

Proper Orthogonal Decomposition (POD) is a technique used extract the dominant modal structures from flowfield data and has been used extensively to understand the dynamical content of turbulent flows [129]. Space-time flowfield data as characterized by the measured velocity field, $q(\boldsymbol{x}, t)$ can be decomposed into a sequence of spatially orthogonal modes using the formula [130] -

$$q(\boldsymbol{x}, t) = \sum_j a_j(t)\phi_j(\boldsymbol{x}) \quad 5.1$$

Where $a_j(t)$ is the scalar time-coefficients and the spatially orthogonal modes are described by $\phi_j(\boldsymbol{x})$. The orthogonal modes required are optimal basis functions and can therefore represent the flowfield data $q(\boldsymbol{x}, t)$ with the least number of modes. The problem can be solved by formulating the eigenvalue problem (EVP) -

$$R\phi_j = \lambda_j \phi_j \quad 5.2$$

Where R is the spatial two-point correlation tensor and consequently the modes, ϕ_j, can be extracted as the right eigenvectors. Another benefit to this formulation is that the eigenvalue, λ_j, which effectively measures the L^2*-norm* and captures the turbulent kinetic energy (TKE) contained in a mode. Therefore, ordering the extracted modes according to the magnitude of the eigenvalues allows for evaluation of the most dominant flow structures.

While there are numerous ways this decomposition can be modified to target specific flow structures/modal content [131], the variant of POD used in this study is known commonly as *Snapshot POD* and essentially refers to the method in which the correlation tensor, R, is calculated. The data matrix which can be consists of m snapshots of the flowfield can be stacked as -

$$X = [\boldsymbol{x}(t_1) \quad \boldsymbol{x}(t_2) \ \ldots \ \boldsymbol{x}(t_m)] \in \mathbb{R}^{n \times m} \quad 5.3$$

and the correlation tensor can be calculated as -

$$R = X^T X \in \mathbb{R}^{m \times m} \quad 5.4$$

The formulated EVP and corresponding modes can be extracted from the following set of equations -

$$X^T X \psi_j = \lambda_j \psi_j \quad 5.5$$

$$\phi_j = X \psi_j \frac{1}{\sqrt{\lambda_j}} \in \mathbb{R}^n \quad 5.6$$

Due to computational constraints, the number of snapshots used for the reconstruction was capped at 6000 (out of a total data record length of 13183) but calculation with different sequences of 6000 flowfields sampled from the total data record show no noticeable variation in the dynamic content of the extracted modes and therefore the results will be reported from the truncated data length of *m* = 6000 snapshots.

5.3.2 Results and discussion

While no physical basis is imposed on the modal decomposition process, based on the spatial structure of the mode and associated frequencies, modes can be associated with specific physical phenomena, such as vortex shedding or coherent structure evolution. POD has been used to quantify the modal structure, using velocity data, along different regions of interest for a JICF, across both reacting and non-reacting conditions. Meyer et al. [132] extracted the dominant modes along the plane of symmetry (*x*-*y* plane) as well as the transverse plane with respect to the jet (*y*-*z*/*x*-*z* plane). They observed that the most energetic modes in the plane of symmetry, tend to be modes associated with jet 'flapping'

while the modes that capture the shear layer structures tend to be lower in the energy ranking. In the wake region, the most energetic modes described the wake vortices that were formed in the leeward region of the jet. Physical phenomena such as the advection of vortices along the shear layer cannot be captured by a single mode and consequently two (or more) POD modes will tend to describe the behavior of an advecting structure. This behavior can be analyzed by evaluating the correlation between the time-coefficients $a_j(t)$ of the modes.

Gevorkyan et al. [133] used POD to further explore the shear layer behavior of jets across different *J* and *S* values. The transition from convectively to globally unstable conditions was noted by tracking the strength of correlation between the time coefficients of the leading energy-ranked POD modes - $a_1(t)$ and $a_2(t)$. Since the current study aims to perform a similar classification of convectively vs globally unstable behavior, the qualitative nature of the POD velocity modes are analyzed and compared with the earlier classification made solely on the spectral behavior (Section 5.2.3). Compared to the previous investigations, the current data set has a high level of time-resolution

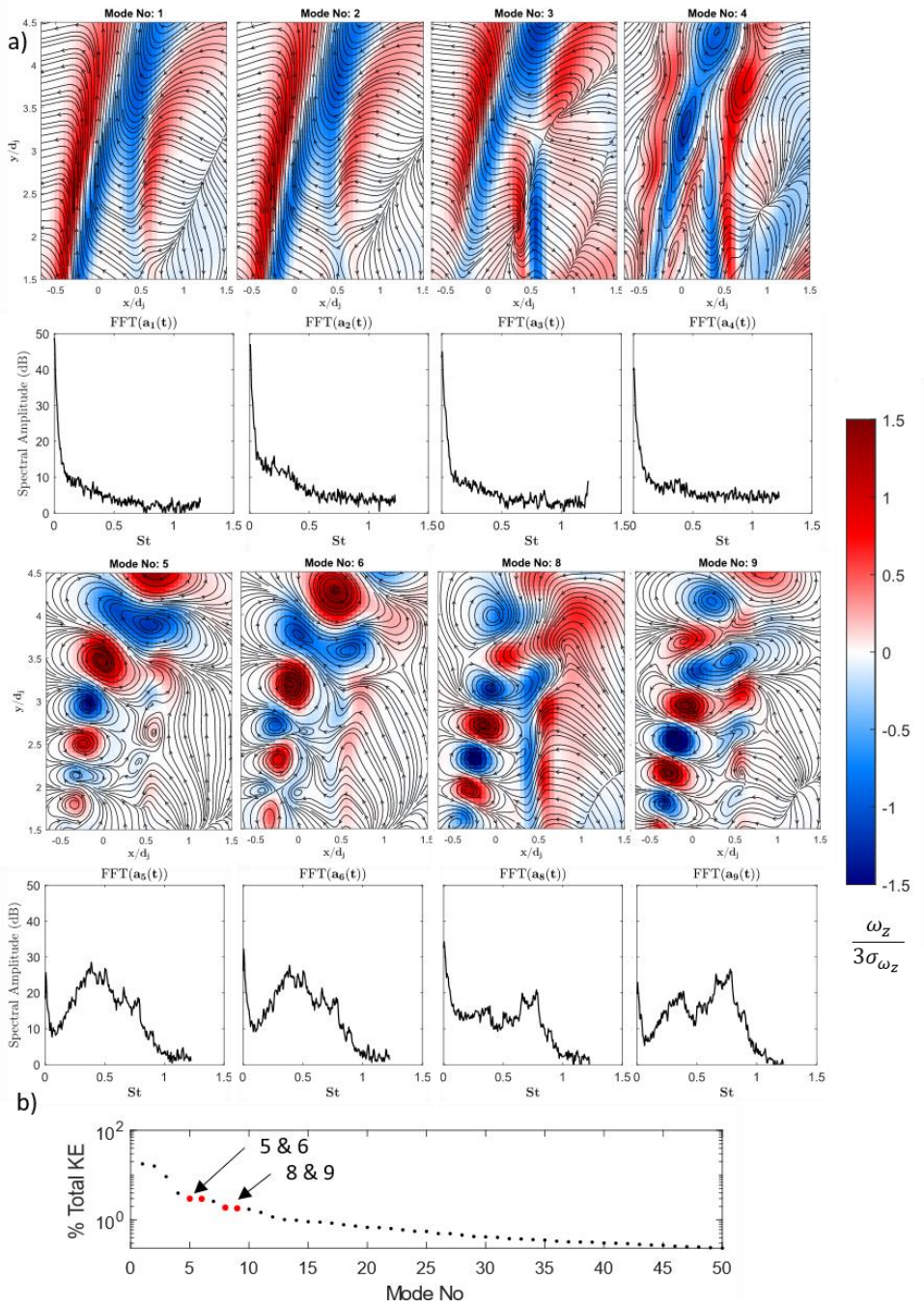

Figure 5.11: a) Leading modes (1-10) along with the spectrum from the associated time-coefficients for Case 2: J = 12, S = 1.75, NR; Modes presented display the out-of plane vorticity normalized by a fluctuation scale along with streamlines computed from the in-plane velocity components (u, v); b) Total kinetic energy of the top 50 modes is displayed with the modes corresponding to advecting SLV structures annotated.

Before proceeding with an analysis of the transitional behavior, all the leading order modes for a non-reacting case (Case 2 - Figure 5.11) are analyzed to understand the spatial structure of the dominant modes. The first four modes contain energy primarily associated with jet flapping, similar to the observations by Meyer et al. [132]. This is also evident from the lack of high-frequency content in the associated spectrum, which is obtained by performing a Fast Fourier Transform (FFT) of the time coefficient ($a_j(t)$). The modes describing advecting structures here are found further down the energy ranking but can be easily identified based on the length scales and orientation of spatial structures in the shear layer as well as the associated high frequency content present in the spectra consistent with the data obtained in Section 5.2.1. Mode 5 and 6 appear to describe the structure of the subharmonic, based on the spectra and the longer length scales in the far field – associated with vortex paring. Mode 8 and 9, describe the spatial structure of the fundamental with stronger variance in the near field and a higher frequency peak. The modal decomposition process does not isolate the spatial structure of specific spectral content and modes will often contain multiple frequency. Here, this split between the subharmonic and fundamental occurs because both have strong spatial presence in different regions of the jet flowfield (near-field vs far-field), and since these disturbances advect at a relatively uniform phase speed, the fundamental and sub-harmonic will have different spatial wavelengths and therefore would not be captured by a single spatial structure. For the sake of brevity, the modes associated with jet flapping will be dropped from the subsequently analyzed cases unless specifically presented.

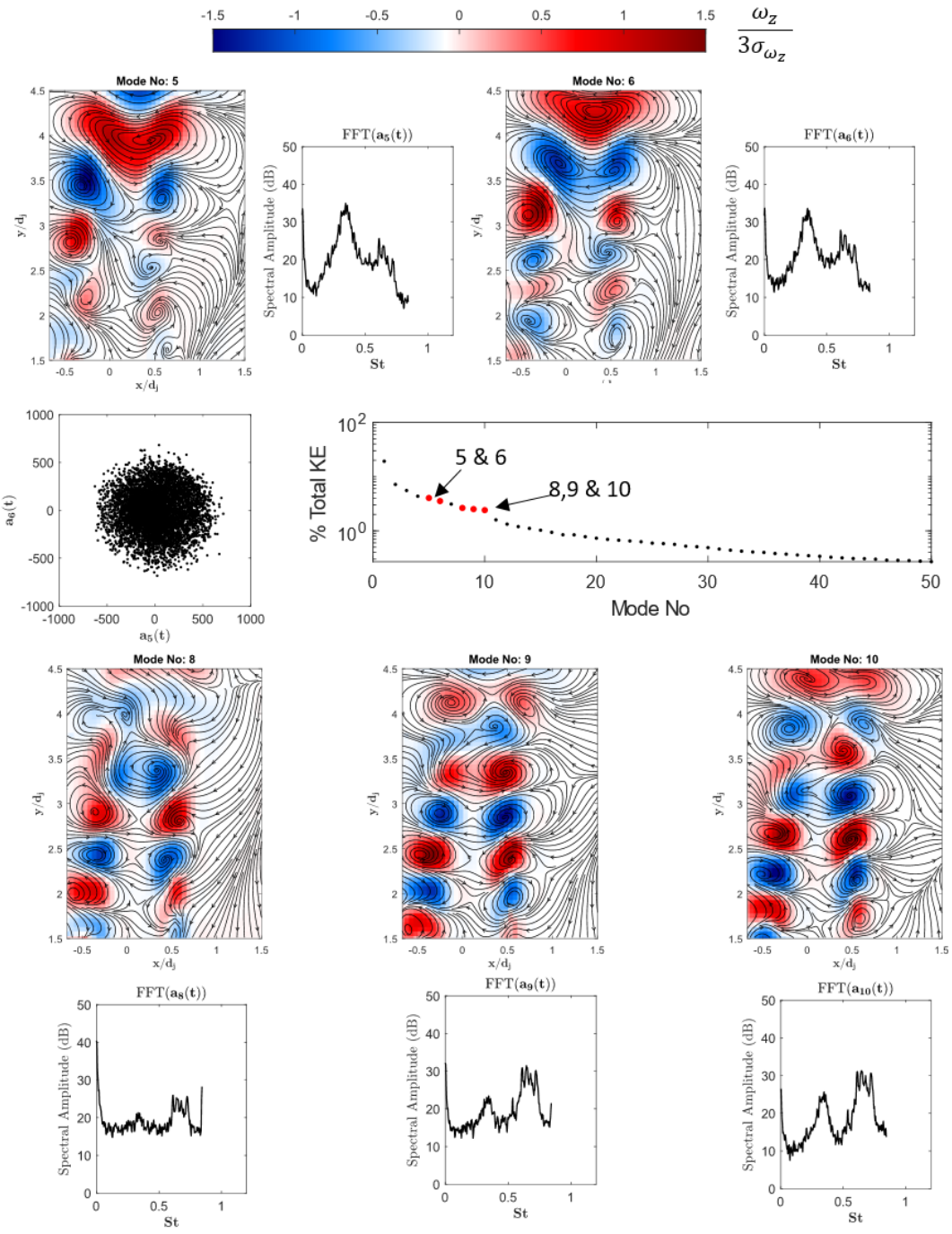

Figure 5.12: Leading modes along with the spectrum from the associated time-coefficients for Case 7: J = 18, S = 1.00, NR; Correlation between the time-coefficients of modes 5 and 6 are presented in the Poincare plot; b) Total kinetic energy of the top 50 modes is displayed with the modes corresponding to advecting SLV structures annotated.

The dominant modes for Case 2 (Figure 5.11) is characteristic of convectively unstable conditions as further supported by analyzing the POD modes from Case 7 (Figure 5.12), another case classified as convectively unstable based on the spectra. Again, the dominant modes that correspond to advecting SLV structures appear at mode 5 and 6, suggesting that the weak instability behavior causes the variability in the flowfield to stem from the jet flapping behavior. As these modes make a 'mode-pair' the correlation between them is evident from the *Poincare plot,* where the cloud of correlated points make up a circular structure, similar to the observation of Gevorkyan et al. [133]. Further down in the energy ranking modes 8, 9 and 10 appear to describe the advection at the higher frequencies associated with the fundamental mode. As discussed earlier, the POD modes are not necessarily spectrally pure and consequently there is some subharmonic content in these modes and correspondingly there is content at the fundamental frequency as described by mode 5 and 6. The energy spanned by mode pair 5-6 is approximately 14% while the cumulative energy in the higher frequency modes – 8, 9, and 10 is roughly 10%.

Next, we consider the modes from a globally unstable case – Case 10 (Figure 5.13). Although the first mode hear appears to be scribing a jet flapping mode, this mode and the four following ones, contain strong spectral information pertinent to the global mode frequency. Modes 2, 3 and 4 all have a spatial structure that describes the advecting vortices along the shear layer and together make up nearly 33% of the total energy. In addition, the correlation between the time coefficients - $a_3(t)$ and $a_4(t)$ appear to be considerably stronger since the 'donut' shape implies strong periodicity. Mode 2 does not appear to be well correlated spectrally and consequently, does not form a pair or triplet with either mode 3 or 4. In general, the qualitative classification based on the spectral behavior can be

extended to the analyses of POD modes by observing the time-correlation of the leading order modes, which capture the advecting SLVs.

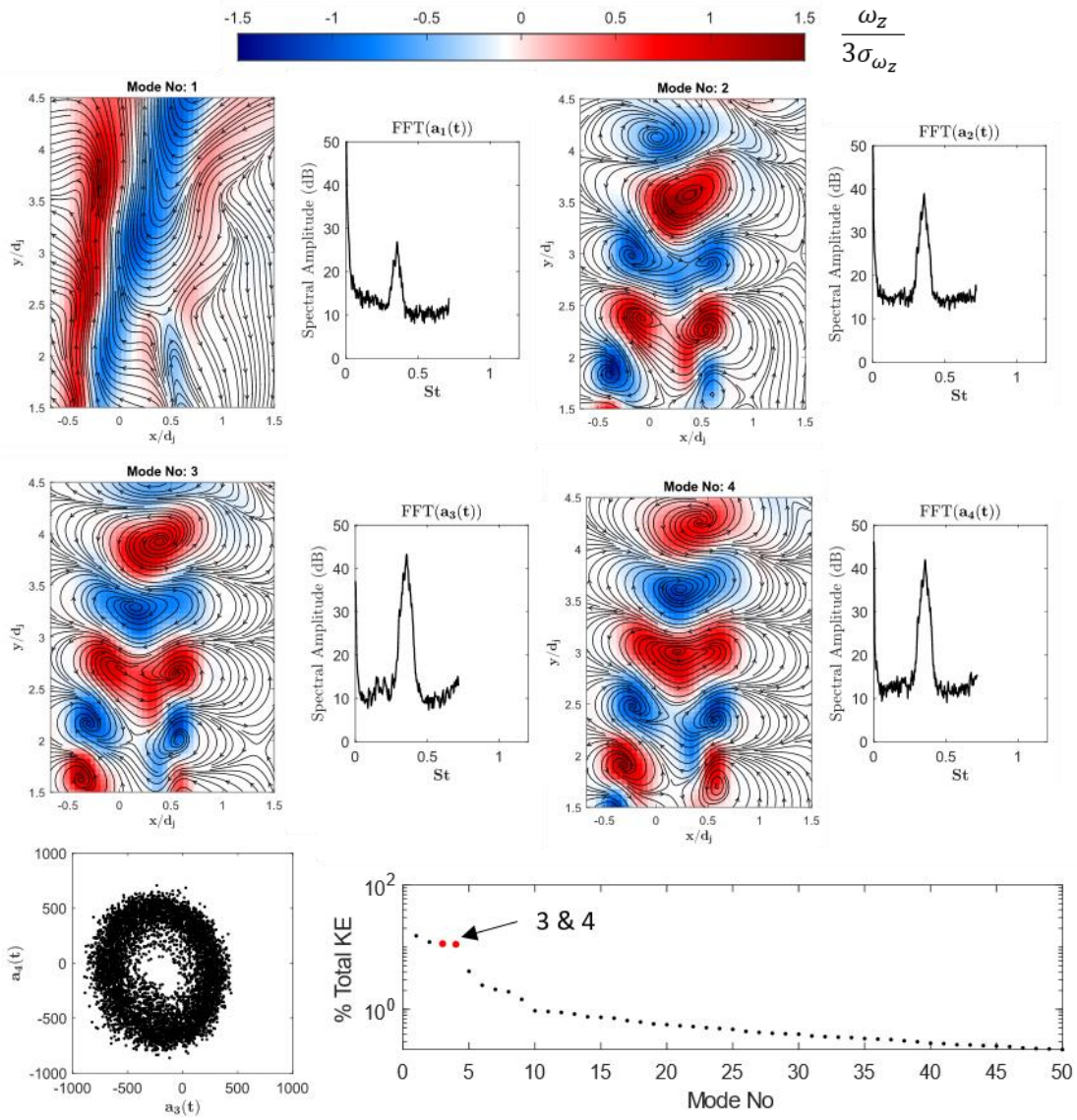

Figure 5.13 Leading modes along with the spectrum from the associated time-coefficients for Case 10: J = 12, S = 0.35, NR; Correlation between the time-coefficients of modes 3 and 4 are presented in the Poincare plot; total kinetic energy of the top 50 modes is displayed with the modes corresponding to advecting SLV structures annotated.

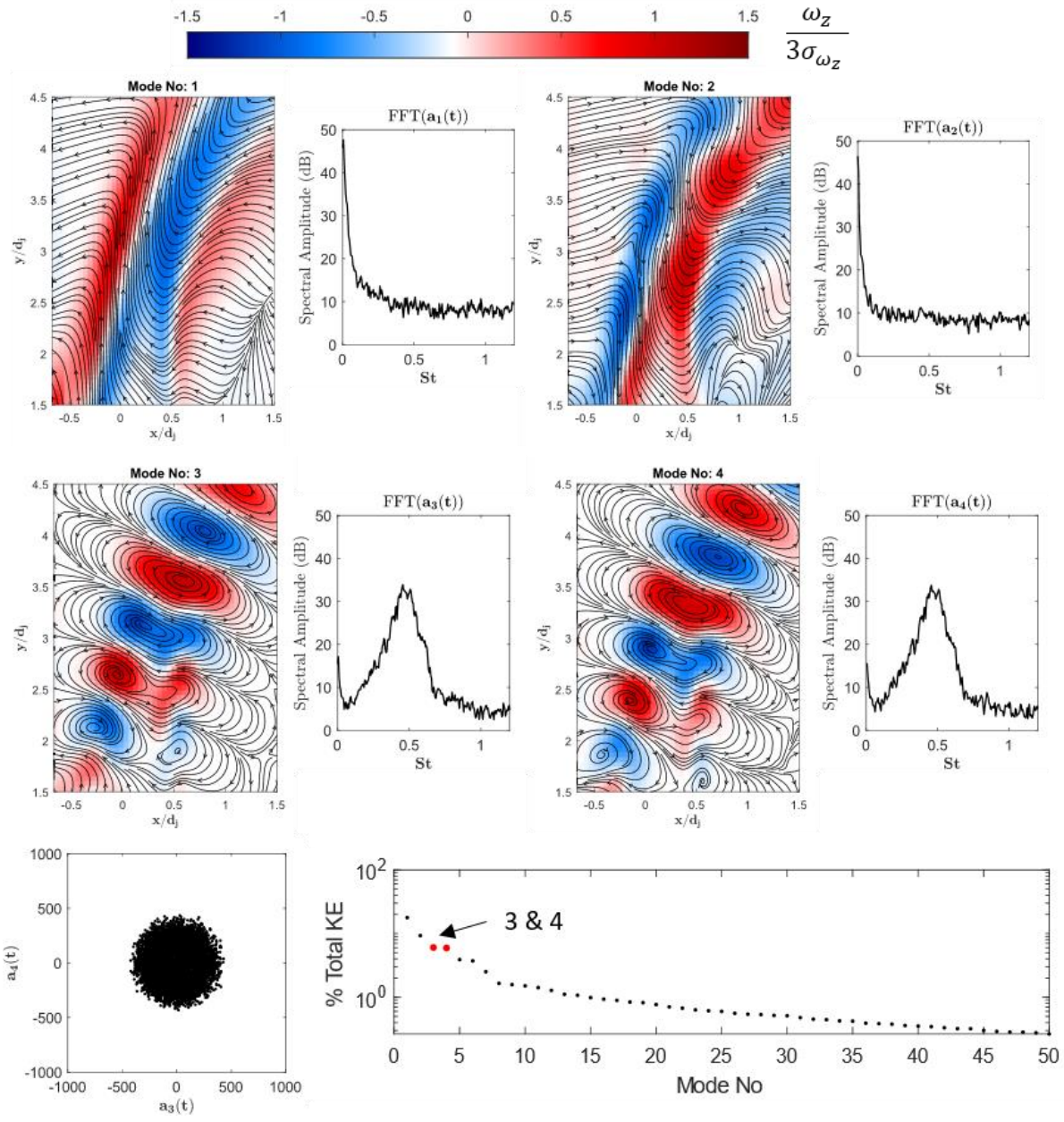

Figure 5.14: Leading modes along with the spectrum from the associated time-coefficients for Case 5: J = 6, S = 1.0, NR; Correlation between the time-coefficients of modes 3 and 4 are presented in the Poincare plot; total kinetic energy of the top 50 modes is displayed with the modes corresponding to advecting SLV structures annotated.

Since the convectively and globally unstable cases have distinct POD characteristics which aid classification, the classification of those transitional cases is

considered by observing the POD modes from case 6 (Figure 5.14). Here, the dominant modes which capture the SLV advection are mode 3 and 4 while mode 1 and 2 have no spectral content corresponding to the single tone visible in the spectra, unlike the globally unstable case (Figure 5.13). The total energy content spanned by these modes totals to 15%, which is less than the energy in the global modes but higher than the convectively unstable case. In addition, the qualitative nature of the time correlation suggests stronger periodicity than the corresponding mode pairs identified in convectively unstable cases.

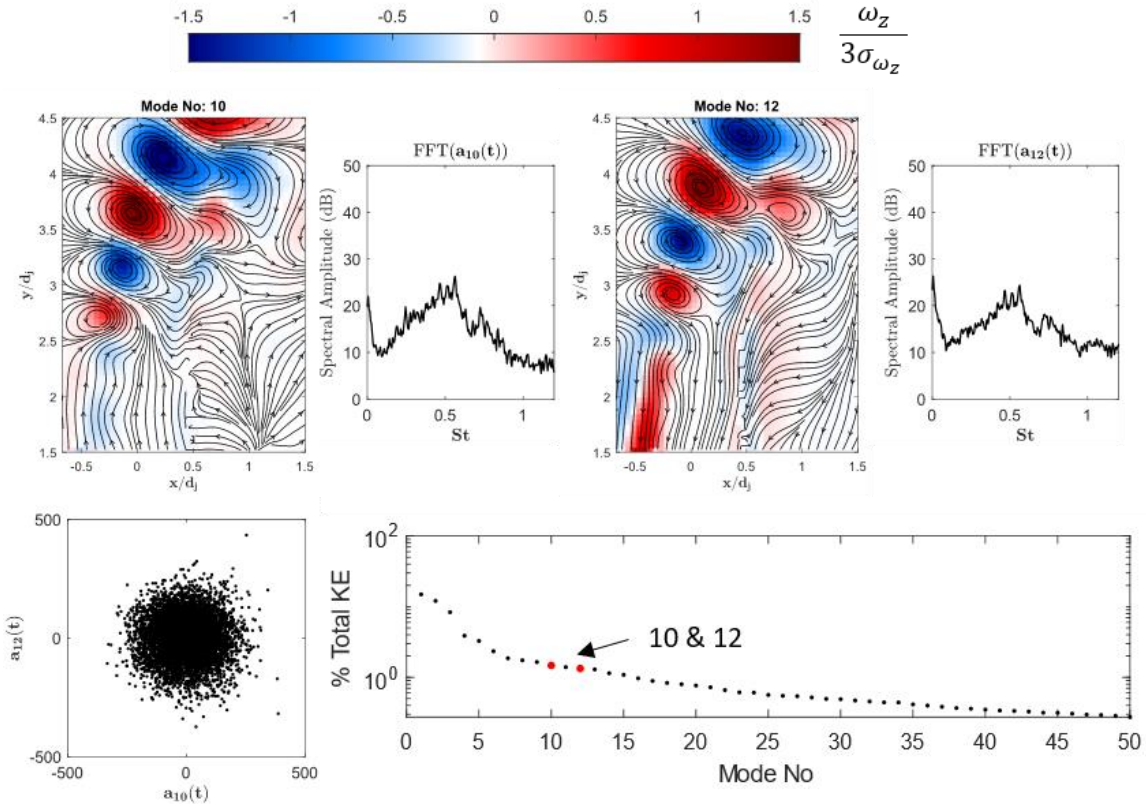

Figure 5.15: Leading modes along with the spectrum from the associated time-coefficients for Case 14: *J* = 12, *S* = 1.75, R1; Correlation between the time-coefficients of modes 10 and 12 are presented in the Poincare plot; total kinetic energy of the top 50 modes is displayed with the modes corresponding to advecting SLV structures annotated.

If we consider the R1-reacting cases, based on the spectra, the reacting flowfield, for the convectively unstable cases is significantly more broadband and diffused. The POD modes for case 14, a reacting case classified as convectively unstable, are described in Figure 5.15. Since the leading order modes corresponding to jet flapping are omitted, mode 10 and 12 capture the shear layer structures based on the spatial mode as well as the dominant frequencies, at the sub-harmonic, captured by the spectra of the time-coefficients. This is expected since for reacting flows, the presence of combustion adds energy to the flow though gas expansion and acceleration. In addition, the jet flapping couples with the flame induced acceleration as the flame is moved along with the jet trajectory and consequently increasing the unsteadiness across a large spatial domain. Thus, the energy from modes exclusively targeted as advecting structures tend to have a much lower energy content (~ 3%) compared to the total TKE.

This effect is observed even for the reacting case which has a strong global mode – Case 21. Figure 5.16 describes the leading order POD modes which capture the advecting structure as modes 4, 5 and 6. While all have a spatial structure and frequency content indicative of the global tone, modes 5 and 6 have a stronger temporal correlation as indicated by the time-coefficients. The level of periodicity exhibited here suggests that these modes have correlation closer to a transitional or convectively unstable NR case and the ‘donut’ shape is much weaker. In addition, the energy content from these modes spans 16%, which is significantly less the share from the NR globally unstable cases. Thus, it would appear that combustion has an effect on disrupting the level of periodicity exhibited by these shear layer modes – most likely through the intermittency of the flame flapping with the jet trajectory and thereby disrupting the energy variance in the shear layer.

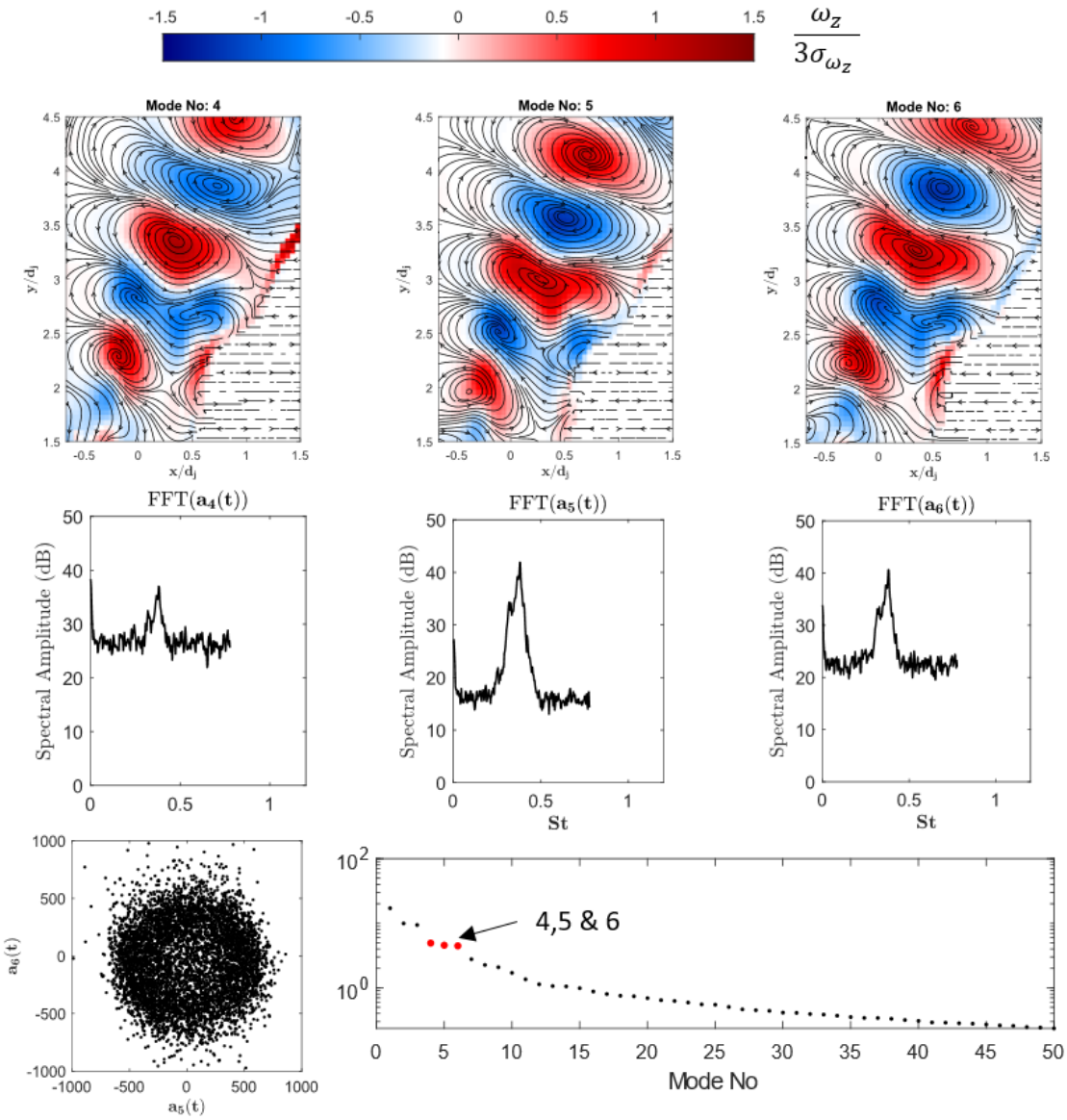

Figure 5.16: Leading modes along with the spectrum from the associated time-coefficients for Case 21: J = 6, S = 0.35, R1; Correlation between the time-coefficients of modes 5 and 6 are presented in the Poincare plot; total kinetic energy of the top 50 modes is displayed with the modes corresponding to advecting SLV structures annotated.

The R2 cases, which showed very little spectral content due to the highly suppressed rollup behavior is analyzed through its leading order POD modes in Figure 5.17. Unsurprisingly, the first 25 modes (1, 3 and 10 shown here) show no modes that resembles advecting structures along the shear layer. This is expected as there is very little

vorticity aggregation (or rollup) within the domain and therefore it is unlikely that the low-frequency tones corresponding to the bands discussed in Figure 5.7 would appear to have high-energy modal content.

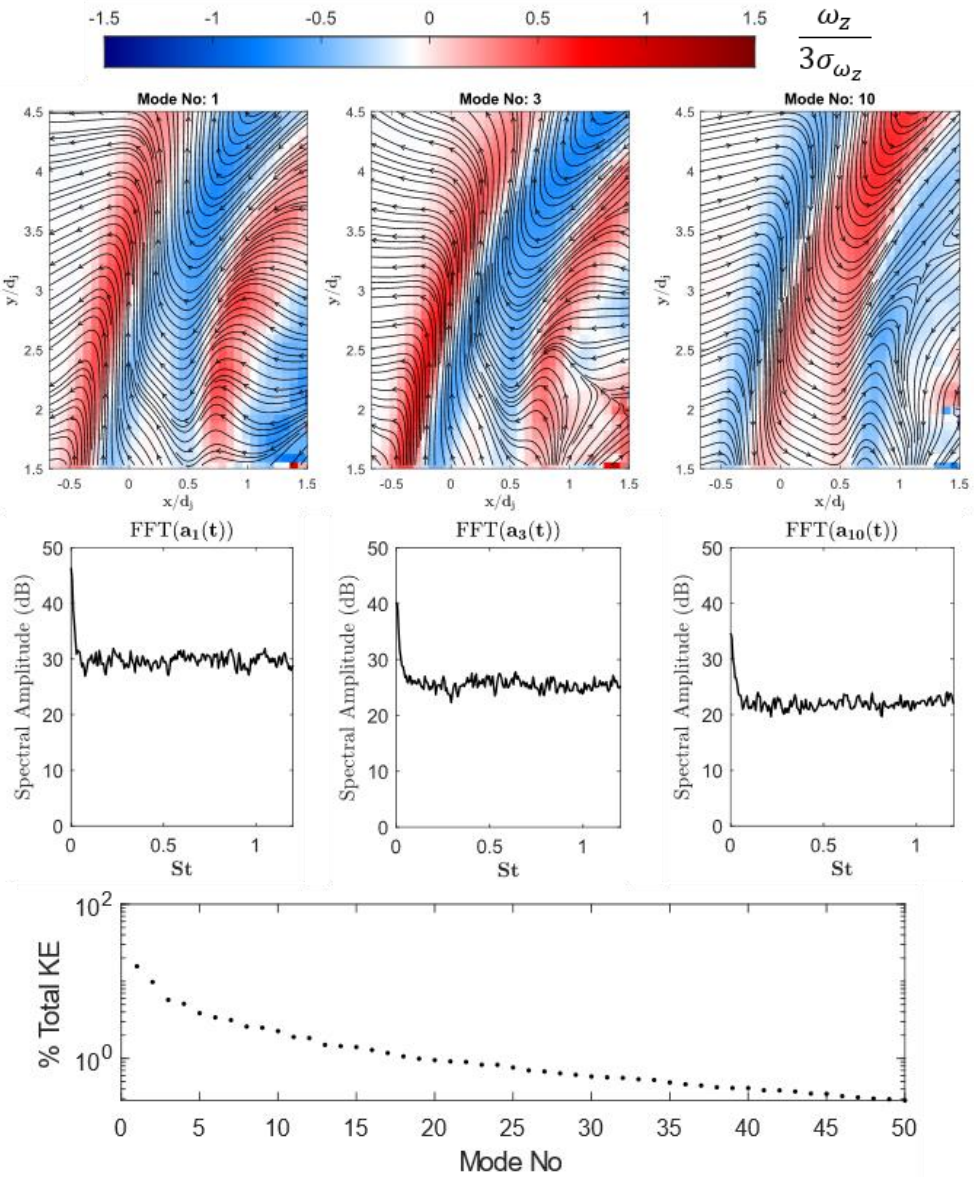

Figure 5.17: Selected leading modes along with the spectrum from the associated time-coefficients for Case 27: J = 6, S = 1.1, R2; total kinetic energy of the top 50 modes is displayed.

5.4 Counter-current shear layer (CCSL) model

For the current set of experiments, across reacting and non-reacting conditions, J is observed to have a much weaker impact on the transition to instability compared to S which contradicts the observations of Getsinger et al. [53] who noted the opposite trend. For example, the $J = 6$ NR cases at $S = 1.0$ and $S = 1.75$ show transitional and convectively unstable behaviour respectively despite having $J < J_{crit}$. In addition, for reacting cases it is likely that the density ratio between the jet and the crossflow is not the appropriate parameter to map instability behavior. The observed instability transitional behavior for both non-reacting and reacting cases therefore suggests that the S and J parameters are unable to uniquely predict the instability characteristics.

For the case of free jet shear layers, Huerre and Monkewitz [50] showed that global oscillations are a consequence of large regions of local absolute instability. From the perspective of parallel flow stability analysis, they mapped out this transitional behavior across different counter-current velocity ratios, $\Lambda = (U_1 - U_2)/(U_1 + U_2)$ and density ratios $S = \rho_1/\rho_2$. U and ρ refer to the base flow axial velocity and density for a two-dimensional shear layer and the subscripts 1 and 2 denote the faster and slower streams respectively. For most cases where S = 1 or higher, the presence of counterflow ($\Lambda > 1$) was necessary for disturbances to propagate upstream while for low-density cases, $S < 0.45$ for low-density jets [54], this transition to global stability is possible even without counterflow, in typically convectively unstable flows like jets. However, unlike free jets, iso-density JICF configurations showed a transition to globally unstable oscillations at low

$J < J_{crit}$, suggesting that there must be some mechanism for these instabilities to propagate upstream in the JICF flowfield.

Iyer and Mahesh [58] demonstrated that the stagnation point created by the crossflow leads to a region of counterflow upstream of the jet – effectively setting up a counter current shear layer (CCSL). Using this magnitude of reverse flow and the jet velocity, they calculated the counter-current velocity ratio (Λ) for cases that were observed to transition from globally to convectively unstable behavior, demonstrating effectively that these J values mapped to Λ's that lay on either side of the theoretical transitional value of Λ = 1.32 (Huerre and Monkewitz [49]). But the relationship between Λ and J is not unique as the counterflow magnitude depends on the crossflow velocity and the level of aerodynamic blockage created by the jet – both independent metrics which are not unique to a given J. Shoji et al. [56] further explored the viability of this model in predicting the transitional behavior across low density cases and over a much larger parameter space. Their observations showed that mapping the jet parameters to the CCSL velocity ratio Λ based on the measured region of counterflow demonstrated that the parameter Λ captures the transitional behavior with remarkably close agreement with Pavithran and Redkopp's [134] theoretical results. In addition, they noted that the viscosity ratio between the jet and the crossflow (μ_j/μ_∞) altered the scaled momentum thickness of the CCSL and consequently altered the transition to global instability.

Based on the observations made in Section 5.2.3, it is likely that S, which is calculated solely on the non-reacting jet parameters, will be unable to predict the general trend of globally to convective transition observed in the reacting cases. As a result, this

CCSL model will be leveraged to classify the stability behavior of NR and R1 cases in the (S', Λ) space as opposed to the traditionally defined (S, J) parametric space. Here, S' is the density ratio pertinent to the CCSL model, equal to S for the non-reacting cases. Since the flame locally changes the viscosity in addition to the local stratification, the impact of changing viscosity thickness will also be evaluated.

5.4.1 Formation of the CCSL

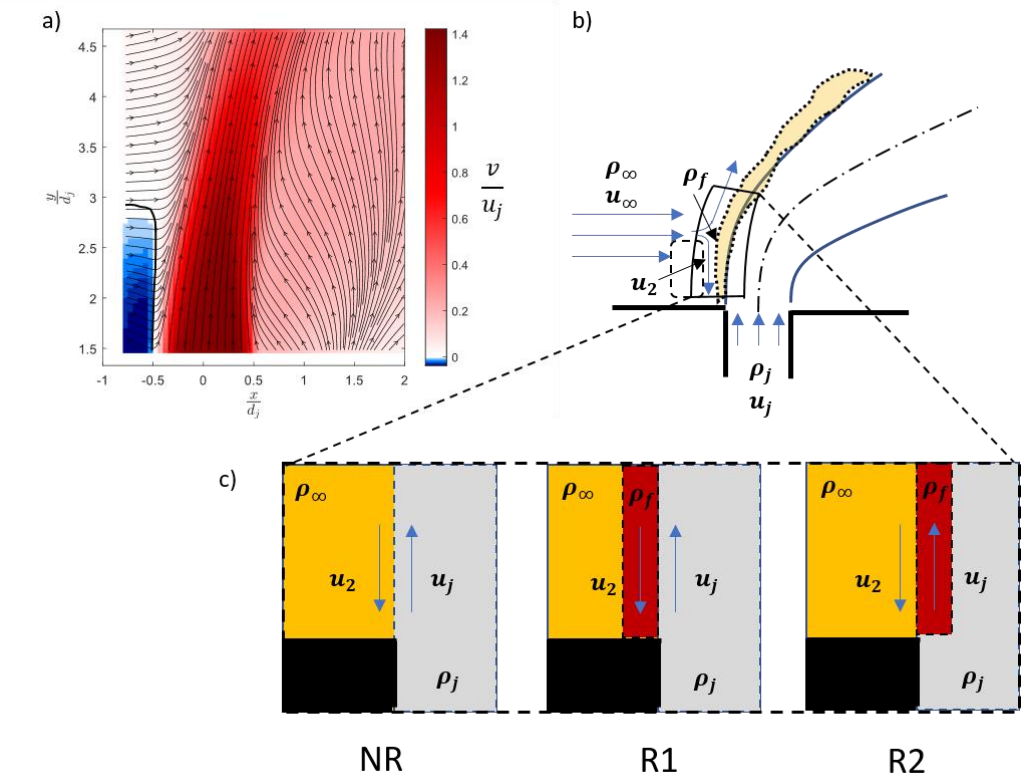

Figure 5.18: a) Mean transverse velocity for Case 6 showing streamlines for the in-plane velocity components with region of negative transverse velocity demarcated with a solid contour; b) Schematic depicting the windward shear layer and the counter-current mixing layer formed from the jet velocity and the reverse flow upstream of the shear layer; c) Demarcation of the different regions of fluid along the mixing layer along with the local properties used in building the CCSL model for NR, R1 and R2 cases

The evidence of counterflow upstream of the shear layer can be clearly observed from the mean flowfield, which shows the region of negative transverse velocity persisting to a height, $y/d_j \sim 3$ for Case 6 (Figure 5.18a). The streamlines show that the flow decelerates and drops as it approaches the jet, before being sheared along the shear layer. The schematic in Figure 5.18b attempts to capture this behavior diagrammatically, while defining the primary region of the windward shear layer considered analogous to a mixing layer. For a traditionally defined mixing layer, the choice of velocity scales come from the boundary conditions that the velocity asymptotes to as you move infinitely far from the mixing interface. Here, the faster stream velocity (U_1) can be assumed to be u_j, particularly within the potential core of the jet. On the slower side (crossflow side), this choice is ambiguous as the flowfield is complex and the velocity does not asymptote monotonically to a fixed boundary condition. Iyer and Mahesh [58] used the minimum (or most negative) transverse velocity in the region of counterflow as the velocity of the slower stream, U_2 (u_2 in Figure 5.18) in the CCSL. While their study explored only iso-density conditions, Shoji et al. [56] was able to extract U_2 based on the same technique for stratified cases ($S < 1.0$), and successfully showed good agreement between the theoretical results and calculated Λ (based on U_2 and U_1). For the current study, we employ a similar approach by extracting the transverse velocity data along lines of constant (s) normal to the windward shear layer and is described in Figure 5.19.

The nature of the counterflow region upstream of the jet is captured by measuring the minimum velocity U_2 across different jet conditions. Following from the line of reasoning introduced by Iyer and Mahesh [58], the magnitude of this counterflow region is likely dependent on the crossflow dynamic pressure since, apart from a modest rise in

static pressure upstream of the windward shear layer [19], the dynamic head of the flow is entirely redirected into the counterflow. This provides the scaling $U_2 \sim ku_\infty$ where k captures the extent of aerodynamic blockage introduced by the jet. Since u_∞ is kept constant across all R1 and NR cases considered here, the ordinate for the plot (Figure 5.20a) is analogous to this constant k and demonstrates that the aerodynamic blockage depends on J, S and the presence of combustion.

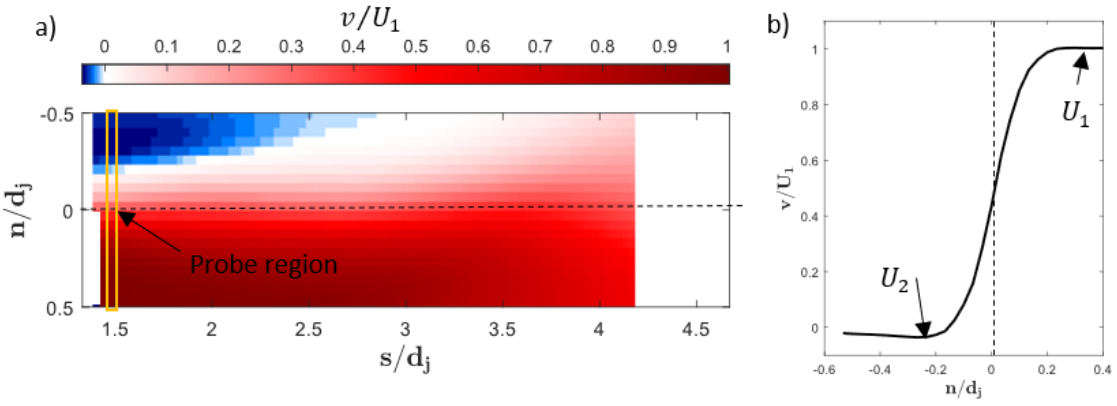

Figure 5.19 a) Normalized transverse velocity field in windward shear layer oriented (*s*, *n*) coordinate system; b) Profile along the probe region demarcating the extracted U_1 and U_2 parameters for each case (case 10 shown here).

The increase in magnitude of k with increasing J is intuitive as a deeper jet trajectory will tend to offer a stronger blockage, but the effect is not necessarily linear as the blockage effect for low J jets will tend to asymptote to some finite limit at high J vales. For the NR cases the dependence on J is relatively weak, other than for the $S = 0.35$ cases, while most of the reacting cases show an increase in the blockage with increasing J. In general, other than the low density NR cases the reacting cases have a systematically higher level of aerodynamic blockage which is likely a consequence of the shielding effect of the diffusion flame as noted by previous studies [10, 18]. This impacts the interaction

between the jet and the crossflow leading to reduced entrainment, as demonstrated in the previous chapter, and marginally deeper trajectory penetration.

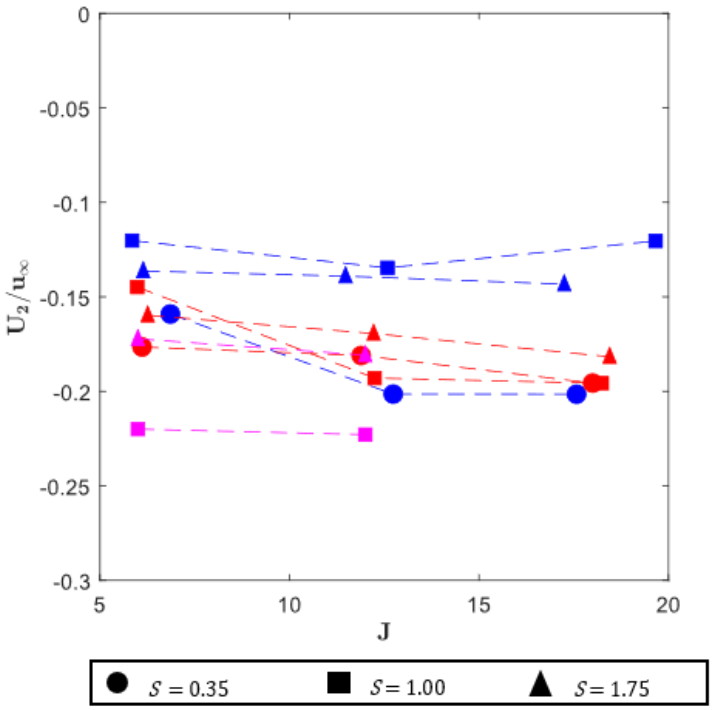

Figure 5.20 Counterflow magnitude with respect to J, line connect points at constant target S; Blue points – NR, Red points – R1 and Magenta points – R2.

The R2 cases have a blockage ratio comparable to the R1 cases except for the low-density cases. The difference in the range of k values measured as a part of this study compared to the value of $k = -0.4$ obtained by Mahesh suggests that in addition to the crossflow velocity magnitude (u_∞), the boundary layer thickness plays an important role in the magnitude of the counterflow. Vitiated, high-temperature crossflows like the one encountered in this study tend to have a significantly larger boundary layer and consequently, the magnitude of the counterflow (compared to the crossflow velocity scale) would be lower since the dynamic pressure at the stagnation point will be a fraction of u_∞.

This implies that flows with a fuller crossflow boundary layer will tend to have a stronger/larger region of counterflow upstream of the shear layer and consequently a larger value of Λ and tend to exhibit stronger transition to global instability. This has an important implication on the mapping of J to Λ as it appears that for a set of experiments, given the number of parameters upon which the counterflow magnitude depends (J, S, u_∞, δ_{bl}), estimating the Λ values corresponding to experimental test conditions will not be possible *a priori* without measurements of the jet and crossflow boundary conditions for a given facility.

5.4.2 Vorticity thickness scaling

Another length scale of interest in a CCSL is the momentum thickness (θ) and is often used to explain the scaling of the characteristic frequencies (St_θ) across different flow conditions. Further, Jendoubi and Strykowski [135] noted for axisymmetric jets that the transitional velocity ratio Λ_{crit} varied with θ for very low values of theta, which occurred for low J jets as noted by Shoji et al. [56]. In addition, θ has been demonstrated to have a linear relationship with respect to the eddy spacing (λ) and should be able to collapse the scaling of characteristic frequencies considered here. But, in stratified, non-isothermal flows, such as the conditions explored in this study, estimating the value of θ is challenging due to lack of density measurements from the base flow. To explore the St scaling between the reacting and non-reacting characteristic frequencies (section 5.2.3), we consider scaling with another length scale associated with instability growth – the vorticity thickness (δ_ω). Previous studies on stratified and constant density mixing layers studies have used this metric [67, 119] as a surrogate for the momentum thickness, θ.

$$\delta_\omega = \frac{1}{|\omega_{z,max}|}\int |\omega_z| dn \qquad 5.7$$

For the current data, the vorticity thickness is evaluated across the extracted transverse velocity profile extracted from the CCSL model (Figure 5.19b). This can further be simplified by simply using the extracted velocity scales U_1 and U_2 and the measured peak vorticity $\omega_{z,max}$ along the probe location in the windward shear layer.

$$\delta_\omega = \frac{U_1 - U_2}{|\omega_{z,max}|} \qquad 5.8$$

The measured vorticity thickness δ_ω, scaled with d_j, is plotted for the different conditions in Figure 5.21a. Between the R1 and NR cases there doesn't appear to be a strong variation for the equidensity ($S = 1.0$) and higher density jets ($S = 1.75$) and it appears that the variation of *S* has a more dominant effect. For the lower density cases ($S = 0.35$) the vorticity thickness of the NR cases appears to be much larger than the corresponding R1 case. Since δ_ω does not directly factor in density variations, the length scale that it captures is related to the shape of the vorticity profile. For reacting flows, Hermanson and Dimotakis [67] demonstrated that δ_ω effectively measures the impact of the heat release on modifying the base flow vorticity distribution which in their case accounted for the variation in characteristic length scales between the reacting and non-reacting conditions.

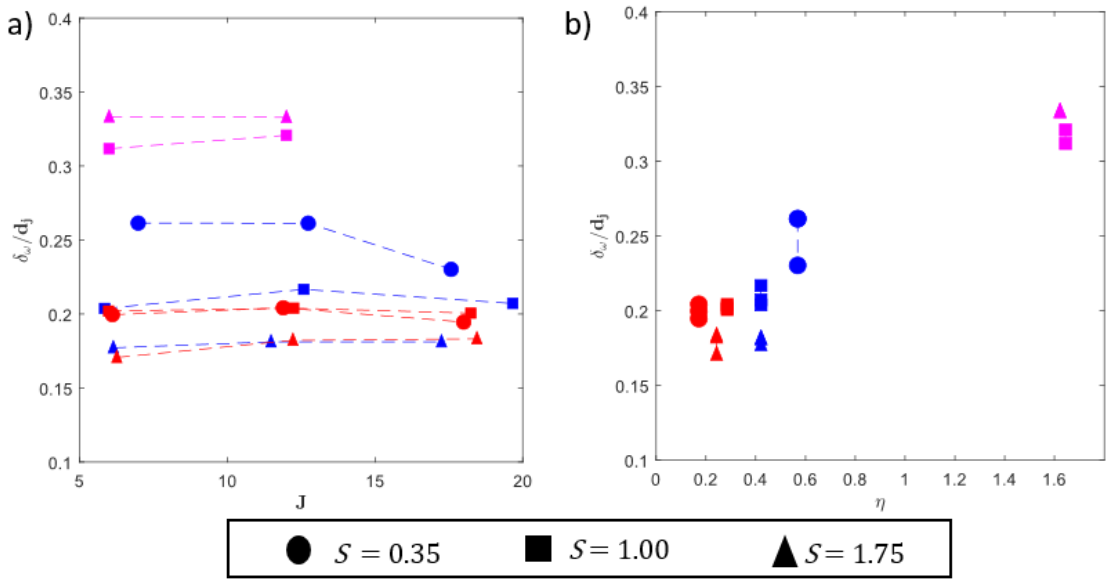

Figure 5.21: a) Extracted δ_ω with respect to J, line connect points at constant target S; b) δ_ω for different viscosity ratios – η; Blue points – NR, Red points – R1 and Magenta points – R2. For R2 S = 1.0 markers were used to represent cases with S = 1.1 and similarly the markers for S = 1.75 correspond to S = 2.2.

Shoji et al. [56] demonstrated that the scaled CCSL momentum thickness (θ/d_j), responsible for the transitional behavior of the windward shear layer, varied with the jet to crossflow viscosity ratio μ_j/μ_∞. To assess whether δ_ω shows a similar dependence, the viscosity ratio for the two streams in the CCSL model are considered. For the non-reacting cases this viscosity ratio $\eta = \mu_j/\mu_\infty$ while for the reacting cases the high viscosity region of the flame (μ_f) is considered. Consequently, $\eta = \mu_j/\mu_f$ for the R1 cases and $\eta = \mu_f/\mu_\infty$for the R2 cases based on the fluids forming the CCSL (Figure 5.18). Figure 5.21b captures the variation of δ_ω with the viscosity ratio η. For the R1 and NR cases, although the δ_ω are comparable, the viscosity ratios change significantly while the R2 cases show a high viscosity ratio as well as a larger vorticity thickness. Larger viscosities tend to increase the spreading rate, and the momentum thickness, for laminar jets [57] but is not necessarily

the case for turbulent jets. Given the high degree of collocation of the flame and the shear layer for the R2 cases it is possible that the increased viscosities in the vicinity of the flame causes a more diffused velocity profile due to viscous diffusion being comparable to inertial scales (low Reynolds number). For the R1 and NR cases it is unclear if viscosity plays a role in modifying the dynamics since the velocity profile shapes do not appear to be well correlated with the calculated viscosity ratio (η). The ratio of the two fluid viscosities may not be appropriate in flows with complex stratification and a better guess for the absolute viscosity scales controlling the shear layer behavior would be required, involving a better estimation for the local temperature field than is possible from the data obtained in this study.

The direct impact of (δ_ω) can be gauged based on its impact on the captured growth rate. Similar behavior was captured by Furi et al. [77] for their experiments and was used to explain the reduction in the linear growth rate since sharper velocity profiles grow faster ($\alpha \sim 1/\theta$). But, as discussed in the introduction, for cases with strong/complex density stratification, the density weighted vorticity profile and not the vorticity profile is the driving parameters for instability behavior and therefore, δ_ω would not necessarily scale linearly with the observed instability growth rate. This is further supported by the captured growth rate observations presented in the previous chapter as well as the amplitude variation from the spectral plots (Section 5.2.1) which suggest that this variation in δ_ω cannot solely explain the variation in the R2 topology compared to the R1 and NR cases. The value of δ_ω is used to form a modified frequency scaling, $St_{\delta_w} = f\delta_\omega/u_j$, which does reduce the variability of the characteristic frequency (particularly between the low density

cases) but cannot completely collapse the observed variation between NR and R1 cases across analogous conditions (Figure 5.22).

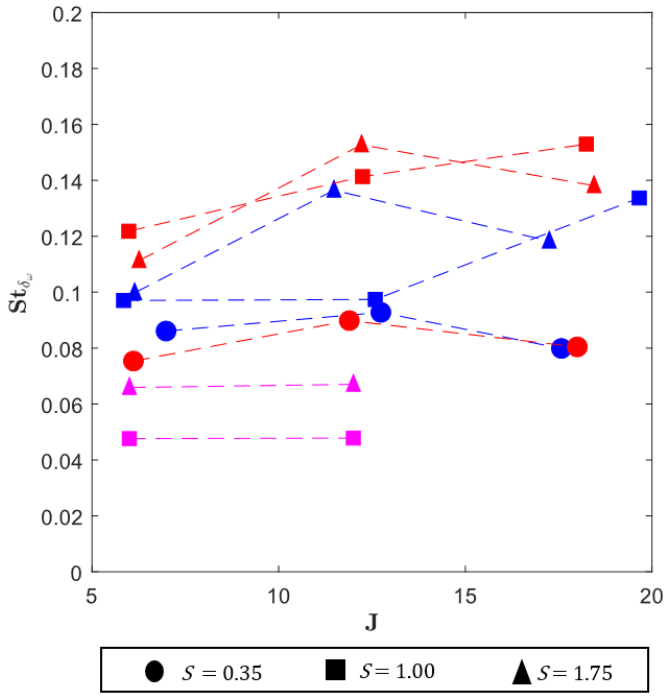

Figure 5.22: Characteristic frequencies calculated using the vorticity thickness – St_{δ_ω}; Blue points – NR, Red points – R1 and Magenta points – R2. For R2 S = 1.0 markers were used to represent cases with S = 1.1 and similarly the markers for S = 1.75 correspond to S = 2.2.

5.4.3 Characteristic convection speeds

In general, the vortex passing frequency can be perfectly scaled by using the characteristic eddy spacing (λ) and the convection speed U_C since $U_C = f\lambda$. While the previous scaling $St_{\delta_w} = f\delta_w/u_j$ (Figure 5.22) attempted to capture the effect of stratification/reactions by using the measured δ_w as the characteristic length scale, the characteristic frequency (St) is also altered through the modification of U_C in the presence of stratification, for a fixed velocity ratio. As postulated by Dimotakis [121] and verified

through observation, density stratification causes a bias in the apparent vortex convection speed from the mean convective flow scale $(U_1 + U_2)/2$ towards the stream with a higher density. If we consider the value of U_2 to be small in magnitude compared to U_1 (Figure 5.19) then the bias can be quantified by calculating the ratio U_C/U_1. This value of U_C can be measured directly from the slope of the *s-t* plots for each case (Figure 5.8b) and is taken as the mean of all the individual realizations.

To verify the extracted U_C values from the slope of the s-t plots, they can be compared to the phase roll-off of the instability amplitudes obtained from the time-domain analysis (Section 5.2.1). The discrete Fourier transform (DFT), used in Section 5.2.1 to extract the instability amplitude, is further used to extract the phase, $\theta_s(s, f)$, at all the probe locations (s) along the windward shear layer. The phase roll-off is measured by tracking the phase variation for the fundamental frequency (f_0) as a function of the streamwise coordinate $\sim\theta_s(s, f_0)$. In addition, for an instability of frequency f_0, convecting with the phase speed U_C, the phase roll-off can be extracted as:

$$\theta_{CV} = \int_0^s \frac{2\pi f_0}{U_C(s')} ds' + \theta_0 \qquad 5.9$$

Where, f_0 is the probe frequency (corresponding to the fundamental frequencies - Figure 5.10), $U_C(s')$ is the vortex convection speed extracted from the *s-t* plots and θ_0 is a constant used to match θ_{CV} and θ_s at the location $s/d_j = 2.0$ to aid direct comparison.

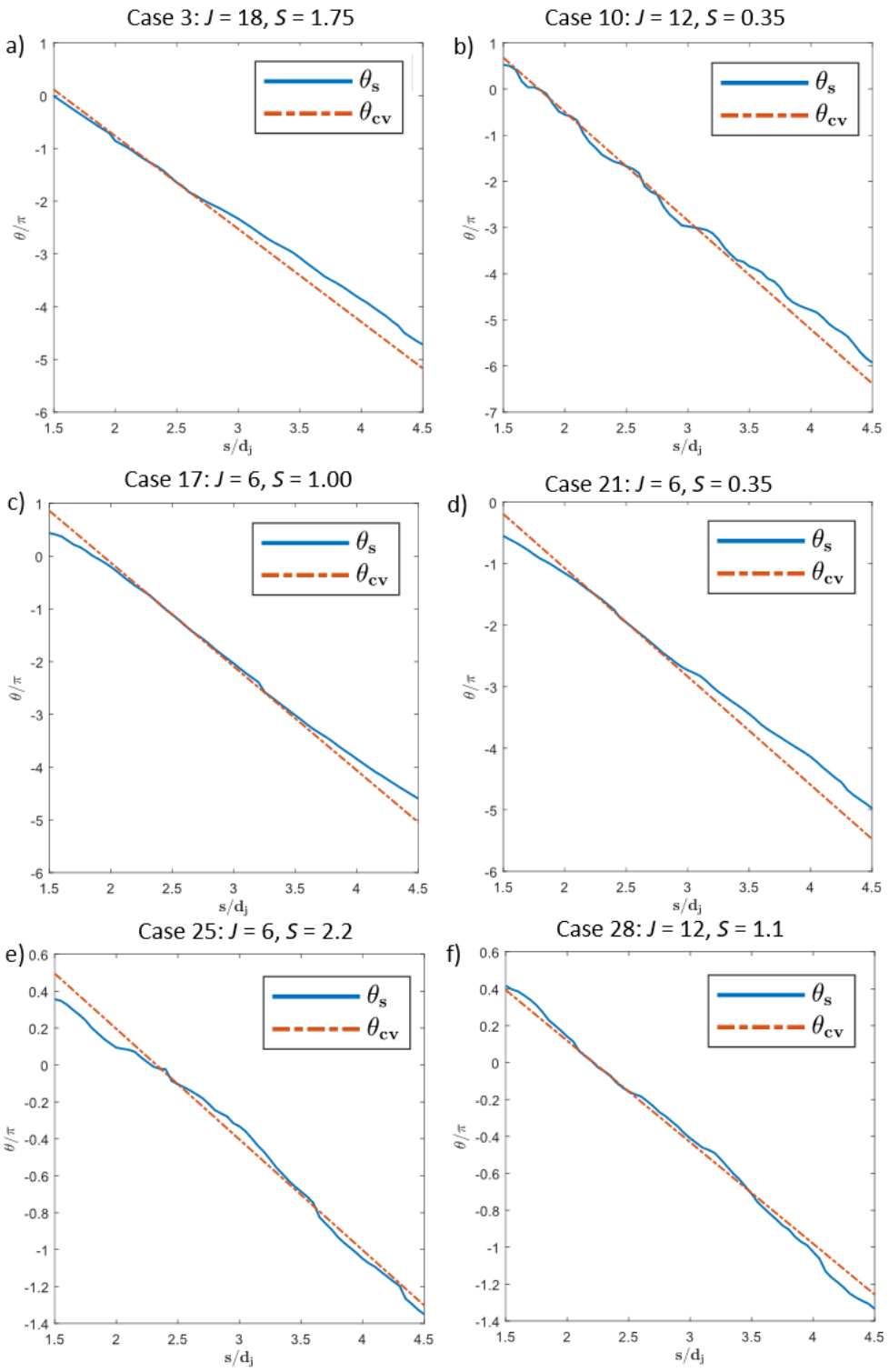

Figure 5.23: Phase roll-off for specific cases comparing the phase extracted from the DFT (θ_s) and the phase roll-off of the vortex convection speeds (θ_{CV}).

The phase roll-off for a few cases, calculated from the time-domain analysis (θ_s), is plotted against the phase roll-off using the extracted vortex convection speed (θ_{CV}) in Figure 5.23. The instability phase speed tends to increase along the jet centerline, due to acceleration in the crossflow direction. For the NR cases (Figure 5.23a and b) the phase roll-off matches well with the slope of the reference phase roll-off of a disturbance with convection speed (U_C) in the region $s/d_j = 1.5$ to $s/d_j = 2.5$. Past this point the phase speed of the instability deviates marginally from the reference convection speed. For the reacting cases (Figure 5.23c and d), the initial slope deviates from the reference slope, likely due to the fundamental instability being weak in the near field region for the reacting cases. Finally, for the R2 cases, due to the absence of clear vortical structures, the vortex tracking technique cannot capture the convection speeds through direct identification of the structures.

$$U_C = \frac{2\pi f_0}{d\theta_s/ds} \tag{5.10}$$

Given that the convections speeds match well with the phase roll-off for the NR and the R1 cases, the phase roll-off can be used to infer a convection speed for the R2 cases using Eq. 5.10. Here the slope $d\theta_s/ds$ is extracted from the phase roll-off plots by using a linear fit between the locations $s/d_j = 2.5$ to $s/d_j = 3.5$ primarily because the instability strength for the R2 cases is very weak upstream of this region (Figure 5.7).

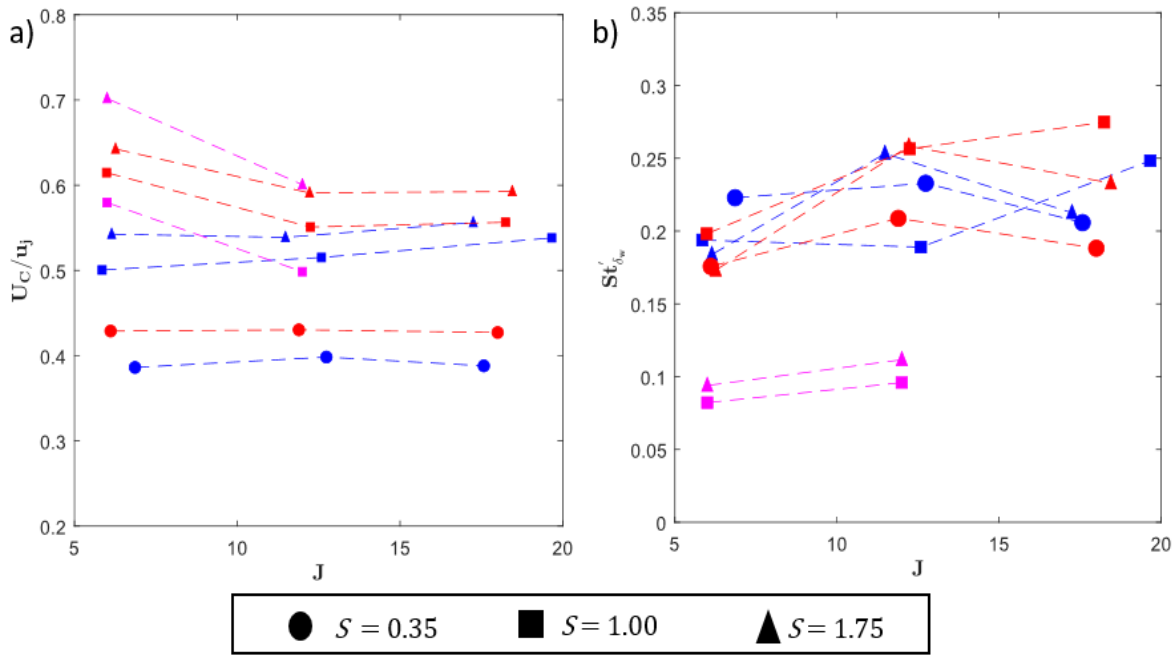

Figure 5.24: a) Normalized convection speed, U_C with respect to J, line connect points at constant target S; b) Characteristic Strouhal numbers using the scaling St'_{δ_w}; Blue points – NR, Red points – R1 and Magenta points – R2. For the R2 cases, S = 1.0 markers were used to represent cases with S = 1.1 and similarly the markers for S = 1.75 correspond to S = 2.2.

The normalized convection speed, U_C/U_1, for all the cases is plotted in Figure 5.24. The bias in the convection speed is apparent across different levels of stratification as well as between R1 and NR cases from Figure 5.24. For iso-density NR conditions there is no bias expected and consequently, $U_C/U_1 \sim 0.5$ which is true for the NR, S = 1.0 cases (blue squares). For lower S values, $U_C/U_1 < 0.5$ and for cases where the jet has a higher density, the jet material tends to drag the vortex due to the momentum bias and $U_C/U_1 > 0.5$. The difference between the R1 and NR cases at analogous J and S values effectively shows that the earlier hypothesis that the R1 cases are governed by a density ratio based on the high temperature region surrounding the flow. The reacting cases show a higher U_C/U_1 which implies that this density ratio, $S' > S$ and consequently the density of the slow stream in

the CCSL model $\rho_2 \sim \rho_f < \rho_\infty$. The R2 cases in general (other than Case 26: $J = 12, S = 2.2$) indicate the presence of a significant bias but, this bias appears to vary significantly with J and not just S. This suggests that the vortex convection speed for these reacting cases is not merely affected by simply a density stratification effect but, is likely influenced by the collocation of heat release with the shear center.

Further, the characteristic frequency scale constructed as $St'_{\delta_w} = f\delta_w/U_C$ appears to collapse the data better than the previous scaling (Figure 5.24) for the R1 and NR cases. Since there is no apparent bias with the variation of St'_{δ_w} with respect to *S* or the presence of reactions (R1 vs NR), the variation in St'_{δ_w} can be attributed to the uncertainty in the measured vortex convection speed as well as any bias effects involved in the estimation of δ_w from PIV obtained velocity data. Again, R2 cases do not appear to follow the same trend as the NR and R1 cases since the St'_{δ_w} scaling reduces the variance between the two R2 cases but does not collapse them with the other two conditions. This would imply that the length scale used for this scaling δ_ω does not accurately capture the characteristic length scale for the R2 cases. For the R2 cases, since the region of heat release, and consequently the region of low density lies at the shear center, the density profile is likely largely non-monotonic compared to the R1 and NR cases, and therefore δ_ω is not a good surrogate for the momentum thickness (θ).

5.4.4 Extracting S' for reacting cases

The bias observed due to the influence of the flame induced density stratification on the vortex convection speeds can be quantified by using the two-dimensional shear layer entrainment model postulated by Dimotakis [121]. The model builds onto the hypothesis

that there exists a stagnation point along the midplane for a two-dimensional mixing layer. From the perspective of an advecting structure (Figure 5.25b), this would imply that the dynamic pressure due to each stream is matched at this location and consequently

$$\rho_1(U_1 - U_C)^2 \cong \rho_2(U_C - U_2)^2 \tag{5.11}$$

This can be rearranged to provide the scaling as –

$$\sqrt{S'} = \frac{U_C - U_2}{U_1 - U_C} \tag{5.12}$$

where the quantities U_C, U_1 and U_2 are directly measured in line with the CCSL model, leaving the only unknown as the effective density ratio S'. For the non-reacting cases S' is expected to be close to S, while for reacting cases as discussed earlier $S' > S$ due to the low-density flame which surrounds the CCSL.

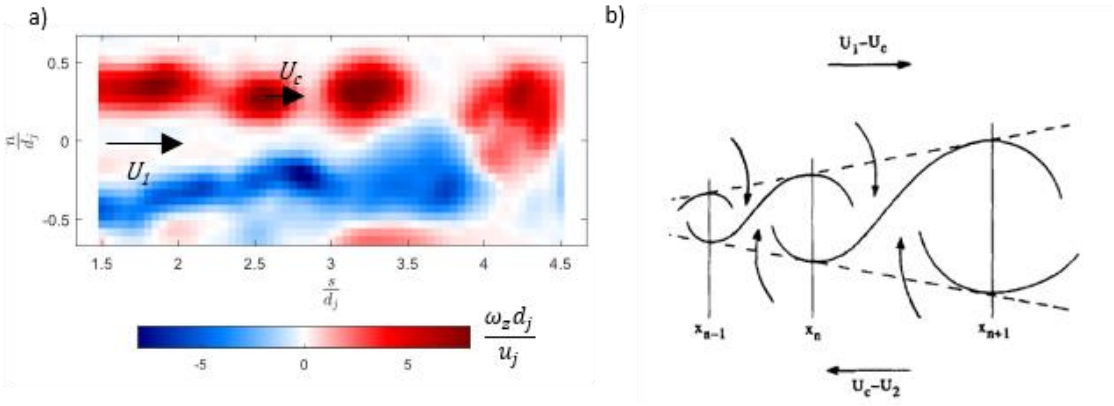

Figure 5.25: a) Orientation of the vorticity field in (s, n) coordinate system depicting the windward shear layer as a mixing layer; b) Schematic for the two-dimensional entrainment model for a mixing layer – Dimotakis [121] in the frame of reference of the vortex convection (U_c).

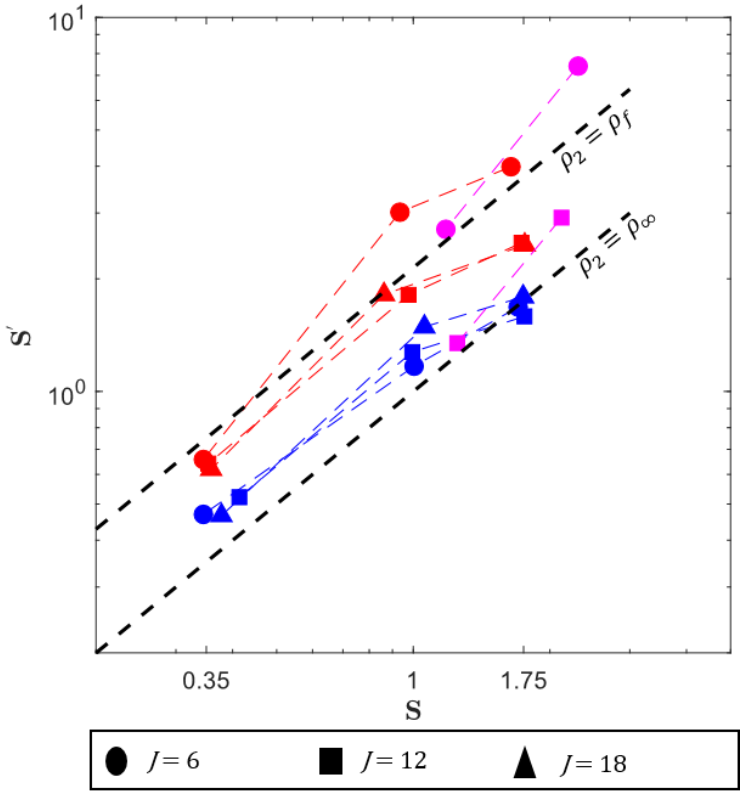

Figure 5.26: Extracted density ratio S' versus the jet to crossflow density ratio S across different NR and R1 conditions; Blue points – NR, Red points – R1.

The density ratio (S') extracted using Eq. 5.12 is plotted versus the jet to crossflow density ratio which is based on the non-reacting flow parameters (Figure 5.26). The two dashed lines represent conditions where $\rho_2 = \rho_\infty$ ($S' = S$) and the case where the density of the slower stream in the CCSL model can be approximated as $\rho_2 = \rho_f$. The distribution of data points across the different *J* cases show that for most of the NR cases $S' \sim S$ as most of them lie along the line defined by the assumption $\rho_2 = \rho_\infty$. For the reacting cases (R1), the cases appear to line along the line defined by $\rho_2 = \rho_f$. Each individual case shows some amount of variance from this scaling, suggesting practically that this density lies in the range - $\rho_\infty > \rho_2 > \rho_f$. Given the variation in the flame position (f_{st}), as discussed in

the previous chapter, with respect to the different R1 jet compositions this is not surprising as ρ_2 will likely depend on the location of f_{st} with respect to the shear center. In addition, the low *J* cases show $\rho_2 < \rho_f$, which is unlikely from a practical standpoint and therefore suggests that the model might not be suitable in cases with high trajectory curvature which likely violates the assumptions in the CCSL model. In addition, the CCSL is a purely two-dimensional model which might not be quantitatively accurate in capturing the convection speeds of coherent structures in a highly three dimensional flowfield. Despite these variations, the R1 cases show a systematic density bias compared to analogous NR conditions. Thus, the predicted S' captures the trends related to the effect of combustion on creating analogous conditions at higher density ratios due to the presence of the flame along the CCSL.

Again, the R2 cases appear to violate this scaling paradigm, since the predicted density ratio appears to lie across both the $\rho_2 = \rho_f$ and $\rho_2 = \rho_\infty$ lines. It appears that the effect of combustion on the R2 cases cannot be captured by simply equating it to an imposed density stratification. For the R2 cases the effect of combustion also appears to depend on the configuration, accelerating the convecting structure by a relatively larger amount for the *J* = 6 cases.

5.4.5 Convective to globally unstable transition

The extracted S' is plotted with respect to the CCSL velocity ratio Λ for the different cases in Figure 5.27. The two reference contours corresponds to the theoretical transitional boundary from Jendoubi and Strykowski [135] for a counter-current axisymmetric jet. They identify two saddle points from the $k_r - k_i$ complex plane which they categorize as

mode #1 (solid line) and mode # 2 (dashed line). Mode #1 essentially requires counterflow at all density ratios to achieve absolute instability similar to the observations by Pavithran and Redekopp [134] for a CCSL. Mode # 2 is generally convectively unstable for $S' > 1$, but for low density ratios, it shows absolute instability for $\Lambda < 1$ (no counterflow). This is in line with the observations by Monkewitz and Sohn [54] who noted absolute instability in hot jets with no external flow.

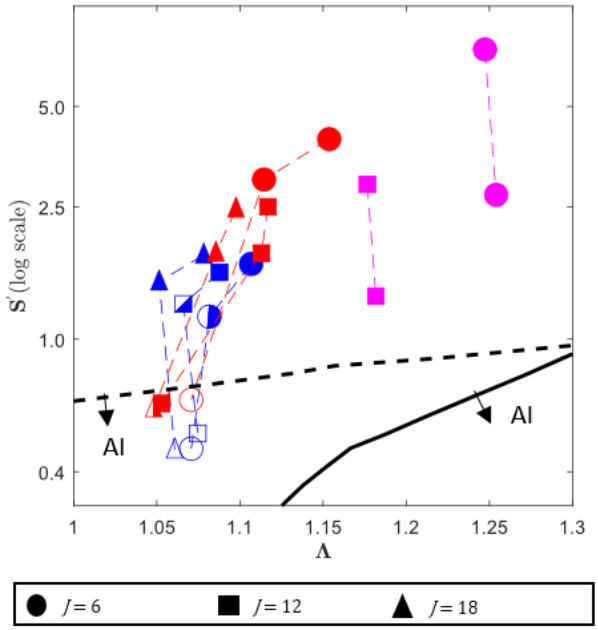

Figure 5.27: Extracted density ratio S' versus the CCSL velocity ratio Λ across different NR and R1 conditions; Blue points – NR, Red points – R1; Filled markers indicate convectively unstable behavior, Empty markers indicate global instability while half-filled markers indicate transitional behavior.

The results from this current study appear to follow transitional behavior based on mode #2 as the hollow data points (globally unstable) cases are clustered below the dashed line while none fall into the AI region with respect to mode #1. This further supports the observations made earlier that for the experimental conditions considered here the driving

parameter for convective to global transition is the density ratio S' and not Λ. On the other hand, Shoji et al. [56] demonstrated that their results showed good agreement with the transitional velocity ratio Λ_{crit} which essentially captures the behavior of mode #1 – similar to a CCSL as opposed to an axisymmetric jet. Given the complex three-dimensional structure of the base flow it is possible that the actual transitional boundary for such a configuration is much more complex and would likely be influenced by the presence of both axisymmetric eigen modes as well as those that resemble a planar shear layer. The relative magnitude of the counterflow observed by Shoji et al. [56] and Iyer and Mahesh [58] were stronger than that observed across all the conditions in this study (Figure 5.24). Consequently, the magnitude of counterflow may essentially decide which parameter, Λ or S', is more dominant and governs the transitional behavior.

Another distinction between the experimental paradigm employed by both Iyer [58] and Shoji et al. [56] compared to this study is the manner in which they vary J. They decrease the momentum flux ratio by essentially increasing the crossflow velocity magnitude (u_∞) while keeping the jet velocity (u_j) fixed. But, because the counterflow magnitude is a function of u_∞ they are essentially increasing the strength of the counterflow as they reduce J, thereby increasing the susceptibility to transition to global instability based on Λ. In this study, due to the constraints of operating a vitiated main burner, the crossflow conditions are fixed while the jet velocity is used to control the value of J. But, as u_j has a relatively negligible effect on altering the counterflow magnitude, changing J by a similar amount will likely cause a significantly smaller variation in Λ. This can be observed by noting that for most S values in this study a change of J from 6 to 18 effectively shifts the value of Λ by less than 5% while based on the data in Shoji et al. [56], a similar

variation in J would increase Λ by 15-25%. Thus, the velocity ratio here is significantly weaker with respect to controlling the transition, primarily because the value of u_j would have to be significantly reduced to get to the transitional values of Λ, predicted for a planar CCSL.

In addition to the inviscid mechanisms discussed above, Shoji et al. [56] demonstrated that J_{crit} decreased with decreasing viscosity ratio. This suggests that cases with a lower viscosity ratio, and consequently a thinner value of θ are likely to show a weaker transition to global instability – requiring a higher counterflow magnitude. The viscosity ratio for the cases considered here were computed considering the CCSL model as listed in Section 5.4.2. The R1 cases show a lower viscosity ratio, on account of being surrounded by high-temperature, high-viscosity fluid. While this decrease in the viscosity ratio for the R1 cases might explain the lower J_{crit}, the vorticity thickness of these cases matches the NR conditions, in contrast to the observations of Shoji et al. [46]. For the R2 cases, the high temperature fluid inside the shear layer results in larger viscosity and a significantly thicker vorticity thickness.

5.5 Summary

This chapter focused on characterizing the high-frequency dynamics of the shear layer across different RJICF conditions. The raw Mie scattering and associated processed vector fields provide a qualitative understanding of the shear layer behavior, including the rollup of shear layer vortices. Similar to the observations in the previous chapter, the NR and R1 cases were qualitatively similar while the R2 cases showed a significantly suppressed shear layer with no vortex rollup.

Spectral content of the transverse velocity data was extracted by probing the windward shear layer at multiple locations along the streamwise coordinate direction (s) and observing the power spectrum. In addition to the dominant frequencies, the qualitative nature of the shear layer spectra was used to infer stability characteristics of the windward shear layer. For the NR cases, the low-density conditions showed a strong narrowband spectral response indicating the presence of global modes while most of the other conditions showed weaker fundamentals with the presence of subharmonics downstream of the jet exit. A few cases were classified as transitional due to their narrowband yet weak spectral response. The R1 conditions demonstrated the combustion (in this configuration) appeared to alter the stability characteristics in the direction of increasingly convectively unstable behavior. Thus, only a single case was observed to show strong global oscillations while most other cases showed a more broadband spectral response. Finally, the R2 cases showed a qualitatively very different spectrum containing significantly weaker low frequency content. An interesting observation was that for these cases, although the fundamental frequencies were weaker, the corresponding noise floor was also significantly reduced which allowed for these narrowband signals to be identified.

In addition to the time-domain analysis, Lagrangian vortex tracking was used to construct *s*-*t* plots which allowed for the characteristic length and timescales to be extracted directly from the identification of vortical structures. These histograms of characteristic vortex passing frequencies helped validate that the extracted St values were not aliased with respect to the sampling frequency. In addition, the source of subharmonics was clearly correlated with the increase in vortex pairing as the vortices advect downstream.

Snapshot POD was used further to extract the spatial structure of the dominant modes capturing the advecting shear layer vortices. The POD modes provided another method of classification of instability behavior since globally unstable cases were characterized with high energy POD mode pairs with strong periodicity (as described by

the correlation between the time coefficients). For the R1 cases, the energy content of the shear layer modes were reduced compared to the energy contained in modes corresponding to jet flapping. Further, in the R2 cases no significant energy attributed to the low frequency tones detected in the spectrum could be observed and an overwhelming majority of the energy in the flow was contained among jet flapping modes.

The counter current shear layer model (CCSL) was evaluated as a means to extract a new set of parameters which would explain the stability effects of combustion. The model was initially formulated by quantifying the counterflow across the different cases. From this, the shear layer velocities U_1 and U_2 were extracted. In addition, a new length scale - δ_ω was introduced as a means to better collapse the St scaling by capturing the effect of stratification on modifying the transverse shear layer strength. The sensitivity of the St scaling was revealed to be sensitive to density stratification through the choice of velocity scale as well. Consequently, the advection speed of the vortices U_C was extracted from the *s-t* plots and used to collapse the frequency scaling (St'_{δ_ω}).

Since the U_C values demonstrated a bias which could be analytically related to the density stratification, the extracted U_C values along with the shear layer velocities U_1 and U_2 were used to quantify the level of stratification for each case using the parameter S'. For the NR cases it was demonstrated that $S' \sim S$ while for the R1 cases $S' > S$ indicating that the ratio between the flame and jet density was a critical parameter (and not the crossflow to jet density ratio like the NR cases). Finally, the S' and Λ, the counter-current velocity ratio were used to demonstrate that the stability behavior of the NR and R1 cases can be captured using these parameters. Comparison with theoretical curves related convective to absolute instability transition demonstrated that the current study shows good agreement with the behavior of shear layer modes associated with low-density jets.

CHAPTER 6. CONCLUSIONS AND RECOMMENDATIONS FOR FUTURE WORK

The current work experimentally investigates multiple flame/flow configurations to better understand the different mechanisms by which combustion affects flowfield dynamics. On a fundamental level, combustion essentially interactions with flow hydrodynamics through various vorticity manipulation mechanisms. While this phenomenological model provides a qualitative understanding, predicting the behavior of practical reacting configurations often require simpler models that broadly capture the effects of combustion, i.e. representing the flame as a base flow density stratification, that can be directly related to design specific parameters.

Given the highly local nature of combustion effects, and highly sensitive and complex nature of flame stabilization, there is a need to isolate flame and flow configurations, where the effects can be captured through a simple model (stratification of the base flow) compared to a more involved analysis (dilatation suppressing vorticity). The current study systematically varies the radial flame location (with respect to the shear center) for a reacting jet in crossflow. The flame is moved from outside to inside the shear layer while ensuring that it is attached and thereby has an impact on the near field dynamics. Juxtaposing the results for these two configurations achieved the aforementioned goal of identifying configurations, where simple stratification models can be used to understand the reacting flow physics. Controlling the flame position essentially behaves as a switch to traverse between the two configurations. A series of experiments were designed to systematically vary the primary non-reacting jet parameters J and S across

these reacting and non-reacting configurations. These method of controlling the flame impact could be extended to assess and isolate the effect of combustion on the dynamics of any free shear flow as well as provide new parameters to capture the effects of combustion.

This chapter further outlines specific contributions from this work as well as provides recommendations regarding the direction of future work.

6.1 Summary of key findings

The first major contribution of this work is the experimental manipulation of the flame position with respect to the shear center. To the authors best knowledge, few studies [77, 81] have experimentally manipulated the flame position in jet diffusion flames to understand the effect on the shear layer rollup. This study is the first to document the flame and flow structure for a JICF type shear configuration where the flame lies inside the shear layer (R2). The OH-PLIF data characterizes reaction zone structure for this configuration capturing interesting phenomena including the auto-ignition stabilized leeward and windward flame branches.

The second major contribution of this work is the characterization of stability trends for NR, R1 (flame outside the shear layer) and R2 (flame inside the shear layer) type JICF configurations. The shear layer behavior was captured by using a vortex identification technique which allowed the ensemble metrics characterizing vortex strength to be calculated for each configuration. The captured swirling strength, circulation and, vortex area allowed for the impact of the different jet parameters (J, S) on the shear layer dynamics to be quantified. The swirling strength allowed for the calculating of the shear layer

instability growth rate, demonstrating that S primarily changes the jet dynamics. This further suggested that the growth rates for the reacting cases (R1) were based on flame induced density stratification. The highly suppressed growth rates extracted for the R2 cases supported the visual evidence of weak vortex rollup in the near field. The other metrics, including the mixing transition distance (l_{trans}) further supported the primary role of the density ratio in predicting shear layer dynamics. While the mixing transition length, and consequently its larger value in reacting flows, have long been thought to strongly scale with Re [79], the data presented here showed a strong inverse correlation with the initial growth rate. This suggests that under the investigated conditions, the impact of combustion can be captured, to a large degree, by considering inviscid instability mechanisms and the role of viscosity is secondary.

The third major contribution of this study was the extensive characterization of the shear layer instability frequencies through high repetition rate SPIV measurements. The qualitative nature of the frequency spectrum was used to identify cases which showed strong narrowband oscillations and those which showed a weaker more broadband natural response. The classification of cases as globally vs convectively unstable for NR and R1 conditions was performed using the spectral characteristics, spectral amplitude as well as the periodicity of the dominant POD shear layer modes, similar to the classification carried out in previous NR JICF studies.

The observed frequencies were collapsed by considering different characteristic scales including the vorticity thickness (δ_ω) and the vortex convection speed (U_C), obtained through Lagrangian vortex tracking. Since the R1 and NR cases collapsed well with the above scaling, the scales were assumed to capture the effects of combustion, both on the

velocity profile as well as density stratification effects. Consequently, the scales presented collapsed R2 cases between themselves but failed to reconcile the characteristic frequencies with the NR and R1 cases. This led to the conclusion that δ_ω cannot accurately capture the characteristic length scale and consequently is not a good surrogate for the momentum thickness (θ) in configurations like the R2 cases where there is a highly non-monotonic density variation concurrent with the shear layer.

The final contribution is the extension of the counter current shear layer (CCSL) model by including the stratification parameter (S') to capture the observed shear layer stability characteristics for both the NR and R1 type conditions. For the NR cases $S' \sim S$, since the density stratification was imposed through the jet and crossflow compositions. For the R1 cases, the S' was shown to be systematically larger than S leading to the conclusion that ρ_f plays an important role in modeling the density stratification in the reacting cases. The extracted S' values for the R2 cases, on the other hand, suggest that the variations cannot be captured simply by an analogous density stratification. The extracted 'density-bias' (S') for these cases appeared to be strongly dependent on J suggesting that the near field heat release likely causes the acceleration of the vortices in the low J, which could mimic the effects of a large density bias.

Extraction of S' allowed for the traditionally defined jet parameters (S, J) to be mapped into a new parameter space defined by the CCSL parameters S' and Λ. The location of the parameters on this space were correlated strongly with the classified instability characteristics (convective vs globally instability). The observed transition to global stability for the current study appeared to be dominated by the low-density transition effects

S'_{crit} and not Λ_{crit}. This apparent insensitivity with respect to Λ was found to be related to the differences between the experimental setups and method of varying the parametric value, J. In either case, the mapping $J \rightarrow \Lambda$ behaves differently. For the current study, decreasing J was shown to have a much weaker effect on increasing the value of Λ, compared with the data from Shoji et al. [56], due to the low counterflow magnitude.

This understanding of the shear layer behavior sensitivity has broad implications on the design of JICF experimental test matrices. Interpreting the impact of changing S and J, the two JICF parameters typically controlled, depends on the nature of crossflow, the boundary layer thickness as well as the method in which that J value is obtained and consequently any exploration of the sensitivity of shear layer stability behavior will require the mapping of (S, J) to the (S', Λ) parameter space.

6.2 Recommendations for future work

6.2.1 Understanding the dynamics of the R2 cases

The work presented here has established the existence of a novel reacting flow configuration where the effect of heat release cannot be understood solely through a imposed stratification. Its unique flow and flame topology as well as stability behavior raises a number of further questions which would benefit from future in-depth experimental and computational investigations. Since the data was analyzed primarily in the centerplane, further studies can focus on characterizing the velocity along transverse cuts (*x*-*z* and *y*-*z* planes) with respect to the jet core. The behavior of wake vortices can be strongly correlated with the level of aerodynamic blockage created by the configuration and consequently one would expect the R2 cases to show strong wake vortex shedding. Further given that the CVP is known to be highly correlated with shear layer behavior it would be

interesting to characterize the structure of the CVP when the shear layer rollup is significantly suppressed.

The current configuration would also benefit from three-dimensional flow characterization through tomographic experimental methods or even detailed computational work. One thing to note is that any computational work that seeks to reproduce the R2 type configuration created here will need to use finite rate chemistry to capture the observed flame topology (with lifted leeward branch) and the effect of H_2 doping. These studies would also shed light on the dominant flame stabilization mechanism for these configurations.

Since the effect of H_2 doping can be considered analogous to increasing the reactivity through increasing the working pressure it would also be interesting to see if the flame configuration can be sustained at high pressures without the need for doping. This would have major implications on the current mixing models used while designing RQL type combustors since it would demonstrate that such a flame attachment configuration is possible which would lead to significantly poorer mixing performance that that predicted by non-reacting entrainment models.

6.2.2 Extending the stability classification for reacting cases

While the spectral data and POD modes provide compelling evidence of the classification of convectively and globally unstable configurations, other evidence including tracing the nature of the Hopf bifurcation and the response to external forcing would help definitively classify the shear layer behavior. The (S', Λ) parameter mapping can be used to find transitional locations and perform detailed investigation at the edges of the transitional contour for reacting cases, similar to the approach Davitan et al. [126] used for non-reacting cases.

Since the fundamental shear layer modes for the current study had high characteristic frequencies, it would be challenging to force the jet at these frequencies. Thus, future studies looking to characterize the forced response of RJICF configurations across similar parameter ranges should seek to scale down the flow velocities. Previous studies have focused on low-frequency crossflow forcing while gaps in literature still exist in quantifying the forced response of the jet in combusting environments. In addition, for the R2 cases, it would be interesting in assessing the role of combustion on damping out any vortex rollup from the forced response of the shear layer. This would help with assessing the exact mechanism by which combustion is creating a fundamentally different flow topology in this configuration.

6.2.3 Understanding paths to global instability

Finally, the CCSL model has been demonstrated to be successful in explaining the transition to global instability for some NR JICF configurations [56]. For the current study on the other hand, the pathway was similar to that observed for low density axisymmetric jets [54] leading to the implication that the CCSL is stronger in cases with a higher level of counterflow – fuller boundary layer, higher crossflow velocity. But, in a flowfield as topologically rich as a JICF it is possible that these are not the only mechanisms that could drive the transition to global instability. Like the recirculation region upstream of the windward shear layer, there is a significant amount of counterflow in the leeward recirculation region leading to the hypothesis that this counterflow could drive transition to global instability. In addition to this, the far field JICF structure for very low J jets often resembles a wake deficit, which could provide a pathway for global instability through interacting shear layers. Global stability analysis could shed some light on the viability of these different transitional mechanism and the regions of the flow that drive global

instability. While it is currently computationally challenging to perform global stability calculations on highly turbulent reacting flows, as computational resources get more powerful, this objective will become realizable.

A. APPENDIX - DESIGN OF EXPERIMENT DETAILS

This appendix presents additional details of the experimental setup, uncertainty quantification of the errors associated with the measured values and details of the calculations involved in choosing and validating test conditions (design of experiments).

A.1 Crossflow temperature estimation

Estimating the temperature of the crossflow is challenging because most thermocouples cannot survive the environment in the hot crossflow and despite the ceramic lining, the heat loss from the rig is too significant to assume adiabatic boundary conditions in the flow channel. During normal operation of the rig a ceramic sheathed R-type thermocouple is introduced in the flow in the flow conditioning section before the honeycomb due to the fact that any thermocouple in the test section would interfere with the RJICF flowfield. In order to obtain an estimate of the temperature in the test section, experiments where a second ceramic sheathed thermocouple was introduced through the jet nozzle in order to obtain an estimate of the temperature in the flow at the jet axial location while the vitiator is run at conditions concurrent with the experimental conditions.

Table A-1: Temperatures measured to characterize crossflow conditions

Case	T_{ad}	$T_{int\#1}$	$T_{int\#2}$	$T_{meas,V}$
Lean	1635	1400	1040	1180
Rich	1705	1450	1100	1150

The temperature in the flow conditioning unit, ($T_{int\#1}$), can be linearly correlated with the temperature at the jet location ($T_{int\#2}$) at constant vitiator conditions ($\dot{m}_{vitiator}, T_{pre-heat}$)

which allows for the estimation of T_∞ from $T_{int\#1}$, which is the only thermocouple present in the flow during normal operation. The ceramic sheathed thermocouples are known to have large bias errors at high temperatures due to the equilibrium state where the temperature inside the sheath, and in contact with the probe, is lower than the temperature outside due to high radiation losses from the sheath. The temperature can also be estimated from the mass averaged flow velocity (u_∞) from the measured velocity profile (section 2.3.1), which can be used to obtain the fluid density (ρ_∞). The temperature can thus, be obtained from the idea gas law by assuming that the pressure through the experiment is constant $p_\infty = p_{atm}$. This temperature, $T_{meas,V}$, is listed in Table A-1 and is on average 150 K higher than the temperature measured by the thermocouple $T_{int\#2}$. Thus, for all the experiments the flow temperature T_∞ is linearly estimated by using the deviation of measured $T_{int\#1}$ from the value of $T_{int\#1}$ listed in Table A-1.

A.2 Experimental measured parameters

A.2.1 4 kHz SPIV + OH-PLIF experiments

Table A-2: Measured test conditions for low speed experiments

Case	Type	T_∞	ρ_∞	u_∞	Re_∞	ρ_j	u_j	μ_j	Re_j	S	J
1	NR	1153	0.30	14.73	1.11E+04	0.53	28.2	0.00002	2225	1.76	6.5
2	NR	1146	0.30	14.73	1.11E+04	0.51	38.8	0.00002	2986	1.71	11.9
3	NR	1141	0.30	14.53	1.10E+04	0.51	47.4	0.00002	3607	1.68	17.9
4	NR	1147	0.30	14.55	1.10E+04	0.50	62.13	0.00002	4650	1.69	30.8
5	NR	1158	0.30	14.76	1.11E+04	0.27	38.44	0.00002	1560	0.91	6.2
6	NR	1154	0.30	14.78	1.11E+04	0.26	54.04	0.00002	2141	0.89	11.9
7	NR	1144	0.30	14.5	1.10E+00	0.26	62.2	0.00002	2426	0.9	16.6
8	NR	1140	0.30	14.5	1.10E+04	0.27	83.76	0.00002	3392	0.89	29.7
9	NR	1156	0.30	14.71	1.10E+04	0.11	61.15	0.000027	727	0.36	6.2
10	NR	1160	0.30	14.89	1.11E+04	0.10	87.33	0.000027	980	0.34	11.7
11	NR	1154	0.30	14.65	1.10E+04	0.10	111.21	0.000027	1096	0.33	15.8
12	NR	1148	0.30	14.57	1.10E+04	0.10	137.39	0.000027	1542	0.34	30.2
13	R1	1124	0.31	14.41	1.11E+04	0.48	27.84	0.000017	2373	1.6	6.0
14	R1	1131	0.30	14.4	1.09E+04	0.52	38.05	0.000017	3487	1.71	11.9
15	R1	1124	0.31	14.4	1.11E+04	0.52	47.37	0.000017	4323	1.69	18.3
16	R1	1132	0.30	14.4	1.10E+04	0.51	61.36	0.000017	5546	1.69	30.7
17	R1	1155	0.30	14.76	1.11E+04	0.27	38.9	0.00002	1564	0.9	6.3
18	R1	1167	0.30	14.95	1.11E+04	0.33	48.85	0.00002	2184	1.1	12.8
19	R1	1160	0.30	14.75	1.10E+04	0.29	64.9	0.00002	2801	0.97	18.8
20	R1	1135	0.30	14.46	1.10E+04	0.26	87.57	0.00002	3353	0.85	31.2
21	R1	1153	0.30	14.77	1.11E+04	0.10	60.3	0.000012	1557	0.347	5.8
22	R1	1140	0.30	14.5	1.11E+04	0.10	85.5	0.000012	2138	0.35	12.2
23	R1	1120	0.31	14.3	1.11E+04	0.11	104.31	0.000012	2738	0.34	18.1
24	R1	1161	0.30	14.69	1.10E+04	0.10	134.8	0.000012	3518	0.3533	29.7
25	R2	1130	0.20	20.8	1.09E+04	0.45	34.9	0.000033	1434	2.3	6.5
26	R2	1150	0.21	20.5	1.12E+04	0.44	43.2	0.000033	1719	2.17	9.6
27	R2	1120	0.19	21.56	1.09E+04	0.21	53	0.000031	1077	1.07	6.5
28	R2	n/a	n/a	n/a	n/a	n/a	n/a	0.000031	n/a	n/a	n/a

A.2.2 40 kHz SPIV + OH Chemiluminescence experiments*

Table A-3: Measured test conditions for high speed experiments

Case	Type	T_∞	ρ_∞	u_∞	Re_∞	ρ_j	u_j	μ_j	Re_j	S	J
1	NR	1177	0.29	14.8	1.09E+04	0.50	28.11	0.00002	2096	1.71	6.1
2	NR	1170	0.29	14.83	1.10E+04	0.52	37.9	0.00002	2931	1.75	11.5
3	NR	1163	0.30	14.73	1.10E+04	0.52	46.3	0.00002	3577	1.74	17.2
4	NR	n/a	n/a	n/a	n/a	n/a	n/a	0.00002	n/a	n/a	n/a
5	NR	1184	0.29	14.94	1.09E+04	0.29	36.05	0.00002	1574	1	5.9
6	NR	1177	0.29	14.9	1.10E+04	0.27	53.16	0.00002	2306	0.93	11.8
7	NR	1170	0.29	14.8	1.10E+04	0.28	63.8	0.00002	2967	0.95	19.7
8	NR	n/a	n/a	n/a	n/a	n/a	n/a	0.00002	n/a	n/a	n/a
9	NR	1150	0.29	14.8	1.08E+04	0.10	66.6	0.000027	740	0.344	7.00
10	NR	1181	0.29	14.96	1.10E+04	0.10	89.69	0.000027	1107	0.348	12.7
11	NR	1179	0.29	14.93	1.10E+04	0.09	112.8	0.000027	1244	0.32	17.6
12	NR	n/a	n/a	n/a	n/a	n/a	n/a	0.000027	n/a	n/a	n/a
13	R1	1144	0.30	14.44	1.10E+04	0.49	28.2	0.000017	2458	1.65	6.3
14	R1	1160	0.30	14.65	1.09E+04	0.51	38.91	0.000017	3509	1.73	12.2
15	R1	1138	0.30	14.4	1.09E+04	0.53	46.62	0.000017	4344	1.75	18.1
16	R1	n/a	n/a	n/a	n/a	n/a	n/a	0.000017	n/a	n/a	n/a
17	R1	1186	0.29	14.98	1.09E+04	0.27	37.91	0.00002	1535	0.93	6
18	R1	1165	0.30	14.71	1.10E+04	0.29	52.1	0.00002	2251	0.98	12.8
19	R1	1180	0.29	14.5	0.00E+00	0.25	66.7	0.00002	2501	0.86	18.2
20	R1	n/a	n/a	n/a	n/a	n/a	n/a	0.00002	n/a	n/a	n/a
21	R1	1181	0.29	14.92	1.09E+04	0.10	62.8	0.000012	1570	0.34	6
22	R1	1156	0.30	14.69	1.10E+04	0.11	85.2	0.000012	2237	0.35	11.9
23	R1	1175	0.29	14.92	1.09E+04	0.10	105.7	0.000012	2748	0.36	17.8
24	R1	n/a	n/a	n/a	n/a	n/a	n/a	0.000012	n/a	n/a	n/a
25	R2	1130	0.20	14.69	1.07E+00	0.45	35	0.000033	1432	2.3	6.7
26	R2	1150	0.20	20.8	1.08E+00	0.42	49	0.000033	1871	2.1	12.2
27	R2	1150	0.20	20.5	1.07E+00	0.23	46	0.000031	1024	1.2	5.9
28	R2	1200	0.20	21.56	1.04E+00	0.25	62	0.000031	1500	1.2	10.6

A.3 Flame-position calculations

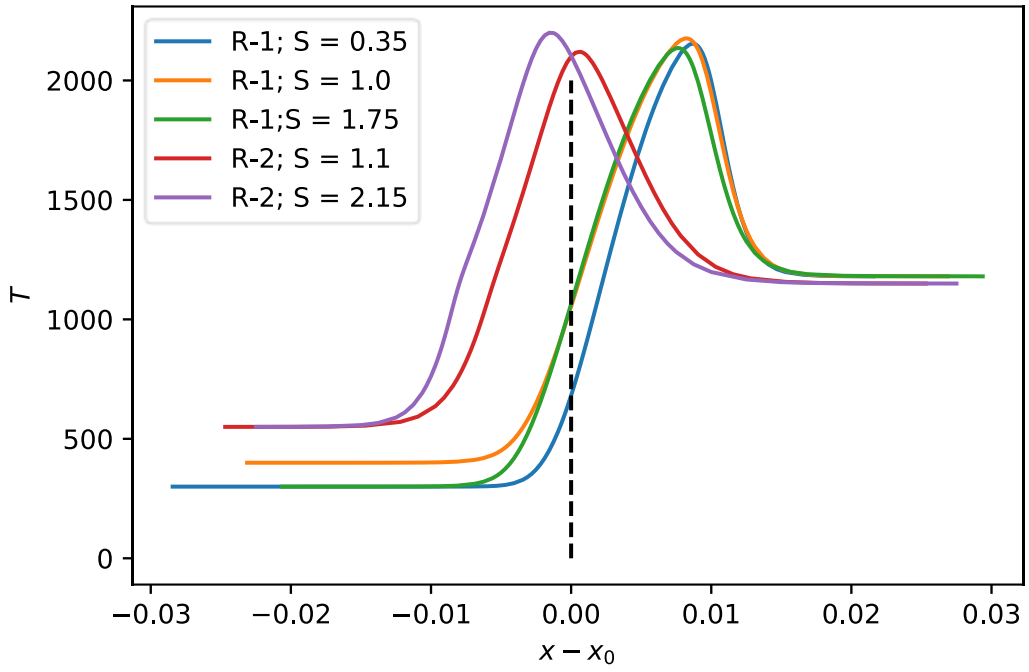

Figure A.1: Temperature profiles for OPPDIFF flames for the 5 reacting jet compositions listed in Table 2-2

In order to estimate the flame position for the premixed flames for the different combinations of jet and crossflow compositions covered in section (), calculations are run using Cantera (). While physically the non-premixed flame lies near the shear layer which acts as an interface between the jet and the crossflow fluid, the calculations here utilize an opposed-diffusion (OPPDIFF) type model to obtain an estimate of the temperature/heat release distribution with respect to the axial location (x). The shear center, x_0 is taken to be the axial location of stagnation ($u_{x,0} = 0$) and thus, the temperature distributions (Figure A.1) help determine whether the flame might lie on the side of the crossflow ($x_f < x_0$) or the jet ($x_f > x_0$).

REFERENCES

1. Kelso, R.M., T. Lim, and A. Perry, *An experimental study of round jets in cross-flow*. Journal of fluid mechanics, 1996. **306**: p. 111-144.

2. Samuelsen, S., *Rich burn, quick-mix, lean burn (RQL) combustor*. The Gas Turbine Handbook, 2006: p. 227-233.

3. Correa, S.M., *Power generation and aeropropulsion gas turbines: From combustion science to combustion technology*. Symposium (International) on Combustion, 1998. **27**(2): p. 1793-1807.

4. Karagozian, A.R., *Transverse jets and their control*. Progress in Energy and Combustion Science, 2010. **36**(5): p. 531-553.

5. Karagozian, A.R., *The jet in crossflow*. Physics of Fluids, 2014. **26**(10): p. 101303.

6. Margason, R.J., *Fifty years of jet in cross flow research*. ceaj, 1993.

7. Schlüter, J.U. and T. Schönfeld, *LES of Jets in Cross Flow and Its Application to a Gas Turbine Burner*. Flow, Turbulence and Combustion, 2000. **65**(2): p. 177.

8. *The Hall of Fame*, in *Gas Turbines for Electric Power Generation*, S.C. Gülen, Editor. 2019, Cambridge University Press: Cambridge. p. 626-650.

9. Sirignano, M.D., et al., *Nitrogen oxide emissions from rich premixed reacting jets in a vitiated crossflow*. Proceedings of the Combustion Institute, 2019. **37**(4): p. 5393-5400.

10. Lyra, S., et al., *Structure of hydrogen-rich transverse jets in a vitiated turbulent flow*. Combustion and Flame, 2015. **162**(4): p. 1234-1248.

11. McKinney, R., et al., *The Pratt & Whitney TALON X Low Emissions Combustor: Revolutionary Results with Evolutionary Technology*, in *45th AIAA Aerospace Sciences Meeting and Exhibit*. 2007.

12. Smith, S.H. and M.G. Mungal, *Mixing, structure and scaling of the jet in crossflow*. Journal of Fluid Mechanics, 1998. **357**: p. 83-122.

13. Kamotani, Y. and I. Greber, *Experiments on a Turbulent Jet in a Cross Flow*. AIAA Journal, 1972. **10**(11): p. 1425-1429.

14. Holdeman, J.D., *Correlation for temperature profiles in the plane of symmetry downstream of a jet injected normal to a crossflow*. 1972.

15. Su, L.K. and M.G. Mungal, *Simultaneous measurements of scalar and velocity field evolution in turbulent crossflowing jets.* Journal of Fluid Mechanics, 2004. **513**: p. 1-45.

16. Pratte, B.D. and W.D. Baines, *Profiles of the round turbulent jet in a cross flow.* Journal of the Hydraulics Division, 1967. **93**(6): p. 53-64.

17. Broadwell, J. and R. Breidenthal, *Structure and mixing of a transverse jet in incompressible flow.* Journal of Fluid Mechanics, 1984. **148**: p. 405-412.

18. Hasselbrink, E.F. and M.G. Mungal, *Transverse jets and jet flames. Part 1. Scaling laws for strong transverse jets.* Journal of Fluid Mechanics, 2001. **443**.

19. Muppidi, S. and K. Mahesh, *Study of trajectories of jets in crossflow using direct numerical simulations.* Journal of Fluid Mechanics, 2005. **530**: p. 81-100.

20. Shan, J.W. and P.E. Dimotakis, *Reynolds-number effects and anisotropy in transverse-jet mixing.* Journal of Fluid Mechanics, 2006. **566**.

21. Megerian, S., et al., *Transverse-jet shear-layer instabilities. Part 1. Experimental studies.* Journal of Fluid Mechanics, 2007. **593**.

22. Karagozian, A.R., *The flame structure and vorticity generated by a chemically reactingtransverse jet.* AIAA Journal, 1986. **24**(9): p. 1502-1507.

23. Kadota, T., J.X. Wang, and T. Kawaoka, *Structure of Propane Jet Diffusion Flame in a Cross Flow.* JSME international journal. Ser. 2, Fluids engineering, heat transfer, power, combustion, thermophysical properties, 1990. **33**(3): p. 575-581.

24. Hasselbrink, E.F. and M.G. Mungal, *Transverse jets and jet flames. Part 2. Velocity and OH field imaging.* Journal of Fluid Mechanics, 2001. **443**.

25. Wilde, B.R., *Dynamics of Variable Density Ratio Reacting Jets in an Unsteady Vitiated Crossflow*. 2014, Georgia Institute of Technology: Atlanta, United States.

26. Wagner, J.A., et al., *Flowfield measurements and flame stabilization of a premixed reacting jet in vitiated crossflow.* Combustion and Flame, 2015. **162**(10): p. 3711-3727.

27. Sullivan, R., et al., *Time-averaged characteristics of a reacting fuel jet in vitiated cross-flow.* Combustion and Flame, 2014. **161**(7): p. 1792-1803.

28. Steinberg, A.M., et al., *Structure and stabilization of hydrogen jet flames in cross-flows.* Proceedings of the Combustion Institute, 2013. **34**: p. 1499-1507.

29. Sirignano, M.D., *Experimental Investigation of Nitrogen Oxide Production in Premixed Reacting Jets in a Vitiated Crossflow*. 2019, Georgia Institute of Technology.

30. Wagner, J.A., M.W. Renfro, and B.M. Cetegen, *Premixed jet flame behavior in a hot vitiated crossflow of lean combustion products.* Combustion and Flame, 2017. **176**: p. 521-533.

31. Ahrens, D., et al., *NOx Formation in a Reacting Premixed Jet in Hot Cross Flow*. 2014(45691): p. V04BT04A016.

32. Fric, T. and A. Roshko, *Vortical structure in the wake of a transverse jet.* Journal of Fluid Mechanics, 1994. **279**: p. 1-47.

33. Kelso, R.M. and A.J. Smits, *Horseshoe vortex systems resulting from the interaction between a laminar boundary layer and a transverse jet.* Physics of Fluids, 1995. **7**(1): p. 153-158.

34. T L Doligalski, a. C R Smith, and J.D.A. Walker, *Vortex Interactions with Walls.* Annual Review of Fluid Mechanics, 1994. **26**(1): p. 573-616.

35. Krothapalli, A., L. Lourenco, and J.M. Buchlin, *Separated flow upstream of a jet in a crossflow.* AIAA Journal, 1990. **28**(3): p. 414-420.

36. Wu, J.M., A.D. Vakili, and F.M. Yu, *Investigation of the interacting flow of nonsymmetric jets in crossflow*. AIAA Journal, 1988. **26**(8): p. 940-947.

37. Panda, P.P., et al., *High-repetition-rate planar measurements in the wake of a reacting jet injected into a swirling vitiated crossflow*. Combustion and Flame, 2016. **163**: p. 241-257.

38. Pinchak, M.D., V.G. Shaw, and E.J. Gutmark, *Flow-field dynamics of the non-reacting and reacting jet in a vitiated cross-flow.* Proceedings of the Combustion Institute, 2019. **37**(4): p. 5163-5171.

39. Batchelor, C.K. and G. Batchelor, *An introduction to fluid dynamics*. 2000: Cambridge university press.

40. Becker, H.A. and T.A. Massaro, *Vortex evolution in a round jet.* Journal of Fluid Mechanics, 1968. **31**(3): p. 435-448.

41. Lim, T.T., T.H. New, and S.C. Luo, *On the development of large-scale structures of a jet normal to a cross flow.* Physics of Fluids, 2001. **13**(3): p. 770-775.

42. New, T.H., T.T. Lim, and S.C. Luo, *Effects of jet velocity profiles on a round jet in cross-flow.* Experiments in Fluids, 2006. **40**(6): p. 859-875.

43. Fearn, R. and R.P. Weston, *Vorticity associated with a jet in a cross flow.* AIAA Journal, 1974. **12**(12): p. 1666-1671.

44. Cortelezzi, L. and A.R. Karagozian, *On the formation of the counter-rotating vortex pair in transverse jets.* Journal of Fluid Mechanics, 2001. **446**: p. 347-373.

45. Muppidi, S. and K. Mahesh, *Two-dimensional model problem to explain counter-rotating vortex pair formation in a transverse jet.* Physics of Fluids, 2006. **18**(8).

46. Gevorkyan, L., et al., *Transverse jet mixing characteristics.* Journal of Fluid Mechanics, 2016. **790**: p. 237-274.

47. Drazin, P.G. and W.H. Reid, *Hydrodynamic stability*. 2004: Cambridge university press.

48. Lieuwen, T.C., *Unsteady combustor physics*. 2012: Cambridge University Press.

49. Huerre, P. and P.A. Monkewitz, *Absolute and convective instabilities in free shear layers.* Journal of Fluid Mechanics, 1985. **159**: p. 151-168.

50. Huerre, P. and P.A. Monkewitz, *Local and global instabilities in spatially developing flows.* Annual review of fluid mechanics, 1990. **22**(1): p. 473-537.

51. Getsinger, D.R., et al., *Structural and stability characteristics of jets in crossflow.* Journal of Fluid Mechanics, 2014. **760**: p. 342-367.

52. Michalke, A., *Survey on jet instability theory.* Progress in Aerospace Sciences, 1984. **21**: p. 159-199.

53. Getsinger, D.R., C. Hendrickson, and A.R. Karagozian, *Shear layer instabilities in low-density transverse jets.* Experiments in Fluids, 2012. **53**(3): p. 783-801.

54. Monkewitz, P.A. and K.D. Sohn, *Absolute instability in hot jets.* AIAA journal, 1988. **26**(8): p. 911-916.

55. Yu, M.H. and P.A. Monkewitz, *The effect of nonuniform density on the absolute instability of two-dimensional inertial jets and wakes.* Physics of Fluids A: Fluid Dynamics, 1990. **2**(7): p. 1175-1181.

56. Shoji, T., et al., *On the origins of transverse jet shear layer instability transition.* Journal of Fluid Mechanics, 2020. **890**.

57. Strykowski, P.J. and D. Niccum, *The influence of velocity and density ratio on the dynamics of spatially developing mixing layers.* Physics of Fluids A: Fluid Dynamics, 1992. **4**(4): p. 770-781.

58. Iyer, P.S. and K. Mahesh, *A numerical study of shear layer characteristics of low-speed transverse jets.* Journal of Fluid Mechanics, 2016. **790**: p. 275-307.

59. Schmid, P.J., *Dynamic mode decomposition of numerical and experimental data.* Journal of Fluid Mechanics, 2010. **656**: p. 5-28.

60. Narayanan, S., P. Barooah, and J. Cohen, *Dynamics and control of an isolated jet in crossflow.* AIAA journal, 2003. **41**(12): p. 2316-2330.

61. M'Closkey, R.T., et al., *The actively controlled jet in crossflow.* Journal of Fluid Mechanics, 2002. **452**.

62. Eroglu, A. and R.E. Breidenthal, *Structure, penetration, and mixing of pulsed jets in crossflow.* AIAA journal, 2001. **39**(3): p. 417-423.

63. Sau, R. and K. Mahesh, *Optimization of pulsed jets in crossflow.* Journal of Fluid Mechanics, 2010. **653**: p. 365-390.

64. Zhang, L. and V. Yang, *Flow Dynamics and Mixing of a Transverse Jet in Crossflow—Part II: Oscillating Crossflow.* Journal of Engineering for Gas Turbines and Power, 2017. **139**(8).

65. Fugger, C.A., *Experimental investigation of a reacting transverse jet in a high pressure oscillating vitiated crossflow*. 2015, Purdue University.

66. Coats, C.M., *Coherent structures in combustion.* Progress in Energy and Combustion Science, 1996. **22**(5): p. 427-509.

67. Hermanson, J.C. and P.E. Dimotakis, *Effects of heat release in a turbulent, reacting shear layer.* Journal of Fluid Mechanics, 1989. **199**: p. 333-375.

68. McMurtry, P.A., J.J. Riley, and R.W. Metcalfe, *Effects of heat release on the large-scale structure in turbulent mixing layers.* Journal of Fluid Mechanics, 1989. **199**: p. 297-332.

69. Shin, D. and J. Ferziger, *Linear stability of the reacting mixing layer*, in *28th Aerospace Sciences Meeting*. 1990.

70. Mahalingam, S., B.J. Cantwell, and J.H. Ferziger, *Stability of low-speed reacting flows.* Physics of Fluids A: Fluid Dynamics, 1991. **3**(6): p. 1533-1543.

71. Maslowe, S.A. and R.E. Kelly, *Inviscid instability of an unbounded heterogeneous shear layer.* Journal of Fluid Mechanics, 1971. **48**(2): p. 405-415.

72. Menkes, J., *On the stability of a shear layer.* Journal of Fluid Mechanics, 1959. **6**(4): p. 518-522.

73. Jackson, T.L. and C.E. Grosch, *Inviscid spatial stability of a compressible mixing layer. Part 2. The flame sheet model.* Journal of Fluid Mechanics, 1990. **217**: p. 391-420.

74. Day, M.J., W.C. Reynolds, and N.N. Mansour, *The structure of the compressible reacting mixing layer: Insights from linear stability analysis.* Physics of Fluids, 1998. **10**(4): p. 993-1007.

75. Emerson, B., et al., *Density ratio effects on reacting bluff-body flow field characteristics.* Journal of Fluid Mechanics, 2012. **706**: p. 219-250.

76. Hajesfandiari, A. and D.J. Forliti, *On the influence of internal density variations on the linear stability characteristics of planar shear layers.* Physics of Fluids, 2014. **26**(5).

77. Füri, M., et al., *The effect of flame position on the Kelvin-Helmholtz instability in non-premixed jet flames.* Proceedings of the Combustion Institute, 2002. **29**(2): p. 1653-1661.

78. Mehta, P. and M. Soteriou, *Wake Dynamics of Bluffbody Stabilized Premixed Combustion - Effects of Exothermicity and Forcing*, in *41st Aerospace Sciences Meeting and Exhibit*. 2003.

79. Yule, A.J., et al., *Combustion-Transition Interaction in a Jet Flame.* AIAA Journal, 1981. **19**(6): p. 752-760.

80. Soteriou, M.C. and A.F. Ghoniem. *The vorticity dynamics of an exothermic, spatially developing, forced, reacting shear layer*. in *Symposium (International) on Combustion*. 1994. Elsevier.

81. Chen, L.D., et al., *Vorticity Generation in Jet Diffusion Flames.* Combustion Science and Technology, 1991. **77**(1-3): p. 41-57.

82. Geikie, M.K., et al., *On the Flame-generated Vorticity Dynamics of Bluff-body-stabilized Premixed Flames.* Flow, Turbulence and Combustion, 2017. **99**(2): p. 487-509.

83. Kazbekov, A., K. Kumashiro, and A.M. Steinberg, *Enstrophy transport in swirl combustion.* Journal of Fluid Mechanics, 2019. **876**: p. 715-732.

84. Nair, V., et al., *Shear Layer Dynamics in a Reacting Jet in Crossflow*. Proceedings of the Combustion Institute, 2019. **37**(4): p. 5173-5180.

85. Nair, V., et al. *Tomographic PIV Characterization of the Near field Topology of the Reacting Jet in Crossflow*. in *AIAA Scitech 2020 Forum*. 2020.

86. Pope, S.B., *Turbulent flows*. 2001, IOP Publishing.

87. Marusic, I., et al., *Wall-bounded turbulent flows at high Reynolds numbers: Recent advances and key issues.* Physics of Fluids, 2010. **22**(6).

88. Chauhan, K.A., P.A. Monkewitz, and H.M. Nagib, *Criteria for assessing experiments in zero pressure gradient boundary layers.* Fluid Dynamics Research, 2009. **41**(2).

89. Zanoun, E.-S., H. Nagib, and F. Durst, *Refined cf relation for turbulent channels and consequences for high-Re experiments.* Fluid dynamics research, 2009. **41**(2): p. 021405.

90. Raffel, M., et al., *Particle image velocimetry: a practical guide*. 2018: Springer.

91. Clemens, N.T. and P.H. Paul, *Effects of heat release on the near field flow structure of hydrogen jet diffusion flames.* Combustion and Flame, 1995. **102**(3): p. 271-284.

92. Lauer, M. and T. Sattelmayer. *On the Adequacy of Chemiluminescence as a Measure for Heat Release in Turbulent Flames With Mixture Gradients*. in *ASME Turbo Expo 2009: Power for Land, Sea, and Air*. 2009.

93. Nair, V., et al., *High-Frequency Imaging of a Reacting Jet in Crossflow*. Bulletin of the American Physical Society, 2018. **63**.

94. Mei, R., *Velocity fidelity of flow tracer particles.* Experiments in Fluids, 1996. **22**(1): p. 1-13.

95. Meier, W., et al., *Raman/Rayleigh/LIF measurements in a turbulent CH4/H2/N2 jet diffusion flame: experimental techniques and turbulence–chemistry interaction.* Combustion and Flame, 2000. **123**(3): p. 326-343.

96. Goodwin, D.G., *Cantera C++ user's guide.* California Institute of Technology, 2002.

97. Cheng, T.S., J.A. Wehrmeyer, and R.W. Pitz, *Simultaneous temperature and multispecies measurement in a lifted hydrogen diffusion flame.* Combustion and Flame, 1992. **91**(3): p. 323-345.

98. Lecuona, A., U. Ruiz-Rivas, and J. Nogueira, *Simulation of particle trajectories in a vortex-induced flow: application to seed-dependent flow measurement techniques.* Measurement Science and Technology, 2002. **13**(7): p. 1020-1028.

99. Wieneke, B., *PIV uncertainty quantification from correlation statistics.* Measurement Science and Technology, 2015. **26**(7): p. 074002.

100. Muniz, L., R. Martinez, and M. Mungal, *Application of PIV to turbulent reacting flows*, in *Developments in Laser Techniques and Fluid Mechanics*. 1997, Springer. p. 411-424.

101. Sung, C.J., C.K. Law, and R. L Axelbaum, *Thermophoretic Effects on Seeding Particles in LDV Measurements of Flames.* Combustion Science and Technology, 1994. **99**(1-3): p. 119-132.

102. GOMEZ, A. and D.E. ROSNER, *Thermophoretic effects on particles in counterflow laminar diffusion flames.* Combustion Science and Technology, 1993. **89**(5-6): p. 335-362.

103. Epps, B., *Review of Vortex Identification Methods*, in *55th AIAA Aerospace Sciences Meeting*. 2017.

104. Kolár, V., *Compressibility Effect in Vortex Identification.* AIAA Journal, 2009. **47**(2): p. 473-475.

105. Hunt, J.C., A.A. Wray, and P. Moin, *Eddies, streams, and convergence zones in turbulent flows.* 1988.

106. Bauer, D. and R. Peikert. *Vortex tracking in scale-space*. in *Proceedings of the symposium on Data Visualisation 2002*. 2002.

107. Gharib, M., E. Rambod, and K. Shariff, *A universal time scale for vortex ring formation.* Journal of Fluid Mechanics, 1998. **360**: p. 121-140.

108. Graftieaux, L., M. Michard, and N. Grosjean, *Combining PIV, POD and vortex identification algorithms for the study of unsteady turbulent swirling flows.* Measurement Science and technology, 2001. **12**(9): p. 1422.

109. Chan, T.F. and L.A. Vese, *Active contours without edges.* IEEE Transactions on image processing, 2001. **10**(2): p. 266-277.

110. Zhou, J., et al., *Mechanisms for generating coherent packets of hairpin vortices in channel flow*. Journal of Fluid Mechanics, 1999. **387**: p. 353-396.

111. Lourenco, L. and A. Krothapalli, *On the accuracy of velocity and vorticity measurements with PIV.* Experiments in Fluids, 1995. **18**(6): p. 421-428.

112. Foucaut, J.M. and M. Stanislas, *Some considerations on the accuracy and frequency response of some derivative filters applied to particle image velocimetry vector fields.* Measurement Science and Technology, 2002. **13**(7): p. 1058-1071.

113. Jimenez, J., M. Cogollos, and L.P. Bernal, *A perspective view of the plane mixing layer.* Journal of Fluid Mechanics, 1985. **152**: p. 125-143.

114. Kyle, D.M. and K.R. Sreenivasan, *The instability and breakdown of a round variable-density jet.* Journal of Fluid Mechanics, 1993. **249**: p. 619-664.

115. Yule, A.J., *Large-scale structure in the mixing layer of a round jet.* Journal of Fluid Mechanics, 1978. **89**(3): p. 413-432.

116. Moore, D.W. and P.G. Saffman, *The instability of a straight vortex filament in a strain field.* Proceedings of the Royal Society of London. A. Mathematical and Physical Sciences, 1975. **346**(1646): p. 413-425.

117. Hernan, M.A. and J. Jimenez, *Computer analysis of a high-speed film of the plane turbulent mixing layer.* Journal of Fluid Mechanics, 1982. **119**: p. 323-345.

118. Bernal, L.P., *The coherent structure of turbulent mixing layers. I. Similarity of the primary vortex structure. II. Secondary streamwise vortex structure*. 1981,

CALIFORNIA INST OF TECH PASADENA GRADUATE AERONAUTICAL LABS.

119. Brown, G.L. and A. Roshko, *On density effects and large structure in turbulent mixing layers.* Journal of Fluid Mechanics, 1974. **64**(4): p. 775-816.

120. Pozrikidis, C. and J.J. Higdon, *Nonlinear Kelvin–Helmholtz instability of a finite vortex layer.* Journal of Fluid Mechanics, 1985. **157**: p. 225-263.

121. Dimotakis, P.E., *Two-dimensional shear-layer entrainment.* AIAA Journal, 1986. **24**(11): p. 1791-1796.

122. D'Ovidio, A. and C.M. Coats, *Organized large structure in the post-transition mixing layer. Part 1. Experimental evidence.* Journal of Fluid Mechanics, 2013. **737**: p. 466-498.

123. Dixit, H.N. and R. Govindarajan, *Stability of a vortex in radial density stratification: role of wave interactions.* Journal of Fluid Mechanics, 2011. **679**: p. 582-615.

124. Sipp, D., et al., *Stability of a vortex with a heavy core.* Journal of Fluid Mechanics, 2005. **526**: p. 67-76.

125. Gans, R.F., *On the stability of shear flow in a rotating gas.* Journal of Fluid Mechanics, 1975. **68**(2): p. 403-412.

126. Davitian, J., et al., *Transition to global instability in transverse-jet shear layers.* Journal of Fluid Mechanics, 2010. **661**: p. 294-315.

127. Grinstein, F.F. and K. Kailasanath, *Exothermicity and Relaminarization Effects in Unsteady Reactive Square Jets.* Combustion Science and Technology, 1996. **113**(1): p. 291-312.

128. Narasimha, R. and K.R. Sreenivasan, *Relaminarization of Fluid Flows*, in *Advances in Applied Mechanics*, C.-S. Yih, Editor. 1979, Elsevier. p. 221-309.

129. Berkooz, G., P. Holmes, and J.L. Lumley, *The Proper Orthogonal Decomposition in the Analysis of Turbulent Flows.* Annual Review of Fluid Mechanics, 1993. **25**(1): p. 539-575.

130. Lumley, J.L., *Stochastic tools in turbulence*. 2007: Courier Corporation.

131. Taira, K., et al., *Modal Analysis of Fluid Flows: An Overview*. AIAA Journal, 2017. **55**(12): p. 4013-4041.

132. Meyer, K.E., J.M. Pedersen, and O. ÖZcan, *A turbulent jet in crossflow analysed with proper orthogonal decomposition.* Journal of Fluid Mechanics, 2007. **583**: p. 199-227.

133. Gevorkyan, L., et al., *Influence of the velocity field on scalar transport in gaseous transverse jets.* Journal of Fluid Mechanics, 2017. **834**: p. 173-219.

134. Pavithran, S. and L. Redekopp, *The absolute-convective transition in subsonic mixing layers.* Physics of Fluids A: Fluid Dynamics, 1989. **1**(10): p. 1736-1739.

135. Jendoubi, S. and P.J. Strykowski, *Absolute and convective instability of axisymmetric jets with external flow.* Physics of Fluids, 1994. **6**(9): p. 3000-3009.